UNIVERSITÉ DU QUÉBEC

THÈSE PRÉSENTÉE À
L'UNIVERSITÉ DU QUÉBEC À CHICOUTIMI
COMME EXIGENCE PARTIELLE
DU DOCTORAT EN INGÉNIERIE

PAR

GÉZA WALTER

COMPARISON OF DIFFERENT FLAME TYPES

JUIN 2006

Bibliothèque Paul-Émile-Boulet

UQAC Université du Québec à Chicoutimi

Mise en garde/Advice

Afin de rendre accessible au plus grand nombre le résultat des travaux de recherche menés par ses étudiants gradués et dans l'esprit des règles qui régissent le dépôt et la diffusion des mémoires et thèses produits dans cette Institution, **l'Université du Québec à Chicoutimi (UQAC)** est fière de rendre accessible une version complète et gratuite de cette œuvre.

Motivated by a desire to make the results of its graduate students' research accessible to all, and in accordance with the rules governing the acceptation and diffusion of dissertations and theses in this Institution, the **Université du Québec à Chicoutimi (UQAC)** is proud to make a complete version of this work available at no cost to the reader.

L'auteur conserve néanmoins la propriété du droit d'auteur qui protège ce mémoire ou cette thèse. Ni le mémoire ou la thèse ni des extraits substantiels de ceux-ci ne peuvent être imprimés ou autrement reproduits sans son autorisation.

The author retains ownership of the copyright of this dissertation or thesis. Neither the dissertation or thesis, nor substantial extracts from it, may be printed or otherwise reproduced without the author's permission.

****

Directeur de thèse : André CHARETTE, Université du Québec à Chicoutimi (UQAC)

Codirecteur : László I. KISS, Université du Québec à Chicoutimi (UQAC)

Soutenue le 15 juin 2006

****

Membres du Jury

M.	M. BOUAZARA	Professeur à l'Université du Québec à Chicoutimi	Président du jury
MM.	A. CHARETTE	Professeur à l'Université du Québec à Chicoutimi	Examinateur
	L. I. KISS	Professeur à l'Université du Québec à Chicoutimi	Examinateur
	J. BOULANGER	Chercheur scientifique au CNRC, Ottawa	Examinateur
	Y. KOCAEFE	Professeur associé à l' Université du Québec à Chicoutimi	Examinateur
M. G. BOUCHARD		Représentant de la doyenne des études de cycles supérieures et de la recherche, UQAC	

SUMMARY

Gas fuelled burners are frequently used as heat sources in metallurgy. The heat transfer between the flame and charge in a furnace depends on the type of the burner, its adjustment as well as on its position and orientation relative to the charge. The terminology used to classify industrial burners often reflects certain easy-to-perceive characteristics of the flame produced by them. An experimental study was performed in order to clarify the effects of burner and flame types and flame-object geometry on the heat transferred to the charge as well as on the mechanism of the heat transfer. In this study, short and long, low and high velocity flames together with a so-called "envelope" type flame were compared experimentally. The luminosity of the flames varied strongly among the different settings. One of the two burners used in the study was a traditional, generic device while the other was a low NO_x, injection type burner. Three different burner-target configurations were analysed and compared to each other, namely the parallel firing burner to the horizontal surface, the downward-firing (inclined) flame and the direct flame impingement on the corner of a solid charge. The study is completed with the analysis of the temperature and velocity fields in the gas phase around the objects. The analysis offers help for the better selection of burners for various industrial heating jobs.

RÉSUMÉ

Les brûleurs au gaz sont fréquemment utilisés comme source de chaleur dans la métallurgie. Dans un four, le transfert de chaleur entre la flamme et la charge dépend du type de brûleur, de son ajustement et ainsi que de sa position et son orientation par rapport à la charge. La terminologie en cours d'utilisation pour classifier des brûleurs industriels est souvent reliée à certaines caractéristiques perceptibles des flammes produites par des brûleurs. Une étude expérimentale a été réalisée afin de clarifier les effets du brûleur, du type de flammes et de la géométrie relative de la flamme et de la charge sur le mécanisme de transfert de chaleur vers la charge.

Dans la présente étude, des flammes courte, longue, à basse et à haute vitesses ont été comparées expérimentalement avec le type de flamme, soi-disant, « enveloppe ». La luminosité des flammes a varié lors des différents ajustements. Un des deux brûleurs utilisés dans cette étude était un brûleur traditionnel (conventionnel), tandis que l'autre était un brûleur à faible production de NO_x. Trois différentes configurations de la flamme par rapport à la charge ont été analysées et comparées entre elles, plus particulièrement lorsque la flamme était parallèle par rapport à la surface horizontale, ou lorsque la flamme était inclinée vers la surface horizontale à la base du four, et finalement lorsque la flamme était

dirigée directement sur la charge représentée par l'arête d'une marche chanfreinée. L'étude a été complétée par l'analyse de la distribution des vitesses et des températures de la phase gazeuse contournant l'objet. L'analyse présentée dans cette étude fournit des connaissances et des outils en vue d'une meilleure sélection de brûleurs pour différents travaux de chauffage industriels.

ACKNOWLEDGEMENTS

This PhD project is part of the research activities of the University Research Center on Aluminium (CURAL) at the University of Quebec at Chicoutimi (UQAC).

I would like to use this opportunity to thank those who helped me complete this thesis. First, I would like to express my sincere appreciation to one of my directors, Professor, Dr. László István Kiss, for his supervision, guidance, support and patience, as well as his generous help during my PhD studies. I would also like to express my gratitude to my director, Professor, Dr. André Charette, for his guidance and help during my project.

The author would also like to thank the technicians of CURAL, especially Mr. Patrice Paquette, as well as Mr. Julien Tremblay and Mr. Sylvain Desgagné for their great assistance during the course of the experimental work. I would like to express my appreciation to my colleagues, particularly Dr. Vincent Goutière, and also to Mr. Saska Zanchetti. I am also indebted to the technicians of the Anti-icing Materials International Laboratory (LIMA) for their contributions to my experimental work.

I would like to show my deepest appreciations to all my friends and collaborators who helped and encouraged me during my work. I would like to record my gratitude to all the members of the CURAL for their sincere help and creation of an enjoyable working

atmosphere, the members of the Department of Applied Sciences (DSA), and several members of UQAC.

I would like to express my gratitude to Dr. Gyula Gróf, professor of Technical University of Budapest (BME), to Dr. Ferenc Horváth and Mr. György Dobozi, of the GEA-EGI Inc. and to Dr. Tibor Kapros, TUKI Inc. for their warm reception during my internship in Hungary.

Financial (in the form of scolarship) and in kind support received from the Ministry of Education of Québec (MEQ), the Research Group for Process and Systems Engineering (GRIPS), the University Research Center on Aluminium (CURAL), the Quebec Aluminium Research and Development Center (CQRDA), the Alcan's Arvida Research and Development Center (ARDC) and the North American Mfg. Co. are gratefully acknowledged.

Finally, I would like to record my warmest thanks to my spouse Berta Simó, whose indescribable patience and encouraging words were essential to the completion of this project. I would express also my sincere thanks for the encouragement of my parents and my family.

TABLE OF CONTENTS

LIST OF FIGURES

LIST OF TABLES

NOMENCLATURE

Symbol	Description	Units
A	area	m^2
b	radial expansion of a jet flow	m
c_p	specific heat at constant pressure	J/(kg K)
c_v	specific heat at constant volume	J/(kg K)
C_v	molar heat capacity (const. vol.)	J/(kmol K)
C	Pitot coefficient	dimensionless
d	diameter	m
d_n	nozzle diameter	m
$d_{n,eqv}$	equivalent nozzle diameter	m
D	characteristic diameter	m
D_{kk}	"self" diffusion coefficient	m^2/s
D_m	molecular (mass) diffusivity	m^2/s
E	emissive power	W/m^2
f	degree of freedom	dimensionless
F_{1-2}	radiation view factor from surface 1 to surface 2	dimensionless
F_c	conversion factor	V/kW
g	gravitational acceleration	m/s^2
G	momentum flux	$(kg\ m)/s^2$
h	convection heat transfer coefficient	$W/(m^2\ K)$
h^C	chemical enthalpy (formation enthalpy or enthalpy of chemical bond)	J/kg
h^S	sensible enthalpy = $\int c_p dt$	J/kg
h^T	total enthalpy = $h^C + h^S$	J/kg
I	radiation intensity	$W/(m^2\ sr)$

k	thermal conductivity	W/(m K)
k	reaction rate coefficient	*
k_B	Boltzmann constant ($1.380658 \cdot 10^{-23}[J/K]$)	J/K
K	equilibrium constant	*
K_a	absorption coefficient for radiation	dimensionless
K_s	scattering coefficient for radiation	dimensionless
l	length	m
l_f	distance from the nozzle mouth to the fully developed region of the jet	m
lj	length of the jet to the stagnation point	m
l_v	potential core length for velocity	m
L	characteristic length	m
L	dimensionless distance between the burner and target (stagnation point) (l_j/d_n)	dimensionless
L	radiation path length through a gas	m
Le	Lewis number ($k/\rho c_p D_m$)	dimensionless
m	mass	kg
$\dot{m}$	mass flow rate	kg/s
M	molar mass	[kg/kmol]
n	exponent of the empirical power law function	dimensionless
N_A	Avogadro number $\left(6.0221367 \cdot 10^{23}[1/mol]\right)$	1/mol
Nu	Nusselt number (h L/k)	dimensionless
p	pressure	Pa
Pr	Prandtl number (c_p μ/k)	dimensionless
q	heat flow	kW
q''	heat flux	W/m^2
q_f	burner firing rate	kW
$\bar{q}^o$	enthalpy of combustion or heat of combustion	kJ/kmol
Q_{vol}	volumetric flow rate	m^3/s
r	radial distance from the burner centerline	m
$r_{1/2}$	radius at which a measured value reaches one half of its maximum value	m
R	dimensionless radius (r/d_n)	dimensionless
$\Re$	universal gas constant (8314,41 J/(kmol K))	J/(kmol K)

* Unity depends on the stoichiometry of the chemical reaction

Ra	Rayleigh number ($g\tilde{\beta}q_f l_j^2 / \rho c_p \upsilon^3$)	dimensionless
Re	Reynolds number (ρ u D /μ)	dimensionless
s	air layer thickness	m
S	source term	W/m^3
t	temperature	K or °C
t	time	s
T	absolute temperature	K
T^*	reduced temperature	dimensionless
Tu	turbulence intensity	dimensionless
u	horizontal (axial) velocity	m/s
u_s	velocity of secondary stream	m/s
u_0	velocity of primary stream	m/s
u_n	horizontal velocity at any radial location of the nozzle exit plane	m/s
u_x	horizontal velocity at any radial location of the axial distance x	m/s
$\overline{u_n}$	average horizontal velocity in the nozzle exit plane	m/s
$u_{n,\max}$	maximal (centerline) velocity at the nozzle exit	m/s
$u_{x,\max}$	maximal horizontal velocity at any one axial station	m/s
U	voltage	V
v	velocity	m/s
V	volume	m^3
x	axial distance from the burner along the length of the furnace	m
x	characteristic length, distance from the leading edge	m
x_{virt}	distance of the virtual origin of the jet from the burner	m
x'	axial distance from the virtual origin of the jet along the furnace length	m
x_{tc}	depth of the thermocouple tip embedded in the refractories	m
X	mole fraction or molar density	dimensionless
X_v	dimensionless potential core length for velocity (l_v/d_n)	dimensionless
y	distance along the furnace width	m
z	distance along the furnace height	m
Z_{rot}	rotational relaxation collision number	dimensionless

Greek Symbols

α	absorptivity	dimensionless

β	velocity gradient	s^{-1}
$\tilde{\beta}$	volume coefficient of expansion	K^{-1}
γ	turbulence enhancement factor	dimensionless
ε	emissivity	dimensionless
ε	Lennard-Jones potential well depth	J
η	ratio of the jet velocity to the secondary stream velocity ($\eta = u_s/u_0$)	dimensionless
Θ	yaw angle	degree
κ	half angle	degree
λ	fuel mixture or excess air ratio	dimensionless
λ	dipole moment	Debye*
λ	wavelength	μm
μ	dynamic viscosity	kg/(m s)
ν	kinematic viscosity	m^2/s
ρ	density	kg/m^3
ρ	reflectivity	dimensionless
ρ_n	density at the nozzle exit	kg/m^3
ρ_∞	bulk density, free stream density	kg/m^3
σ	Stefan-Boltzmann constant ($5.67 \cdot 10^{-8}$ $W/m^2 K^4$)	$W/m^2 K^4$
σ	collision diameter	m, angstrøm
ϕ	equivalence ratio = $\frac{\text{stoichiometric oxygen / fuel volume ratio}}{\text{actual oxygen / fuel volume ratio}}$	dimensionless
$\phi_{i,j}$	interaction parameter between gas components	dimensionless
Ω	oxidizer composition = $\frac{O_2 \text{ volume in the oxidizer}}{O_2 + N_2 \text{ volume in the oxidizer}}$	dimensionless
$\Omega_{i,i}^{(2,2)*}$	collision integral	m^2

Subscripts and superscripts

atm	atmospheric
b	stagnation body or target
b	backward
conv	convective heat transfer

---

* Note : a Debye is 10^{-18} $cm^{3/2}erg^{1/2}$. (1 erg = 10^{-7}Joule)

corr	correction
e	edge of boundary layer
e	entrained
eqv	equivalent diameter
ext	external
f	forward
g	gas
int	internal
∞	ambient conditions
j	jet
l	load
max	maximum
mano	manometer
n	burner nozzle
p	primary stream
$\bar{p}$	see definition on page 56 (Eq. 1.26)
$\bar{\bar{p}}$	see definition on page 56 (Eq. 1.25)
rad	thermal radiation
rec	recovery temperature
ref	reference temperature
s	stagnation point
s	secondary stream
s	surface
tot	total heat transfer (radiation + convection)
w	wall (target surface)

Common abbreviations

EMF	electromotive force
HVI	high velocity injection
LDV	laser Doppler velocimeter
LNI	low NO_x injection
SNR	signal-to-noise ratio

INTRODUCTION

The Research Group for Process and Systems Engineering (GRIPS) at the University of Quebec at Chicoutimi (UQAC) developed a testing facility for gas-fired burners more than a decade ago. The potentials offered by this facility attracted the interest of the research personnel at Alcan's Arvida Research and Development Center (ARDC) who needed accurate information on the heating patterns produced by various burners on aluminium charges in both melting and melting/casting furnaces.

The marketing of burners for aluminium melter and melter-holder furnaces shifted historically from high-radiation to high-convection (high-velocity) through high luminosity or fiber burners as each of the principal manufacturers fought for market share. The claims that certain burners are "better" than the others are not supported by sufficient, quantitative description of their heat transfer characteristics.

The introduction of a radically different, so-called "envelope flame" technology into the North American and European market by the North American Mfg Ltd. triggered a cooperative university-industry research project at UQAC. With the financial support of Alcan International, the Quebec Aluminium Research and Development Center (CQRDA), and with the in-kind and personal support of North American Mfg Inc, the project started at

the beginning of 2000.

From February to June 2000, I participated in the preparation of this project in the framework of my Master thesis. From fall of 2000 until 2005, a scholarship of the Ministry of Education of Québec (MEQ) permitted me to participate in this project as a framework of my PhD study under the direction of the Professors László István Kiss and André Charette.

The main motivation of the project is to obtain independent and as accurate as present measurement technology permits data about the flame-charge heat transfer for various burner designs and adjustments. An important aspect of the project is the analysis of the thermal performance of the environmentally friendly combustion technologies like for example the above mentioned "envelope flame" produced by a low NO_x injection (LNI) burner.

Besides the overall heat transfer characteristics, we aimed at the measurement of the distribution of the local heat transfer rates, at the determination of the convective and radiative components as well as at the analysis of the velocity and temperature distributions and stack gas composition.

The experimental work can be divided into three phases in pursuance of the experimental works for different flame-target configurations. The objective of the first part of the work was to determine the spatial distribution of the total heat flux as well as its convective and radiative components under horizontally fired flames. The burners are installed in a modular design experimental furnace with a square cross section. The heat fluxes are measured along the horizontal, cooled bottom surface of the furnace. The heat

flux measurements were supported with detailed velocity and gas temperature measurements. The gas composition was also recorded. Four different flame types were measured.

The objective of the second phase of the work was to determine the spatial distribution of the heat flux by downward firing (inclined) burners. In this experimental series, the burner was tilted at 11.4° downward; the flame hits the calorimetric plates. This flame-object impingement point is located about the centerline of the furnace. This is not a direct flame-object impingement, with perpendicular impact. Similar to the first phase, the same four flame types were studied.

In the third experimental phase, the objective was to determine the spatial distribution of the heat flux in the case of direct perpendicular flame-object impingement. The total heat fluxes, as well as its convective and radiative components were also measured in the stagnation point. The heat flux measurements are supported with detailed velocity and gas temperature measurements.

The thesis is composed of five chapters. The first chapter gives a general overview of the fluid dynamics and of the heat transfer mechanisms of flames. The experimental program, the applied methods and instruments are presented in chapter two. The third chapter presents all the results except the heat fluxes. The heat flux results obtained in the three test phases are presented and discussed in chapter four. In addition, general comparison is given. In the last chapter, the conclusions and suggested future works are summarized.

CHAPTER 1.
FLUID DYNAMICS, HEAT TRANSFER AND POLLUTANT FORMATION IN VARIOUS FLAME TYPES

1.1 Fluid dynamics of jets

1.1.1. Free jets

The term free jet describes motions which are not affected by the presence of solid boundaries. A round jet, issuing from a nozzle as in the case of the high velocity and envelope flames produced by the LNI burner, is one example of these kinds of flows (Figure 1.1). In all these cases, velocity gradients are generated. If the Reynolds number is sufficiently high, the flow is unstable and zones of turbulent mixing are developed.

The analysis of free turbulent motions is in general somewhat easier than that of wall turbulence. In free turbulence, the viscous (molecular) shear stresses usually can be neglected in comparison with the turbulent eddy stresses throughout the entire flow fields. On the contrary, in conduit flow due to the damping of turbulence by the wall, the existence of the viscous stresses in the laminar sublayer must be considered. In addition, in jets and wakes in large bodies of fluid, it is usually found that the pressure gradient in the direction of motion is zero, except thoses cases when an obstacle is placed in the flow. This latter is

the case at the impingement arrangement and partially also at inclined burner position, which will be discussed later[1].

In Figure 1.1, a special example is shown where a gas jet is immersed in an ambient fluid at rest through an infinitesimally small nozzle. Due to this particular geometry, the flow is immediately turned into fully developed turbulent motion. The moving jet entrains the surrounding fluid. At the boundaries, both mass and momentum exchanges occur which causes a continuous spread out of the jet. The straight lines are the jet boundaries, which in three dimensions have a conical form. For circular jets, the relation $b = const \cdot x$ is valid.

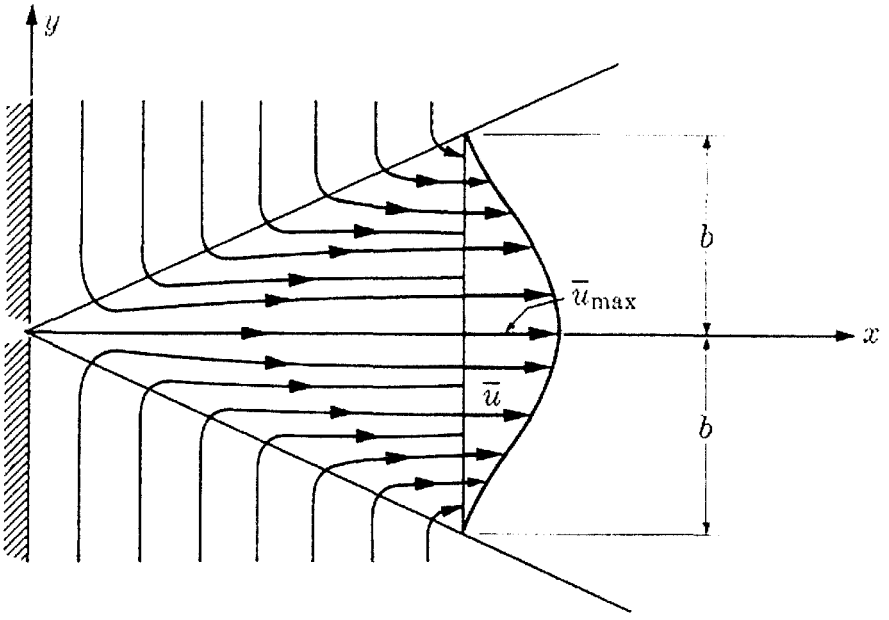

Figure 1.1. Free turbulent flow : velocity distribution in a fully developed immersed jet[5]

1.1.2. Confined jets

For an enclosed jet, such as a jet issuing into a combustion chamber, two basically different cases can be distinguished. In the first case, there is ample supply of secondary

flow surrounding the jet so that entrainment by the jet is uninhibited until it expands to reach the wall of the combustion chamber. In the second case, the secondary flow is less than that which the jet can entrain. In this latter case, a recirculating flow is set up. In spite of several influencing factors, a rule of thumb can be applied. Recirculation form, when the nozzle diameter is greater than 1/10 of the duct diameter[2].

1.1.3. Bibliographic review

The round free jet has been the subject of many experimental investigations. The earlier basic experiments have been concerned with a jet issuing in a still ambient fluid (Trüpel, Förthmanns, etc.). The first to make an extensive investigation of a jet in a secondary stream, which on the other hand is the more general case, were Forstall[7] and Shapiro. Later Acharya, and Alexander et al. made similar experiments. All these cases can be considered as constant density systems. In 1977, Martin[17] gave a comprehensive survey of literature, which is chiefly destined for the heat and mass transfer in impinging cold gas jets.

Experiments on heated jets (without chemical reaction) have been made by Ruden, Corrsin, Corrsin and Uberoi[19], and by Hinze and Van der Hegge Zijnen[9,18]. In all their experiments, the temperature and concentration differences were sufficiently small to exclude appreciable density effects.

For non-constant density systems, the concept of an equivalent orifice diameter was introduced by Thring and Newby[10], which will be briefly discussed later. Non-constant density systems were also investigated by Keagy and Weller[20], Corrsin and Uberoi[19],

Sunavala, Hulse, and Thring[21], where heated fluid jets were injected in a second fluid of ambient temperature[1,2,3,5,6,14].

The confined jets have been studied, theoretically and experimentally, by Thring and Newby[66], Craya and Curtet[67], Barchilin and Curtet[68], Becker, Hottel and Wiliams, Wingfield and Martin as well as by Beér and Chigier[2].

Flame jets in combustion processes were investigated by Beér and Chigier[4], Anderson and Stresino[22], Fay[24], Reed[25], Woodruff and Giedt[23], Popiel, van der Meer and Hoogendoorn[13]. Studies, related mainly to the heat transfer in impinging jets, are presented below in this chapter in Section 1.2.

1.1.4. Description of round free jets and their velocity profiles in constant density system

When fluid emerges from a nozzle, it interacts with the fluid from the surrounding to form a jet. Jet flows are classified as fully separated flows because, after separation from solid surfaces, the solid surfaces no longer play a significant role in their development. Figure 1.2 represents regions of turbulent free jets. Immediately downstream from the nozzle there is a region, the potential core (inner dotted line), within which the velocity and concentration of nozzle fluid remain unchanged. At the flow outlet, the velocity distribution is nearly uniform and can be described by an empirical power law. The axial location of the core's peak was specified as the "critical point" which is referred as l_v. This is the farthest axial distance from the burner where the centerline velocity is the same as it was at the burner outlet. The dimensionless form of l_v is X_v, which is the ratio of the core length to the

nozzle diameter ($X_v = l_v / d_n$). Outside this region a free boundary layer develops in which momentum and mass are transferred perpendicular to the direction of flow. The fully developed region of the jet is preceded by a transition region. The outer dashed lines represent the nominal boundaries of the jet, that is, the points where the horizontal velocities u are some arbitrary small fraction of the velocity on the centerline of the jet. If these outer dashed lines are extended in the upstream direction they have an intersection on the x axis. This point of intersection is the virtual origin of the jet and its distance from the nozzle exit is marked by x_{virt}.

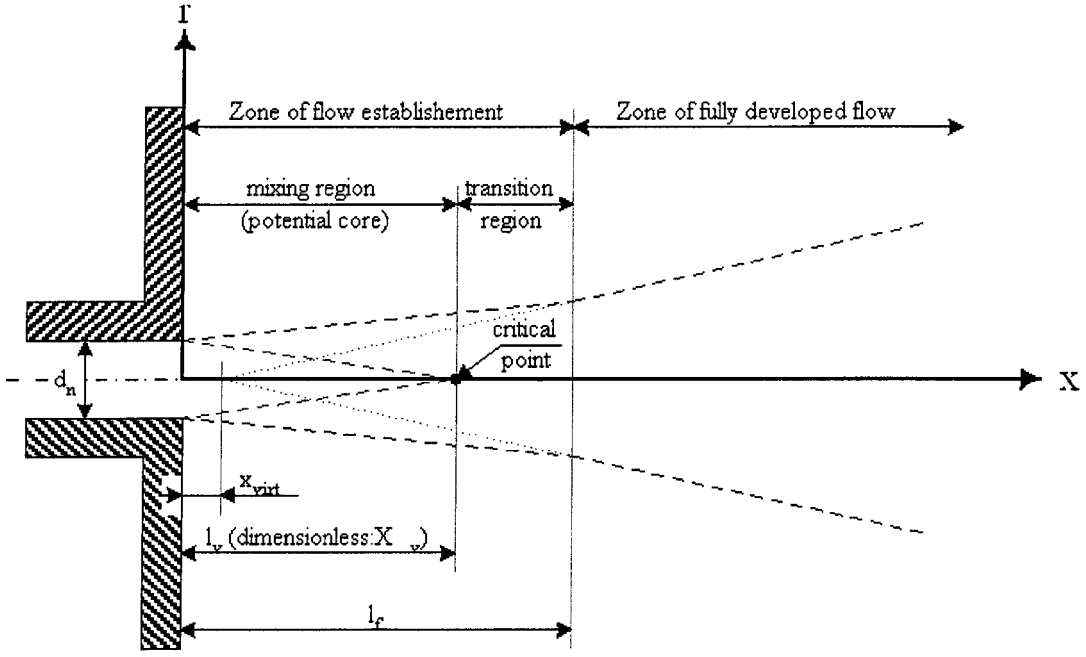

Figure 1.2 Regions of a jet

The lengths of the potential core (l_v) and transition regions (l_f) are differently given in the literature. After Beér and Chigier[2], the length of the potential core is 4 to 5 nozzle diameters, while the length of the transition region is 10 nozzle diameters. According to

Forstall[7], the length of the core region is determined mainly by the parameter $\eta = u_s/u_0$; it increases with increasing η. The following empirical relation is also given

$$\frac{l_v}{d_n} = 4 + 12\eta$$

Eq. 1.1

Forstall carried out his measurements in the range of $\eta \cong 0.2$ to 0.5. Obviously, the relation (Eq. 1.1) cannot be applied to cases differing too much from those covered by the experiments. Hinze[3] acutely doubt the accuracy of these results. He stated that from Eq. 1.1 it follows that $l_v = 4d_n$ for $\eta = 0$, but experiments on free jets issuing in still ambient fluid have disclosed much greater values of l_v. Hereafter, Hinze[3] is citing the results of his own measurements made together with van der Hegge Zijnen[9], where the potential core length was found to be $l_v \cong 6$ to $8d_n$. Kataoka[8], later in 1985, used the following correlation to determine the dimensionless core length (X_v) which is the ratio of the core length to the nozzle diameter ($X_v = l_v/d_n$):

$$X_v = 2.82(\rho_n/\rho_\infty)^{0.29}\,\mathrm{Re}_{n,X=0}^{0.07}$$

Eq. 1.2

where the indexes ∞ and n refer to the average fluid condition inside the combustion chamber, and to the nozzle exit conditions respectively as well as the index n, X = 0 refers to the centerline parameters at the nozzle exit.

After discussing the geometry of the potential core, the structure of the jet is analyzed. The fully developed regions of turbulent jets are similar, and therefore the axial and radial distributions of velocity and concentration can be described by relatively simple and

general relationships. The equation given by Beér and Chigier[4], which describes a hyperbolical velocity decay, is

$$\frac{u_{x,\max}}{u_{n,\max}} = \frac{d_{n,eqv}}{0.16(x - x_{virt})}$$

Eq. 1.3

where $d_{n,eqv}$ is the so-called equivalent nozzle diameter based on the density difference (discussed later in section 1.1.5.1) and x_{virt} is the distance to the virtual origin of the jet, (see Figure 1.2). The virtual origin of the jet is obtained by extrapolation to $\frac{u_{n,\max}}{u_{x,\max}} = 0$, as it is represented in Figure 1.3.

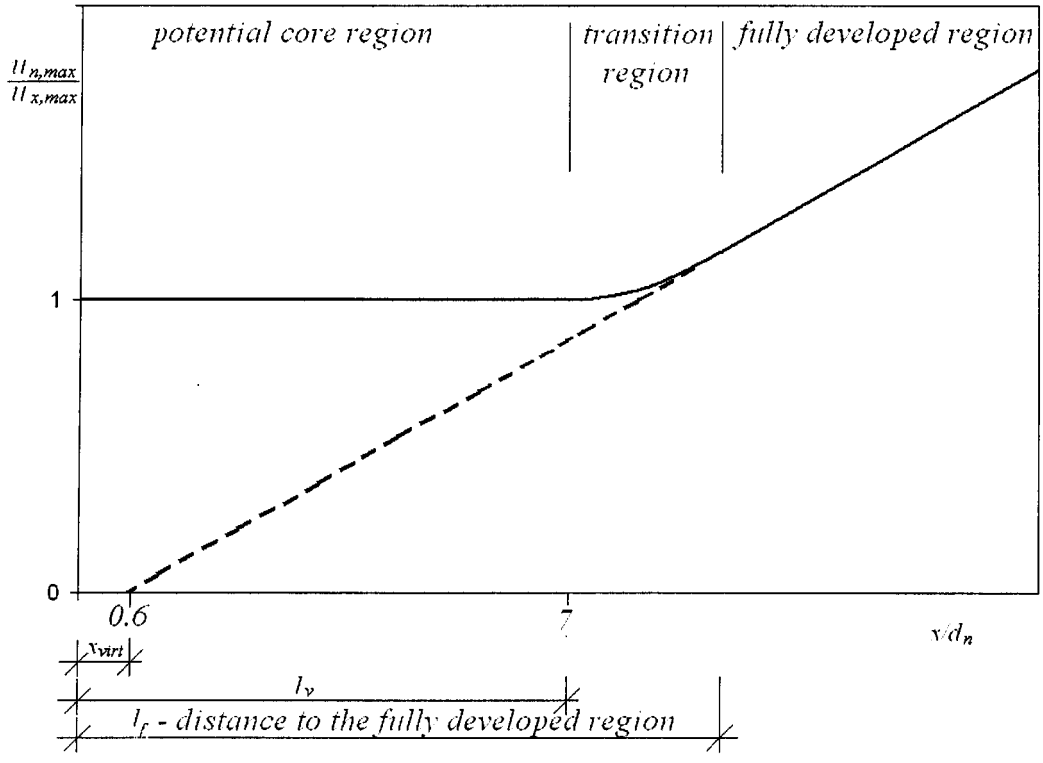

Figure 1.3 Extrapolation of nozzle velocity ratio to centerline velocity for determination of apparent origin (x_{virt}) of a round jet[2]

Hinze gives the radial velocity distribution in the zone of the established flow by

$$\frac{u_x}{u_{x,\max}} = \frac{1}{\left[1 + r^2/0.016x'^2\right]^2}$$

Eq. 1.4

as well as the longitudinal variation of the centerline velocity, which is similar to that given by Beér and Chigier[4]:

$$\frac{u_{x,\max}}{u_{n,\max}} = 6.4\left(\frac{d_n}{x'}\right)$$

Eq. 1.5

In the above equations, the longitudinal distance x' is measured from the geometrical origin of similarity which, as shown in Figure 1.4, is a distance of 0.6 d_n from the actual origin of the jet. From Eq. 1.5, the jet is fully developed if $x' = 6.4d_n$, and hence the distance $l_v = 6.4d_n + 0.6d_n = 7d_n$. So, while Beér and Chigier[2] received the virtual origin of the jet by extrapolation (Figure 1.3), Hinze and van der Hegge Zijnen[3] fixes it to the nozzle diameter.

If we introduce a translated coordinate system x-r whose origin is located at the actual origin of the jet, we obtain:

$$\frac{u_{x,\max}}{u_{n,\max}} = 6.4\left(\frac{d_n}{x'}\right) = 6.4\frac{d_n}{x - 0.6d_n}$$

Eq. 1.6

Forming its reciprocal value, we get:

$$\frac{u_{n,\max}}{u_{x,\max}} = 0.16\left(\frac{x}{d_n}\right) - 0.094$$

Eq. 1.7

which is also represented graphically on Figure 1.3. Eq. 1.7 is valid for $\frac{x}{d_n} = 8$ to 20.

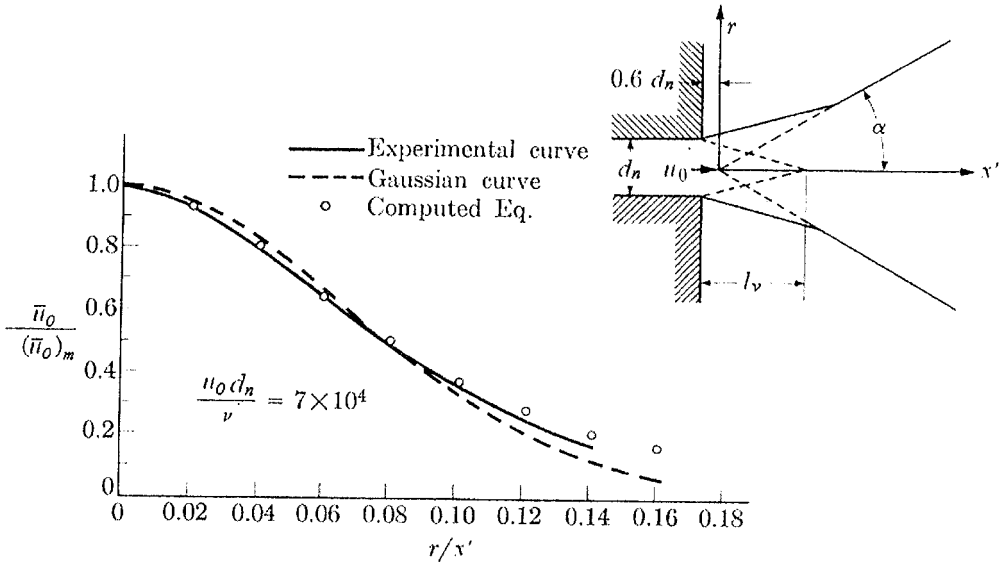

Figure 1.4 Radial velocity distribution in a round jet[1,3]

1.1.5. Description and velocity profiles of jets in non constant density systems

1.1.5.1. General notions

The general relationships, which have been developed for single, free, round and isodensity jets, can be extended to more complex systems by using the concept of an equivalent nozzle diameter. This concept was introduced by Thring and Newby[10]. In its simplest form, it is based on the conservation of momentum flux[2]. In non-constant density system, the jet entrains fluid of ambient density ρ_∞; because of the high rate of entrainment, the density of fluid within the boundaries of the jet approaches the density of the surrounding within a short distance from the nozzle exit. The momentum flux can

therefore be written in the form:

$$G_n = \frac{d_{n,eqv}^2 \pi}{4} \rho_\infty u_n^2$$

Eq. 1.8

This is equivalent to considering the fluid emerging from a nozzle of diameter $d_{n,eqv}$ with the same momentum and same initial velocity, but with the density of the entrained fluid rather than the nozzle fluid. From the above equations, it follows that:

$$d_{n,eqv} = d_n \left(\frac{\rho_n}{\rho_\infty} \right)^{\frac{1}{2}}$$

Eq. 1.9

When the mass flow rate and the momentum flux (thrust) are known, the equivalent nozzle diameter can be calculated from

$$d_{n,eqv} = \frac{2\dot{m}_n}{(G_n \pi \rho_\infty)^{1/2}}$$

Eq. 1.10

1.1.5.2. Non constant density applications in combustion processes

Non-constant density circumstances are present in almost all combustion systems. In most cases, premixed or diffusion flames are produced, while the combustion chamber is filled with hot combustion products. The density difference for perfect gases in atmospheric combustion system is due to temperature and molar mass differences. In the case of dilute gas combustion, the molar masses are nearly identical for the reacting mixture and for the combustion product, so the determining factor is not the molar mass but the temperature difference.

The biggest temperature difference, which can be produced in a traditional combustion system, is in the case when a hot jet of combustion products from a complet chemical reaction at nearly adiabatic flame temperature is injected into a cold ambient air. This phenomenon has been experimentally investigated by Popiel, van der Meer and Hoogendoorn[13] using a rapid heating tunnel burner. The created density ratio is $\rho_\infty / \rho_n = 7.6$. They proved that for such density differences, the centerline velocity decay can be described with the same equation (Eq. 1.5) as used by Hinze and van der Hegge Zijnen[3] for constant density systems ($\rho_\infty / \rho_n = 1$).

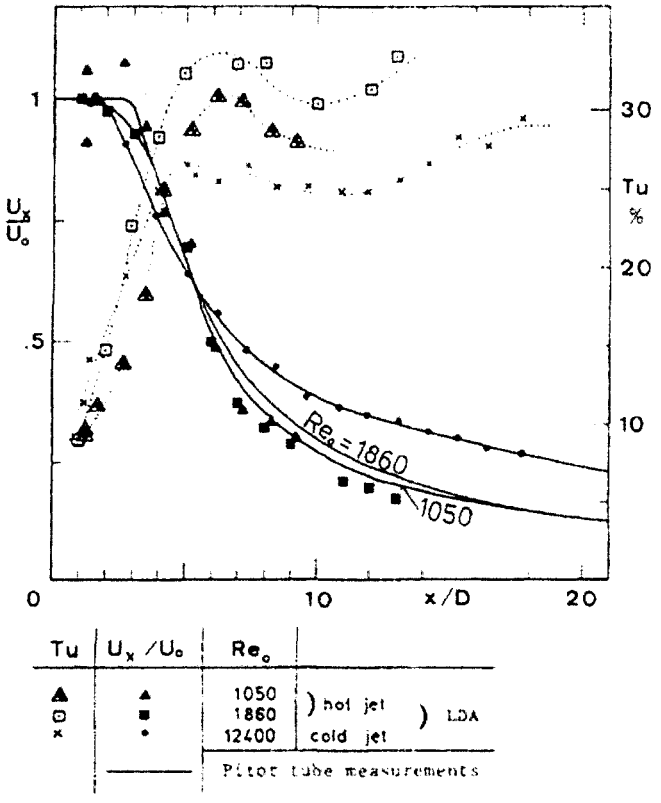

Figure 1.5 Axial relative turbulence intensity and mean velocity distributions along the axis in the experimental work of Popiel, van der Meer and Hoogendoorn[13]

Popiel, van der Meer and Hoogendoorn[13] have also investigated the axial distribution of the relative turbulence intensity using the LDA technique. Their results are represented in Figure 1.5. Near to the nozzle exit, the turbulence intensities are almost the same. Further downstream, a rapid rise in turbulence can be observed, which is coming from the mixing region and is more pronounced at higher Reynolds numbers. Over the distance of twelve nozzle diameters (after the transition region) the turbulence intensities stabilise about 30 percent. The reason of this stabilisation for fully developed turbulent flames is that downstream a certain limit (envelope of breakpoint, see Figure 1.6) the flow became stable and uniformly turbulent.

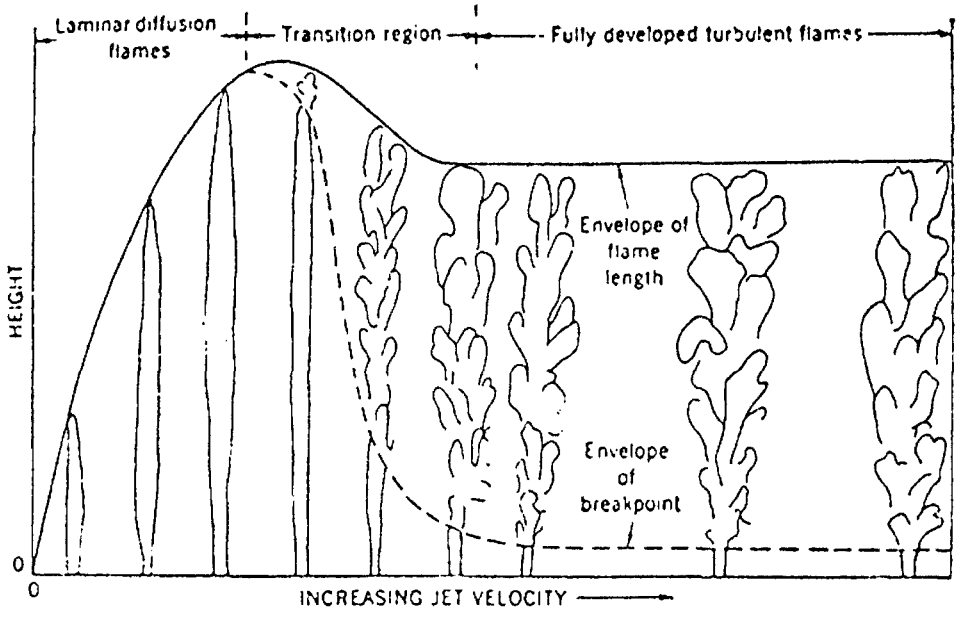

Figure 1.6 Change in flame length with increase in nozzle velocity (Hottel and Hawthorne[15])

The velocity spread is also given by Popiel, van der Meer and Hoogendoorn[13] within the distance of $x / d_n = 5$ to 17. It can be characterized by the equation

$$r_{1/2} = 0.093(x + x_{virt})$$

Eq. 1.11

which can be transformed to have the same form as given by Hinze and van der Hegge Zijnen[3] in Eq. 1.4. So one obtains

$$\frac{u_x}{u_{x,\max}} = \frac{1}{\left[1 + r^2/0.02088x'^2\right]^2}$$

Eq. 1.12

Finally, in Eq. 1.4 and Eq. 1.12 only the constant differs slightly.

1.1.6. Temperature profiles of jets

Generally, the isodensity systems are also isotherms. However, for non-constant density systems there are two basically different possibilities. The first case is when chemical reaction occurs and the second when there is no chemical reaction. Reichardt[16] made theoretical work and experimental measurements on the temperature distribution in a heated circular turbulent jet without chemical reaction. He gives the following relation between the temperature and the velocity distribution:

$$\frac{T}{T_{\max}} = \left(\frac{u}{u_{\max}}\right)^{1/2}$$

Eq. 1.13

However, in the case when chemical reaction occurs, there is an internal heat source in the jet which greatly modifies the temperature distribution, so Eq. 1.13 is no more valid. For different flame types, as the mixing conditions change, the procedure of heat deliberation changes also, so it becomes more difficult to predict the temperature distribution in a flame than the velocity distribution.

1.2 Heat transfer in flames

1.2.1. General heat transfer modes in furnaces

In this section a general overview of heat transfer modes in industrial furnaces will be given. In the metallurgical industry, the heat source is frequently assured by natural gas flames. The flames are generally enclosed in a furnace enveloped by hot refractory walls while the charge is usually situated at the bottom. From the point of view of heat transfer, a very explicative illustration is shown in Figure 1.7. The flame enters in the combustion chamber through the burner where the bounded chemical energy is released in the form of heat. As it is presented in Figure 1.7, there is a proportion of the total heat transfer, which arrives directly from the flame to the charge in the form of convection and radiation. These are marked by primary convection as well as primary radiation. Similarly to the interaction with the charge, the flame transmits also its energy toward the refractories in the form of convection and radiation. Consequently, a very significant proportion arrives to the charge by indirect or secondary radiation from the hot refractory bricks. At last, the hot combustion products exit toward the chimney where additional energy would be extracted by reducing its enthalpy using different methods.

To calculate the heat transfer in a furnace, Hottel[27] developed a relatively simple equation. The simplified model is referred to as a one-gas-zone furnace model, which assumes also that the gas is isothermal in the combustion chamber. The refractory and load temperatures are both assumed to be constant and the furnace walls are assumed to be adiabatic for radiation. The heat transfer to the load can be calculated as follows:

$$q_l = \frac{\sigma\left(T_g^4 - T_l^4\right)}{\dfrac{1-\varepsilon_l}{A_l\varepsilon_l} + \dfrac{K_s}{4K_aV} + \dfrac{1}{A_l\varepsilon_g + \dfrac{1}{\dfrac{1}{A_lF_{lw}\left(1-\varepsilon_g\right)} + \dfrac{1}{A_w\varepsilon_g}}}} + h_lA_l\left(T_g - T_l\right)$$

Eq. 1.14

where σ is the Stefan-Boltzmann constant. T_g and T_l are the absolute temperatures of the gas and load, respectively. ε_l and ε_g are the emissivities of the load and the gas, respectively. K_s and K_a are the scattering and absorption coefficients of the gas, respectively. V is the volume of the gas. F_{lw} is the view factor to the wall from the load and h_l is the convection coefficient to the load. The equation is only valid when multiple scatter is negligible ($K_sL << 1$), where L is the radiation path length through a gas.

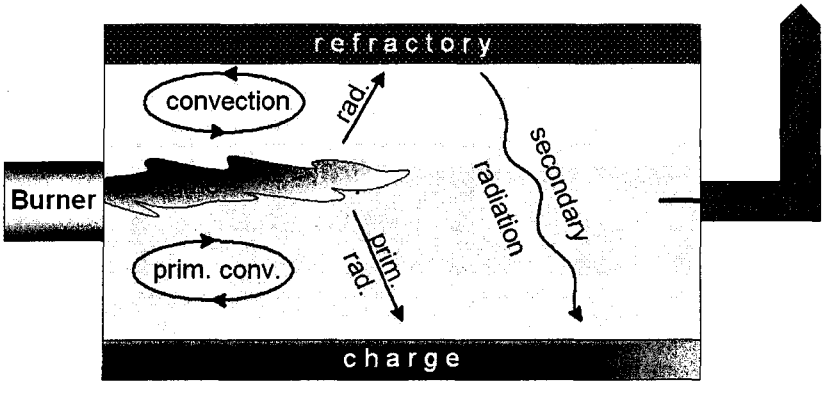

Figure 1.7. General heat transfer modes in a furnace

If the high enthalpy stack-gases are directly emitted in the ambience, important energy loss occurs. Figure 1.8 presents a Sankey diagram, which is often used to show how the energy is distributed in a combustion system. It follows obviously from this, at the first sight, surprising figure that the simplest way to improve the efficiency of the overall combustion process is the heat loss reduction over the chimney. The most widely used

technics of heat recovery are the application of regenerative and recuperative type burners. Their objective is to preheat the combustion air with the hot stack gas using different heat exchange methods. The heat recovery system determines the thermal efficiency of the system and influences the heat transfer modes and proportions because of higher flame temperatures. Energy saving by this way will no more be discussed here because it is not the objective of the present study.

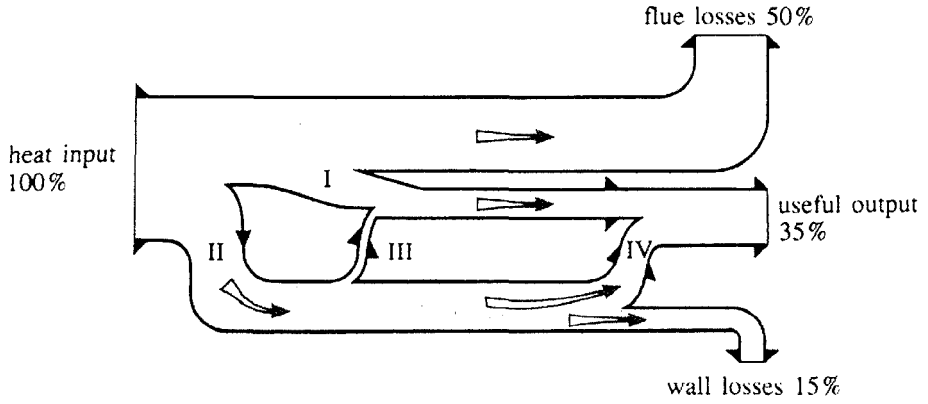

Figure 1.8. Energy flow (Sankey diagram) for a gas fired furnace with no heat recovery – I: gas radiation and convection to load; II: gas radiation and convection to walls; III: wall radiation to gas; IV: wall radiation to load[70]

The easiest way to measure the overall incident heat-flux to the charge is the method of calorimetry. This technique is presented below in section 1.2.2. The heat transfer toward the charge can be intensified by changing the flame-target orientation. Heat transfer in flame impingement is discussed in section 1.2.3.

1.2.2. Total heat flux measurement by calorimetry

In a semi-industrial experimental furnace, the charge can be represented by water

cooled calorimetric plates. The average total heat flux can be determined in the covered section, if the surface exposed to the flame is perfectly absorbent. For each calorimetric plate i, the total heat absorbed can be calculated using:

$$q''_{tot,i} = \frac{c_p \dot{m}_i \left(t_{out,i} - t_{in,i}\right)}{A_i}$$

Eq. 1.15

where $\dot{m}_i$ is the mass-flow rate of the cooling water to plate i, c_p is the average specific heat of the cooling water, $t_{out,i}$ and $t_{in,i}$ are the outlet and inlet temperatures of the cooling water to plate i and A_i is the impingement surface area of plate i.

1.2.3. Heat transfer in flame impingement

1.2.3.1. General overview

Heat transfer in impinging jets has been extensively investigated in the literature because of their overriding importance in a wide range of applications. The impinging flame jets have great importance not only in the metallurgical industry but also for exemple in the aeronautical studies or certainly in many other fields. It has to be mentioned here, for example, the parallel project in the University of Quebec at Chicoutimi, which is related to the thermal spallation of rocks. In this project, an impinging flame jet with supersonic-velocity bores through rock. The cold surface of rock is fragmented due to the important thermal stresses arising from the very intensive heat fluxes. Depending on the rock type, this method can be more economic and rapid than traditional mechanical drilling.

On the aeronautical research field, objects returning in the Earth's atmosphere and

space vehicles were simulated in laboratories with impinging, high-intensity flames. To create the highest possible temperatures and heat fluxes, fuels are generally combusted with pure oxygen. In these intensified flames, high amount of uncombusted fuel, and dissociated species were generated. As these species cool due to the impact on the relatively low temperature target surface, they exothermically combine into thermodynamically more stable species at lower temperatures. This mechanism, which is referred to as thermochemical heat release (TCHR), can be neglected in moderate temperature flames (up to 1800 K) where the Lewis number is close to unity. The Lewis number is defined as:

$$Le = \frac{k/\rho c_p}{D}$$

Eq. 1.16

that is the ratio of the thermal diffusivity to the molecular diffusivity for the fluid. The Lewis number is represented graphically as a function of the combustion product temperature as well as the oxidizer and fuel compositions in Figure 1.9 and Figure 1.10 respectively. In high-intensity flames (oxy-fuel combustion; from 1800 K up to 3200 K in the case of CH_4), the heat transfer rate caused by the thermochemical heat release on the surface, may be comparable in magnitude with the forced convection. However, in our experiments, the effect of TCHR was always negligible.

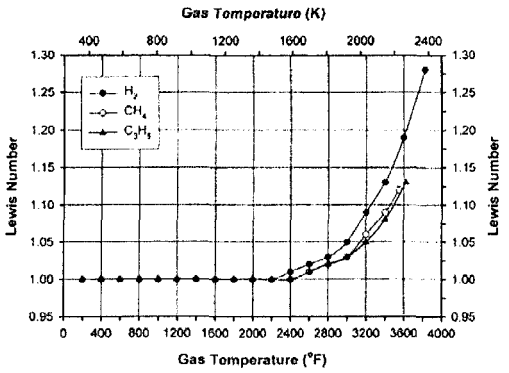

Figure 1.9 Calculated Lewis number for equilibrium stoichiometric air-fuel flames as a function of the combustion product temperature and fuel composition (Source: Baukal[6])

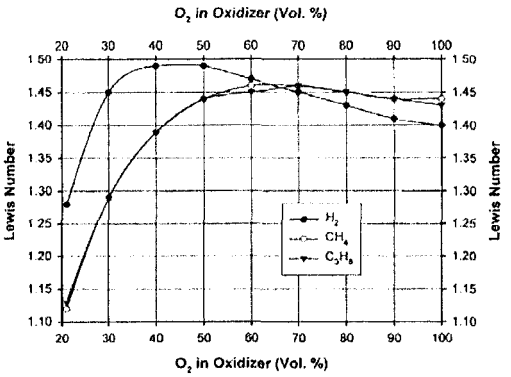

Figure 1.10 Calculated Lewis number for adiabatic equilibrium stoichiometric air-fuel flames as a function of the oxidizer (O_2+N_2) and fuel compositions (Source: Baukal[6])

As it was mentioned in the above section, Martin[17] gave a comprehensive survey of literature in 1977, which was devoted to the heat and mass transfer in impinging cold gas jets. Very recently (in 2000), Baukal[6] made an up-to-date, overall survey about works, both experimental and theoretical, that have been done on impinging flame jets. The different studies have been very well classified in his work and uniform nomenclature has been also elaborated. The given nomenclature and the established classification by Baukal will be adopted in the present work. It will be briefly demonstrated furthermore. In spite of the large amount of studies, in many cases, the heat transfer distribution can only be approximated very roughly.

The most important parameter in flame impingement studies is the overall geometric configuration that specifies the relative orientation of the target surface to the flame. (For the text diversity, besides the word configuration also arrangement as well as orientation is frequently used in the same sense.) The four commonly studied configurations in flame

impingement experiments are presented in Figure 1.11.

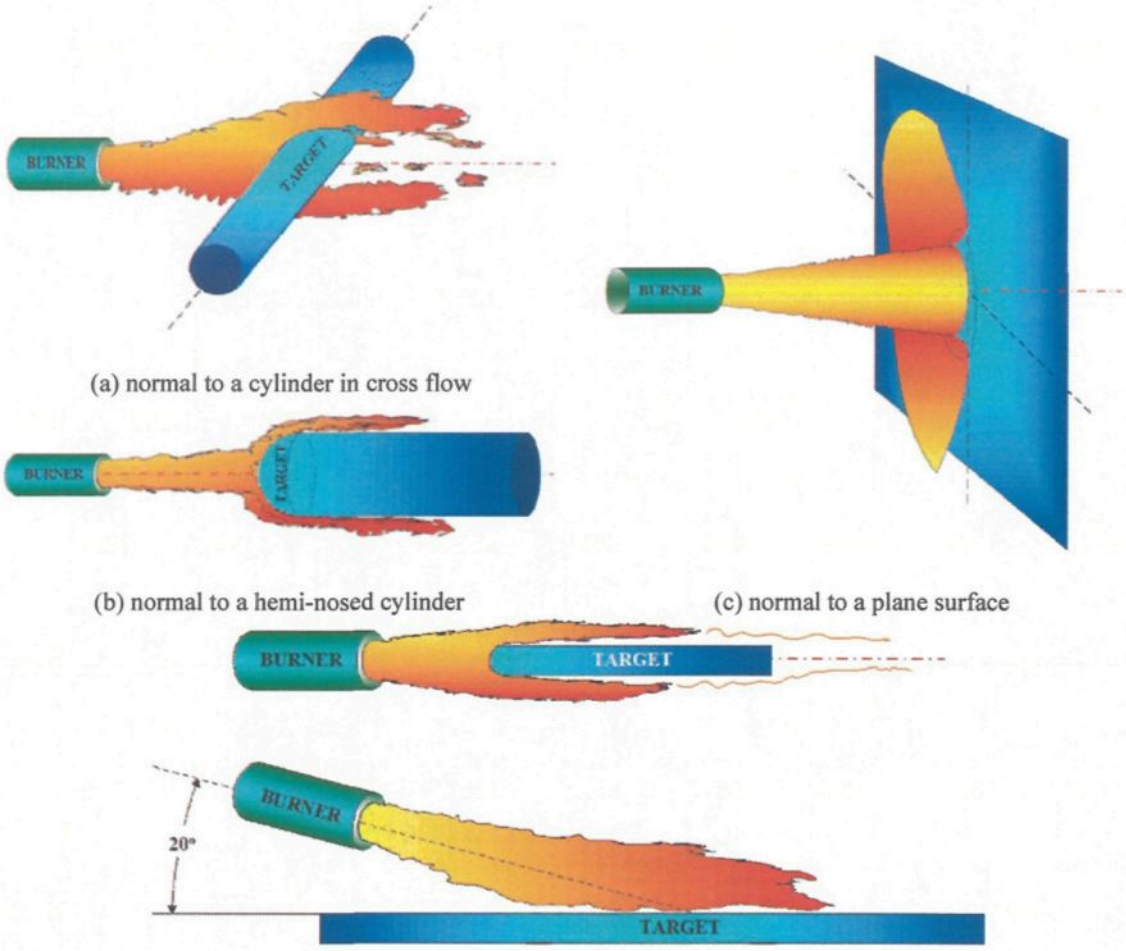

Figure 1.11 The four most common geometric configurations in flame impingement studies (Baukal[6])

The first configuration, when the flame is perpendicular to the axis of the cylinder (Figure 1.11.a.), applies mainly in industrial processes (heating of round metal billets or fire modeling on pipes in a chemical plant). The second arrangement (Figure 1.11.b.) when the flame impinges on the hemispherical end of a cylinder, is very useful in aeronautics (rockets and missiles) but less important in the industrial applications. The third configuration (Figure 1.11.c.) is the classical flame impingement arrangement. It was the

most intensively studied because this arose in many industrial applications. Finally, the fourth case, when the flame is parallel to a plane surface or inclined at a certain angle above the horizontal, is important in flight applications. In spite of its importance, this arrangement was the least studied.

There are also other important parameters, which influence strongly the heat transfer rate. These parameters are the burner type, the nozzle diameter, the Reynolds number at the nozzle exit, the distance of the target from the burner, the firing rate, the oxidizer and fuel composition, the flame equivalence ratio as well as whether the flame operates in a furnace, surrounded by hot refractory gases, or in cold ambient air.

The two different approaches to establish heat transfer relationships are either the semianalytical heat transfer solutions, based on the equation of Sibulkin[46], or the empirical heat transfer correlations. The semianalytical solutions were derived from the laminar, two-dimensional, axisymmetric boundary layer equations applied in the stagnation region. Using similarity flow formulations, the obtained equations were simplified and the constant was numerically determined in the resulting heat flux solutions. Radiation effects were ignored. Sibulkin[46] has given the following equation, which includes only the effect of forced convection:

$$q_s'' = 0.763(\beta_s \rho_e \mu_e)^{0.5} \, \mathrm{Pr}_e^{-0.6} \, c_{p_e} (t_e - t_w) \qquad \text{Eq. 1.17}$$

where the indexes s, e, w refer respectively to the stagnation point, to the edge of the stagnation zone and to the target wall at the stagnation point. The term β is the velocity gradient at the stagnation point as well as $\mu, \rho, \mathrm{c_p}$, Pr and t are respectively the dynamic

viscosity, the density, the specific heat the Prandtl number and the temperature.

The empirical heat transfer correlations are generally given in two different forms:

$$Nu \approx a \,\mathrm{Pr}^{b}\,\mathrm{Re}^{c} \qquad \text{Eq. 1.18}$$

$$q'' = (k/d)\{Nu\}\Delta t \qquad \text{Eq. 1.19}$$

where a,b,c are constants, k is the thermal conductivity and d is the characteristic dimension.

1.2.3.2. Geometric consideration and fluid dynamics of impinging round jets normal to a plane surface

A typical schema of surface impingement of single round gas jet is shown in Figure 1.12. The fluid dynamics of the discharging free gas jet was discussed in details above in this chapter. Upstream from the limit of the stagnation or impingement zone, there is no difference between the flow properties of free jets and impinging jets. However, within the stagnation zone, the flow is influenced by the target surface and is decelerated in the normal (z) and accelerated in the transverse (r) directions.

As it is shown on the schema, the stagnation zone has also a border in the transverse direction (dashed lines). This is the limit where the transverse acceleration of the fluid changes to deceleration due to the continuous entraining of ambient, zero momentum secondary fluid. The region further downstream is called to wall-jet region. The velocity profiles in this region are characterized by zero velocity at both the free and impingement surfaces.

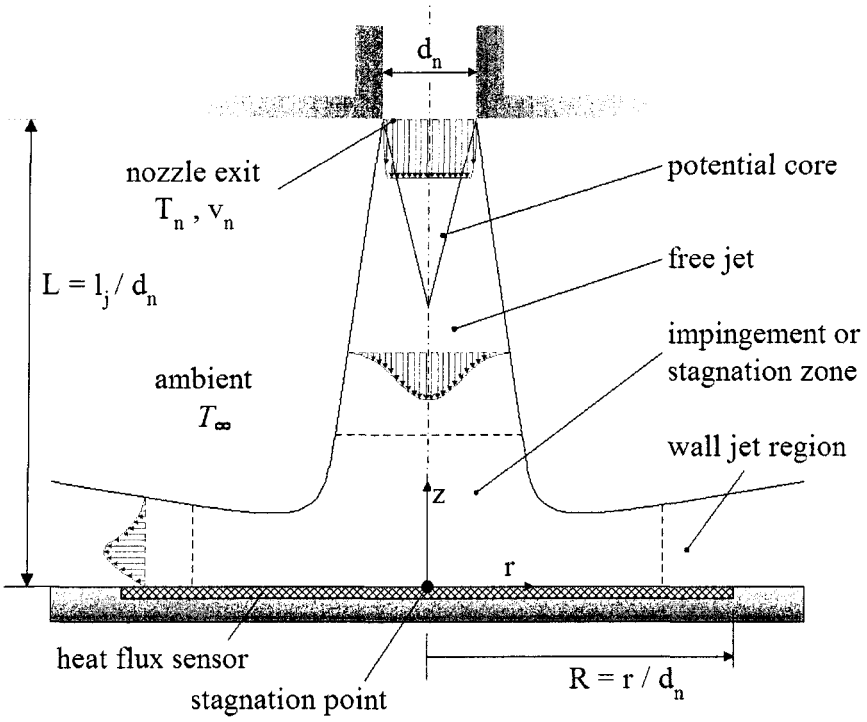

Figure 1.12. Surface impingement of a single round gas jet

If the temperature of the target surface differs from the temperature of the impinging jet, convection heat transfer occurs in both the impingement and wall jet regions. Martin[32], Popiel and Bogusiawski[33] as well as Goldstein and Timmers[34] have also studied such configurations for cold gas jets. The average Nusselt number of an impinging jet emerging from a single circular nozzle can be calculated as follows:

$$Nu = 2 \cdot \frac{\left(1 - 1.1 \cdot \frac{1}{R}\right) \cdot \frac{1}{R} \cdot \sqrt{1 + 0.005 \cdot \mathrm{Re}^{0.55}}}{1 + 0.1 \cdot (L - 6) \cdot \frac{1}{R}} \cdot \mathrm{Re}_{n,ave}^{0.5} \cdot \mathrm{Pr}_n^{0.42} \qquad \text{Eq. 1.20}$$

where $\mathrm{Re}_{n,ave} = \frac{v_{n,ave} \cdot d_n \cdot \rho_n}{\mu_n}$, $\mathrm{Pr}_n = \frac{c_{p_n} \mu_n}{k_n}$, $L = \frac{l_j}{d_n}$, $R = \frac{r}{d_n}$.

This formula gives the average Nusselt number for a circular surface, which is located on the impingement target, is coaxial with the nozzle and has the diameter of $2r$ (see Figure 1.12). In the above equation, d_n is the diameter of the burner nozzle, and L is the dimensionless distance between the nozzle outlet and the impingement target. The transport and thermodynamic properties (subscript n) as well as the characteristic velocity in the Reynolds number are average values at the nozzle exit instead of being the centerline values. The average velocity at the nozzle exit is calculated by dividing the volumetric flow rate of the entering gas mixture by the nozzle area. The average convective heat transfer on the circular surface with the diameter of 2r can be calculated as follows:

$$q''_{s.conv,ave} = \frac{k}{d_n}\{Nu\}(t_e - t_w)$$

Eq. 1.21

1.2.3.3. Thermodynamic and transport properties of gas mixtures using the CHEMKIN data base

Besides the geometrical properties (l_j, d_n, r) and the measured velocities and temperatures ($v_{n,ave}$, t_e, t_w) also the thermodynamic parameters (c_p) as well as the transport properties (μ, k) of the gas mixture have to be determined to calculate the Nusselt number and the heat flux in Eq. 1.20 and Eq. 1.21. In the available encyclopedies, these wanted properties are only included up to 1000 K. Nowadays, to obtain these kinds of properties, the complex chemistry databases are used. This approach is more and more pursued in the field of combustion. The temperature range is given between 300 K and 4-5000 K. In addition, these databases are published on the internet and except for commercial use, these are free of charge, as for example the GRI-Mech database of the University of Berkeley or

the CHEMKIN[69] database. The latter was used in the present work to calculate the requested parameters. It will be very briefly presented below.

The CHEMKIN programs use three files: (1) 'chem.inp' or 'chem.dat' file for the Arrhenius terms; (2) 'therm.dat' file for the thermodynamic parameters (h and c_p); (3) 'tran.dat' file for the transport coefficients (μ, k).

The first file is not requiered in our case; therefore, it is no more discussed here. To calculate the specific heat, the file of the thermodynamic parameters has to be used. The polynomial coefficients are given in this second file for the correlation:

$$c_p/R = a_1 + a_2T + a_3T^2 + a_4T^3 + a_5T^4 \qquad \text{Eq. 1.22}$$

Different coefficients are given in the datafile for low and for high temperature ranges. The temperature interval and the formula of species are also specified in the file.

To determine the transport coefficients, as the dynamic viscosity and the thermal conductivity (μ, k), the third CHEMKIN file has to be used. There are seven columns (plus one for the commentary) given for each species. These are the followings: (1) species name; (2) atomicity index (0 for single atom, 1 for linear molecule, 2 for nonlinear molecule; (3)-(4) Lennard-Jones coefficients; (5)-(6) polarity parameters; (7) collision parameter.

The transport properties of single components are calculated first. Subsequently, the coefficients are determined for the entire gas mixture. The relevant equations are presented in Appendix A.

A computational module was developed using the CHEMKIN database for a gas

mixture of eight components. The mixture is composed of the following species: CH_4; C_2H_6; C_3H_8; C_4H_{10}; CO_2; H_2O; N_2; O_2. The temperature range of validity is between 300-5000 K in the case when the mixture do not contain any C_2H_6 and C_4H_{10}. Otherwise, the validity range is only up to 4000 K. The following properties are calculated by the computational module: thermal conductivity (k), dynamic viscosity (μ), enthalpy (h), density (ρ), Prandtl number (Pr), and the molar mass of the gas mixture (M_{mix}). This computational module will be referred furthermore as "Computational module for gas mixtures".

1.2.3.4. Thermophysical properties

These include all properties, which are temperature dependent (all the above presented properties except of the molar mass of the gas mixture). Various methods have been used in different studies to evaluate the thermophysical properties. These methods are discussed below. As it was mentioned, the nomenclature of Baukal[6] was adopted, which is presented in Figure 1.13.

In many studies, the gas temperature at the edge of the stagnation zone, t_e, has been used to determine some of the properties:

$$p_e = p(t_e)$$

Eq. 1.23

where p is the property being calculated. The wall temperature at the stagnation point of the target body, t_w has been also commonly used:

$$p_w = p(t_w)$$

Eq. 1.24

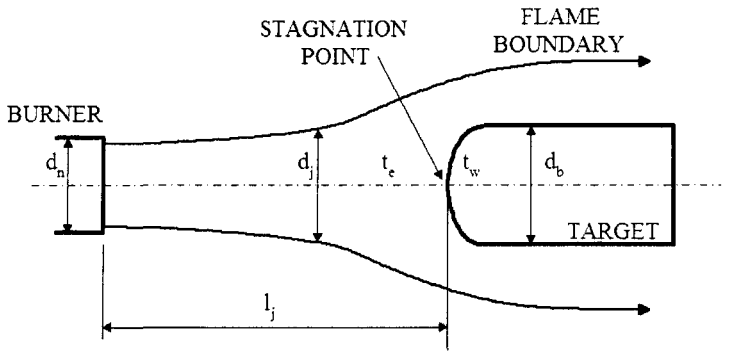

Figure 1.13 Nomenclature for the flame impingement correlations – Exemple: flame impingement on a hemi nosed cylinder (From Baukal C.E. and Gebhart B.[47])

In certain other studies, the weighted average over the temperature range between the edge and the wall temperatures has been used:

$$\bar{\bar{p}} = \frac{\int_{w}^{e} p\,dt}{t_e - t_w}$$

Eq. 1.25

Many studies have used the film temperature, which is the mean temperature between the edge and the wall temperatures:

$$\bar{p} = p\left(\frac{t_e + t_w}{2}\right)$$

Eq. 1.26

The reference temperature has been used in the study of Hoogendoorn et al[45] and Popiel et al[13]:

$$p_{ref} = p\left\{t_e + \frac{t_w - t_e}{2} + 0.22\left(t_{rec} - t_e\right)\right\}$$

Eq. 1.27

where

$$t_{rec} = t_e + \frac{v_e^2 \, \mathrm{Pr}_e^{0.5}}{2c_{p_e}}$$

Eq. 1.28

For low speed flows, $t_{rec} \approx t_e$, so $p_{ref} \approx \bar{p}$.

The maximum temperatures have been used at any axial location in the work of Beér and Chigier:

$$p_{\max} = p(t_{\max})$$

Eq. 1.29

Also the shorthand notation of Baukal[6] was adopted for the dimensionless quantities such as the Re, Nu, and Pr numbers. When only transport properties are required, this will be designated by a single subscript (e.g., $\mathrm{Pr_e}$ which is Pr evaluated at t_e, i.e. $\mathrm{Pr}_e = c_{p_e}\mu_e / k_e$). In the case, when both a characteristic length and a property temperature are required, these will be indicated by the first and second of two subscripts, respectively. For example, $\mathrm{Re_{n,e}}$ is shorthand notation of $\mathrm{Re}_{n,e} = \rho_e v_e d_n / \mu_e$ where the characteristic dimension is d_n and all thermophysical properties are evaluated with the temperature at the edge of the stagnation zone.

1.2.3.5. Semianalytical heat transfer solution

In the semianalytical solutions, the surface velocity gradient has been developed using potential flow theory, normal to different stagnation body shapes. The applications are valid for approximately inviscid flows as for example high altitude flight. The following equations have been established:

$\beta_s = 4v_e / d_b$ for a cylinder in a cross flow

Eq. 1.30

$$\beta_s = 3v_e/d_b \quad \text{for a sphere}$$

Eq. 1.31

$$\beta_s = 4v_e/d_b\,\pi \quad \text{for a disk}$$

Eq. 1.32

$$\beta_s = \frac{3\pi}{16}\frac{v_e}{d_j} \quad \text{for an infinite plane}$$

Eq. 1.33

The result of Sibulkin[46], considered for a body of revolution for uniform (except the boundary layer), laminar, incompressible, axisymmetric, and of low speed flows, was given in Eq. 1.17. All other semianalytical solutions presented here are based on this equation. Fay and Riddell[52] have included the effect of chemical dissociation and slightly modified the equation of Sibulkin[46] by adding a factor which contains the ratio of $\rho\mu$, evaluated at the wall and at the edge of the boundary layer, and by interchanging the driving force from temperature to enthalpy. The resulting heat transfer equation in the stagnation point for equilibrium TCHR is the following:

$$q_s'' = 0.76(\beta_s \rho_e \mu_e)^{0.5}\left(\frac{\rho_w \mu_w}{\rho_e \mu_e}\right)^{0.1} \mathrm{Pr}_e^{-0.6}\left[1+\left(Le_e^{0.52}-1\right)\frac{h_e^C - h_w^C}{h_e^T}\right](h_e^T - h_w^T)$$

Eq. 1.34

In those cases when the TCHR is negligible (e.g. for flame temperatures below about 1800 K – Le=1), the term between brackets becomes unity. Fay and Riddell have also proposed a second equation to calculate the heat transfer rate for catalytic TCHR, forasmuch as the only difference to Eq. 1.34 is in the exponent of the Lewis number, it is not presented here.

Several impingement experiments have been made, in which the obtained heat flux was compared to some of the semianalytical solutions. Only those studies will be presented here, where the flow regime was turbulent and where the forced convection was the dominant mechanism while TCHR could be neglected. Forced convection is generally the dominant mechanism in air/fuel flames. Even besides these studies, there are some works, in which $\left(h_e^T - h_w^T\right)$ was taken as the driving potential although this is essentially the same as $\left(h_e^S - h_w^S\right)$. The discussed experimental studies using semianalytical solutions are presented in Table 1.1; supplementary information about the experimental conditions is available in Table 1.2.

Horsley et al[50] tested flame impingement on flat plate. The distance of the target to the burner, L, was set up to having maximal surface heat flux. Notwithstanding that the Reynolds number at the nozzle exit was between 7050 and 16200, Horsley also inserted metal grids into burners to control turbulence. The proposed modified form of Eq. 1.17 is:

$$q_s'' = 1.12(\beta_s \overline{\rho\mu})^{0.5} \overline{\mathrm{Pr}}^{-0.6} (h_e^S - h_w^S)$$

Eq. 1.35

Hargrave and Kilham[51] studied flame impingement on a hemi-nosed cylinder up to Re_n of 10000 for methane/air flames. The following equation was determined:

$$q_s'' = 0.763\left(\beta_s \overline{\overline{\rho\mu}}\right)^{0.5} \overline{\overline{\mathrm{Pr}}}^{-0.6} (h_e^T - h_w^T)$$

Eq. 1.36

This equation, for example, takes the driving potential of the total enthalpy. However, Hargrave and Kilham[51] have found that TCHR was not important.

Target	Oxi-dizer	Re_n	ϕ	Fuel	β_s	d_b [mm]	v [m/s]	t_j [K]	Reference
flat plate	air	7050-16200	1.05	natural gas	$v_e/r_{0.5t}$	5.6 diam.	not measured	1643-2165	Horsley et al.[50]
hemi-nosed cylinder	air	1200-10000	1.0	CH_4	$(2.67+0.0926Tu)v_e/d_b$	22	2-3	1900-2100	Hargrave et al.[51]
cylinder in cross flow	air	12600	1.05	natural gas	$2v_e/r_{0.5t}$	32.6-59.8	not measured	not measured	Hemeson et al.[48]
hemi-nosed cylinder	air	12600	1.05	natural gas	$3v_e/r_{0.5t}$	50-150	not measured	not measured	Hemeson et al.[48]
flat plate	air	1700-4250	1.0	natural gas	v_e/d_b	not given	up to 50	up to 2130	van der Meer[49]

Source : C. E. Baukal and B. Gebhart, Int, J. Heat Mass Transfer, 39(14), 2989-3002, 1996.[47]

Table 1.1 Experimental studies using semi analytical solutions

Hemeson et al[48] made experiments on both hemi-nosed cylinder and cylinder in cross flow also. A wide variety of burners has been tested for a range of cylinder diameters. The recommended equation is the following:

$$q_s'' = 0.763\left(\beta_s \overline{\rho\mu}\right)^{0.5} \mathrm{Pr}^{-0.6}(h_e^T - h_w^T)$$

Eq. 1.37

The interesting conclusion is that the heat flux does not depend on the radius of cylinder's curvature but it is dependent on the burner design.

Van der Meer[49] has studied flame impingement normal to flat plate. The experimental heat flux data was correlated by linear regression. The suggested equation is:

$$q_s'' = (1+\gamma)0.763\left(\beta_s \rho_{ref} \mu_{ref}\right)^{0.5} \mathrm{Pr}_{ref}^{-0.6}\left(h_e^S - h_w^S\right)$$

Eq. 1.38

where γ is the turbulence enhancement factor which is an experimentally determined function of $\mathrm{TuRe}^{0.5}$.

firing rate q_f [kW]	Burner	d_n [mm]	L	R	Reference
0.3, 0.4	flame retention head	5.6- 15.3	16-27	0	Horsley et al.[50]
1-8	tube	16	1.6-3.8	0	Hargrave et al.[51]
not given	flame retention head	22.4, 41.0	0-4.5	0	Hemeson et al.[48]
not given	tunnel	13.8, 27.6	1-12	0	van der Meer[49]
Source :C.E.Baukal and B. Gebhart, Int, Comb. Sci. Tech., 104, 339-357, 1995[53]					

Table 1.2 Experimental conditions in studies using semi analytical solutions (supplements to Table 1.1)

1.2.3.6. Empirical heat transfer correlations for flames impinging normal to a plane surface

This geometrical arrangement is shown in Figure 1.11.c and Figure 1.12. Both disks and rectangular plates were used in the following experiments. Only those correlations are presented where forced convection was the dominant heat transfer mechanism. In the studies presented directly next, the flow was laminar at the nozzle exit but turbulent free jet flow developed prior to the impact. The experiments, where the discharging flow from the nozzle was already turbulent, are discussed subsequently. The experimental conditions for the presented studies are classified in Table 1.3. In the presented studies, the heat transfer correlations referred to the stagnation point, except the study of You[56] in which the average convective heat transfer rate were given.

Hoogendoorn et al[45] and Popiel et al[13] studied the heat transfer in the stagnation point. The recommended equations are based on the axial distance L between the burner and the

target. For $2 \le L \le 5$, the suggested correlation is:

$$q''_{s,conv} = \frac{k_{ref}}{d_n}\left\{(0.65 + 0.084L)\mathrm{Re}_{n,ref}^{0.5}\,\mathrm{Pr}_{ref}^{0.4}\right\}\frac{h_e^S - h_w^S}{c_{p_{ref}}}$$

Eq. 1.39

For L > 12, they recommended:

$$q''_{s,conv} = \frac{k_{ref}}{d_n}\left\{(137 - 1.8L)\cdot 10^{-3}\,\mathrm{Re}_{n,ref}^{0.75}\,\mathrm{Pr}_{ref}^{0.4}\right\}\frac{h_e^S - h_w^S}{c_{p_{ref}}}$$

Eq. 1.40

Both correlations closely matched the experimental data in the given range. However for $5 < L \le 12$ no correlations was given.

A modified correlation was also given for $8 \le L \le 20$:

$$q''_{s,conv} = \frac{k_{ref}}{d_n}\left\{2.37(L+1)^{-0.5}\,\mathrm{Re}_{n,ref}^{0.5}\,\mathrm{Pr}_{ref}^{0.4}\right\}\frac{h_e^S - h_w^S}{c_{p_{ref}}}$$

Eq. 1.41

which significantly, as much as 60%, underpredicted the experimental data. In this range of the axial distance, the free jet is already a fully developed flow. It was believed that the underprediction of Eq. 1.41 has been caused by the failure to include free jet turbulence. A modified correlation is also given that included those effects:

$$q''_{s,conv} = \frac{k_{ref}}{d_n}\left\{\left[\frac{2.37}{(L+1)^{0.5}} + 2.22\left(\frac{Tu\,\mathrm{Re}_{n,ref}^{0.5}}{100}\right) - 2.76\left(\frac{Tu\,\mathrm{Re}_{n,ref}^{0.5}}{100}\right)^2\right]\mathrm{Re}_{n,ref}^{0.5}\,\mathrm{Pr}_{ref}^{0.4}\right\}\frac{h_e^S - h_w^S}{c_{p_{ref}}}$$

Eq. 1.42

This matched favourably the data. It was also found that for $L \ge 4$, the maximum heat flux occurred at R=0, however for L = 2 and 3, the highest heat flux was measured at

R = 0.5 and 0.2 respectively.

Kataoka et al.[54] tested air-O_2/CH_4 flames. The recommended formula to calculate the heat transfer in the stagnation point is:

$$q''_{s,conv} = \frac{k_e}{2r_{1/2v}}\left\{1.44\,\mathrm{Re}^{0.5}_{2r_{1/2v},e}\,\mathrm{Pr}_e^{0.5}\left(L - X_v\right)^{0.12}\right\}\left(t_e - t_w\right)$$

Eq. 1.43

where $r_{1/2v}$ is the radius at which the measured gas velocity is half as big as the centerline velocity at the axial location close to the stagnation point. The above equation is only valid for L >X_v with X_v correlated as given in Eq. 1.2. Kataoka measured the maximum heat flux in the same flame at L = X_v.

You[56] investigated flame impingement of pure diffusion flames. The recommended correlation was the average convection heat-transfer as a function of the dimensionless distance from the stagnation point. The discharging fuel from the burner nozzle was laminar but the buoyant plume impinging on the plate was turbulent. Due to the small velocities, buoyancy effects are important. Therefore, the Rayleigh number was included in the given correlations. In this impingement field, a special definition of Ra number is used, which is defined as:

$$Ra = g\tilde{\beta}_e q_f l_j^2 \,/\, \rho_e c_{p_e} v_e^3$$

Eq. 1.44

where $\tilde{\beta}$ is the volume coefficient of expansion. It was found that in the stagnation zone, the convective heat flux was mainly constant, while in the wall jet region the heat flux decreased with R. The dimensionless radius, R, of the stagnation zone was assumed to be R=0.16. The concerning correlation is:

$$q''_{b,conv} = 31.2\left(q_f / l_j^2\right) Ra_e^{-1/6}\,\mathrm{Pr}_e^{-3/5}$$

Eq. 1.45

In the wall jet region, for R > 0.16, the following formula was recommended:

$$q''_{b,conv} = 1.46 R^{-1.63}\left(q_f / l_j^2\right) Ra_e^{-1/6}\,\mathrm{Pr}_e^{-3/5}$$

Eq. 1.46

In both cases, $10^9 < Ra < 10^{14}$ and $\mathrm{Pr} \cong 0.7$ was assumed. The radiant heat flux was accounted for up to 26% of the total heat flux, which was excluded from the above correlations. However, no correlation was given for the radiative heat flux.

Shorin and Pechurkin[35] studied flames already turbulent at the nozzle exit. The following, empirically determined correlation was given, valid for $L \le X_v$:

$$q''_{s,conv} = \frac{k_e}{d_n}\left\{4.04\,\mathrm{Re}_{n,e}^{0.2}\,\mathrm{Pr}_e\right\}\left(t_e - t_w\right)$$

Eq. 1.47

Another correlation was also suggested as a function of R, for $X_v < L < 14$ and for $0 < R/L < 0.9$:

$$q''_{r,conv} = \frac{k_e}{r}\left\{3.22\,\mathrm{Re}_{n,e}^{0.4}\,\mathrm{Pr}_e\; e^{-0.36\frac{(L-X_v)^2}{L} - 3.6\frac{R}{L}}\right\}\left(t_e - t_w\right)$$

Eq. 1.48

Oxi-dizer	Fuel	ϕ	q_f [kW]	Burner	d_n [mm]	Re_n	L	R	Reference
air	natural gas	1.0	not given	tunnel	13.8	1050-1860	2-20	0-5	Hoogendoorn et al.[45]
air	natural gas	1.0	not given	tunnel	13.8	1050-1860	2-20	0-10	Popiel et al.[13]
air/O_2	CH_4	0.61	not given	converging nozzle w/precombustor	10	857-2000	2-20	0-3	Kataoka et al.[54]
air	town gas	0.67-0.95	not given	water cooled tube w/precombustor	25, 46	1500-19000	0-14	0-5	Shorin and Pechurkin[35]
air	CH_4	2.58-2.76	1.0-160	partial premix	13, 16	17680-22700	13-65	0-10	Buhr et al.[58, 59] Kremer et al.[57]
air	coke oven gas	not given	606	tunnel w/air preheat	100	turbulent	5-9	0-7	Matsuo et al.[55]
air	natural gas	∞	1.67, 8.51	tube	55	70, 356	7.3	0-7.3	You[56]
Source :C.E.Baukal and B. Gebhart, Int, Comb. Sci. Tech., 104, 339-357, 1995[53]									
air	natural gas	0.91	70	traditional (premix)	118	6500-8000	6.7	0-0.1	present work
air	natural gas	0.91	70	LNI	38	30000-40000	20.4	0-0.4	present work

Table 1.3 Experimental conditions in studies for flame impingement normal to a plane surface

Buhr et al[58, 59] and Kremer et al[57] tested turbulent flames of $17680 \le \mathrm{Re}_n \le 22700$, valid for $13 \le L \le 65$. The following modification of Sibulkin's equation was recommended:

$$q''_{s,conv} = 0.0371 \mathrm{Pr}_e^{-0.6} \rho_e v_e \left(h_e^S - h_s^S\right)$$

Eq. 1.49

Matsou et al[55] also investigated turbulent flames but inside a furnace. For the heat flux in the stagnation point, the following correlation was given:

$$q''_{s,conv} = 0.010353\left(q_f^{0.936} / L^{1.032}\right)\left(t_e - t_w\right)$$

Eq. 1.50

1.2.3.7. Empirical heat transfer correlations for flames impinging normal to a cylinder

This configuration is shown in Figure 1.11.a. The experimental conditions are given in Table 1.4. For this configuration, the only one study, which considers the TCHR mechanism, is also presented.

Hustad and co-workers[43, 60] studied both laminar and turbulent methane-air as well as propane-air diffusion flames for a wide range of firing rates, Reynolds numbers and dimensionless target distances. Radiation and total heat fluxes were measured. The radiative heat flux was also calculated. The convection heat transfer was determined by subtracting the calculated radiation from the measured heat flux. Local and average convective heat transfer as well as average radiative and total heat transfer correlations were also recommended.

They suggested the following equation for the local convection heat-transfer rate at the stagnation point:

$$q''_{s,conv} = \frac{k_e}{d_b}\left\{0.41\,\mathrm{Re}_{b,e}^{0.6}\,\mathrm{Pr}_e^{0.35}\,Tu^{0.15}\left(\frac{\mathrm{Pr}_e}{\mathrm{Pr}_w}\right)^{0.25}\right\}\left(t_e - t_w\right)$$

Eq. 1.51

Baukal[6] stated that for a pure fuel-jet diffusion flame, due to the possibly significant quantity of uncombusted species, the TCHR mechanism might have been important.

However, TCHR was not discussed by Hustad and co-workers. If it were present, it would have been included with forced convection in Eq. 1.51, suspected Baukal.

Oxi-dizer	Fuel	ϕ	q_f [kW]	Burner	d_n [mm]	Re_n	L	R	Reference
air	CH_4, C_3H_8	∞	37-1600	tube	5-40	200-330000	20-200	0	Hustad et al.[42, 43, 60]
air	CH_4	0.8-1.2	1.2-10	tube	16	2000-8000	3.1-11	0	Hargrave et al.[61]
air	CO	1.0, 1.19	0.51-0.75	slot	4×50	laminar	2.5-7.5	0	Kilham[40]
air, O_2	CO, H_2	1.0-2.0	2.1-6.1	annular port w/ precombustor	not given	laminar	n. given	0	Jackson & Kilham [41]
air	C_3H_8	1.25	3.5-9.4	tunnel	18	not given	1.7-6.9	0	Fells and Harker[62]
air, air/O_2, O_2	natural gas	0.5-1.3	0.56-1.7-2.8	premix, slot shaped torch	not given	not given	(a)	0	Davies[63]
air, O_2	town gas	lean-rich	7.1-28	tunnel	13, 26	not given	0.5	0	Davies[44]
Source :C.E.Baukal and B. Gebhart, Int, Comb. Sci. Tech., 104, 339-357, 1995[53]									
(a) – target located at point of maximum heat release									
air	natural gas	0.91	70	traditional (premix)	118	6500-8000	6.7	0-0.1	present work
air	natural gas	0.91	70	LNI	38	30000-40000	20.4	0-0.4	present work

Table 1.4 Experimental conditions in studies for flame impingement normal to a cylinder in cross flow

Hustad et al.[43] have also suggested a correlation for the average forced convection heat transfer:

$$q''_{b,conv} = \frac{k_e}{d_b}\left\{0.23\,\mathrm{Re}_{b,e}^{0.6}\,\mathrm{Pr}_e^{0.35}\,Tu^{0.15}\left(\frac{\mathrm{Pr}_e}{\mathrm{Pr}_w}\right)^{0.25}\right\}(t_e - t_w)$$

Eq. 1.52

They have given also average radiation heat-transfer correlations. For CH_4 flames, the following equation was proposed:

$$q''_{b,rad} = 5 + 3.9(l_j - x_{liftoff}) \qquad [\mathrm{kW/m^2}]$$

Eq. 1.53

The average radiation heat-transfer for C_3H_8 flames was given as:

$$q''_{b,rad} = 19 + 7.8(l_j - x_{liftoff}) \qquad [\mathrm{kW/m^2}]$$

Eq. 1.54

where $x_{liftoff}$ is the length between the nozzle and the closest part of the reaction zone. All distances are used in meters. The length $l_j - x_{liftoff}$ was termed the radiation height. For a traditional burner, the $x_{liftoff}$ is zero, since the flame is attached to the nozzle exit.

Finally, based on a thermal input of $q_f = 60$ to 1600 kW, Hustad et al.[60] have recommended the following equation to calculate the maximum total heat transfer, which was located at the center of the flame:

$$q''_{\max,conv+rad} = 10 q_f^{0.3} \qquad [\mathrm{kW/m^2}]$$

Eq. 1.55

Hargrave et al.[61] studied the effect of turbulence in laminar and turbulent premixed methane-air flames. For the local convective heat transfer in the stagnation point, the following formula was given:

$$q''_{s,conv} = \frac{\bar{\bar{k}}}{d_b}\left\{\overline{\overline{\mathrm{Re}_b}}^{0.5}\left[1.071 + 4.669\left(\frac{Tu\overline{\overline{\mathrm{Re}_b}}^{0.5}}{100}\right) - 7.388\left(\frac{Tu\overline{\overline{\mathrm{Re}_b}}^{0.5}}{100}\right)^2\right]\right\}(t_e - t_w)$$

Eq. 1.56

Kilham[40] and Jackson and Kilham[41] measured the total and radiative heat fluxes in laminar air/CO, air/H_2, O_2/H_2 and O_2/CO flames. The convective heat transfer was calculated by subtracting the radiation from the total heat flux. The average convection was correlated for air/CO flames by:

$$q''_{b,conv} = \frac{\bar{k}}{d_b}\left\{\overline{\mathrm{Pr}}^{0.3}\left(0.35 + 0.47\overline{\mathrm{Re}_b}^{0.52}\right)\right\}(t_e - t_w)$$

Eq. 1.57

as well as for air/H_2, O_2/H_2 and O_2/CO flames by:

$$q''_{b,conv} = \frac{\bar{k}}{d_b}\left\{\overline{\mathrm{Pr}}^{0.3}\left(0.35 + 0.50\overline{\mathrm{Re}_b}^{0.52}\right)\right\}(t_e - t_w)$$

Eq. 1.58

Baukal[6] doubt the accuracy of these results for non-reacting jet impingement. In the O_2/H_2 and O_2/CO flames, Baukal expected significant TCHR, but this effect was not discussed in the related study of Jackson and Kilham.

Fells and Harker[62] studied air/C_3H_8 flames, but the flow type was not specified. The following relation for the average convection heat-transfer was empirically determined:

$$q''_{b,conv} = \frac{\bar{\bar{k}}}{d_b}\left\{\left(0.573 - 0.0179l_j\right)\overline{\overline{\mathrm{Re}_b}}^{0.5}\right\}(t_e - t_w)$$

Eq. 1.59

Davies[63] tested impingement for air/natural gas flames. The flow type was not specified. The following equation was used to calculate the average convective heat

transfer:

$$q''_{b,conv} = \frac{\bar{k}}{d_b}\left\{1.32\overline{\mathrm{Pr}}^{0.4}\overline{\mathrm{Re}}_b^{0.5}\right\}(t_e - t_w)$$

Eq. 1.60

In a latter study, Davies[44] measured air/town gas flames. The following correlation was used to determine average forced convection and TCHR heat flux:

$$q''_{b,conv+TCHR} = \frac{\bar{\bar{k}}}{d_b}\left\{0.615\overline{\mathrm{Re}}_b^{0.466}\right\}(t_e - t_w)$$

Eq. 1.61

1.2.3.8. Empirical heat transfer correlations for flames impinging normal to a hemi-nosed cylinder

This refers to flames impinging to cylinders whose axis is parallel to the flame as presented in Figure 1.11.b. One end of the cylinder has a hemispherical nose on which the flame impinges. Only the forced, local convection mechanism is considered in the discussed correlations. The experimental conditions are presented in Table 1.5.

Galloway and Sage[64] suggested the following equations for non-reacting flows:

$$Nu_{s,e} = 1{,}255\,\mathrm{Re}_{b,e}^{0.5}\left(\mathrm{Re}_{b,e}\,Tu\right)^{0.0214} \qquad \text{for } \mathrm{Re_{b,e}Tu}<7000$$

Eq. 1.62

$$Nu_{s,e} = 1{,}128\,\mathrm{Re}_{b,e}^{0.5}\left(\mathrm{Re}_{b,e}\,Tu\right)^{0.2838} \qquad \text{for } \mathrm{Re_{b,e}Tu}>7000$$

Eq. 1.63

To calculate the local, heat transfer rate in the stagnation point, the above correlations were modified as follows:

$$q''_{s,conv} = \frac{k_e}{d_b}\{Nu_{s,e}\}(t_e - t_w)$$

Eq. 1.64

Fairweather et al.[65] studied premixed methane-air and methane-air/O_2 flames in both laminar and turbulent flow conditions. The following modification of Galloway and Sage's equation was recommended:

$$q''_{s,conv} = 1{,}743(\mathrm{Re}_{b,e}\,Tu)^{0.0214}\frac{\rho_e v_e c_{p_e}}{\mathrm{Re}_{b,e}^{0.5}}(t_e - t_w)$$

Eq. 1.65

Oxi-dizer	Fuel	ϕ	q_f [kW]	Burner	d_n [mm]	Re_n	L	R	Reference
air, air/O_2	CH_4	0.943-1.171, 0.84-1.14	not given	converging nozzle, bundle of tubes	12 10	laminar, turbulent	4.6-11, 0.3-1.4	0	Fairweather et al.[65]
air	CH_4	0.8-, 1.2	1.2-10	tube	16	2000-12000	1.9-15	0	Hargrave et al.[61]
Source :C.E.Baukal and B. Gebhart, Int, Comb. Sci. Tech., 104, 339-357, 1995[53]									
air	natural gas	0.91	70	traditional (premix)	118	6500-8000	6.7	0-0.1	present work
air	natural gas	0.91	70	LNI	38	30000-40000	20.4	0-0.4	present work

Table 1.5 Experimental conditions in studies for flame impingement normal to a hemi-nosed cylinder

Hargrave et al.[61] measured methane-air flames in turbulent flow conditions. The following equation was given for local, forced convection heat transfer in the stagnation point:

$$q''_{s,conv} = \frac{\bar{k}}{d_b}\left\{\overline{\overline{\mathrm{Re}_b}}^{0.5}\left[0.993 + 5.465\left(\frac{Tu\overline{\overline{\mathrm{Re}_b}}^{0.5}}{100}\right) - 2.375\left(\frac{Tu\overline{\overline{\mathrm{Re}_b}}^{0.5}}{100}\right)^2\right]\right\}(t_e - t_w)$$

Eq. 1.66

In the reaction zone, the measurement data was underpredicted by up to 15%. However, very good agreement was found further downstream.

1.2.3.9. Empirical heat transfer correlations for jets impinging parallel or oblique to a plane surface

The flame-object arrangement for jets impinging parallel or oblique to a plane surface is shown in Figure 1.11.d. This configuration is very useful in many cases. Numerous experiments were made to study cold gas impingement, however, research with real flame impingement were much less elaborated. Although, there are a few dozen published works, the results were frequently controversial.

1.2.3.9.1 The flat plate in parallel laminar flow of cold gases

This is the most general case using the classic work of Blasius[39], Schlichting[14] and Pohlhausen[28]. If the enclosure walls are relatively distant, this kind of flow can be considered as external flow from the point of view of the boundary layer development, even if the examinated parallel object is situated inside a combustion chamber. However, from the point of view of the total heat transfer, the hot refractory walls have important contribution. As it is discussed in literature, laminar boundary layer development begins at the leading edge (x=0) and the transition to turbulence may occur at a downstream location (x_c) for which a critical Reynolds number $\mathrm{Re}_{x,c}$ is achieved. Near the leading edge, we

consider a developing laminar sublayer. For laminar flow, the local Nusselt number can be calculated as:

$$Nu_x \equiv \frac{h_x x}{k} = 0.332\,\mathrm{Re}_x^{1/2}\,\mathrm{Pr}^{1/3} \qquad \text{for } \mathrm{Pr} \geq 0.6$$

Eq. 1.67

x is the distance from the leading edge.

1.2.3.9.2 Local convection heat transfer in turbulent flames parallel to a plane surface

Eckert[30] has studied the heat transfer and friction in high-velocity laminar and turbulent boundary-layer flow over surfaces with constant pressure and temperature. The following equation was recommended for the local convection heat transfer:

$$q''_{x,conv} = \left(\bar{k}/x\right)\left\{0.0296\overline{\mathrm{Re}}_x^{0.8}\,\overline{\mathrm{Pr}}^{1/3}\right\}\left(t_e - t_w\right)$$

$$\overline{\mathrm{Re}}_x = \frac{v_x \cdot x \cdot \rho_{ave}}{\mu_{ave}},\ \overline{\mathrm{Pr}} = \frac{c_{p_{ave}}\mu_{ave}}{k_{ave}}$$

Eq. 1.68

where x is the distance from the leading edge.

Giedt et al.[31] tested an array of fuel-rich C_2H_2 flames in parallel flow over a flat plate where TCHR was an important mechanism besides forced convection. It was found that the equation of Eckert[30] underpredicted the experimental data by 25%. Giedt et al recommended a modified equation in which a derived correction factor was added for taking into account the recombination reaction of the hydrogen atom.

1.2.3.9.3 Local convection and radiation heat transfer in turbulent flames oblique to a plane surface

Beér and Chigier[4] studied flame impingement of stoichiometric coke-oven-gas/air

flames by inclined burner setup (see Figure 1.11.d.). The angle of burner inclination was 20°. The burner had two concentric tubes for the gas and the air inlets with an equivalent nozzle diameter of 150 mm. A non-premixed high velocity jet flame was produced with an equivalence ratio, ϕ=0.91. The firing rate was 1470 kW and the dimensionless distance, L, between the burner nozzle and impingement target was $L = 15.6$. The heat flux measurements were supported by detailed analysis of the velocity and temperature fields. The correlation for the total heat flux was given as:

$$q_{x,conv+rad} = \frac{k_{\max}}{x}\left\{0.13\,\mathrm{Re}_{x,\max}^{0.8}\right\}\left(t_{\max} - t_w\right)$$

$$\mathrm{Re}_{x,\max} = \frac{v_{\max} \cdot x \cdot \rho_{\max}}{\mu_{\max}}$$

Eq. 1.69

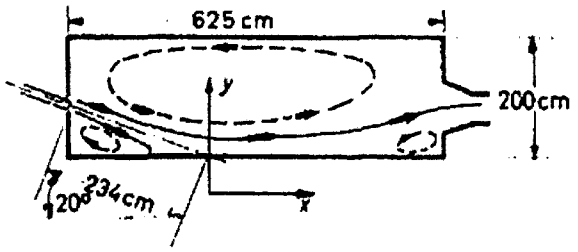

Figure 1.14 Schematic diagram of flame impingement on furnace hearth in the experiments of Beér and Chigier[4]

The velocity in the Reynolds number is always the maximum velocity at any of the axial stations. Similarly, all the thermophysical properties are evaluated taking the maximum temperatures at any one axial station. A Prandtl number of 0.7 was assumed. The experimental study of Beér and Chigier was one of the six experiments out of more than seventy, which had been performed in a furnace. The scale of this furnace is presented in Figure 1.14.

1.2.4. Radiative heat transfer in furnaces and flames

Thermal radiation is one of the most important heat transfer mechanisms in industrial furnaces. For radiative energy transport, no transmitting medium is required. Radiation is the transmission of energy by electromagnetic waves, which are characterized by their wavelength.

As it was presented in Figure 1.7, there is a direct proportion of radiation toward the charge, arriving from the hot gas mixture and an indirect proportion, arriving from the refractory surfaces. The first mechanism is referred to as gaseous radiation (volumetric radiation), while the second mechanism as surface radiation. The gaseous radiation can also be separated to nonluminous and luminous gaseous radiations.

The detailed presentation of these mechanismes is beyond the scope of this text. The methods are discussed in details in various advanced radiative heat transfer books[84, 29, 85]. Nevertheless, a general overview is given in Appendix E about the basic radiative heat-transfer mechanisms. Certainly, those particularities are emphasized that are related to the present experimental program. The analysis of both direct and indirect radiative heat transfer between the flame and the (simulated) charge had prime importance. During the experimental test, the radiative heat fluxes were continually measured. All the results presented here are empirical or semi-empirical. Advanced radiative heat transfer calculations and modeling were out of the scope of this program.

1.3 NO_x Emission

NO_x is formed in nearly all air breathing combustion devices as a by-product of the reaction process. NO_x emission consists of mostly nitric oxide (NO). Less significant are nitrogen dioxide (NO_2) and nitrous oxide (N_2O). A small part of nitric oxide is oxidized to nitrogen dioxide (NO_2) in the flame itself, but most of the oxidation takes place after the exhaust of the combustion products in the atmosphere. NO_x is a precursor for photochemical smog, contributes to acid rain, and causes ozone depletion. Thus, NO_x is a pollutant.

In the last 30 years, a wide range of research was carried out on the NO_x reduction techniques all around the world. The principal tendencies of the NO_x formation are better and better known. Notice that the second burner applied in our comparative research project (Low NO_x Injection /LNI/ Burner – North American Mfg.) was already a product of this NO_x development work. This burner meets the limits established by the new severe environmental regulations.

Appendix D is devoted to describe furthermore the general NO_x formation and destruction processes. The measured data using the BACHARACH gas analyser are presented in section 3.4. Finally, the results of a simplified numerical model are compared with the measurements in section 3.8. A short discussion is also given here.

CHAPTER 2.
EXPERIMENTAL PROCEDURES

2.1 Introduction

In the present chapter, the experimental program is presented first. The experimental program can be divided into three phases. Subsequently, the experimental setup, the applied methods and the measurement instruments are briefly discussed. Supplementary information as well as the description of the calibration procedures and methods are presented in the appendixes.

2.2 Experimental program

Two different burners were used in the tests. Each of the two burners can be adjusted to produce two different flames, so altogether four different flame types were tested. The four cases are as follows:

Burner	Flame type	
Conventional (Traditional) burner (adjustable)	Short flame	Long, luminous flame
LNI burner (Low NOx Injection type burner)	High-velocity flame	Envelope flame

Table 2.1 The available burners and produced flame types in the present study

In the first two phases, two different test series were realized. The first one was made by horizontal burner position in which case the flame is parallel to the furnace floor (Figure 2.1.a). In a second series of experimentation, we tilted the burner from horizontal to 11.4^0 downward which position permitted the flame to hit the calorimetric plates between the second and third sections (Figure 2.1.b). In these two phases, the calorimetric plates and the heat-flux sensors were the same. On the other hand, major transformation of the furnace hearth occurred to realize the third experimental phase. In this latest phase, flame impingement at the chamfered corner of raised solid blocks was studied (Figure 2.2). The concept of both the calorimetric plates and the heat flux sensors, were different.

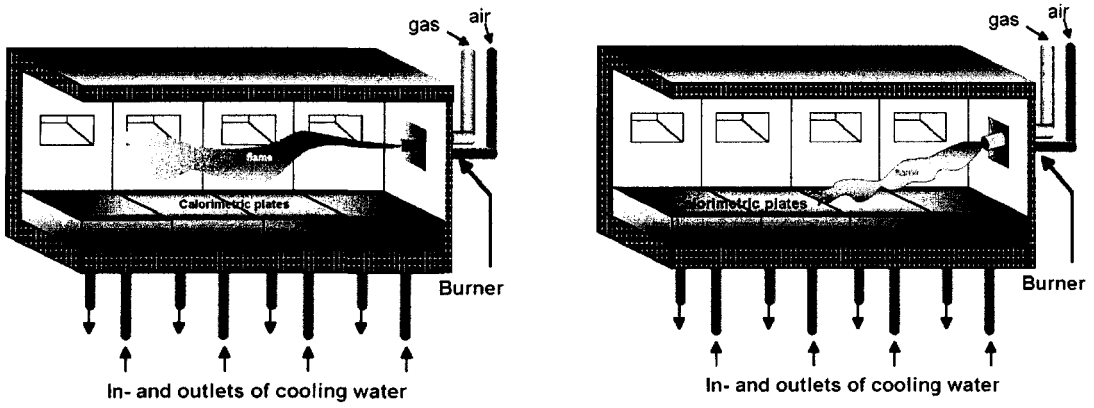

(a) (b)

Figure 2.1 Schematic view of the experimental furnace (a) by horizontal burner position (flame is parallel to the furnace floor) and (b) at inclined burner setup (inclination angle: 11.4°)

In order to create a common base for the comparison, all flames were tested at the same power setting, 70 kW. The excess air ratio was set always to keep the same low level of CO formation, according to the recommendations of the manufacturer of the burners.

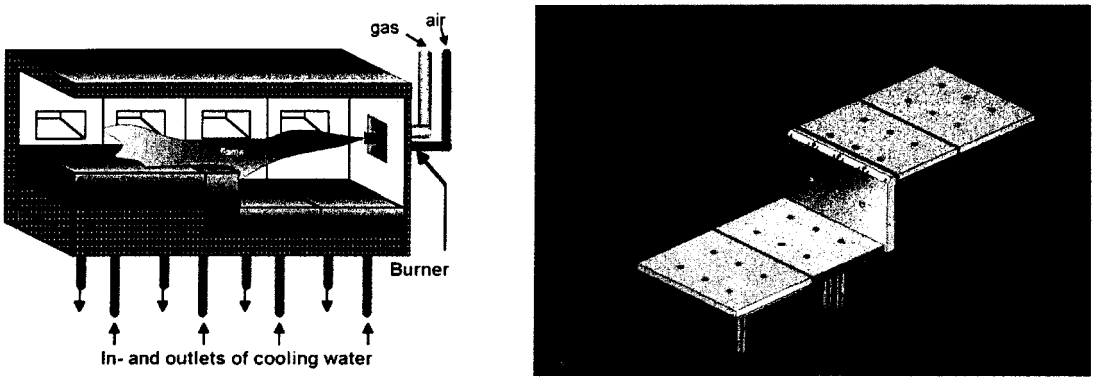

(a) (b)

Figure 2.2. (a) Schematic view of the experimental furnace by impingement arrangement (b) 3D technical drawing of the calorimetric plates – Autodesk Inventor 5

For all four flame types the measurements were continued long enough to reach an average furnace temperature level of about 1000 °C. During the first two phases, data were recorded continuously during the heating-up, which allows for the analysis of the wall temperature effects. For every flame types, at least two "good" measurement series were completed, not counting neither the preliminary experiments nor those where technical difficulties arose.

In a special series of tests, the structure and movement of all four flames were visualized. Using different metallic compounds, those high temperature regions of the flame were coloured where the self-illumination is weak in lack of solid (soot) particles. Comparison is shown in Figure F.2 and F.3 in Appendix F.

In addition, incandescent particles were introduced in order to show the streamlines in the combustion chamber. Using different exposure times even the magnitude of the velocities can be estimated (Figure F.1 in Appendix F).

In order to facilitate the analysis of the measurement results, measurements of the heat

flux distribution in the heated-up furnace were made after suddenly turning off the burner (see section E.3.3 in Appendix E.).

The convective, radiative, and total heat fluxes, as well as the stack gas composition were measured in every experimental phase. In the first and third phases, the LDV instrument, the one-hole Pitot-tube and the suction-pyrometer were used to obtain the velocity profiles and the temperature distribution for the different flame types.

In the following section, the instrumented furnace and the available burners are presented first. Next, the concept of the stainless-steel calorimetric plates and the plug-type heat flux sensors are presented which were used during the first and second experimental phases. Subsequently, the transformation of the furnace is discussed. This inevitable procedure was an occasion to improve the applied measurement system. Therefore, all accumulated information about the calorimetric plates and the heat flux sensors were considered during the planification of the new instruments. Efforts were done to conserve the simplicity and all the other advantages of the system and simultaneously correct its weaknesses.

Finally, the other measurement instruments, namely the suction pyrometer, the laser Doppler velocimeter, the Pitot tube, and the gas analyser are discussed at the end of this chapter.

2.3 Experimental setup

The main components of the burner test facility are the experimental furnace, the sensors, measurement instruments, and the data acquisition system.

2.3.1. Instrumented furnace

The experimental furnace has a modular design, with four longitudinal sections. The bottom of each section is removable and serves as a platform for different heat sinks and instrumentation. The furnace has a 0.5 m x 0.5 m cross-section, the size of the combustion chamber permits the application of 150 kW maximal burner power. In the first two phases of experiments (parallel firing and inclination), four calorimetric plates formed the furnace floor as shown in Figure 2.1.a et b. In the third experimental phase (impingement), two horizontal plates at the furnace hearth, one vertical plate at the middle of the furnace and two other horizontal plates at raised position formed the furnace floor (Figure 2.2).

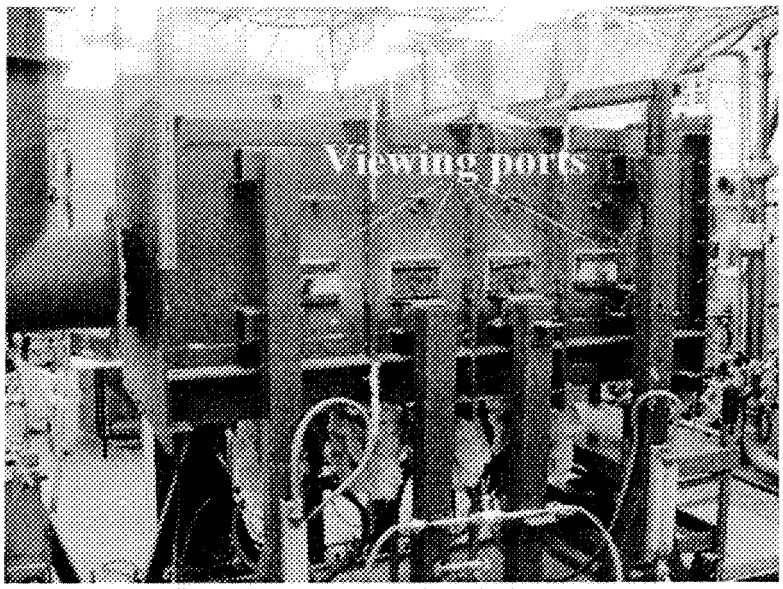

Figure 2.3 External view of the experimental furnace

The generally applied Cartesian coordinate system in the measurements and in the numerical computations is shown in Figure 2.4. The origin of the coordinate system is translated to the centerline of the burner nozzle.

The burner port permits the tilting of the burners from horizontal to 11.4° downward, Figure 2.1.b. Each section is equipped with two viewing ports on opposite sides for visual observation and filming as well as for the introduction of different probes (Figure 2.3). The axial distances of the center of the viewing ports from the burner are presented in Table 2.2. The gas and airflow rates are metered before entering the burner; the temperatures are measured along the length and thickness of the refractory walls as well as at the chimney exit.

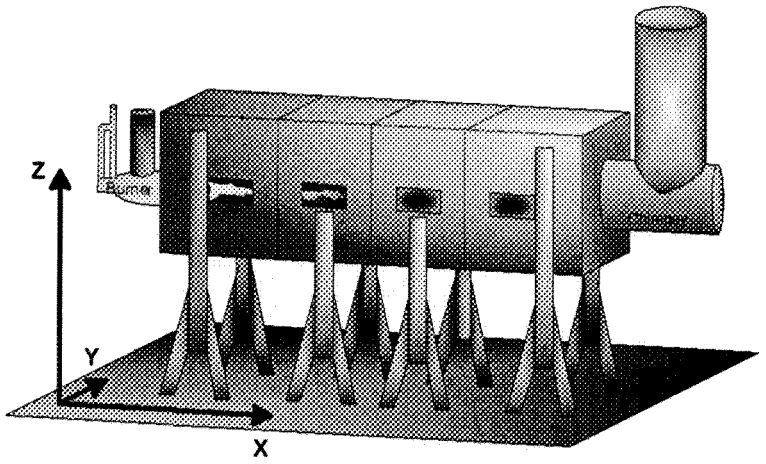

Figure 2.4. Orientation of the experimental furnace – applied coordinate system – the origin is translated to the centerline of the burner nozzle

Several burner test stands were designed with calorimetric sections that fully envelope the flame (water cooled cylindrical rings – for example M.I.T. Boston USA., KTH Heat and Furnace Technology- Royal Institute of Technology- Stockholm, Sweden, Research and Development Company for Combustion Technology- Miskolc, Hungary). The furnace used in the present project follows a different design philosophy in order to provide maximum flexibility for the analysis of the heat transfer between flame and charge. Heat is

extracted from the flame and is directed toward objects that mimic the form of charges in real furnace operations. The horizontal water-cooled plates (calorimetric plates) shown in Figure 2.1 simulate the horizontal surface of a molten metal bath.

Viewing port	distance (centerline) from the burner (mm)
1st	230
2nd	560
3rd	920
4th	1250

Table 2.2 Distance (direction x) of the test sections (viewing ports) from the burner nozzle

The calorimetric plates are cooled with water at a flow rate that keeps the temperatures always under the boiling point. The control of the rate of heat removal - together with the control of the surface temperature of the heat sinks - is realized by placing thermal barriers over the furnace floor. The measurement of mass flow rates and inlet-outlet temperature differences individually for each plate provides information about the average values of the total heat flux in the sections.

The furnace is equipped with a variety of sensors, measuring instruments and probes like: suction pyrometer, gas analyzer, one-hole Pitot tube, laser-Doppler velocimeter, visualization and imaging tools, infrared camera, plug type heat flux sensors. Beside the determination of the heat fluxes on the charges, the additional instrumentation makes possible a detailed analysis of the flame structure by measuring temperature, gas composition, velocity and turbulence intensity distributions.

2.3.2. Burners and flame types

In the present experimental study, two burners were studied. Both two burners are the in-kind support of the North-American Mfg. Co.

One of the burners is a conventional device, presented in Figure 2.5. This burner can produce two different flame types: a short flame, and a long luminous flame. The entering of the combustion gases and the mixing procedure between the fuel and oxydizer in the burner mouth will be discussed more in detail below in Section 3.6.1 (Figure 3.47 and Figure 3.48). The other burner is a low NO_x injection (LNI) burner, shown in Figure 2.6. The particularity of the LNI burner is the low NO_x emission. Similar to the conventional burner, this second one can also produce two flame types: the high velocity and the envelope flames. On the other hand, only the high velocity flame can be ignited at the burner start from cold condition. To start with the injection mode (envelope flame), the refractories must be heated up to more than 800°C in the entire furnace.

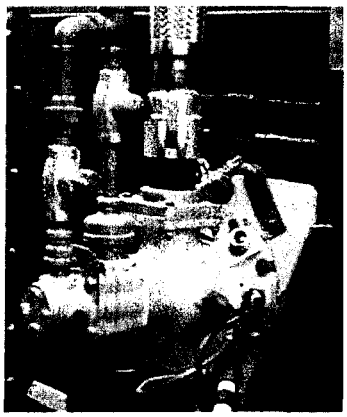

Figure 2.5. The conventional (traditional) burner

The high velocity flame is a concentrated jet flame with high momentum flux. On the other hand, in the case of the envelope flame cold air and gas are injected separately in the

combustion chamber. The mixing and heating occurs in the furnace. Thus, the hot refractories have a very important role in the heating-up of the gases. The name of the envelope flame is a registered trademark of the North American Mfg. Co. This technology is similar to the FLOX (flame less oxidation) technology of the Ijmuiden Institut.

Figure 2.6. The low NO_x Injection (LNI) burner

2.3.3. Heat flux measurements in the first and second experimental phases

The calorimetric plates provide an option for the determination of the total heat flux as an average over their horizontal area exposed to the flame. To provide more detailed information on the heat transfer between flame and charge, an array of heat flux sensors along the surface of the calorimetric plates has been used.

There are several methods and instruments for the experimental determination of heat fluxes in combustion chambers. An up-to-date overview of the available methods can be found in Baukal[6]. In our experimental furnace, we used the calorimetric plates designed and fabricated at UQAC. In addition, heat-flux sensors have also been developed earlier at

UQAC by Kiss et al.[112]. First the calorimetric plates are presented and subsequently the plug-type heat flux sensors.

2.3.3.1. The calorimetric plates

The calorimetric plates have multiple functions during the experiments. They serve as heat sinks in the furnace, which represent the cold charge in the furnace (cold is meant relative to the refractories). Secondly, the extracted heat fluxes are also determined by the use of the plates. In addition, the imbedded plug-type heat flux sensors are cooled by the calorimetric plates.

There are four calorimetric plates installed on the furnace floor. Due to the different sizes of the furnace sections, the sizes of the calorimetric plates are also different. In the first and last furnace sections the bigger plates are installed with the surface area of $A = 0{,}183\ m^2$ (381x479mm). On the other hand, in the middle (second and third furnace sections) the plates of the surface area of $A = 0{,}158\ m^2$ are mounted (330x479mm).

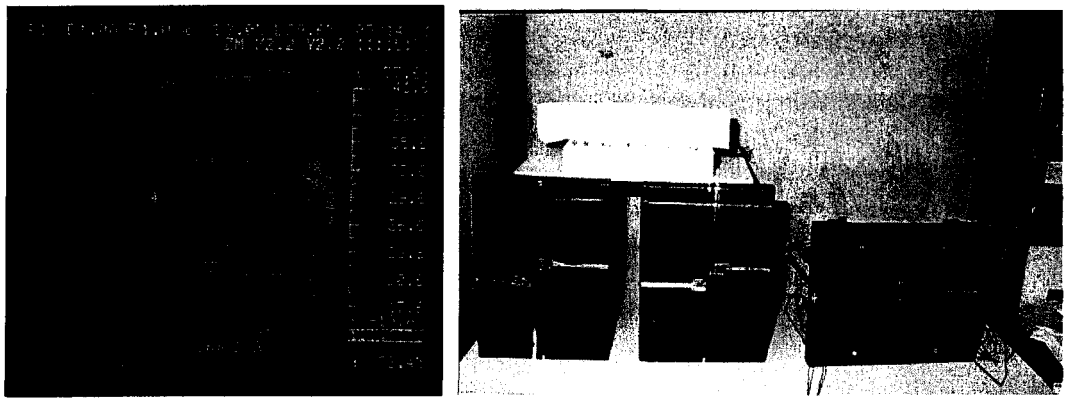

Figure 2.7 Calorimetric plates, left: Visualisation of the cooling canals with the infrared camera, right: the calorimetric plates before installation in the furnace

To visualize the cooling channels of the calorimetric plates, cold and hot water was

introduced from the opposite sides in the plates. The surface was photographed using the infrared camera. As it can be very well seen in Figure 2.7, the channels are configured in counter-flow. This is to produce the most homogeneous possible temperature distribution in the plates. It is important, because the temperature of the calorimetric plates serve as reference temperature for the imbedded heat flux sensors.

As it was mentioned above, one of the functions of the calorimetric plates was the measurement of the average heat fluxes per furnace sections. Originally, the surfaces of the calorimetric plates were painted with black absorbant coating with an emissivity of at least $\varepsilon = 0{,}95$ for measuring the total heat flux. The painted plates are shown in Figure 2.7, before the installation to the furnace. However, during the preliminary experiments, a serious problem arose with the envelope flame. As it was discussed in section 2.3.2, the envelope flame needs to be surrounded by adequately preheated refractories for ignition. Due to the very large, intensively cooled emissive surface, the envelope flame could not be ignited. In addition, the accumulated unburned CO at the bottom of the furnace produced a CO explosion. For this reason, the surfaces of the water-cooled calorimetric plates have been covered with Fiberfrax insulation. (Fiberfrax is a registered trademark). The heat flux sensors were placed in slightly raised position, compassed with additional metal rings that were welded on the calorimetric plates (see Figure 2.9). Thus, the heat flux sensors and the Fiberfrax insulation are coplanar, so no additional perturbation in convective fluxes was produced.

2.3.3.2. The plug type heat flux sensors

These plug-type heat flux sensors (Figure 2.8) have a cylindrical shape and they

function according to the steady-state principle. Their robust and relatively simple design allows for easy fabrication and reliable operation. The sensor consists of a cylindrical copper core, an insulating ring (PTFE or ceramic) and an outer copper ring as it is shown in Figure 2.8. Despite the fact that machinable ceramic was used during the preliminary experimental series as isolating ring, the machinability and close fitting of these ceramic rings were not ideal. Significant differences were noticed between the responses of the 24 heat flux sensors during the calibration procedures. Finally, all the insulating rings of the sensors have been replaced by teflon (PTFE) rings.

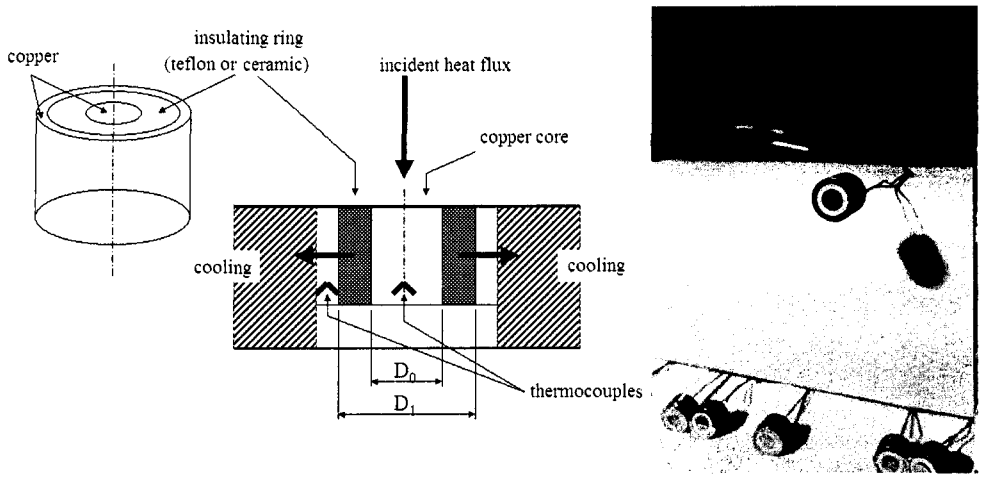

Figure 2.8 Plug type radial flow heat flux transducer[112]

The sensors are built into machined vertical tubes passing through the body of the water-cooled heat sinks, Figure 2.9. To be able to measure not only the total heat flux but also its convective and radiative components separately, two heat flux sensors with different radiation properties are used (Figure 2.10). Ideally, the ensemble of a perfectly black and a perfectly reflective sensor would offer a simple mean to separate convection and radiation. The reading of the perfectly black sensor gives the total flux while the

perfectly reflective one measures only the convective part. Under ideal conditions, the radiative part is obtained simply by substracting the reading of the reflective sensor from that of the black sensor. In practice, we are not able to fabricate absolute black and perfect mirror surfaces. The bigger difficulty is with the reflective coatings as the smallest dust or soot deposition turns them easily into a "gray" surface. We use polished gold coatings on the convective sensors and a ceramic powder based black paint on the total flux sensors.

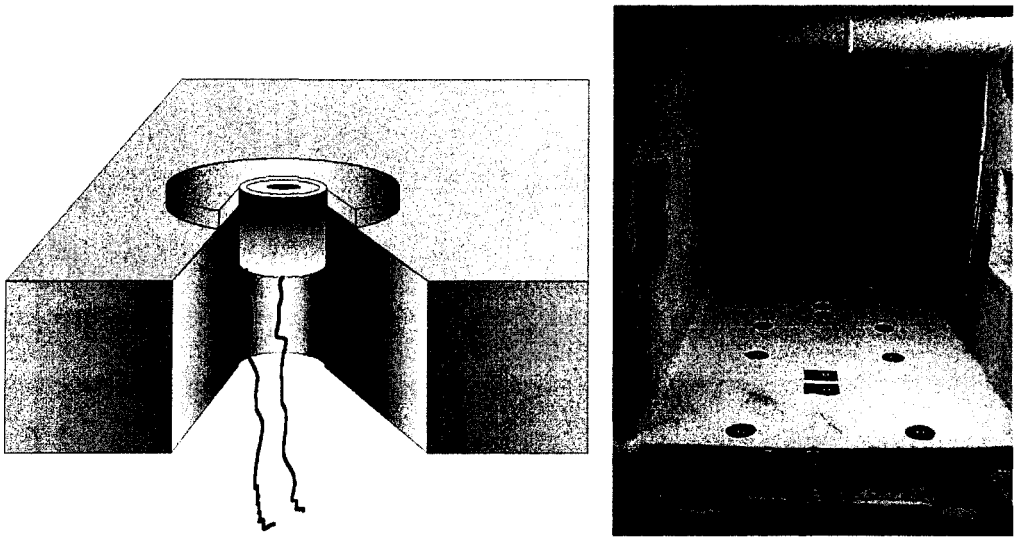

Figure 2.9 Leftside: Integration of the heat flux sensors into the calorimetric plates
Rightside: Calorimetric plates and heat flux sensors inside the furnace

As the sensitivity of the reflective sensors to radiation is bigger than zero, and the sensitivity to the radiation of the blackened sensors is less than 100%, the evaluation is more complex than a simple subtraction of the readings from each other. The readings of both sensors include contributions from radiation and convection but with different sensitivities. The sensitivities are determined during the calibration. The evaluation of the readings is based on the solution of the two sensor equations for the two unknown flux

components[112].

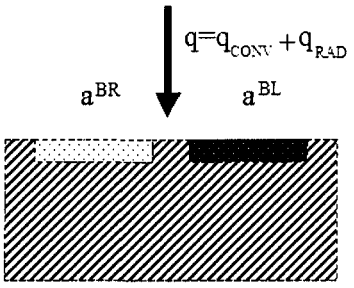

Figure 2.10 The principe of the two radiometer method

The calibration of the heat flux sensors is a long and labor consuming process. First the black ones are calibrated against a NIST traceable black-body radiator both for normal and hemispherical radiation[113]. The calibration for the normal radiation serves basically the verification purposes. For the determination of the sensitivities of both sensors to radiation and convection, a relatively simple method was developed that is based on the heating of the sensors through a thin, horizontal, thermally stable air layer. This way, known radiative and convective (more precisely conductive through stagnant air layer) heat fluxes can be produced. The method can be used even for the regular verification and recalibration of the built-in sensors inside the furnace.

The arrangement of the sensors inside the furnace is shown in Figure 2.9. Six sensors are installed in each calorimetric plate, which means a total of 24 sensors in the furnace.

2.3.3.3. Heat transfer in furnaces

It is known that clean, non-oxidized metallic surfaces are good reflectors for both visible and thermal radiation. The solid surfaces of equipment and materials handled and processed at high temperatures in the metallurgical industry rarely stay good reflectors. The

smallest dust deposition or slightest oxidation rapidly increases the emissivity and absorptivity in the longer (thermal) wavelength domain, promoting the radiative energy exchange. However, there are certain cases when the absorptivity of the surface of the heated targets is not too high and convection can play a more important role. In the aluminum industry, the absorptivity of the free surface of the molten metal can vary strongly as a function of the thickness and composition of the covering dross layer. The effect of the dross layer in the overall heat transfer is a subject of a certain controversy. Without any dross and oxide the absorptivity of the free surface of the metal is only 0.03-0.05 depending on alloy type, the formation of a thin oxide layer can rapidly increase it to 0.1-0.2. Thicker dross with high porosity can effectively increase the emissivity/absorptivity into the 0.5-0.7 range. The surface properties of aluminium raise a controversial issue for the effective heating of aluminium: without dross and oxide layer the absorption of radiant energy is nearly negligible, a dross layer increases absorption but represents a thermal insulation. In cast shop practice, to find the optimum thickness, is not easy to achieve.

In our experimental furnace the refractory lining of the ceiling and sidewall acts the same way as the lining of a reverbatory furnace in the industry. During the heating-up of the furnace the radiation from the furnace walls represents an increasing proportion. When the internal surface temperature reaches the 800-1000 °C range, the radiation from the walls can reach or exceed the self-radiation of the flame, depending on the flame type.

2.3.4. Transformation of the furnace for realizing the third experimental phase

As it was mentioned above, the furnace transformation was inevitable for realizing the third experimental phase. In addition, this necessity was also a great opportunity, a challenge for us. Are we able to replace our former system, which in spite of some imperfections is very well operating, to another that will be still better? Can we keep the most important advantage of the system, namely its simplicity?

Multitudinous suggestions, conceptions, configurations, materials and methods were evaluated. All the calorimetric plates were individually designed using Autodesk Inventor 5. In addition, the concept of the newly developed heat-flux sensors should has been fully adapted to the calorimetric plates. Parallel with the long design procedure, a CFD code was developed in Visual FORTRAN. This code computes the internal heat conduction in a cylindrical coordinate system in two dimensions. The dimensions of the new, T-plug-type heat-flux sensor were determined by the help of this computational module (see Appendix K).

The calorimetric plates were fabricated under CNC (computerized numerical control) at the manufacturing facility of the "Mercier Industries". On the other hand, the heat flux sensors were fabricated at the workshop of UQAC by the technicians of the CURAL. This kind of work required much of elaborateness on the part of the technicians.

Subsequently, the transformation of the furnace took place as follows: construction of the internal part of the furnace using the refractory bricks (Figure 2.11), inserting of the calorimetric plates, setting and sticking of the Fiberfrax isolations, calibration of the heat flux sensors, preliminary tests, several modifications and final adjustement.

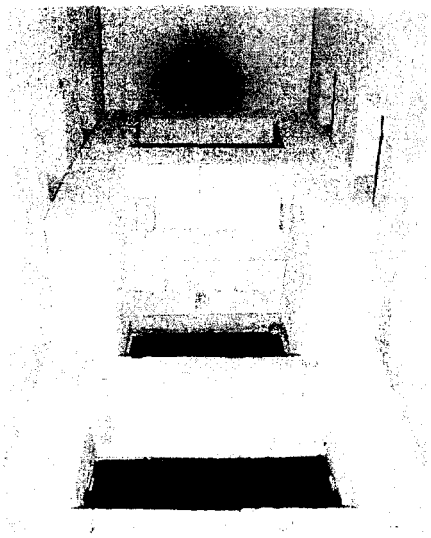

Figure 2.11 The experimental furnace during the transformation

2.3.4.1. The calorimetric plates in the impingement configuration (third experimental phase)

The new calorimetric plates are shown in Figure 2.12. The technical drawing was made using the "Autodesk Inventor 5" software (design is shown in Appendix L.). Each calorimetric plate was individually designed. The important differences in comparison to the former calorimetric plates are the following:

1.) the material is aluminium instead of steel

2.) the upper and lower part of the plate is screwed and not welded

3.) the cooling channels are in serpentine instead of parallel counter-flow arrangement

4.) instead of being tightly fitt the heat flux sensors are removable

5.) the calorimetric plates do not provide the water cooling for the HFS (heat flux sensors).

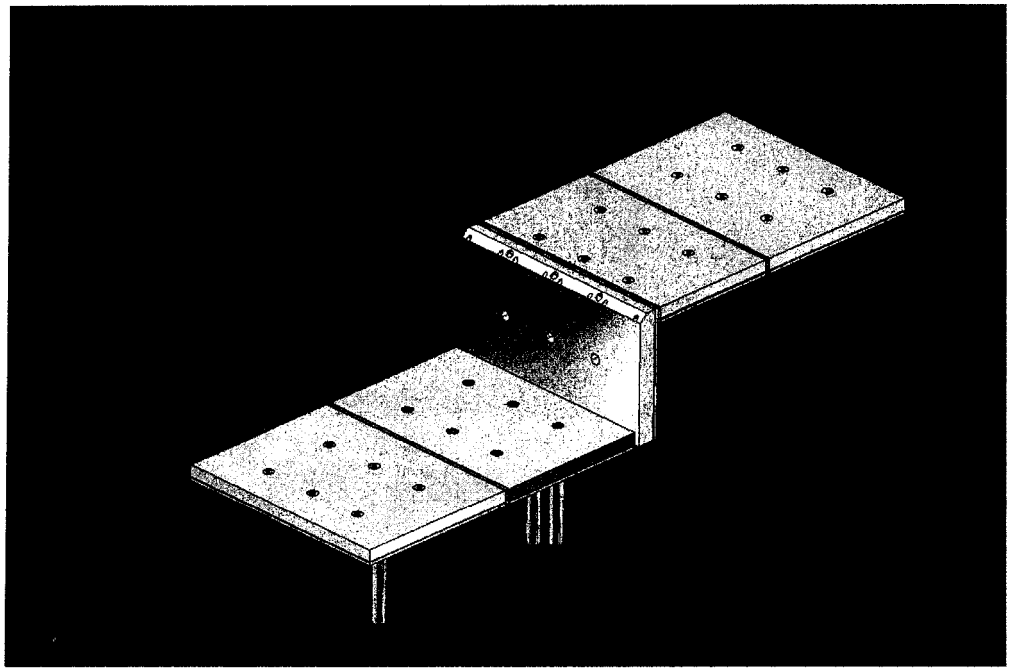

Figure 2.12 The technical drawing of the calorimetric plates in 3D using the Autodesk Inventor 5 software

The measurement holes for the heat flux sensors are symmetrically positioned. The distance between the central and lateral measurement points is ±120 mm. On the vertical plate, the upper corner is chamfered by 45° as it is shown in Figure 2.13.

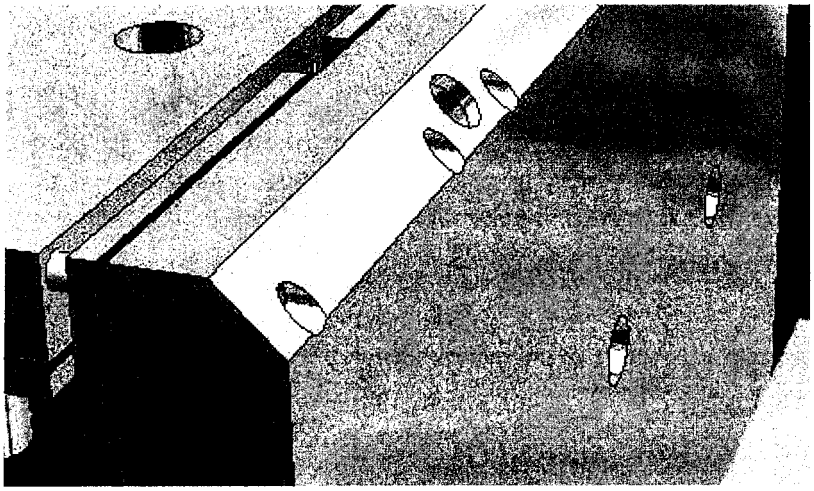

Figure 2.13. The corner of the vertical plate is chamfered by 45°.

There are several advantages of the new calorimetric plates. They are lighter, can be opened to have access to the canals for verification or cleaning.

The disadvantage of the new concept is that the plates can melt in the furnace more quickly if the cooling water circulation stops during the experiments. In the case of low mass flow rate of the cooling water, the homogeneity of the surface temperature will be lost.

2.3.4.2. The new plug-T-type heat flux sensors for the impingement configuration

As it was discussed earlier, the plug-type heat flux sensors were developed at UQAC around 1990. The present comprehensive experimental research started in the beginning of 2000. In the frame of this experimental program, the plug-type heat flux sensors were applied principally and they responded very well to all the expectations. Owing to their very simple design and accurate planning, many advantages were unified in this type of sensor, namely the good signal-to-noise ratio, the right sensibility for separating the heat-flux component, smallness, construction without internal cooling, mass-productibility, etc.

During the planning procedure of the plug-type transducers, analog mathematical calculations were executed to find the optional geometrical scale[112]. These calculations were easily feasible due to the simple geometry of the sensor.

In the case of the newly developed plug-T-type heat-flux sensors, the geometry is more complex. That is the reason why a numerical method was applied for optimizing the geometry of the sensors. The temperature difference in steady state condition between two selected points of the calculated domain is converted to heat-flux. The finite volume method was used for calculating the temperature field. The numerical calculation was

carried out for different sensor geometries and the best concept was selected and fabricated. Further description is given in Appendix K.

The concept and the working principle of this new heat flux sensor is the same as its predecessor. Similarly, this is a plug type radial flow heat-flux transducer. In addition, the two-radiometer method is also the same to separate the heat-flux components. A schematic view and a photo are shown in Figure 2.14 and Figure 2.15. Observing these figures, the obvious differences compared to the former plug-type sensor are the form « T » of the central core as well as its integrated water-cooling system. The new sensor has many advantages relative to the old one. On the contrary, the simplicity was lost. Thus, the biggest disadvantage of the plug-T-type sensor is the complexity, which results that its fabrication is a very labor-consuming process. The advantages are listed next:

1.) The most important advantage is the facility of the comparison of heat-fluxes between two measurement locations, because only one sensor is in use (1-1 black and bright sensors) oppositely to the ancient method, where 24 sensors (12-12 black and bright) were embedded in the calorimetric plates.

2.) It is better adapted to the impingement configuration where extremely high heat fluxes are expected in the stagnation point. With this concept, the sensors are only exposed to the heat flux during the measurement procedure. In the direct impingement point, the continous exposition to the elevated heat fluxes can seriously damage the heat flux sensors.

3.) Verification and cleaning of the surfaces and recalibration of the sensors can be made at any time, even during the operation of the furnace.

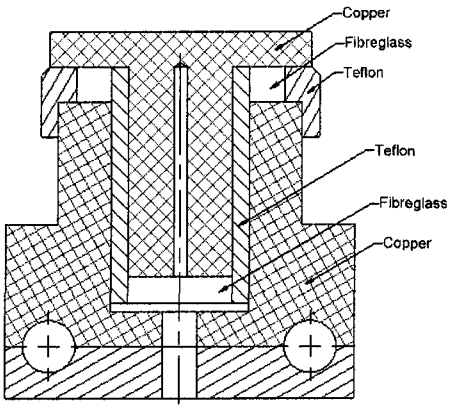

Figure 2.14 Schematic view of the T-type heat flux sensor

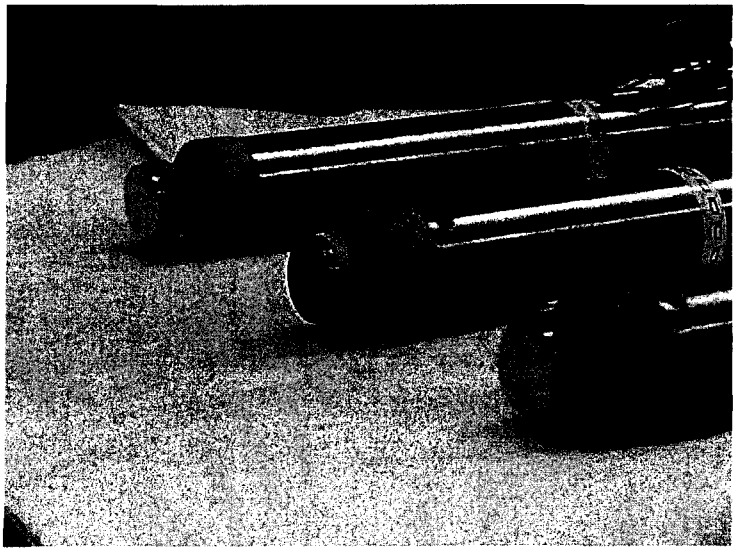

Figure 2.15 External view of the heat flux sensors

4.) Recalibration of the sensors can be effected outside the furnace, in favourable (quasi laboratory) conditions.

5.) The new sensors have greater sensitive surfaces and a very important

advantage is that there is no parasite heat-flux incident to the insulating ring as in the case of the plug type sensors.

2.4 Other measurement instruments

2.4.1. The suction pyrometer

Temperature measurement methods in gas streams are presented in Appendix G. Only the characteristics of the temperature-probe used in the experiments will be shortly presented here.

The suction pyrometer applied in our laboratory is special prototype, which had been unically adapted to our experimental, 150 kW furnace. In the suction pyrometer, a platinum-rhodium thermocouple, protected from chemical attack by sintered alumina sheath, is surrounded by two concentric radiation shields. (Figure 2.16) The gases are drawn between the shields and over the sheath with high velocity (min. 150 m/s) so that the equilibrium thermocouple temperature is nearly that of the gases without the need of a correction. However, it was experimentally verified, whether the adequate gas-suction velocity was achieved during the experiments. The suction pump was connected to a "Y-type" valve. One of the flanges was joined to the suction pyrometer while the other has been opened to the atmosphere. By measuring the gas temperature, the flange, which was opened to the atmosphere was gradually closed, allowing to increase the suction velocity in the pyrometer. First, the detected temperature increased with increasing suction velocity, but finally the temperature converged to a certain value, so with increasing velocity a temperature plateau was achieved.

The thermocouple element is of type S, which can be used up to 1700°C (1973K). However, at that elevated range, 1600°C to 1700°C, the exposure to heat should only be of a very short duration (just long enough for the EMF output to reach steady state).

It is important to use as high a flowrate as possible for maximum cooling effect and to reduce expansion and contraction while operating the probe.

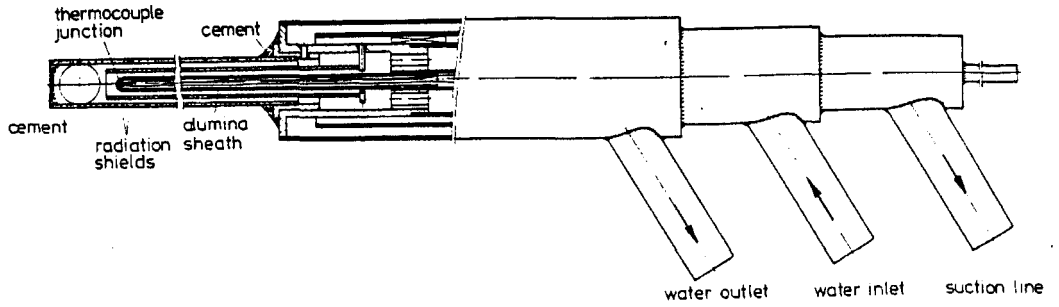

Figure 2.16. Scheme of the applied Suction Pyrometer

Gas temperature measurements were performed in the first (parallel firing) and third (impingement) experimental phases for the four different flame types (long, short, high velocity and envelope). In the case of parallel firing configuration, the temperature profiles were also measured at partial burner power of 50%. Figure 2.17 shows the suction pyrometer in work. The results of the temperature measurements are presented later in CHAPTER 3. (Figure 3.1 to Figure 3.10).

The gas temperature measurements were effectuated using the four viewing ports of the experimental furnace (Figure 2.3). The water-cooled suction pyrometer has just two degrees of freedom (z and y in Figure 2.4). Because of its robust joint, only the up and down tilting of the probe (movement in direction z) is permitted but the movement in the x direction is not. Systematically, only one temperature profile (y-direction at $z = 0$) was

recorded in each viewing port.

Figure 2.17. The suction pyrometer in work

Undoubtedly, the temperature of the flame depends on many conditions as air-preheating, quenching in the flame, refractory temperatures, cooled calorimetric plates, opened window, object in the flame, etc. The temperature of the refractories, which has one of the major influences on flame temperature, reflects the condition of the furnace preheating. The different measurement data (heat flux, gas velocity, flame temperature) were not recorded at the same instant after the same preheating period. Therefore, as it will be discussed later in CHAPTER 3, the measured flame temperatures were corrected using the refractory temperature data, which were continually recorded during all experiments.

2.4.2. Velocity measurements using the Pitot probe and the LDV instrument

Various methods are available to obtain the velocity profiles of high temperature

flows. Each method has its own characteristics, advantages and disadvantages. Two different instruments, the laser Doppler velocimeter (LDV) and the one-hole Pitot tube, have been used in our experiments for the velocity measurements. The theory of these methods are given in Appendix H.

Similarly to the gas temperatures, the velocity measurements were made in the first (parallel firing) and third (impingement configuration) phases for the four different flame types. In the case of parallel firing arrangement, the velocity profiles were also measured at the partial burner power of 50%. The measured velocity profiles are presented in Figure 3.11 to Figure 3.16 of CHAPTER 3.

Many problems arise during the application of the laser Doppler velocimeter. Due to a failure of its electronic system for effective frequency shifting, the LDV system was not able to sample the seeding particles in the high-velocity range, namely above about 20 m/s. When in the case of the LNI Burner, the velocities are in the range of 40 and 90 [m/s]. The second function of the frequency shifting mechanism is the determination of the velocity direction. As this functionality has also failed, the system was not able to detect eventual recirculations. In addition, the detection sensitivity depended widely on the tracer type in use, the way of injection, and the working temperature as well as on the burner power. Finally, in the experimental tests, very fine alumina powder was used as tracer to obtain the velocity profile. In the rear part of the combustion chamber, this tracer was hardly detected by the LDV system, especially at 100% burner power, since the powder was desintegrated before. Considering all these drawbacks, it was necessary to replace the LDV technology by the Pitot-tube method.

On the other hand, the LDV system, which provides absolute accuracy without the need of calibration, was very useful in the period of the verification of the performance and calibration of the Pitot probe. In Figure 2.18, the velocity profiles are presented in the first furnace section for the short flame at 50% burner power. The position of the 0 mm is an arbitrarily chosen reference point, which is not in the centerline of the furnace. Each point on the diagram is the average value resulting from a curve of normal distribution (Gaussian curve) which contains about 500 velocity values.

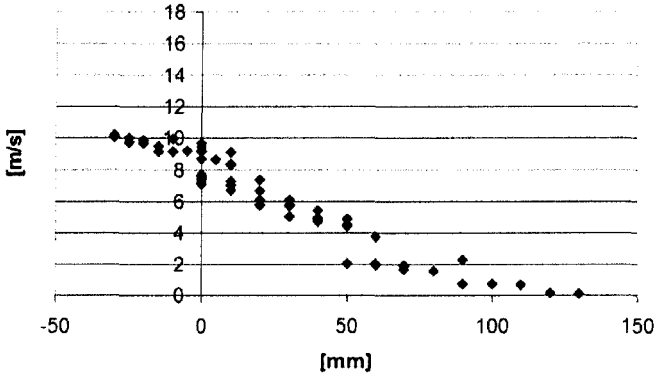

Figure 2.18. Velocity measurements using the LDV system – short flame at 50% burner power in the first furnace section. Reminder: The position of 0mm is not in the centerline of the furnace

In the case of the short flame (at 50% burner power), the obtained velocity profiles are compared using different methods in Figure 2.19. One of the curves was obtained using the LDV instrument. The other two curves had been determined using the Pitot tube. The measured pressures are corrected either with the reading of the unshielded thermocouple located on the top of the Pitot probe or with that of the suction pyrometer. It is obvious at first sight that the three methods have similar trends and they are relatively close to each other. The velocity profiles obtained using the unshielded thermocouple are always below

those taken using the suction pyrometer. It can be explained by the fact that the sensor of the suction pyrometer is shielded against radiation. On the contrary, the unshielded thermocouple has a considerable amount of radiative heat loss toward the "cold" refractories. ("Cold" is meant relative to the flame temperature.)

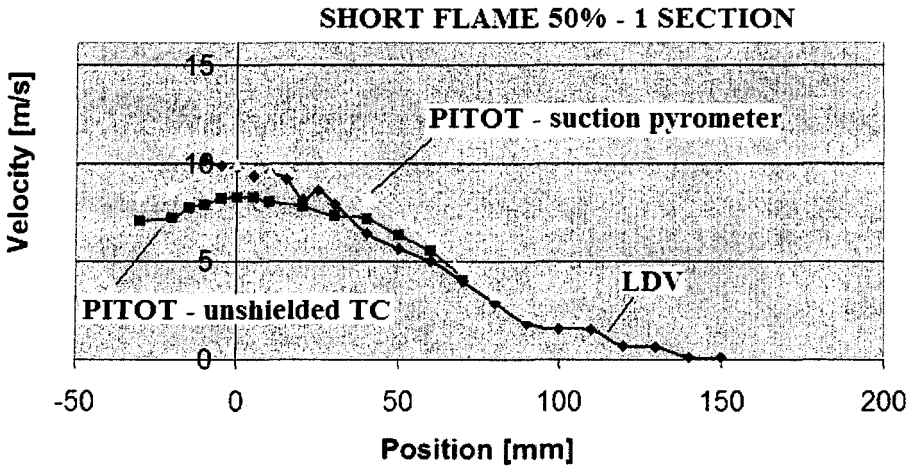

Figure 2.19 Comparison of velocity results obtained using different measurements techniques – Short flame at 50% burner power in the first furnace section

In this low velocity flow case, the results of the LDV system were considered as reference. As it can be seen in Figure 2.19, the velocity results of the Pitot probe, which is corrected with the temperature of the suction pyrometer, and the results of the LDV method are similar in the furnace centerline. However, at the radial distance of about 30 mm, the Pitot probe results higher velocities. Away from the centerline, the velocity-vectors are not parallel to the longitudinal direction. While the one-component LDV system measures only one velocity component, which is parallel with the direction x, the one-hole Pitot tube measures the maximal velocity if its declination from the axial direction is below of about 30 degree. This declination limit was both computed, basing on the literature and

experimentally verified. For further details, see the directional sensitivity of the Pitot probe in Figure H.10 of Appendix H.

Due to the above-discussed reasons, we were not able to measure recirculation in the flame. The measurements are less reliable where the normal component of the velocity is considerable in comparison to the tangential part, as well as where the turbulent fluctuations are elevated. Recirculation zones are present in the near wall regions and in the rear part of the furnace while the highly turbulent zones are at the edge of the jet zone in the case of the high-velocity flame.

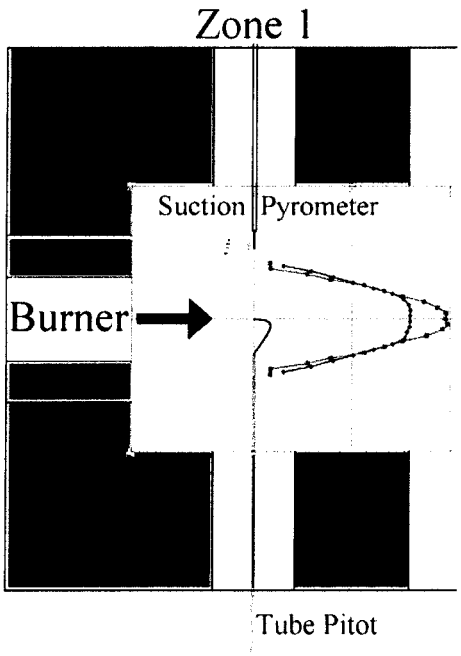

Figure 2.20. Schematic of the velocity measurement using the Pitot probe

During the velocity mapping in the furnace, the temperature correction was made using the readings of the suction pyrometer. Figure 2.20 shows the schematic of the velocity measurement. After the pressure data were recorded using the Pitot probe in a

certain coordinate point of the furnace, the suction pyrometer was placed from the opposite viewing port to the same coordinate point to measure the gas temperature. The velocity can be calculated from the following equation

$$u = \sqrt{\frac{2 \cdot p_{mano} \cdot \Re \cdot T_{corr}}{M_{mixture} \cdot p_{atm}}}$$

Eq. 2.1

where p_{mano} and p_{atm} are the pressures indicated by the manometer connected to the pitot probe and the atmospheric pressure respectively.

As it was discussed above, the directional sensitivity and the effect of turbulence are possible error factors in the measurements made by a square-head one-hole pitot tube. However, the accuracy of this method depends also on the precision of the pressure detection. The pressure was measured with an inclined-tube/tilting manometer of the Dwyer Company. The smallest detected pressure is $5 \cdot 10^{-3}$ inches of water, which corresponds about to 4 [m/s] at general operating conditions.

Farther, as seen in Eq. 2.1 there are some other factors that can influence the precision of the calculated velocity. These errors can occur during the correction. As it is seen in Eq. 2.1, the determination of the molar mass of the mixture, the accurate temperature measurement of the hot gases, and the error due to the replacement of the static pressure with the atmospheric pressure are all the influencing factors that can affect the accuracy of measurement.

Although the actual value of the molar mass of the mixture depends also on the proportion of the unburnt and burnt components of the reacting gases, but considering the

nitrogen (72 mass%) which is dominant in the process, the molar mass of the mixture does not vary greatly.

However, the temperature correction is based on the suction pyrometer measurements so the accuracy of this factor is acceptable.

The error due to the replacement of the static pressure with the atmospheric pressure in the correction Eq. 2.1 depends on the static pressure variation in the combustion chamber and also on the furnace pressure. During the experiments the furnace pressure was kept at about 0.05 [inches of water] ($\cong 10Pa$) below atmospheric pressure, which is negligible.

In short, the one-hole pitot-tube gives good results in the velocity range above about 5 [m/s] in the case when the velocity fluctuations to the normal of the main velocity are small. The existence of recirculation zones can be predicted but accurate measurements cannot be done. In the near-wall regions (boundary layer) where the flow velocities are small and the opened viewing ports disturb the developed boundary streams, the one-hole Pitot-tube is not the appropriate technique for the velocity measurements.

2.4.3. Gas composition measurement

The gas composition was measured with a portable combustion analyzer (PCA) of the BACHARACH Inc.

The applied instrument is a commercial grade, hand held, combustion efficiency analyzer that is designed for continous sampling of small industrial and residential furnaces, boilers and appliances.

The PCA directly measures, displays and stores the room temperature (°C), the flue

gas oxygen content (%), the flue gas temperature (°C), the carbon monoxide and nitric oxide content of the flue gas (ppm) and the pressure (Pa). For natural gas, the PCA can compute the combustion efficiency (%), the excess air ratio (%), the flue gas carbon dioxide content (%), the carbon monoxide and the nitric oxide content of the flue gas referenced to 0% oxygen (ppm). For further details, the reader is reffered to [111].

2.4.3.1. The combustion reaction equation using the available gas composition

The composition of the natural gas provided by Polygaz is presented in Table 2.3. The combustion reaction is shown for 1 mol fuel in three different cases. In the first case, the given gas composition is burnt with a 10 percent of excess air. In the second case, the real gas composition again is burnt with a stoichiometric quantity of air. In the last case, a simplified equation is given. The fuel is assumed to be 100 % methane, which is burnt with a 10 percent of excess air.

Real gas composition with 10% excess air:

$$0.952CH_4 + 0.022C_2H_6 + 0.002C_3H_8 + 0.004CO_2 + 2.190O_2 + 8.255N_2 \rightarrow \\ \rightarrow 1.006CO_2 + 1.978H_2O + 0.199O_2 + 8.255N_2$$

Eq. 2.2

Real gas composition – stoichiometric:

$$0.952CH_4 + 0.022C_2H_6 + 0.002C_3H_8 + 0.004CO_2 + 1.991O_2 + 7.506N_2 \rightarrow \\ \rightarrow 1.006CO_2 + 1.978H_2O + 7.506N_2$$

Eq. 2.3

Simplified gas composition (100% methane) – with 10% excess air:

$$CH_4 + 2.2O_2 + 8.272N_2 \rightarrow CO_2 + 2H_2O + 0.2O_2 + 8.272N_2$$

Eq. 2.4

Mass percent [%]	Component	Molar mass [g/mol]	Number of moles in 100g of mixture
95%	CH_4	16	5.95
0.4%	CO_2	44	0.0091
2.0%	N_2	28	0.07143
2.2%	C_2H_6	30	0.0733
0.2%	C_3H_8	44	0.0045

Table 2.3 The composition of natural gas provided by the local Gas Company (Polygaz)

2.5 Execution of the experimental program

During the execution of the experimental program, several problems arose. Only those will be mentioned here, which effected the planning of the experiments.

As it was discussed in section 2.3.3.2, the bigger difficulty is with the reflective sensor coatings as the smallest dust or soot deposition turns them easily into a "gray" surface. We were shortly confronted this kind of problem. Thus, a method had to be found, which can be used to verify the sensor surfaces. The sensor surfaces needed also to be repolished and repainted at place, inside the furnace. Therefore, the goals to realize heat flux measurements at lateral positions were given up, because the recalibration of these lateral sensors, embedded in the calorimetric plates, were not realizable with the available instruments. Simply, due to the proximity of the refractories, there were not enough places to install the portable calibration unit. Therefore, in the first two experimental phases, the heat fluxes using the plug-type sensors were only measured in the furnace centerline.

In the case of the envelope flame, the simultaneous opening of two viewing ports (e.g. at the opposite sides) can risk the quenching of the flame. Therefore, in this case, the dynamic pressure and the gas temperature were not measured simultaneously.

CHAPTER 3.
PRESENTATION AND ANALYSIS OF THE VELOCITY FIELDS, THE TEMPERATURE DISTRIBUTIONS AND THE GAS COMPOSITIONS

3.1 General objectives

In this chapter, the velocity field, the temperature distribution and the pollutant formation measurements are discussed for the four different flame types. Temperature and velocity measurements were made for the parallel firing and impingement arrangements at 50% and 100% burner powers. In the case of the parallel firing configuration, except for envelope flame, the partial burner power (50%) was also tested.

At first, in the following two sections (3.2 and 3.3), the experimental temperature and velocity results taken in the four furnace viewing ports are presented for all the studied cases without any discussion and analysis. The differences in velocities and temperatures between the four flame types, the two configurations as well as the different burner powers are represented in various figures and diagrams. The computed velocity and temperature fields, which are obtained by interpolation between the measurement profiles, are also presented here.

Detailed analysis and discussion about the velocity fields and the temperature distributions are given in sections 3.5 and 3.6. Measurements were done in the first, second, third and forth test sections. However, it is important to know the velocity field and the temperature distribution between the nozzle exit and the first test section also. This can only be determined, by calculations using iteratition, interpolation or in some cases maybe just by approximation. As a first step, a « Computational module for the nozzle exit parameters » was developed which permits to calculate the required velocities and temperatures at the nozzle exit by iteration. With the help of these calculated parameters, we expand with backward extrapolation the measured velocity and temperature fields to the burner-mouth region. In effect, interesting methods and ideas are presented in sections 3.5 and 3.6, which marry the measurements and computations.

The high velocity and envelope flames can be analysed using the free jet theorem in which case the description of the turbulent motion is somewhat easier than that of wall turbulence. However, the long and short flames cannot be considered as free jet flows, so these flames will be analysed applying the confined jet theorem. The furnace refractory temperatures are presented in section 3.7. A detailed analysis is important to calculate the indirect radiative heat transfer. The refractory temperatures in the sidewalls and ceiling are presented for the four various flame types and the three different flame-object configurations. The occurred differences due to the various preheating times are also compensated using the refractory measurements.

The pollutant emission is presented in section 3.4. Discussion is given in section 3.8. Thermal NO_x formation was also calculated in the envelope flame. The numerical model

and important results are presented in section 3.8.

3.2 Temperature distribution

As it was discussed in the previous chapter, the temperature profiles were captured in the four test sections using the suction pyrometer. The interpolated temperature contours are presented in Figure 3.1 to Figure 3.4 for the short, the long, the high velocity and the envelope flames respectively. The horizontal axes are the distances from the burner in millimetres while the vertical axes are the distances from the burner centerline also in millimetres.

The temperature contours of the four flame types are compared using the same temperature scale (between 800°C and 1600°C) in Figure 3.5 and Figure 3.6 for parallel firing and impingement arrangements.

The normalized temperature profiles are presented in dimensionless diagrams in Figure 3.7 to Figure 3.10. The three diagrams in each figure represent the temperature profiles of impingement arrangement at 100% burner power, as well as the profiles of parallel firing arrangement at full and 50% burner powers. The normalized diagrams permit to compare the form of the profiles instead of the temperature levels, which depend also on the operational conditions. However, the maximum values of each normalized diagrams are also given in parenthesis over each graph.

Apart from the envelope flame, the temperatures in the centerline are decreasing downstream in each graph. However, in the case of the envelope flame, the relevant measurement sections are indicated next to the profiles.

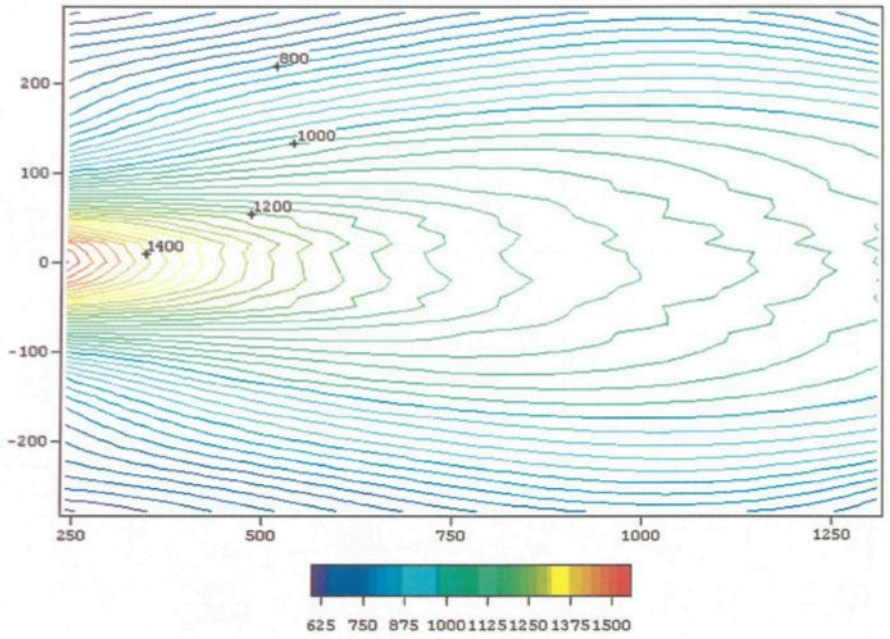

Figure 3.1 Temperature contours in the short flame – parallel firing arrangement

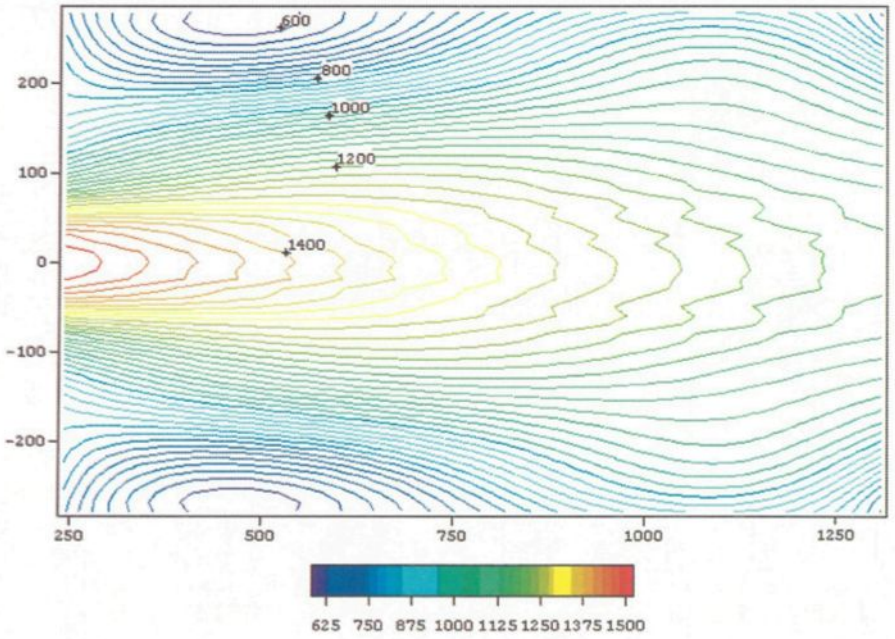

Figure 3.2 Temperature contours in the long flame – parallel firing arrangement

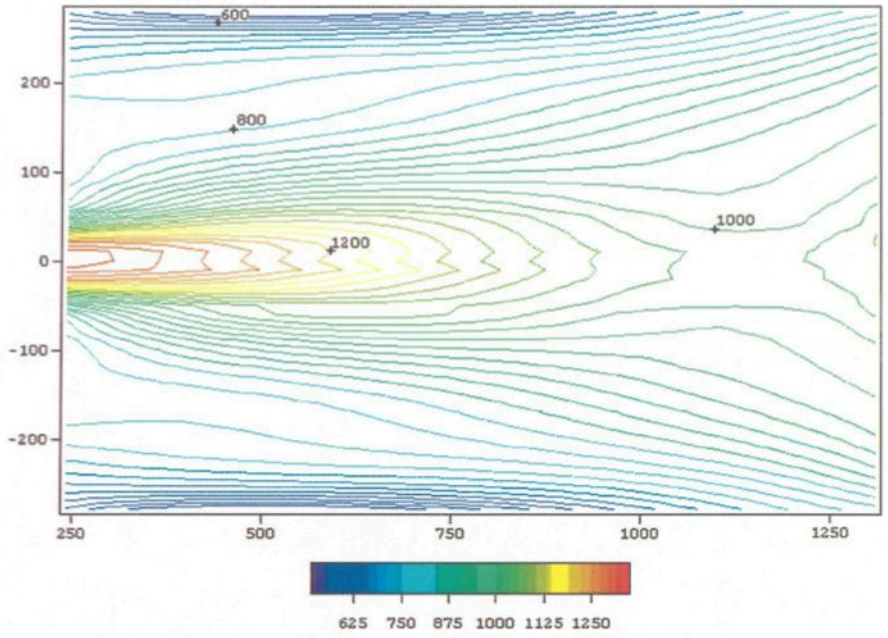

Figure 3.3 Temperature contours in the high velocity flame – parallel firing arrangement

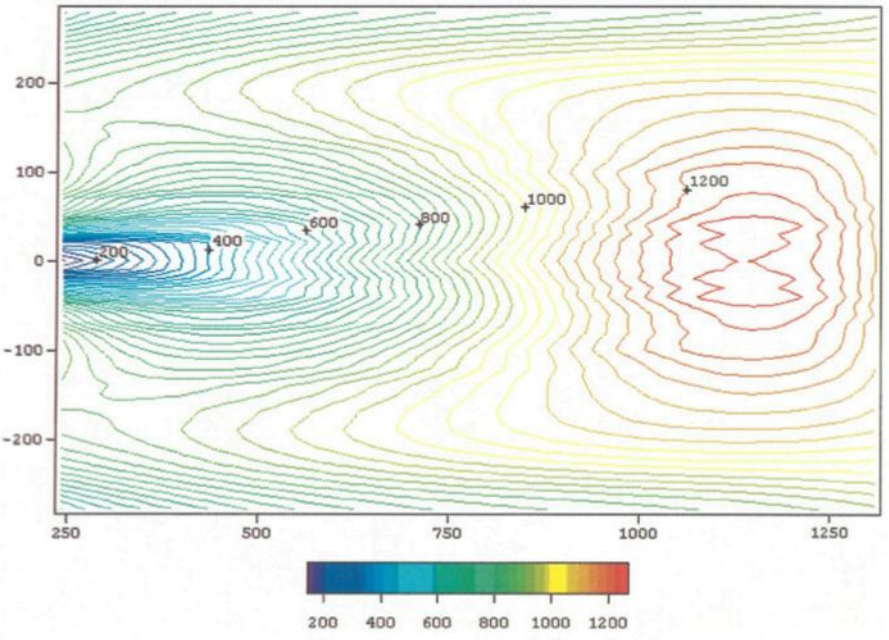

Figure 3.4 Temperature contours in the envelope flame – parallel firing arrangement

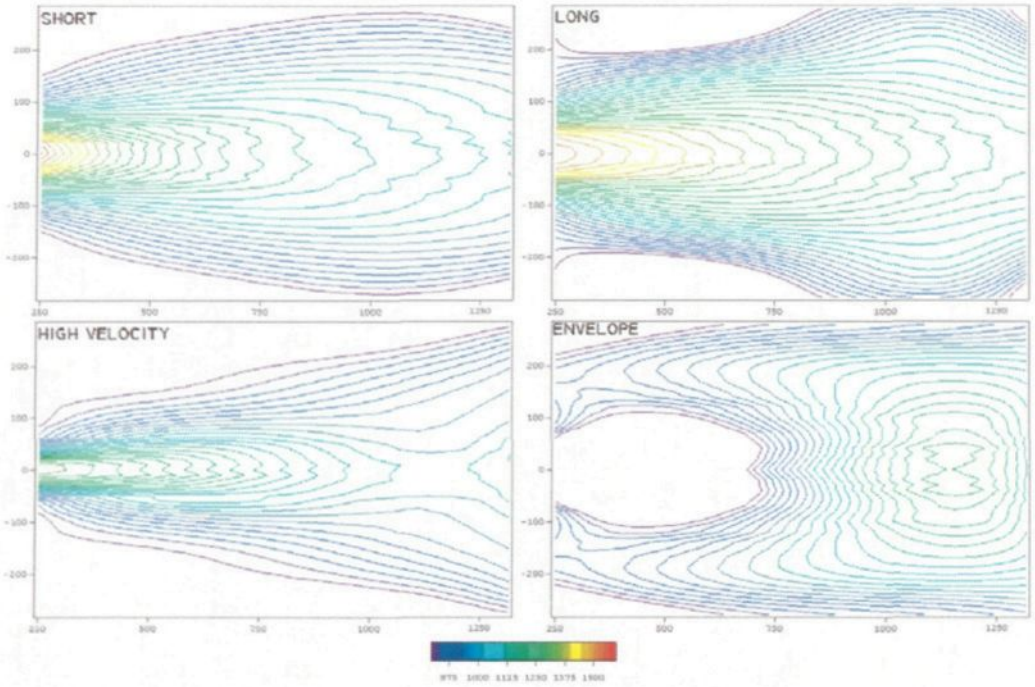

Figure 3.5 Comparison of the temperature contours at parallel firing arrangement – scale: 800°C -1600°C

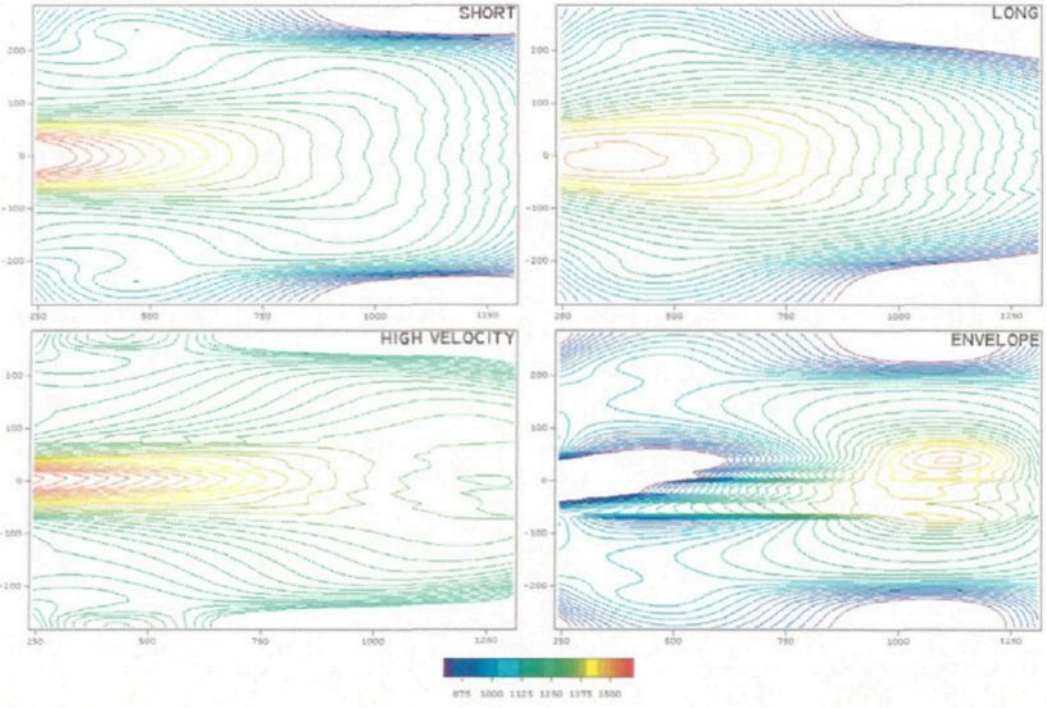

Figure 3.6 Comparison of the temperature contours at impingement arrangement – scale: 800°C -1600°C

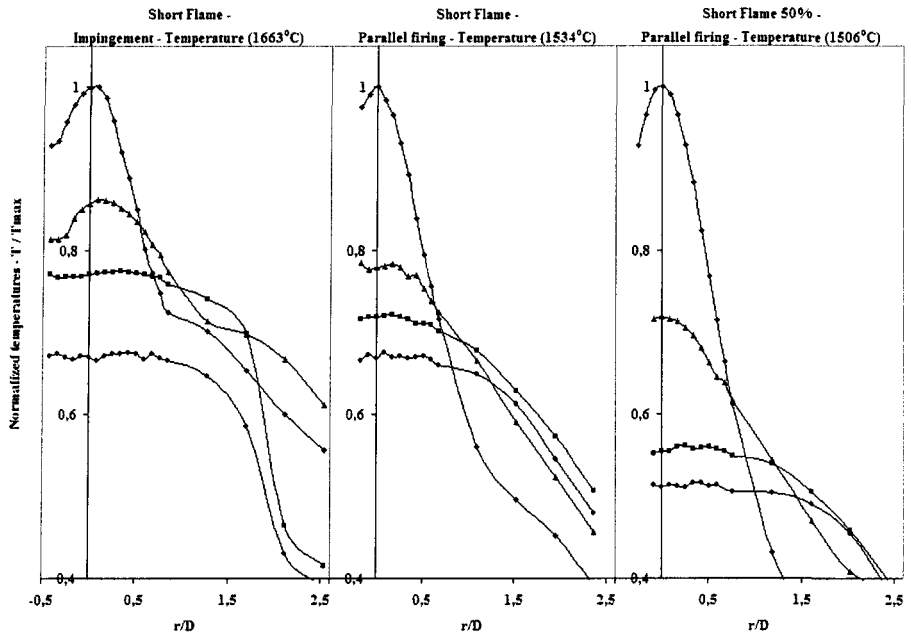

Figure 3.7 Normalized temperature profiles in the short flame

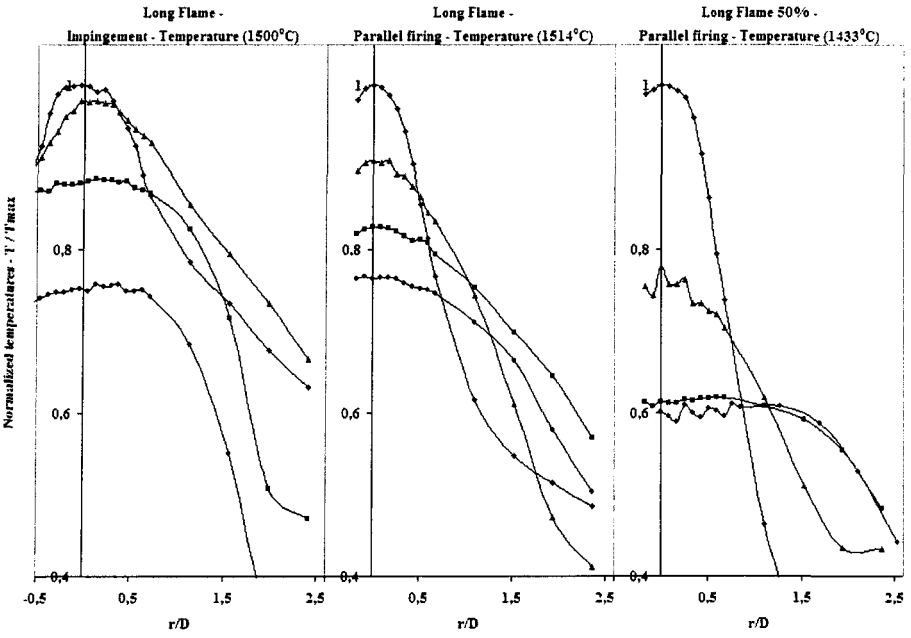

Figure 3.8. Normalized temperature profiles in the long flame

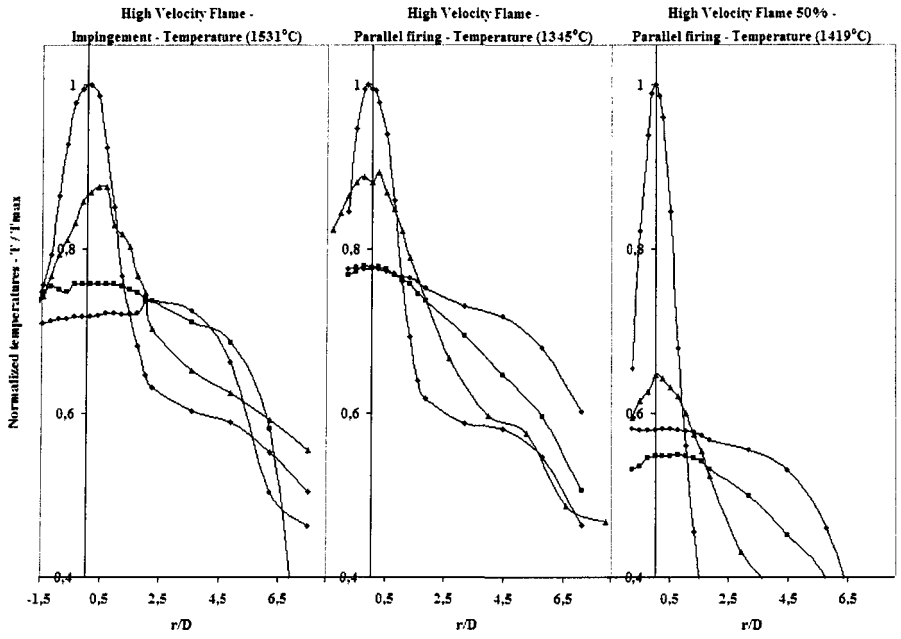

Figure 3.9. Normalized temperature profiles in the high velocity flame

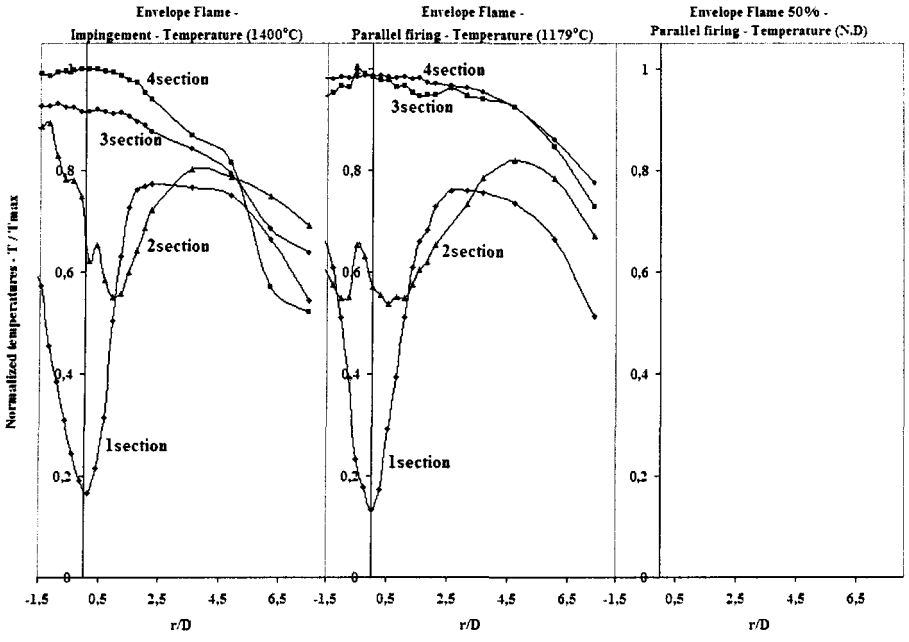

Figure 3.10. Normalized temperature profiles in the envelope flame

3.3 Velocity profiles

The measured velocity profiles are compared in Figure 3.11 for the short and the long flames and in Figure 3.12 for the long and the high velocity flames. The normalized velocity profiles are presented in Figure 3.13 to Figure 3.16 for the short, the long, the high velocity and the envelope flames respectively. These diagrams contain the profiles of impingement arrangement, parallel firing arrangement at full burner power as well as the profiles of parallel firing arrangement at 50% burner power. The real maximum values of the velocity are shown between brackets at the top of each diagram.

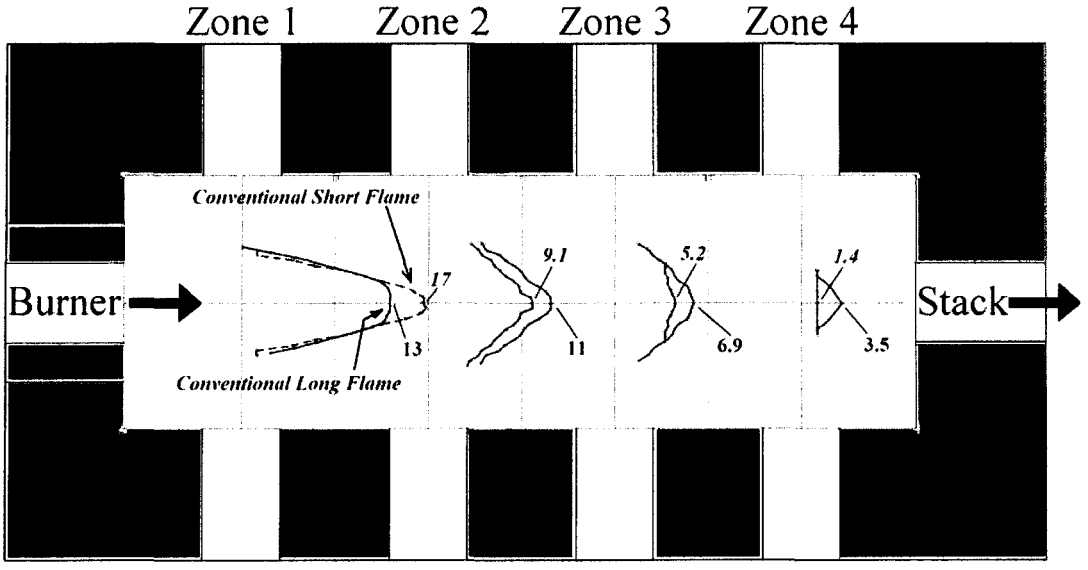

Figure 3.11 Comparison of the measured velocity profiles in the four test sections for the short and long flames

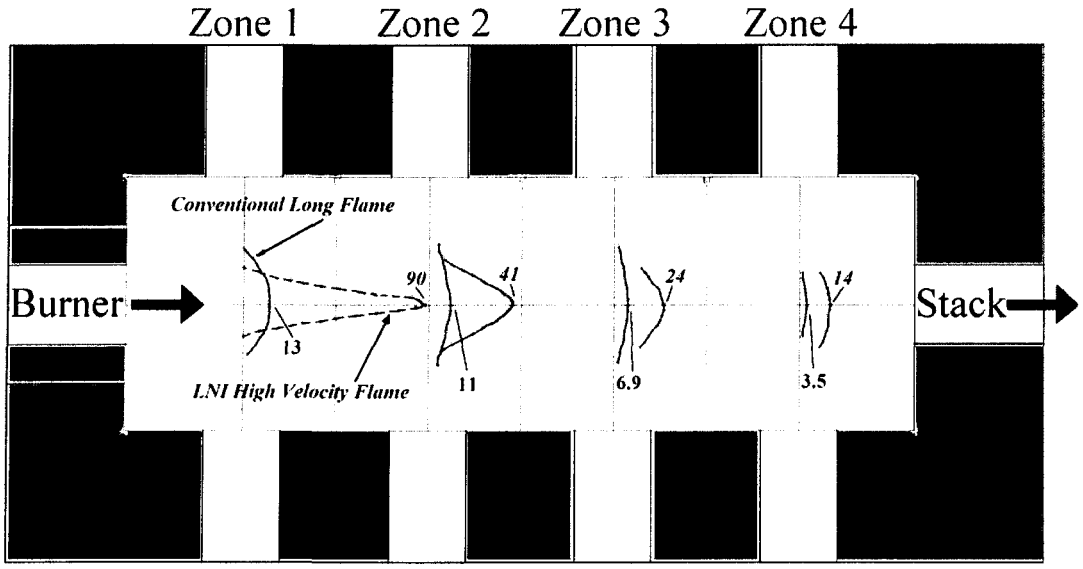

Figure 3.12 Comparaison of the measured velocity profiles in the four test sections for the long and high velocity flames

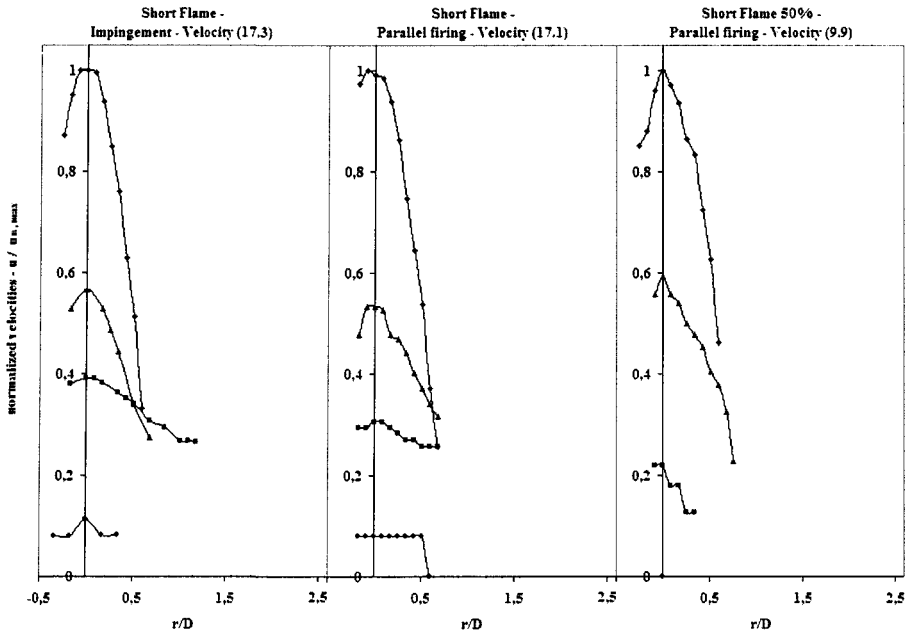

Figure 3.13. Normalized velocity profiles in the short flame

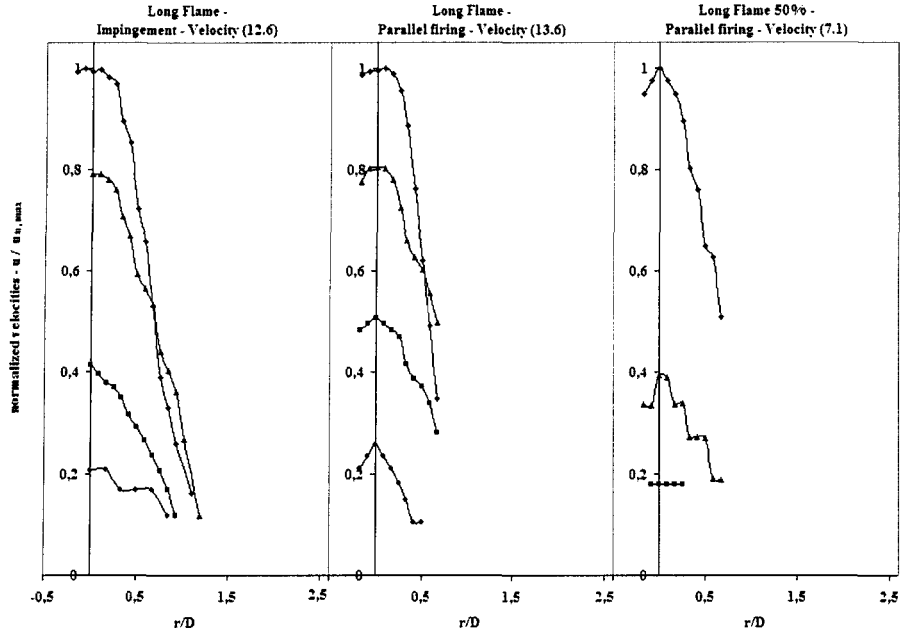

Figure 3.14. Normalized velocity profiles in the long flame

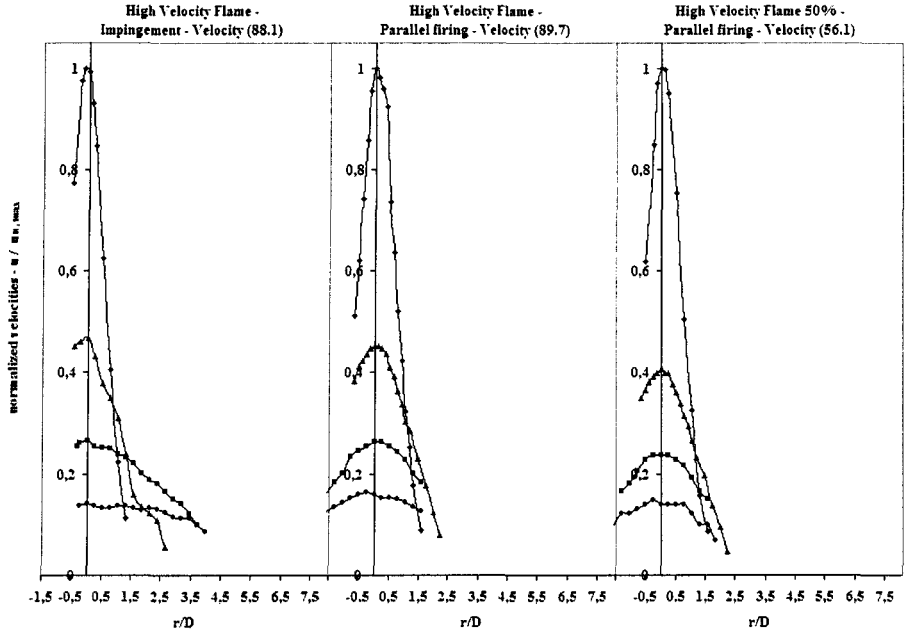

Figure 3.15. Normalized velocity profiles in the high velocity flame

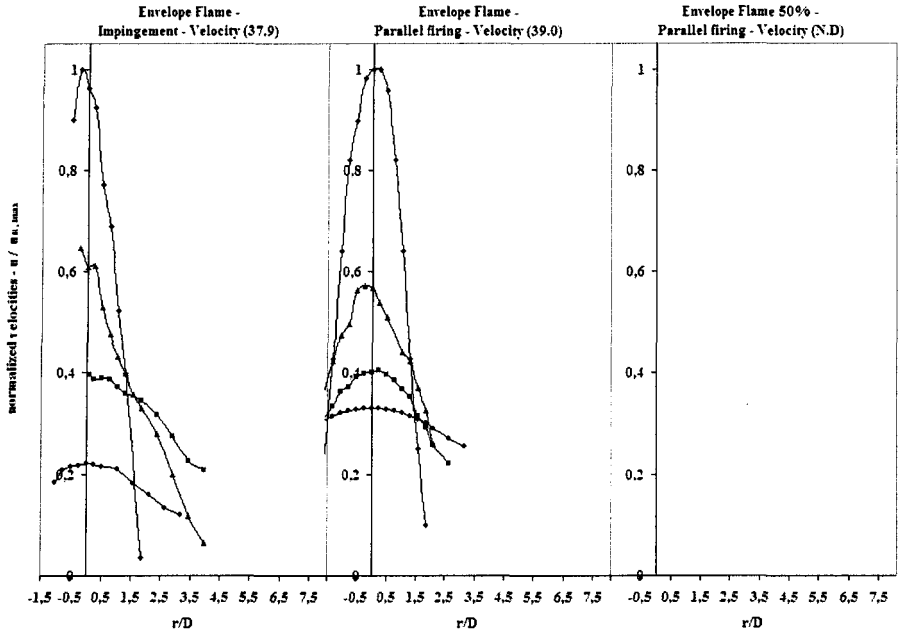

Figure 3.16. Normalized velocity profiles in the envelope flame

3.4 Gas composition

In our comparative research program, the NO_x concentration in the exhaust was measured in almost every experiment. We have a large amount of experimental data for different flame types (long, short, high velocity and envelope), burner powers (between 25% and 100%), and burner positions (parallel firing, inclined, impingement). However, the main objective of this research program is not the developpement of NO_x reduction techniques, but the comparison of the flame-object heat transfer between an already developed low NO_x burner and a traditional one. Thus, Annexe D is devoted to present briefly the general NO_x formation and destruction processes. Measurement results are presented next, while numerical calculations are discussed further below in this chapter.

The gas composition was detected using the Bacharach Gas Analyser close to the

furnace outlet at the beginning of the chimney. The measurement data for the different flame-object configurations and for the various flame types are presented in Table 3.1.

Burner type	Flame type	Configu-ration	NO_x [ppm]				CO [ppm]				Excess O_2
			Number of measuring points	MIN	AVE	MAX	Number of measuring points	MIN	AVE	MAX	range in [%]
TRADITIONAL	***Short***	horizontal	*12pts*	117	141	154	*4pts*	0	13	40	2.0 - 2.2
		inclined	*9pts*	107	134	143	*1p*	7	7	7	2.2
		impingement	*4pts*	117	131	151	*2pts*	0	2	4	2.0
	Long	horizontal	*6pts*	140	173	202	*3pts*	3	5	7	1.9 - 2.1
		inclined	*10pts*	155	172	187	*2pts*	17	52	87	2.0 - 2.2
		impingement	*7pts*	121	149	178	*6pts*	0	33.5	86	1.8 - 2.3
LNI	***High-velocity***	horizontal	*6pts*	20	45	64	*3pts*	13	25	44	2.0 - 3.3
		inclined	*7pts*	57	63	68	*0p*	N/D	N/D	N/D	-
		impingement	*3pts*	66	68	70	*3pts*	0	5	13	1.9 - 2.0
	Envelope	horizontal	*4pts*	5	8	11	*0p*	N/D	N/D	N/D	-
		inclined	*5pts*	2	4	5	*0p*	N/D	N/D	N/D	-
		impingement	*2pts*	16	16	17	*2pts*	27	27	28	2.0 - 2.2

Table 3.1 The measured NO_x and CO emissions for different flame types and configurations at 100% burner power - the excess air ratio was always kept about 2%.

3.5 Fluid dynamics of the high velocity and envelope flames

3.5.1. Nozzle exit parameters of the high velocity flame

The LNI burner used in the experimental measurements is a reduced scale reproduction of the commercially available industrial burner of the North American Mfg. Company (Figure 3.36). We were not able to make temperature measurements inside the burner and the details of the mixing procedure inside the burner are not known. However, the upper and lower bounds can be established. Using these limits and all the available data and information, the wanted parameters - which are related - can be determined.

To calculate the potential core length, Eq. 1.2 as given by Kataoka[8] will be applied. All the thermodynamic and transport properties of the gas mixture will be obtained using the

« Computational module for gas mixtures » based on the CHEMKIN database, as it was discussed in section 1.2.3.3 of CHAPTER 1.

The flame in the high velocity mode is well mixed and is ignited before the nozzle outlet. Both the burnt and unburnt gas compositions are known as well as the incoming mass flow rates. However, the ratio of burnt and unburnt species, or more precisely, how far the combustion process advanced, is not known. Some calculations have been executed and represented graphically to check the differences of the transport properties between the burnt and the unburnt gas-mixtures. These diagrams are shown in Appendix B. Compared to other errors rising from assumptions and simplifications, these differences are negligible.

In the impossible case when the reacting gas mixture exited at the adiabatic flame temperature (2150 K), the flow would be turbulent (Re=17400). In all other cases, i.e. when the mixture is at a lower temperature, the Reynolds number is even higher (see Table 3.2). In the case of turbulent entry, the velocity profile can be well approximated with the empirical power law [12]:

$$\frac{\overline{u_n}}{u_{n,\max}} = \frac{2n^2}{(n+1)(2n+1)}$$

Eq. 3.1

where n is the exponent of the power function, shown in Figure 3.17, which depends logarithmically on the centerline Reynolds number; $u_{n,\max}$ is the centerline velocity while $\overline{u_n}$ is the average velocity at the nozzle exit plane. The average velocity at the nozzle exit can be calculated as:

$$\overline{u_n} = \frac{Q_{vol}}{A_n} = \frac{\dot{m}}{\rho_n \cdot A_n}$$

Eq. 3.2

where A_n is the nozzle area, Q_{vol} is the volumetric flow rate and $\dot{m}$ is the mass flow rate at the nozzle outlet. The gas mixture can be considered as a perfect gas without significant errors, so the density of the mixture at the nozzle outlet is:

$$\rho_n = \frac{pM}{\Re T}$$

Eq. 3.3

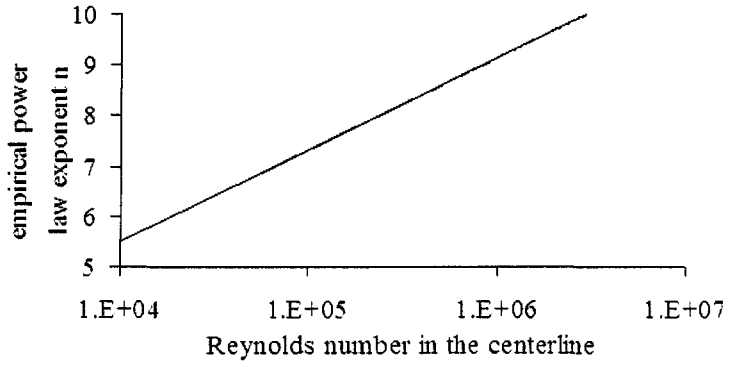

Figure 3.17 The empirical power law exponent as function of the centerline Reynolds number[12]

In all experimental cases, the flames were enclosed in a furnace; consequently, the entering jet was sourrounded by hot gases. Measurements showed that the temperature of the surrounding fluid varied strongly along the length of the furnace, and as a function of the flame-charge arrangement. In the case of the horizontal arrangement, the temperature of the surrounding gases varied between 800 and 1000°C having a continuous increase from the first measurement section to the last. In the calculations, we used an extrapolated temperature value of 760°C. In impingement case, similarly to the horizontal arrangement, the longitudinal temperature variation of the surrounding gases has the same characteristic.

Only the temperature range is different, which varies between 900 and 1100°C.

A computational module has been developed that asks for the following inlet parameters:

- nozzle diameter
- nozzle exit temperature of the jet
- mixture composition of the jet
- mass flow rate
- temperature of the surrounding gases
- composition of the surrounding gases

High Velocity Flame						
T_{inlet} [K]	2150	1730	1273	**981**	960	500
T_{inf} [K]	1033.15					
v_{inlet} [m/s]	200	160	117	**90**	88	45
d_{nozzle} [m]	0.038					
X_V [-]	4.517	4.857	5.381	**5.871**	5.914	7.362
l_V [m]	0.172	0.185	0.204	**0.223**	0.225	0.280
Re_{outlet} [-]	17400	20000	24000	**28452**	29000	44300
	MAX				MIN	

Table 3.2 Velocity inlet and potential core length as function of the inlet temperature for the high velocity flame – results from the « Computational module for the nozzle exit parameters »

Using Eq. 1.2, Eq. 3.1, Eq. 3.2 and Eq. 3.3 as well as the « Computational module for gas mixtures » based on the CHEMKIN database the following parameters can be calculated:

- average velocity at the nozzle exit
- centerline (maximum) velocity at the nozzle exit
- potential core length
- nozzle outlet Reynolds number
- density ratio between the primary and secondary streams

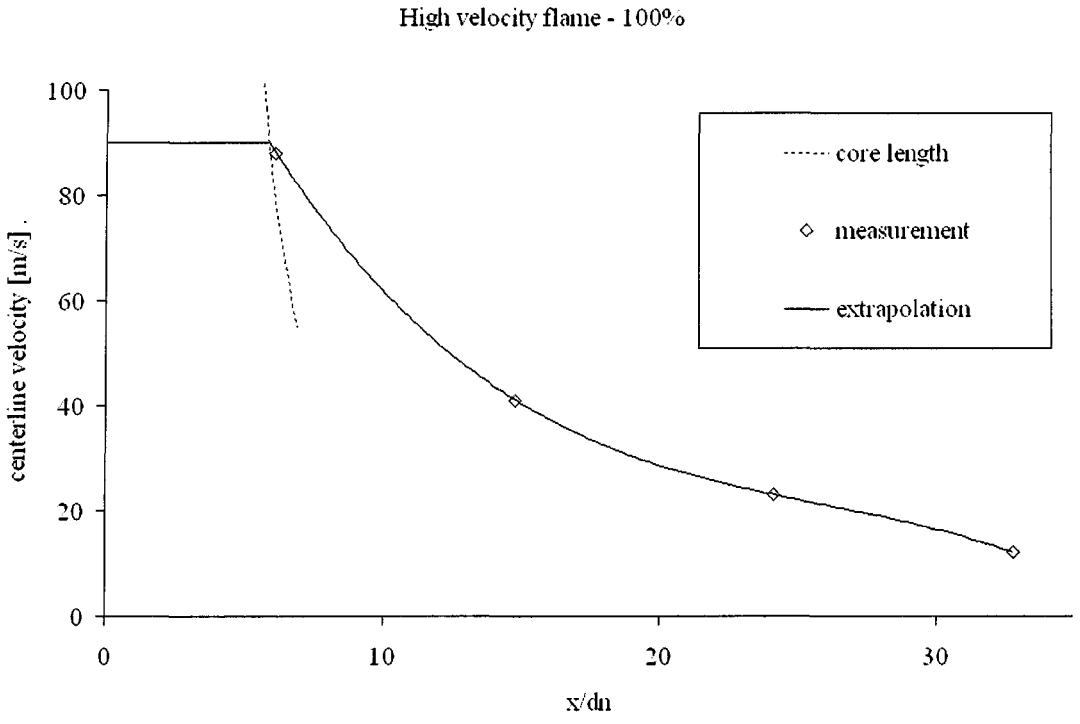

Figure 3.18 The core length correlation curve and the experimental velocity curve (both for impingement and parallel firing arrangements)

The only requiered parameter, which is not known, is the nozzle exit temperature of the jet. However, the velocity profile in the first test section of the experimental furnace is known, so with backward extrapolation the possible value of the inlet velocity can be found. Inlet velocities, core lengths and nozzle outlet Reynolds numbers are presented in

Table 3.2 as function of some arbitrary chosen inlet temperatures. The indications MIN and MAX in the last row mean the physical limits of the solution range. MIN is determined from the measured velocity in the first test section (88 m/s), hence no acceleration is possible downstream the nozzle. MAX is determined from the adiabatic flame temperature, consequently higher temperature than the adiabatic is not possible.

Two curves are presented in Figure 3.18. The dotted line shows the distances of the "critical point" from the burner mouth (length of the potential core) as function of the nozzle exit velocities (in the centerline) which are the outlet parameters of the computational module related to the arbitrary chosen nozzle exit temperatures (results of Table 3.2). The second line is the experimentally measured axial velocity in the centerline for the high velocity flame. The difference between the data of impingement and parallel firing configurations is not significant, so only one curve is presented. Analyzing Figure 3.18, it seems that the first test section is downstream from the critical point. However, looking to Figure 3.19 where the velocity profile in the first measurement section for the impingement arrangement is enlarged, one can see the little flattening of the velocity in the centerline, which means that the potential core overpass the first test section. The heavy dotted line should be the velocity profile in the absence of the potential core. On the other hand, in the horizontal case, which is not presented here, there is no flattening on the curve at the centerline. As it was mentioned, the difference between the measurement data of the two different configurations is not significant (less than 2 m/s in the first test section). However, this difference is enough to slightly displace the critical point. Anyway, it is obvious that the critical point is very close to the first measurement section and if the

accuracy of the above presented computation and all the preceding measurements is taken into account, this uncertenity is understandable.

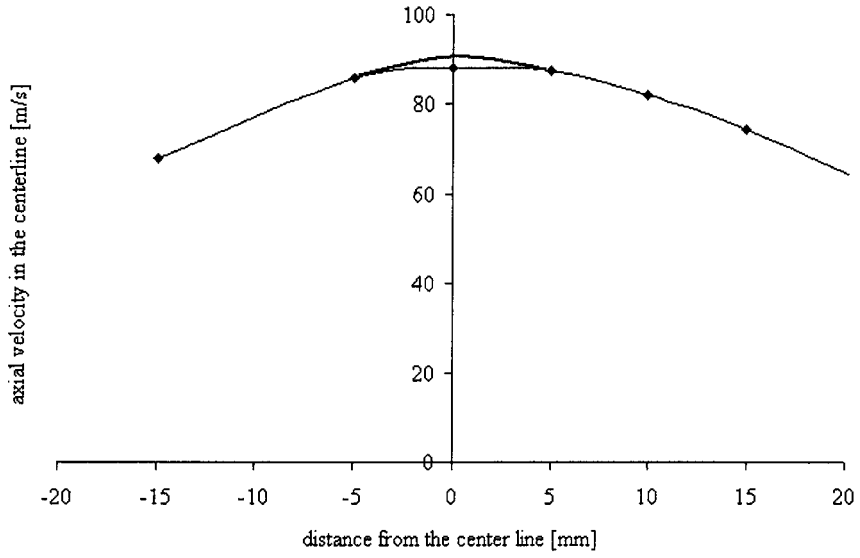

Figure 3.19 Flattening of the velocity profile in the centerline

Summarizing the above results, the inlet velocity of the high velocity flame is 90 m/s, the flame temperature at the nozzle outlet is 981 K, the outlet Reynolds number is about 28500, and the length of the potential core is 0.223 m, that corresponds to a dimensionless core-length of $X_v = 5.872$. The potential core needs the length of 0.0095 [m] to reach the first test section. These results will be used in all later calculations. The computational module, which calculates these parameters, will be referred later as « Computational module for the nozzle exit parameters ».

For the horizontal arrangement, we made also experimental measurements at 50% burner power. The nozzle parameters were determined using the same technique, which was presented just before in the full power case. According to the results of the

computational module, the flame temperature for 50% burner power at the nozzle outflow is significantly higher than for full burner power (1301 K instead of 981 K). The dimensionless potential core length becomes also shorter; (4.65 in place of 5.9) so the first test section is significantly downstream to the critical point. The centerline velocity at the nozzle plane is 65 [m/s] and the Reynolds number at the nozzle outlet is about 13000.

3.5.2. Longitudinal temperature distribution in the high velocity flame

As it was repeatedly mentioned, the measurement possibilities were restricted to the four viewing ports of the experimental furnace. Radial temperature distributions captured in these viewing ports were presented in CHAPTER 3. In the normalized diagram in Figure 3.20, the measured centerline temperatures are represented with diamonds for parallel firing arrangement at 100% burner power. The heavy line is the simplest extrapolation between the measurement points, but the doubts are raised whether the thin line do not characterize better the real longitudinal temperature distribution. Anyway, after an abundant data collection in all the available test sections neither the location of the maximum temperature nor its value were exactly known.

To find the axial location of the temperature maximum, further measurements were made in the first viewing port. For easier comprehension, the positions of the viewing ports are marked with rectangles in Figure 3.20. Unfortunately, as it was already mentioned above, the water-cooled suction pyrometer has just two degrees of freedom (z and y). Because of its robust joint, only the up and down tilting of the probe (movement in direction z) is permitted but the movement in the x direction is not. However, the Pitot

probe can be positioned everywhere inside the viewing port, but the temperature values indicated by the unshielded thermocouple located on the top of the Pitot probe have significant deviation from the real temperatures. Nevertheless, experimental tests had shown that in despite of this deviation the measured values follow correctly the character of the temperature distribution. Therefore, the measured values were normalized and applied on the results obtained by the suction pyrometer.

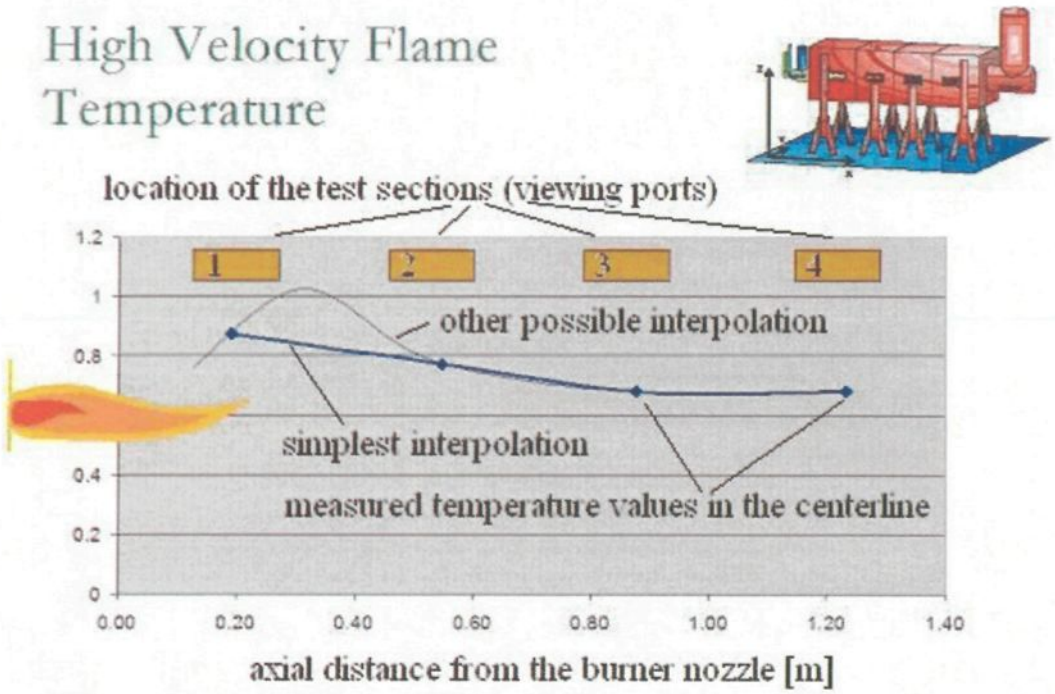

Figure 3.20 Two hypothetic interpolated temperature distribution through the measured points – high velocity flame 100% - parallel firing arrangement – normalized temperature diagram - maximum temperature: 1535°C

It can be seen in Figure 3.21, where the temperature distribution is presented in the centerline of the high-velocity flame at 100% burner power by parallel firing arrangement, that approaching the burner proceeding from the reference point of the normalization, the temperature decreases. Receding from the reference, the temperature is still rising until

attaining a peak, which is located approximately 5 centimetres downstream. Further downstream, the temperature begins to decrease slightly. In this case, it was fortunate that the maximum temperature was located in the range accessible from the viewing port.

Now, using all the corrected information, the longitudinal temperature distribution can be drawn. This is presented in Figure 3.22 for the parallel firing as well as for the impingement arrangements. The temperature value at $x/d_n = 0$ is the computed value concluded in the above section (3.5.1).

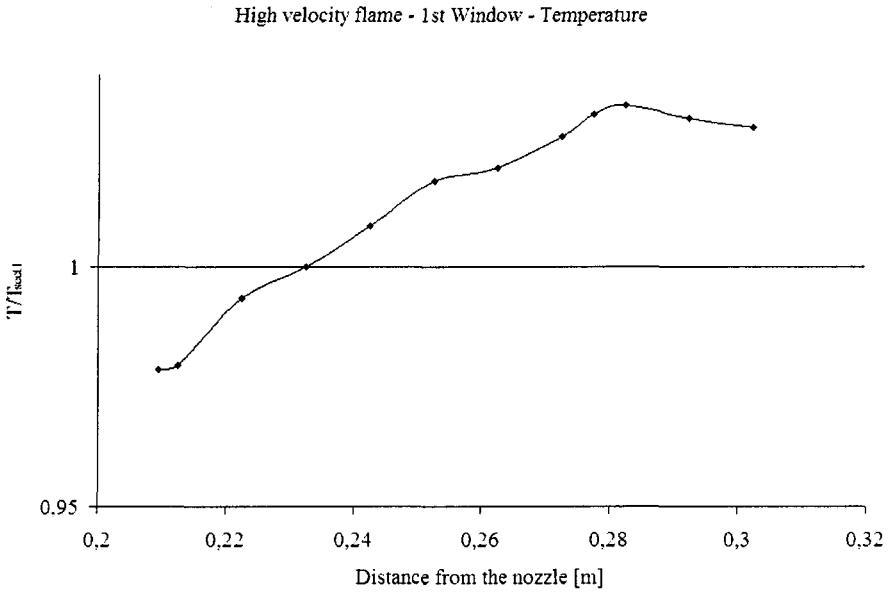

Figure 3.21 Centerline temperature distribution in the first viewing port for the high velocity flame at 100% burner power by parallel firing arrangement – measured with the unshielded thermocouple on the Pitot tube

It was presented in the above section using the results of the « Computational module for the nozzle exit parameters » that the jet temperature at the nozzle outlet is more than 300 degrees higher in the case of 50% burner power as in full burner case. This result is also confirmed by experiments where the maximal temperature in the centerline of the first

test section was measured by increasing burner power. The result is shown in Figure 3.23, where the burner power varies from 48 to 100 percent and the captured temperature is between 1360 and 1460°C. As it was expected, the flame temperature decreases with the increasing burner power. One of the reasons is that the peak of the flame front (the hottest point in a flame) shifts rearwards in the furnace by increasing power, but the most important cause is the higher incoming jet temperature. The latter is absolutely the determining factor, which affects also the NO_x formation (discussed below in section 3.8 of this chapter). When the fuel is decreased by half (50% power), combustion takes place close to the first furnace section. Consequently, temperature attained in this section is higher than that obtained with full power. The longitudinal temperature distribution for 50% burner power is shown in Figure 3.24.

Experiments at 50% burner power for the impingement arrangement were not performed, so the comparison between parallel firing and impingement mode at reduced furnace power could not be made. However, due to the relatively rear position of the vertical object, important deviation from the horizontal case is absolutely not expected.

While the velocity distribution of turbulent jets is widely discussed in the literature the temperature distribution is rarely analyzed. In section 1.1.6, Eq. 1.13 was given based on the experimental and theoretical work of Reichardt[16]. This equation gives the radial temperature distribution related to the radial velocity distribution. Consequently, in order to discuss the radial temperature distribution, the radial velocity distribution has to be analysed first. Before this, the longitudinal velocity distribution will be discussed.

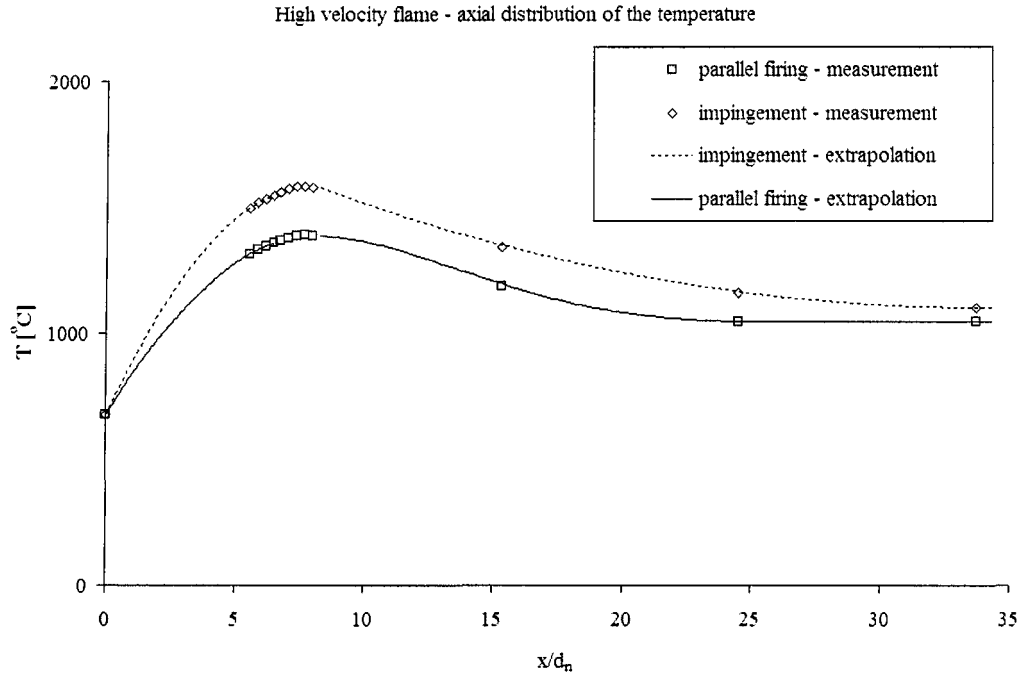

Figure 3.22. Longitudinal temperature distribution in the high velocity flame at 100% burner power

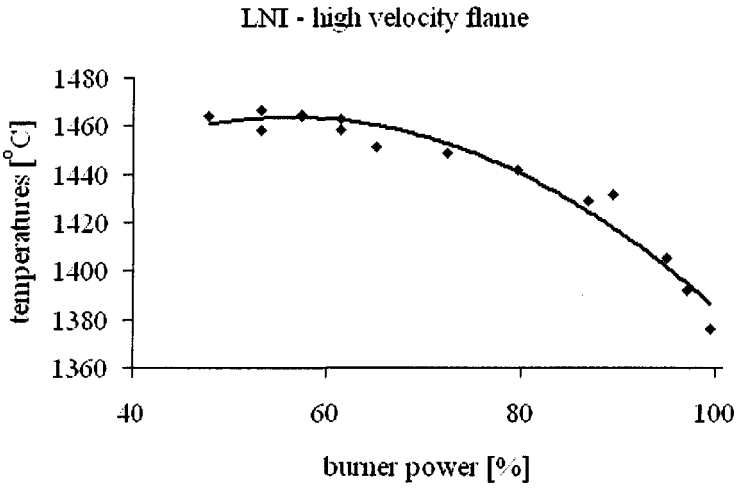

Figure 3.23. Detected temperature in the first test section (suction pyrometer) as function of the burner power – high velocity flame

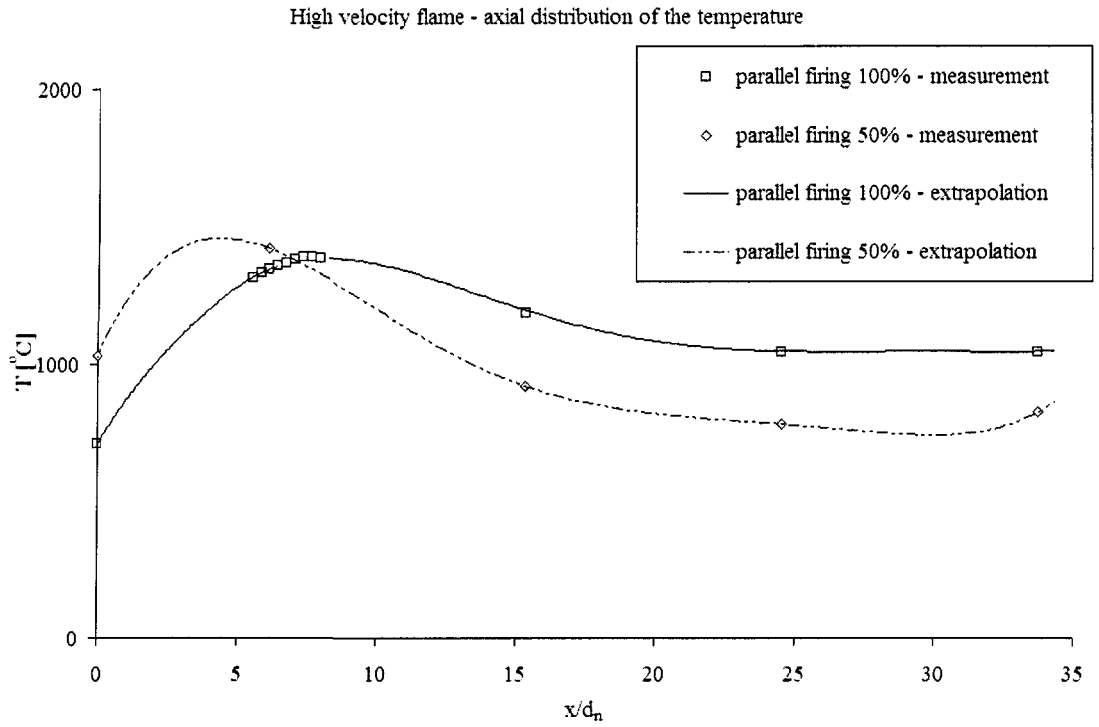

Figure 3.24. Longitudinal temperature distribution in the high velocity flame at 50% and 100% burner power by parallel firing arrangement

3.5.3. Longitudinal velocity distribution in the high velocity jet flame

As it was discussed in the first section of CHAPTER 1, the fully developed regions of free turbulent jets are similar. Therefore, the axial and radial velocity distributions can be described by relatively simple and general relationships. For constant density case, Hinze and van der Hegge Zijnen[9] has given Eq. 1.7 which was extended for non-constant density systems by Beér and Chigier[4] (Eq. 1.3) using the concept of equivalent nozzle diameter after Thring and Newby[10]. It is also more favourable to represent inversely the hyperbolical function of the longitudinal velocity decay. Thus, we have to deal with simple linear equations. The longitudinal velocity decay of the high velocity flame is represented in this

inverse way in Figure 3.25.

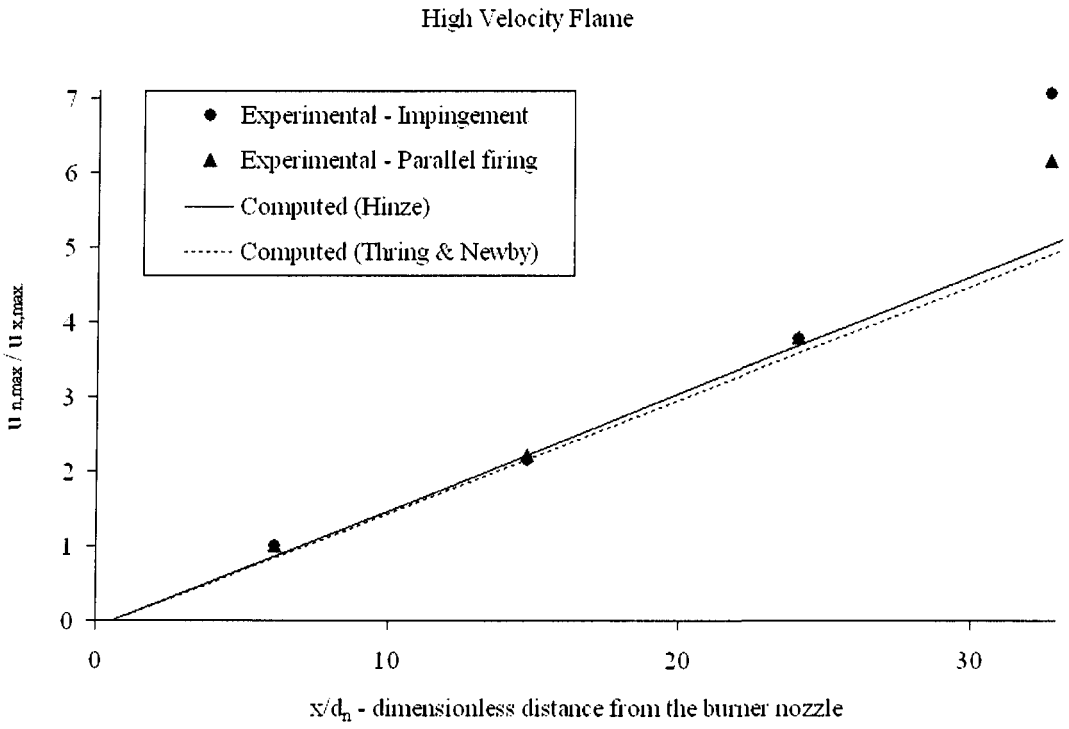

Figure 3.25. High velocity flame - reciprocal of the longitudinal velocity decay as a function of distance from the nozzle

The four triangles and the four stars are the experimental values measured in the test sections for parallel firing and impingement arrangements respectively. The solid line is computed using Eq. 1.7 given by Hinze and van der Hegge Zijnen[3] for constant density systems. The dotted line is the computed inverse velocity decay for non-constant density systems using Eq. 1.3 after Beér and Chigier[4].

The two computed lines are very close to each other, because the equivalent nozzle diameter, $d_{n,eqv}$ =0.040 m, differs just very slightly from the real diameter, d_n=0.038 m. The equivalent nozzle diameter is calculated using Eq. 1.9. In this equation, due to the similar

molar masses of the two streams (jet and surroundings) as well as the applicability of the perfect gas approach, the density ratio depends uniquely on the temperature differences. In the case of the high velocity flame at full burner power, the difference between the temperature of the jet at the nozzle exit and the temperature of the surrounding gas in the combustion chamber immediately around the discharging jet is very small. This small temperature difference is aleatory and occurs only in this unique case. In all other cases (e.g. high velocity flame at 50% burner power, envelope flame) the differences between these temperatures are much accentuated, thus the equivalent nozzle diameters differ strongly from the real nozzle diameter.

Apart from the last furnace section, the calculated graph matches very well the experimental points. The measurement points of the rear furnace section are otherwise slightly beyond the validity range of the given equation. In addition, the back wall of the furnace is in the proximity of these points. Furthermore, in the case of the impingement configuration, the flow is also influenced by the developed wall boundary layer, which explains the larger declination of the measured velocity from the calculated trend line (Figure 3.25).

For the horizontal arrangement at 50% burner power, the surrounding gas is much colder than at full burner power (470°C instead of 780°C). However, as it was discussed above, the jet temperature at the nozzle exit is considerably higher at 50% burner power. Consequently, the equivalent nozzle diameter differs significantly from the real nozzle diameter (0.029 m instead of 0.038 m). Thus, combining the experimental and the computed data, the longitudinal variation of the centerline velocity can also be drawn. This

is presented in Figure 3.26 for both power levels (50% and 100%).

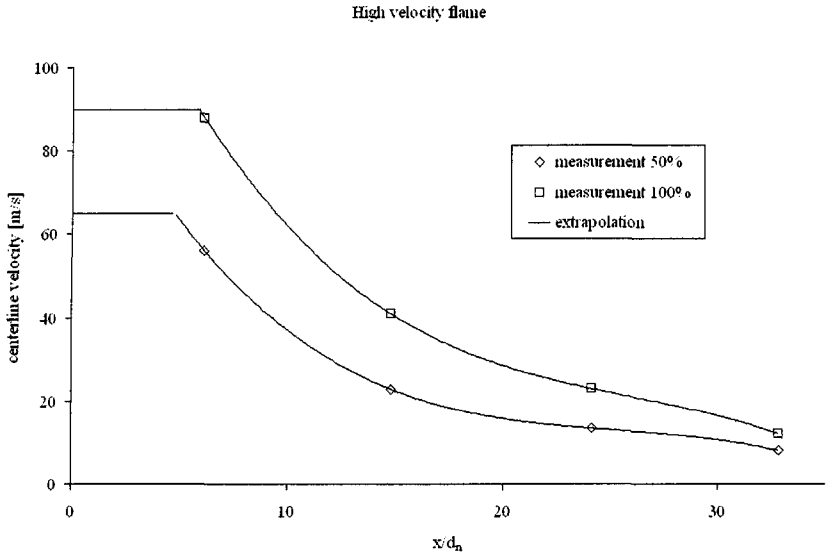

Figure 3.26. Longitudinal velocity distribution in the centerline of the high velocity flame at 50% and 100% burner powers.

Using the concept of the equivalent nozzle diameter (Eq. 1.9), the reciprocal of the longitudinal velocity decay in the centerline has been calculated and is represented in Figure 3.27. The measurement points fit very acceptably the computed curve except in the last measurement section where the gas flow is already influenced by the furnace back wall. It is distinctly visible in Figure 3.26 that the location of the critical point is upstream from the first test section at 50% burner power. However, the two curves are very similar and the velocity varies linearly over the entire furnace length.

The differences between the two curves in Figure 3.27 are due to the various equivalent nozzle diameters. However, as discussed above, these are calculated from the density differences that depend mostly on temperature. At partial burner power (50%), the discharging jet has a much higher temperature than at full power, while on the contrary the

surrounding gases are colder, even for steady state conditions. The jet temperature is burner dependent; however, for the same burner, fuel composition and for unchanged air equivalence ratio identical jet temperatures occur. On the other hand, the temperature of the surrounding gases depends on the operational conditions of the furnace. The partial burner power results in Figure 3.27 were taken shortly after the burner start (cold refractories). The differences should be smaller at steady state refractory conditions.

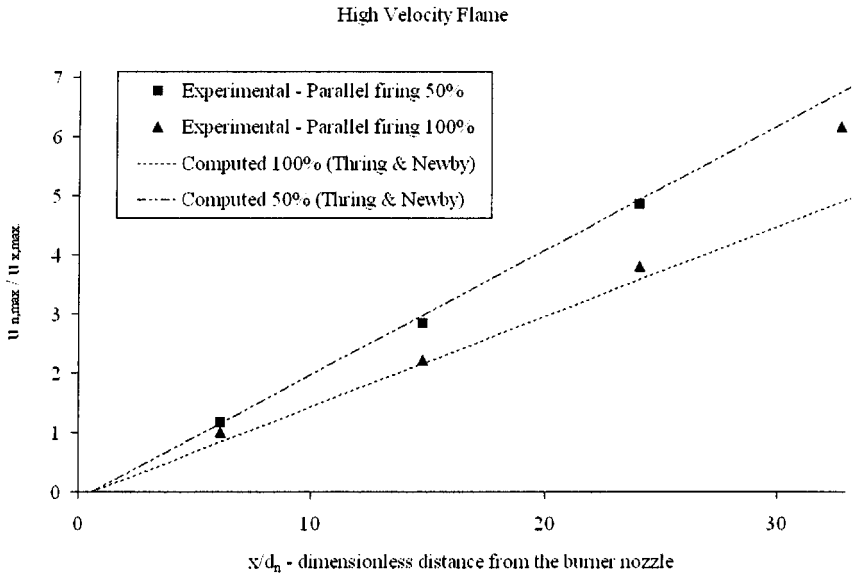

Figure 3.27. High velocity flame - reciprocal of the longitudinal velocity decay in the centerline as a function of distance from the nozzle – parallel firing at 50% and 100% burner powers

3.5.4. Radial velocity distribution in the high velocity jet flame

The radial velocity distribution in a fully established jet region is described by Eq. 1.4. As it was discussed above, the fully developed region of the high velocity flame begins at $X_v = 8$, so only the second, third and fourth viewing ports are located in the validity range. Consequently, only these results are presented (Figure 3.28 to Figure 3.30). In these

figures, the stars and the triangles are the experimental results of impingement and parallel firing configurations. In the second furnace section, the measurement points coincide for the impingement and parallel firing experiments. However, in the rear furnace sections, the jet tends to spread out more markedly over the elevated furnace hearth at impingement arrangement. The differences become less important between the centerline velocity and the lateral velocities. In addition, a very interesting radial fluctuation can be observed in the impingement curve of Figure 3.30. Albeit can be noticed that this fluctuation seems to be also initiated in the precedent furnace section (Figure 3.29). Moreover, the number and the position of the inflexion points coincide in the two diagrams. The reason of this fluctuation is not known.

The solid lines in Figure 3.28 to Figure 3.30 are the computed velocity distributions obtained using Eq. 1.4. These computed curves do not fit the experimental points. Therefore, we attempted to modify the constant in the equation of Hinze and van der Hegge Zijnen[3] in such a way that the new equation correlates the experimental data in all furnace sections of the validity range. The constant of 0.022 was found that acceptably match the data. We only found the experimental study of Popiel, van der Meer and Hoogendoorn[13] in later bibliographic research. They also measured the velocity spread for free hot jets within the distance of x/D = 5 to 17. The radial velocity distribution is not given by them, but they give the following equation, which characterizes the scattering of the points where the velocity is half of the centerline velocity.

$$r_{1/2} = 0.093(x + x_{virt})$$

Eq. 3.4

Transforming this equation in the same reciprocal form as before, one obtains:

$$\frac{\bar{u}_x}{\bar{u}_{x,\max}} = \frac{1}{\left[1 + r^2/0.02088x'^2\right]^2}$$

Eq. 3.5

Despite of the constant found by us (0.022), the constant of Popiel, van der Meer and Hoogendoorn[13] (0.02088) was used to calculate the radial velocity distribution. These curves are represented in Figure 3.28 to Figure 3.30 by the dotted lines. As it can be seen in the figures, these computed curves match well the experimental data.

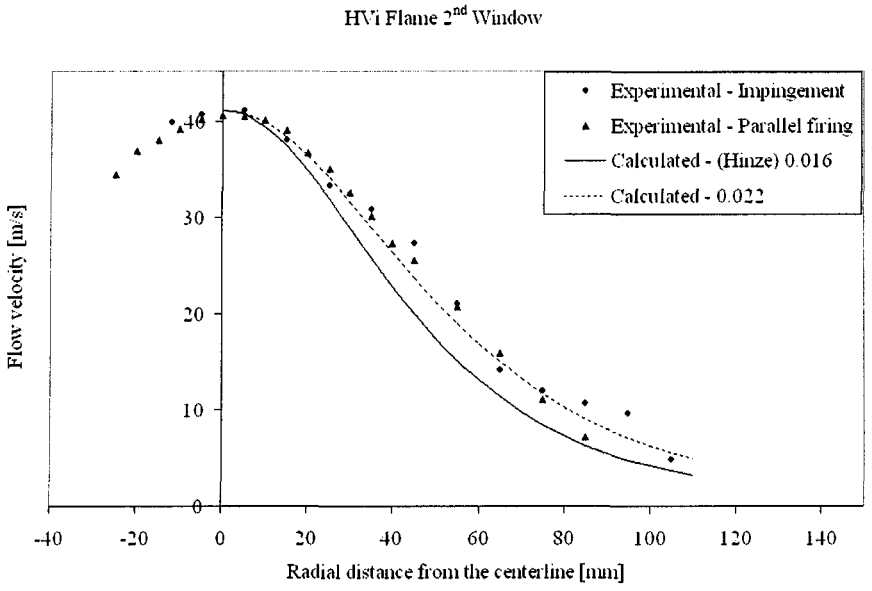

Figure 3.28 Radial velocity distribution of the high velocity flame in the second viewing port

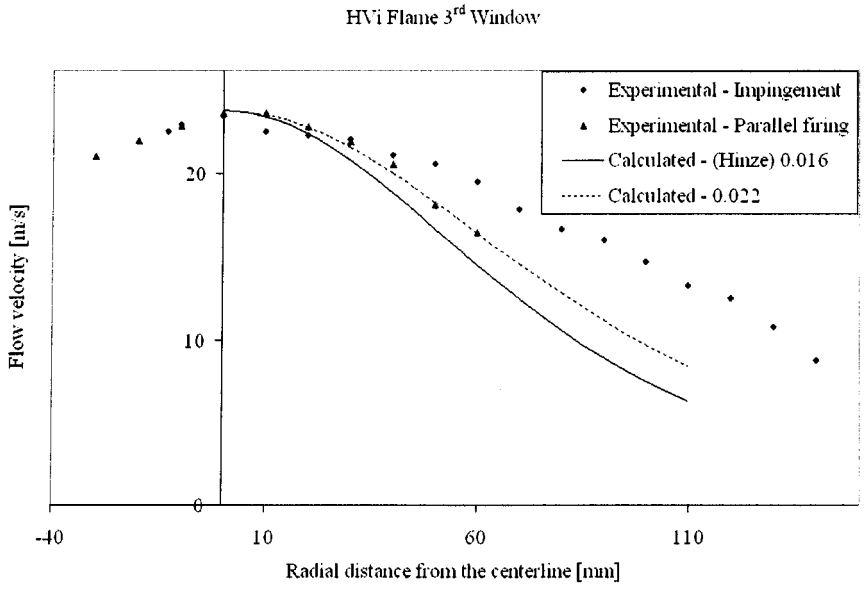

Figure 3.29 Radial velocity distribution of the high velocity flame in the third viewing port

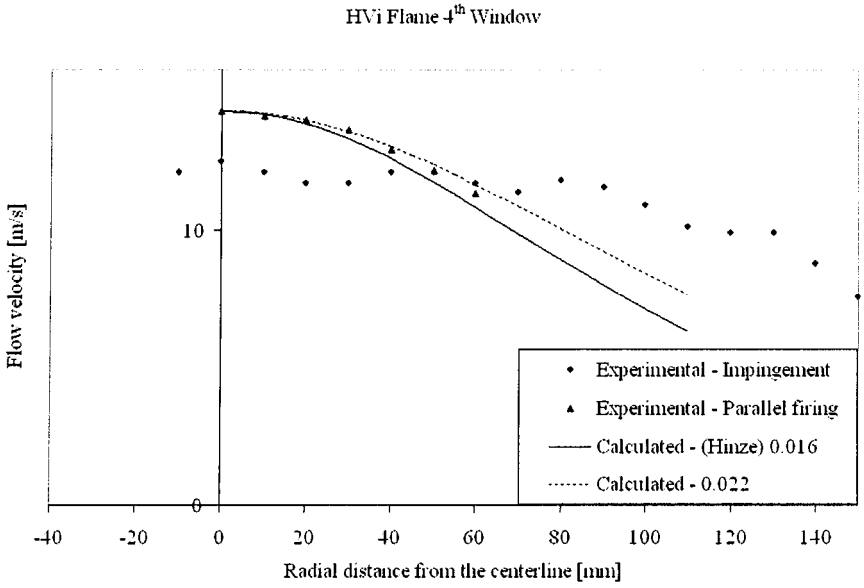

Figure 3.30 Radial velocity distribution of the high velocity flame in the fourth viewing port

Could be mentioned that in the experimental study of Popiel, van der Meer and

Hoogendoorn[13] a tunnel burner was used where combustion was 98 per cent completed at the exit of the burner. On the other hand, the chemical reaction is already completed even in our case in the rear furnace sections, thus not the chemical reaction is responsible for the fact of Eq. 1.4 not represented well the radial velocity distribution.

In the section 3.5.3, where the longitudinal velocity distribution was discussed, we analysed and compared the results made at 50% burner power by horizontal arrangement. It was mentioned that for 50% burner power, conversely to the full power mode, the first test section is located already in the fully developed region. However, in the first measurement section, the experimental data fit on none of the computed curves. This can be caused by the combustion process, which will become completed just further downstream, approximately in between the first and second test sections. Therefore, we tried to modify again the constant in equation Eq. 1.4 in such a manner that the new formula matches the measurement points in the active combustion zones. The best fitting curve to the velocity profile in the first measurement section at 50% burner power has the constant of 0.040 (see Figure 3.31). Thus, the modified equation will be the following:

$$\frac{u_x}{u_{x,\max}} = \frac{1}{\left[1 + r^2/0.040x'^2\right]^2}$$

Eq. 3.6

Retroactively the full power results were also checked. Applying Eq. 3.7, the computed curve correlates well the experimental results (Figure 3.32). Another interesting observation is that the radial velocity distribution of the envelope flame can also be better approximated with this modified equation. In the envelope flame, the combustion takes place in the opposite furnace locations as for the high velocity flame, namely at the second

third and forth furnace sections. Hence, in the case of the envelope flame, the effect of the chemical reaction influence the velocity scattering in all test sections except the first one. This effect can be corrected using the above presented constant. Further discussion will be given below in the section 3.5.9, where the concerning figures will also be presented.

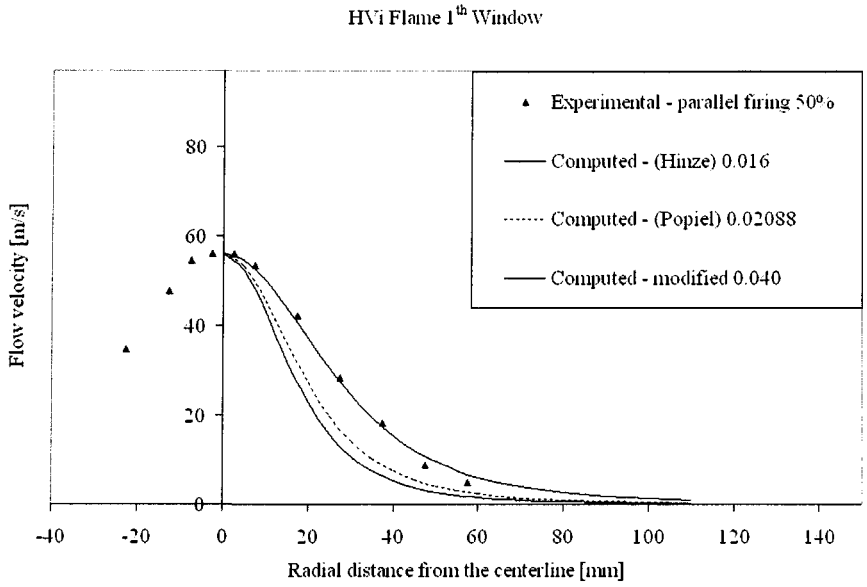

Figure 3.31 Radial velocity distribution of the high velocity flame at 50% burner power in the first viewing port

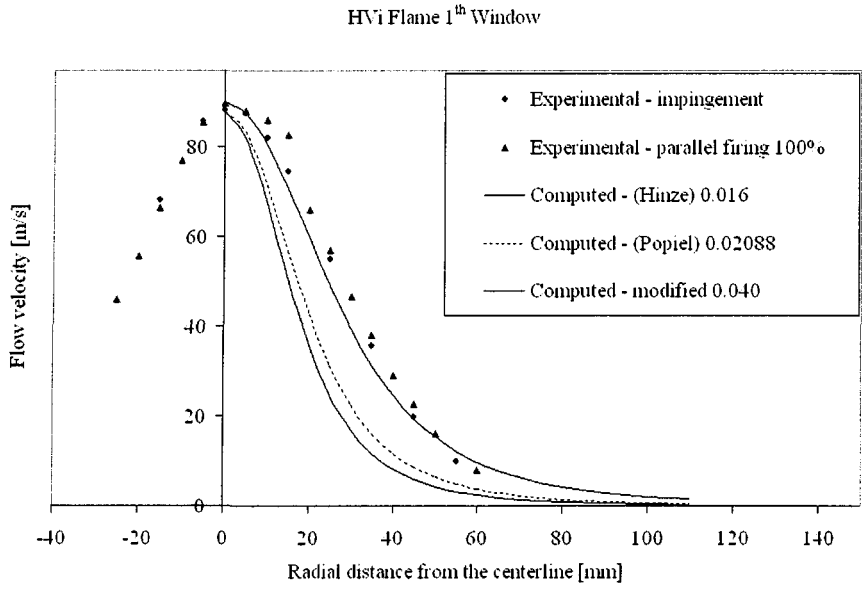

Figure 3.32 Radial velocity distribution of the high velocity flame at full burner power in the first viewing port

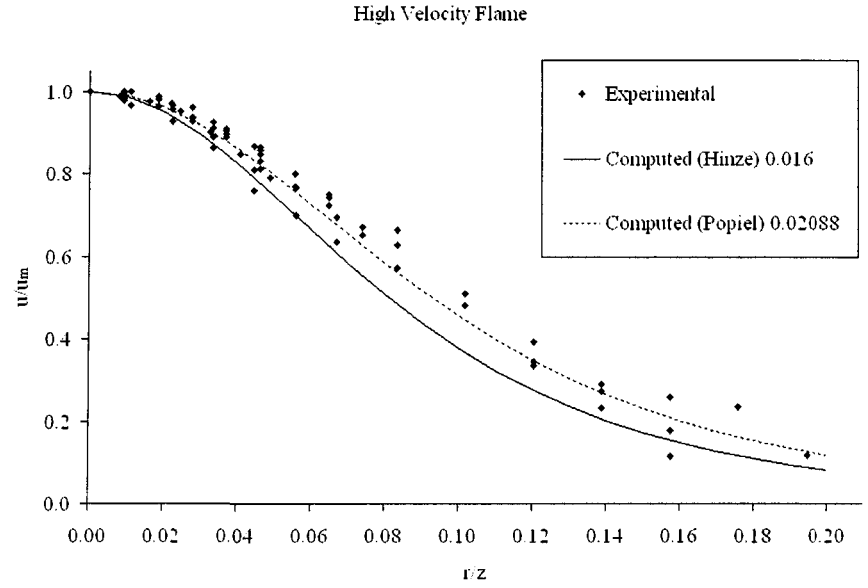

Figure 3.33 Generalized dimensionless radial velocity distribution in the high velocity jet

Results: Impingement 100%, Parallel firing 50%, Parallel firing 100%

Returning to the high velocity flame, the combustion process has influence only in the first measurement section. As it was presented above, in all other furnace sections, the experimental points fit well the computed curve given by Popiel, van der Meer and Hoogendoorn[13]. Finally, all the experimental points, which are located outside the combustion zone and are not affected by the elevated target, are shown in a single diagram in Figure 3.33 for both the impingement and parallel firing arrangements as well as for 50% and 100% burner powers. The relative velocity is shown as a function of the relative radial distance. It is eye-catching again that the modified curve (Popiel et al) correlates better the experimental points.

3.5.5. Radial temperature distribution in the high velocity flame

After completed the discussion about the velocity distribution, the radial temperature distribution can finally be analyzed. The radial temperature curve based on the velocity distribution is computed using Eq. 1.13 given by Reichardt[16] . As it can be seen in Figure 3.34, the computed curve calculated according to Eq. 1.13 does not match at all the measured temperature values. Finally, the doubt for the inapplicability of Eq. 1.13 in flows where chemical reaction occurs was justified.

The experimental temperature results presented in Figure 3.34 are very largely distributed. The small points on the diagram are the valid test results both for impingement and parallel firing arrangements as well as at 50% and 100% burner powers. Under valid results, those points are meant which are neither affected by the wall boundaries due to the elevated furnace level (impingement arrangement) nor the potential core at the early, flow

developpement zone.

If the measurement points in Figure 3.34 are filtered in the way that only the points located at the rear furnace section where the combustion is fully completed are considered, on the remaining points a modified equation can be fitted (see Figure 3.35). The new relation between the temperature and the velocity distribution can be described with the following equation:

$$\frac{T}{T_{max}} = \left(\frac{u}{u_{max}}\right)^{0.1} \qquad \text{Eq. 3.7}$$

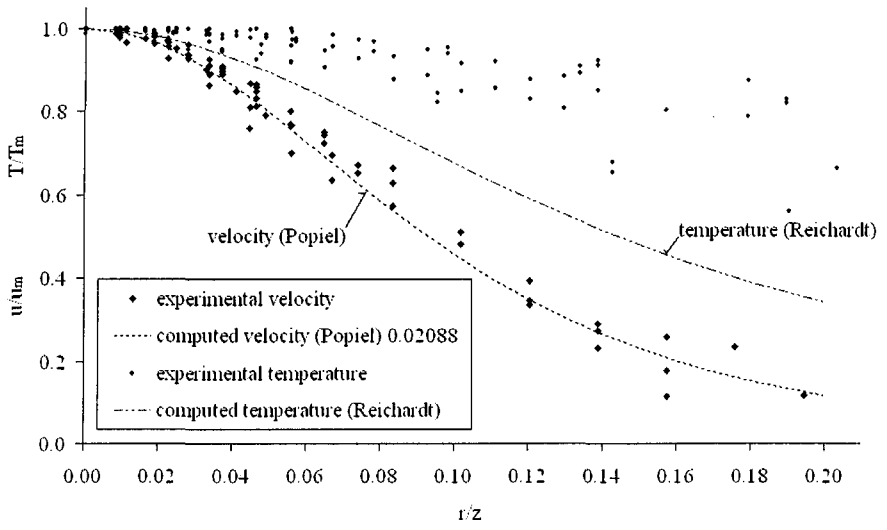

Figure 3.34 Relationship between the radial temperature and velocity distributions in the high velocity flame

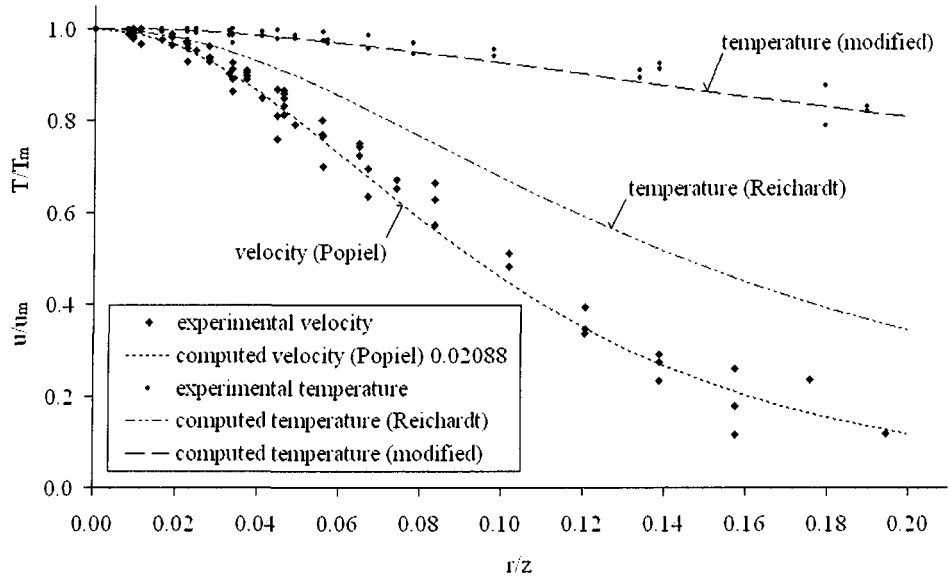

Figure 3.35 Relationship between the radial temperature and velocity distributions in the high velocity flame

3.5.6. Nozzle exit parameters of the envelope flame

The envelope flame is the second flame produced by the LNI burner. Similar to the high velocity flame, we were not able to make measurements closer to the burner than the first viewing port. In addition, the details of the mixing procedure inside the burner are not known. Thus, we have to deal with all the available information and make assumptions to find the unknown nozzle parameters. The same methodology has been used to calculate the potential core length, the nozzle outlet velocity as well as the nozzle outlet temperature, which was presented above in the case of the high velocity flame.

The burner port and its dimensions are shown in Figure 3.36. In the envelope operational mode, the natural gas is injected at the small lower nozzle separately from the combustion air, which is injected at the main nozzle in the center. In fact, a very small portion of the natural gas is mixed in the main air stream, but it will be consequently

neglected in the following calculations.

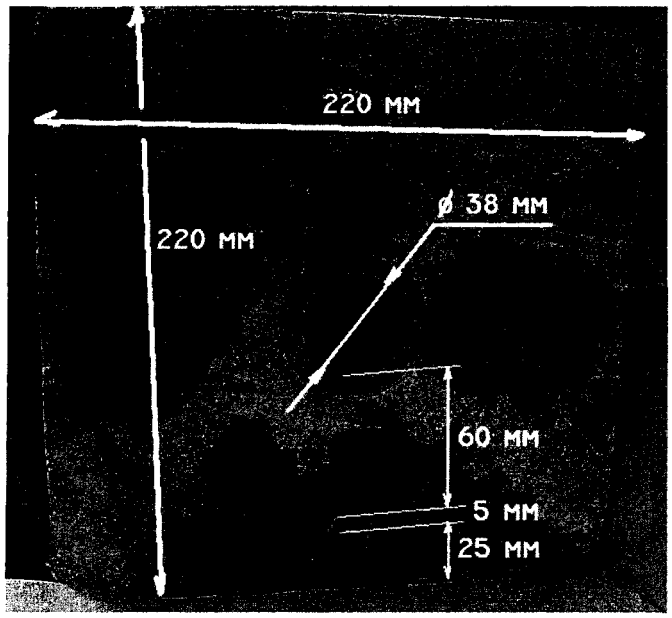

Figure 3.36 The burner port dimensions of the LNI burner

Due to the incertitude of the inlet parameters, only approximate upper and lower bounds can be established for the inlet temperature (T_{inlet}) and for the potential core length (X_v, l_v) as a function of the velocity inlet (v_{inlet}), the temperature of the surrounding gas, the mass flow rate, the gas composition as well as the nozzle diameter. These parameters were calculated using the « Computational module for the nozzle exit parameters » basing on Eq. 3.1 to Eq. 3.3 and Eq. 1.2. Calculations predict that the dimensionless potential core has to be in the range of 7.67 to 8.11. These correspond to the distance of 0.291 to 0.308 meters. Recall that this is the distance from the burner exit to the critical point. Consequently, both the upper and lower limits exceed the first test section (0.2325 m). It is obvious that the potential core of the envelope flame is much longer than that of the high velocity flame. Thus, it exceeds the length of $7.0d_n$ given by Hinze and van der Hegge Zijnen[3].

The above-discussed parameters are presented for the two configurations (parallel firing and impingement arrangement) in Table 3.3. In both cases, the velocity values were choosen as a reference and the inlet temperatures were calculated. In the last row of the table, the temperatures captured in the first test section are given for comparison. In the case of the impingement arrangement, the tendencies are realistic. The cold air discharging from the nozzle warms slightly up while reaches the first test section. On the other hand, the temperature changes in the case of the parallel firing arrangement are inconsecutive. Computations predict that the "cold" inlet air slightly cools down before reaching the first measurement section. In the real case, this could not happen. The only possible explanation of this antagonism is an artifact related to the measurements. Contrary to other flame types, simultanous temperature and velocity measurements are not feasible because the opening of two viewing ports at the same time risks instabilizing the flame. A similar problem arose at the beginning of the experimental program when the calorimetric plates were not equipped with adequate Fiberfrax isolation (see CO explosion in section 2.3.3.1). Consequently, the colder refractory bricks and the opened viewing ports prevent locally the ignition of the reacting mixture. This effect is amplified when either the suction pyrometer or the Pitot probe are inserted into the gas stream. However, the impact of the water-cooled suction pyrometer is more significant than the effect of the non-cooled Pitot tube. In addition, the effect of the perturbation is also time dependent. The refractory bricks locally begin to cool down when an adjacent viewing port is opened. Cold air can be also entrained through this port. When a certain temperature limit is exceeded, the reacting mixture in this zone cannot be ignited anymore. In this case, the cooling down of this part of the furnace is accelerated.

As time progresses, the original structure of the flame restitutes when all those perturbations disappear.

		Envelope Flame	
v_{inlet}	m/s	39	37.9
$T_{surrounding\ gas}$	K	1143	1343
T_{inlet}	K	488	474
d_{nozzle}	m	0.038	0.038
X_v	-	7.667	8.114
l_v	m	0.291	0.308
Configuration :		Parallel firing	Impingement
$v_{1\text{-section}}$	m/s	39	37.9
$T_{1\text{-section}}$	K	430	505

Table 3.3 Envelope flame – nozzle inlet parameters

Owing to the above-mentioned phenomenon, we tried to minimize the effect of perturbation during the measurements by reducing the size of the viewing port as it is presented in Figure 3.37. However, the water-cooling of the suction pyrometer cannot be interrupted.

Due to the non-simultanous measurements, the dynamic pressure value of the Pitot tube as well as the temperature value of the suction pyrometer was captured under slightly different conditions. Recall that the velocity is mainly calculated using the dynamic pressure, but it is corrected by using the gas temperature (see Eq. 2.1). This effect contributes to the contradiction of the results in Table 3.3. However, as it was mentioned above, the results of the impingment configuration are realistic contrarily to those obtained for parallel firing arrangement. This fact is due to the differences in the refractory temperatures. These temperatures are compared in Figure 3.62 and Figure 3.63 in the

refractory ceiling and the sidewalls respectively for impingement and parallel firing configurations. Both the ceiling and the sidewall bricks have significantly higher temperatures in the case of the impingement arrangement. The difference is between 100-200°C in the first furnace sections.

If direct measurements of temperatures and velocities at the nozzle exit were possible and the details of the burner geometry were be known, the parameters in Table 3.3 might be determined more accurately.

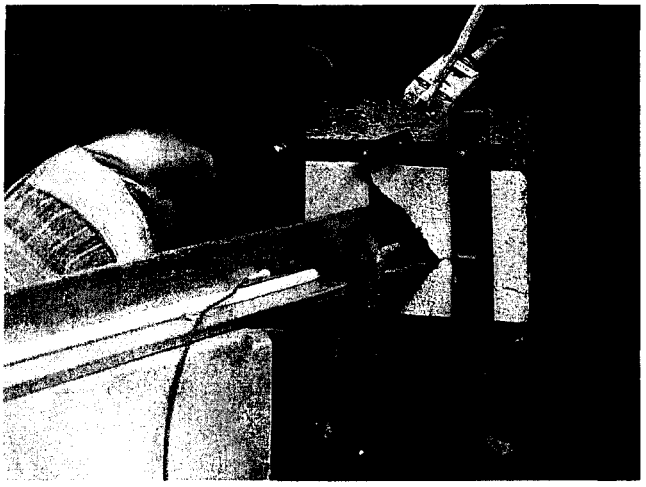

Figure 3.37. Pitot tube measurements in the envelope flame – heat loss reduction

3.5.7. Longitudinal temperature distribution in the envelope flame

The longitudinal temperature curves in the centerline of the envelope flame were determined using the measurements made in the four test sections of the furnace. Between the measurement points, the temperatures were interpolated. On the other hand, it was assumed that no change in the temperature occurs between the nozzle exit and the first measurement section. The approximate curves are shown in Figure 3.38 for the

impingement and parallel firing arrangements.

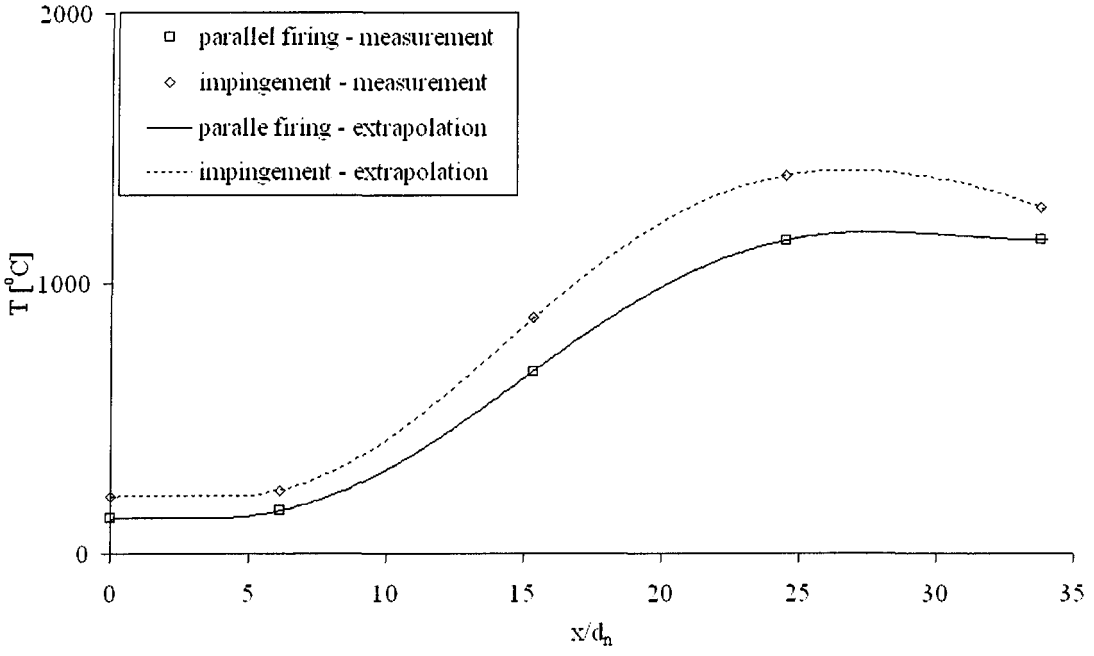

Figure 3.38. Longitudinal temperature distribution in the centerline of the furnace for the envelope flame

3.5.8. The longitudinal velocity distribution in the envelope flame

The inverse of the axial velocity decay as a function of the distance from the burner nozzle is presented in Figure 3.39. The stars and the triangles are both experimental results taken in impingement and parallel firing arrangements respectively. The solid line is the computed value using Eq. 1.7 given by Hinze and van der Hegge Zijnen[3] for constant density systems. In the case of the envelope flame, the constant density approach is inapplicable.

Hence, for a non-constant density system, the equivalent nozzle diameter has to be calculated using Eq. 1.9. Therefore, the temperature of the surrounding gas directly around the discharging jet needs to be extracted from the measurements. The input parameters and

the calculated equivalent nozzle diameters are shown in Table 3.4 for both parallel firing and impingement arrangements. It has to be mentioned that all the input parameters presented here are based on the experimental measurements.

Envelope flame			
		parallel firing	impingement
surroun-ding gas	molar mass [kg/kmol]	27.76	27.76
	temperature [C]	870	1070
	density [kg/m^3]	0.2959	0.2519
airjet	molar mass [kg/kmol]	28.85	28.85
	temperature [C]	157	232
	density [kg/m^3]	0.8174	0.6960
nozzle diameter [m]		0.0380	0.0380
calculated equivalent nozzle diameter [m]		0.0632	0.0632

Table 3.4. Equivalent nozzle diameter for the envelope flame

It is very interesting that in these two different cases, the equivalent nozzle diameters are identical. The effect of the higher inlet temperature of the impingement case in comparison to the parallel firing configuration is counterbalanced by higher surrounding temperatures. The two effects neutralize each other. Unfortunately, this phenomenon was not studied in detail.

The computed curve using Eq. 1.3 for non-constant density systems given by Beér and

Chigier[4] with the concept of equivalent nozzle diameter (Thring and Newby[10]) correlates well with the experimental data. This is represented by the dotted line in Figure 3.39. As it is shown in Figure 3.40, the virtual origin of the jet is located upstream the nozzle exit, in the negative range ($X_v = -2$).

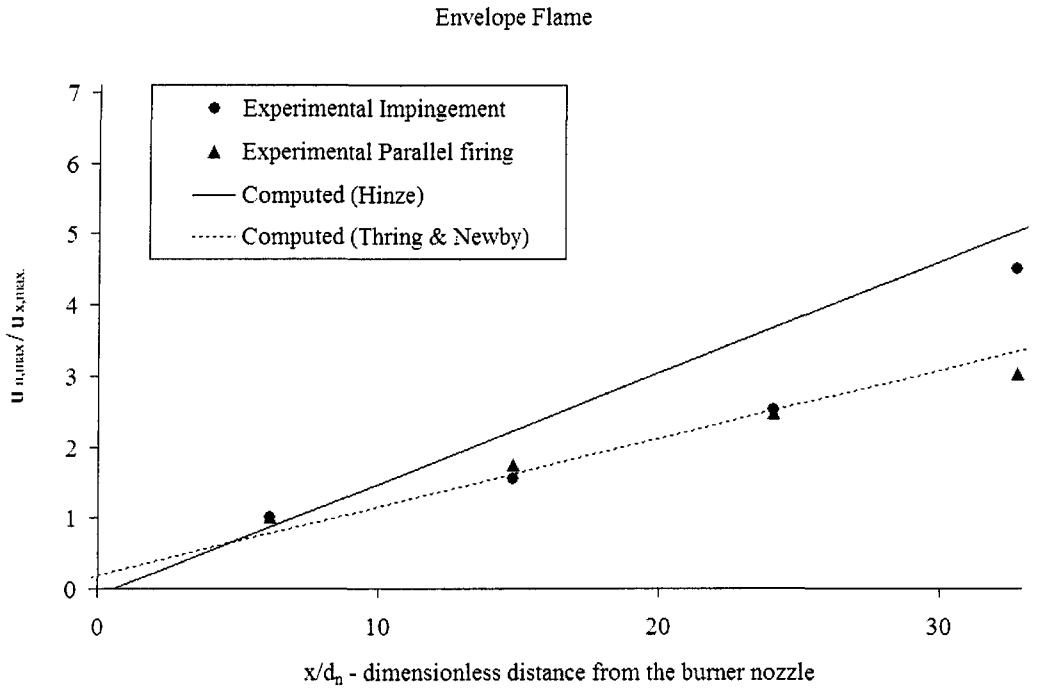

Figure 3.39 Envelope flame - reciprocal of the longitudinal variation of the centerline velocity as a function of distance from the nozzle

In the case of the impingement configuration, the measurement point at the rear furnace section is not matched by the computed curve. The reasons are similar as it was for the high velocity flame, that is, the elevated furnace hearth, the close backwall and the slightly exceeded validity range. On the other hand, the relative difference is smaller. It is only 35% instead of 47%. In addition, the measurement data is below the predicted value in the case of the parallel firing arrangement, which did not occur in any other case. This can

be attributed to the particularity of the envelope flame, in which the chemical reaction takes place mostly in the rear furnace section. This can be seen on the temperature contours presented in Figure 3.4. Thus, the volumetric expansion of the gas mixture relative to the fluid flow is converted to both longitudinal velocity increase and radial spreading. This resulted in the deceleration of the flow smaller than in a free jet.

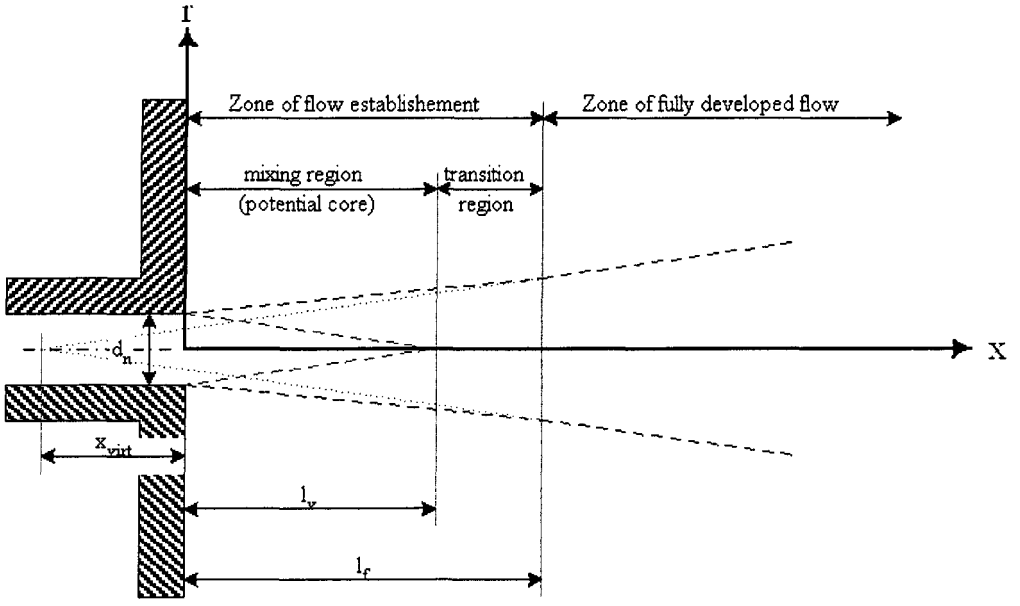

Figure 3.40 Virtual origin of the envelope flame in the negative range

3.5.9. The radial velocity distribution in the envelope flame

The computed curve using the formula of Hinze and van der Hegge Zijnen[3] (Eq. 1.4) do not correlate at all with the measurement points. Similar to the analysis of the high velocity flame, the radial velocity distribution was also calculated using Eq. 3.5 given by Popiel, van der Meer and Hoogendoon[13]. However as this is valid in the fully established jet region, the computed curve do not predict the measurement points as well as for the high

velocity jet. As it was discussed above in the section 3.5.5, Eq. 3.6 was also established, which matches very well the measurement data in the active combustion zones.

The radial velocity curves at the four test sections are presented in Figure 3.41 to Figure 3.44 for the envelope flame. The unfilled and filled markers in the figures are the experimental points of the parallel firing and impingement arrangements respectively. The solid lines are the computed curves using Eq. 3.5 given by Popiel, van der Meer and Hoogendoorn[13] while the dotted lines are the curves computed using Eq. 3.6 of the present work.

In the first measurement section (Figure 3.41), none of the computed curves matches the experimental data. This was expected because the free jet is not developed yet in this section.

Later downstream, in the second measurement section (Figure 3.42), the experimental points are distributed between the two curves. It can be seen, analysing the temperature diagrams in Figure 3.10, that the flame is the most instable in the proximity of the centerline of the second measurement section. This is due to the fact the reacting mixture is close to its spontaneous ignition temperature in this zone. Depending on multiple factors (mainly on different kinds of perturbations), the mixture is locally spontanously ignited or quenched depending on the fluctuation of gas concentration. On the other hand, in the proximity of the refractories of the second measurement section (see Figure 3.10 again), the presence of hot combustion zone can be deduced from the elevated temperatures. In addition, the prediction of Eq. 3.6 matches better the experimental points (above the radial distance of 100 mm).

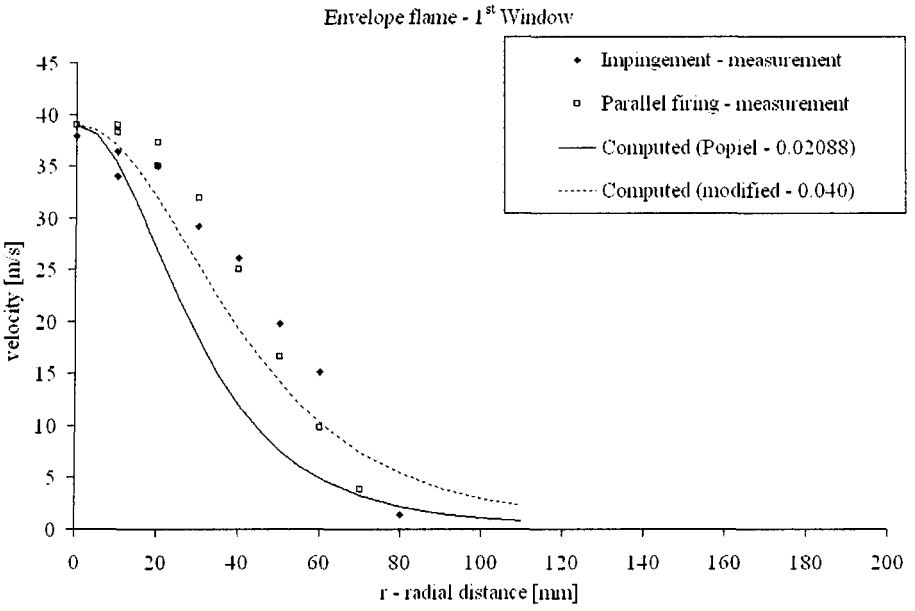

Figure 3.41. Radial velocity distribution in the envelope flame – 1st viewing port

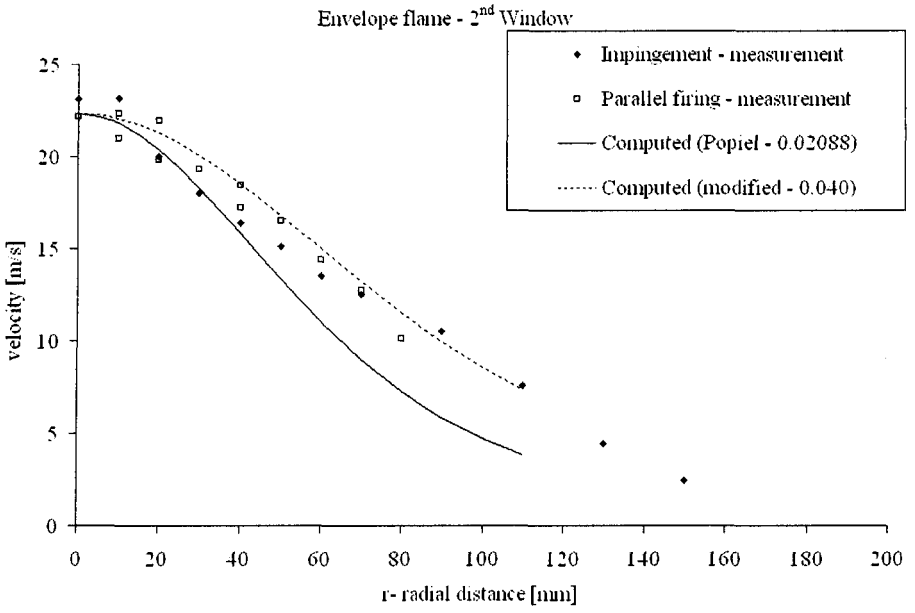

Figure 3.42. Radial velocity distribution in the envelope flame – 2nd viewing port

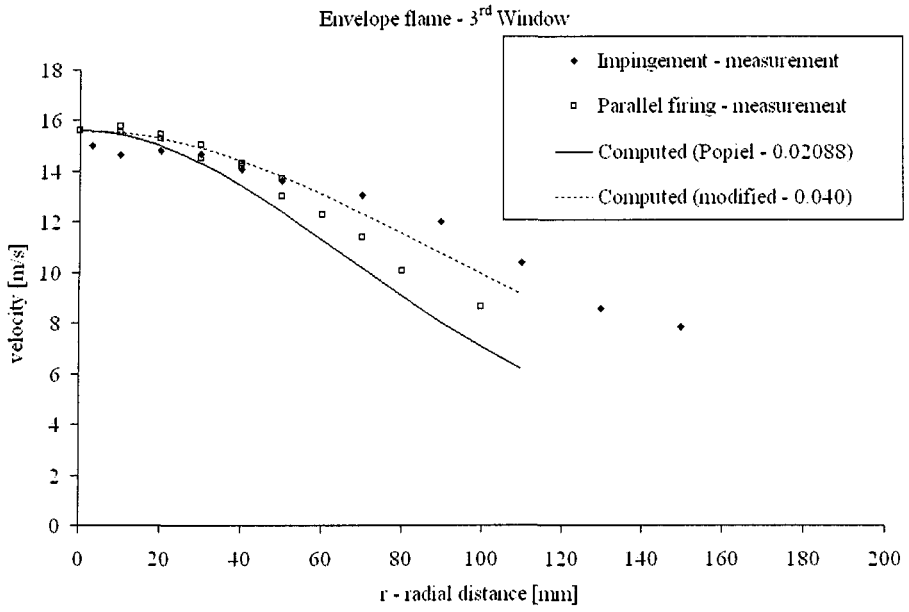

Figure 3.43. Radial velocity distribution in the envelope flame – 3rd viewing port

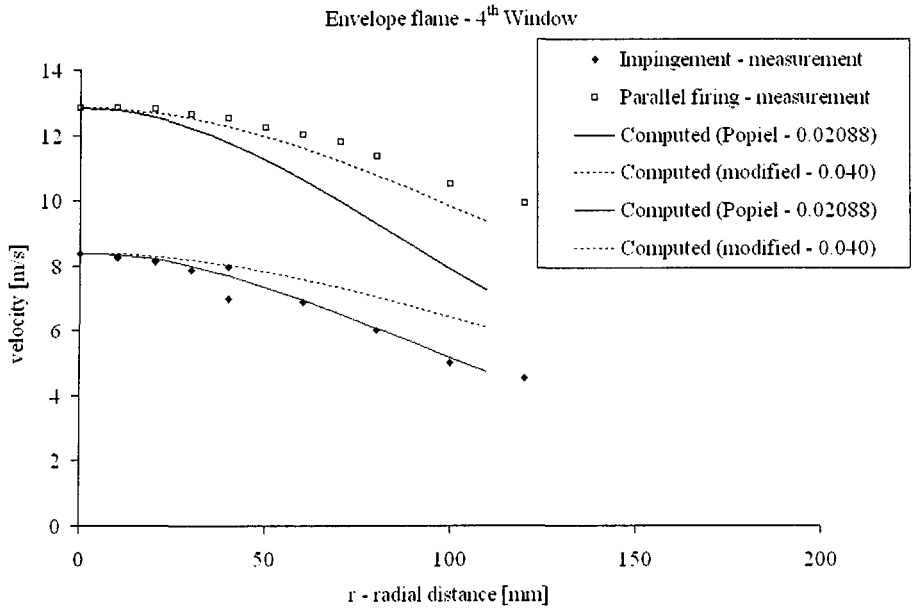

Figure 3.44. Radial velocity distribution in the envelope flame – 4th viewing port

In the third test section (Figure 3.43), the experimental data taken at the parallel firing configuration lie between the two calculated curves. On the contrary, the measurement

points taken at the impingement arrangement slightly exceed the predictions given by Eq. 3.6.

Finally, in the case of impingement arrangement, the velocity curves in the last observation section are greatly influenced by the elevated furnace hearth (Figure 3.44). For that reason, the measurement points needed to be separated for treatment. However, the prediction of Eq. 3.6 in the case of the non-influenced flow (parallel firing configuration) is close to the measurement data.

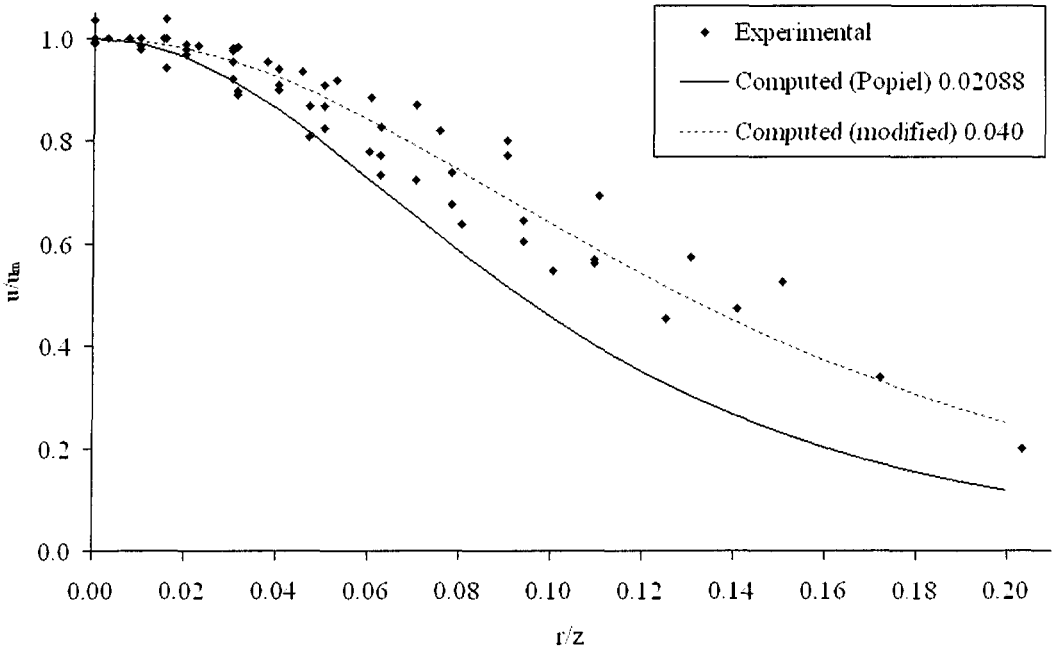

Figure 3.45. Generalized dimensionless radial velocity distribution in the envelope flame

A generalized dimensionless radial velocity distribution diagram is presented in Figure 3.45. The points, which are affected by the elevated furnace hearth, as well as the measurement data of the non-developped flow regions, are not included in the diagram. In spite of the important scattering of the measurement points, the relationship established in

the present work correlates better with the experimental data.

3.5.10. Summary of the analysis of axial velocity distributions in jets

As it was presented above in section 1.1.5.2, Popiel, van der Meer and Hoogendoorn[13] studied convective heat transfer in impinging flame jets. In their work, the centerline velocity distribution was compared with many other experimental results. The novelty in their work was the expanding of the validity of Eq. 1.4 by Hinze and van der Hegge Zijnen and Eq. 1.9 by Thing and Newby for such cases, where the density ratio ρ_∞ / ρ_n is as high as 7.6. This density ratio was created using a tunnel burner, which discharges hot combustion products into air of ambient temperature. All the other experimental works were done for density ratios (ρ_∞ / ρ_n) of 1 or 2.

In the present work, a high velocity jet flame and a so-called envelope type flame were tested. The measurement data are compared with those of other works in Figure 3.46. In the case of the high velocity flame, the density ratio is nearly one. However, for the envelope flame investigated in the present work, the density ratio was about 0.36. Recall that in this case, cold air of ambient temperature was discharged into hot combustion products. Independently of the fact that we did not found affirming studies published in the literature, it can be seen in Figure 3.46 that Eq. 1.4 and Eq. 1.9 are also valid for density ratios less than one.

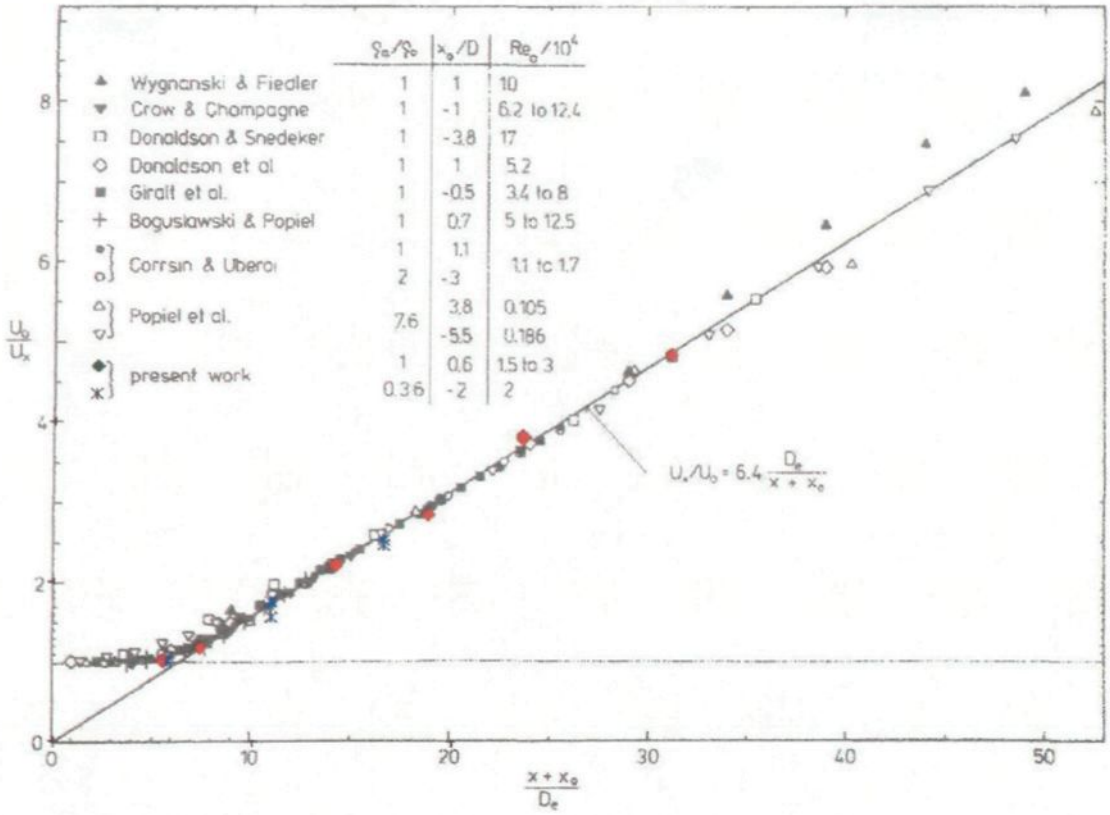

Figure 3.46. Centerline velocity decay

3.6 Fluid dynamics of the short and long flames

The two flame types, short and long ones, produced by the traditional burner are discussed together in this section. First, we tried to apply the same free jet equations, which were presented during the analysis of the high velocity and envelope flames produced by the LNI burner. On the other hand, there are several discrepancies between the two burners. One of the differences is the diameter of the nozzle. For the same mass flow rate, the nozzle diameter for the traditional burner is three times as large as that for the LNI burner. Consequently, the flow velocities at the nozzle exit are substantially lower. In addition, the nozzle diameter is bigger than 1/10 of the furnace cross section, which favorizes the

evolution of flow recirculation. This happens, because the available secondary flow is less than that which the jet can entrain (section 1.1.2). Another difficulty in the analysis is the velocity inhomogeneity of the issuing jet. This latter is due to the special geometry of the burner mouth as well as the not sufficiently long mixing section of the nozzle.

As a conclusion, these flames cannot be characterised with the free jet theorem. Nevertheless, the mixing particularities in the burner mouth, the approximate nozzle exit velocities and temperatures as well as the flame particularities preceding the first test section are discussed applying some assumptions and backward extrapolation. This will be presented in the following section. Subsequently, the longitudinal velocity and temperature distribution is presented in the furnace centerline.

3.6.1. Nozzle exit parameters

As it was presented in Figure 3.11, the velocities in the centerline of the first test section are about 13.5 m/s and 17 m/s for the long and short flames respectively in both horizontal and impingement arrangements. To find the reasons of these differences, first the temperatures of the reacting mixtures at the nozzle exit have to be calculated, using the « Computational module for the nozzle exit parameters ».

For the long flame, the calculated gas mixture temperature at the nozzle exit is 1373 K. On the contrary, in the case of the short flame, this same parameter is significantly higher, 1730 K. Since both flames are mixed and ignited inside the burner mouth, elevated gas temperatures at the nozzle exit were expected. However, these velocity and temperature differences between the short and long flames have to be caused by the different mixing

conditions.

The burner mouth geometries of the long and short flames are shown in Figure 3.47 and Figure 3.48. The long flame has a gas inlet in the center of the nozzle (red line) as well as eight air inlets around the centerline (blue lines, Figure 3.47). In the case of the short flame, the air inlet is the same. In opposition, the natural gas is injected radially through eight tiny holes in the space between the air nozzles (Figure 3.48). The potential cores and the boundaries of the jet shown in Figure 3.47 and Figure 3.48 are real-scale sketches in proportion of the presented geometry. The potential core lines for each jet are computed according to Eq. 1.2 given by Kataoka[8], while the jet boundaries are determined using Eq. 1.4 after Hinze and van de Hegge Zijnen[3]. The outer straight lines, which represent the jet boundaries, are the points of the jet where the horizontal velocity $\overline{u}$ is some arbitrary small fraction of the velocity on the centerline. In their study, Beér and Chigier[2], Matthieu[11], Kataoka[8] etc. defined the jet boundary line is marked, where the velocity is half of the centerline velocity. On the contrary, in the present work, the smallest measurable fraction of the centerline velocity is marked in Figure 3.47 and Figure 3.48 as well as in Figure 3.51 and Figure 3.52.

In Figure 3.47 and Figure 3.48, the mixing characteristics of the long and short flames are compared. It can be seen in the figures that the mixing in the long flame occurs farther downstream than in the short one. For that reason, the gas mixture at the nozzle exit is colder for the long flame, as well as its motion is also slower. On the other hand, contrary to the short flame, the proportion of the already released heat at the nozzle exit to the overall heating value is smaller in the long flame. Thus, the long flame release more heat

further downstream in the combustion chamber. The heat release occurred in the combustion chamber promotes mostly the radial expansion of the flame, as well as it moderates slightly the deceleration of the gas.

The planar section of the velocity distributions at the nozzle outlet section are also shown in Figure 3.47 and Figure 3.48. In the case of the long flame, the velocity inhomogeneity at the nozzle exit is expected to be more pronounced than for the short flame. It is due to the differences in the length of the mixing section at the burner mouth. For the long flame, the mixing section is not sufficiently long to homogenize the flows discharging from the little nozzles.

In addition to the analytical computations, a numerical mathematical model has also been solved using the CFX[71] computational fluid dynamics software package. The inlet velocities for the long and short flames are represented in Figure 3.49 and Figure 3.50 respectively. The above-mentioned differences in the mixing characteristics of the two flame types can easily be distinghished on the basis of these figures.

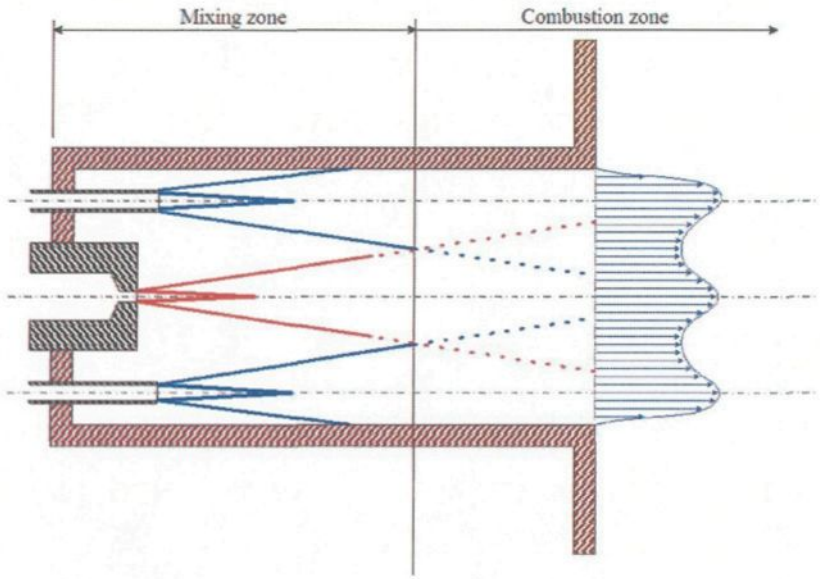

Figure 3.47 Burner port of the long flame

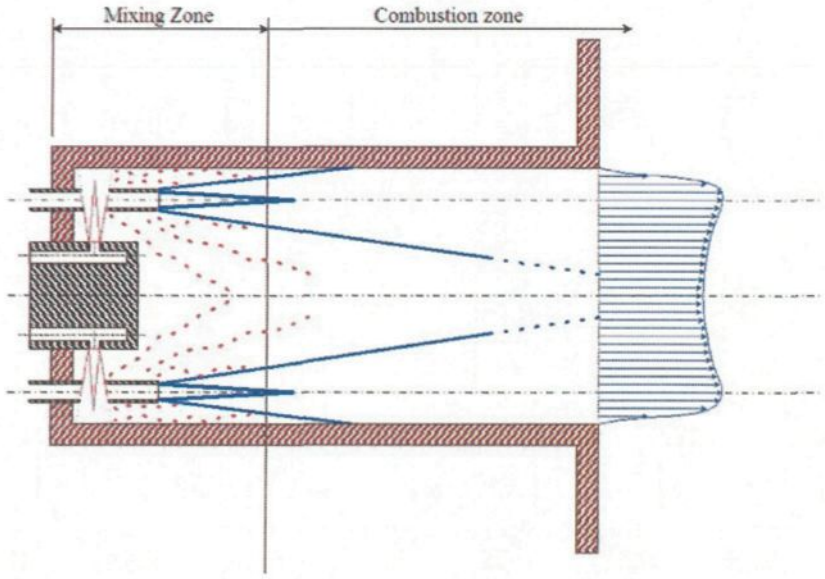

Figure 3.48 Burner port of the short flame

Figure 3.49 CFD model - velocity inlet of the long flame

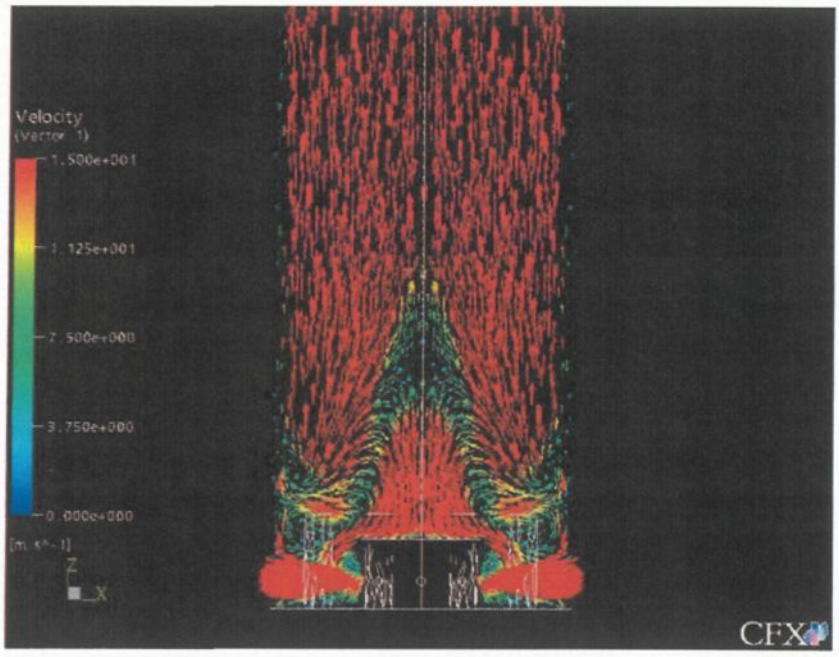

Figure 3.50 CFD model - velocity inlet of the short flame

As it can be seen on the normalized velocity diagrams in Figure 3.13 and Figure 3.14,

the experimental velocity profiles taken in the first measurement section show a plateau at the centerline for both flame types. This refers to the presence of the potential core. In the case of the long flame, the radius of this plateau is 25 mm. For the short flame, this is only 10 mm. For both flames, the potential core lengths were determined geometrically using the size of this plateau measured at the first test section. This method is shown in Figure 3.51 and Figure 3.52. Several important nozzle exit parameters are presented in Table 3.5, where the potential core lengths, X_v and l_v are experimental results. However, the calculation of the potential core length according to Eq. 1.2 yields to significantly different results. Recall, that Eq. 1.2 is only valid for single, homogenous, free jets.

The velocity distributions in the burner mouth and in the first furnace sections are shown in Figure 3.51 and Figure 3.52 for the long and short flames respectively. In the burner nozzle, where the mixing occurs, the discharging air and natural gas streams are distinguished with blue and red colours. On the contrary, in the combustion chamber the red lines represent the boundaries of the experimentally determined potential cores while the velocity vectors as well as the jet boundary lines are colored blue. The potential cores and the jet boundaries are both determined based on the experimental measurements.

As it was discussed above, the inhomogeneity at the nozzle exit is estimated to be more pronounced for the long flame compared to the short one. However, downstream at the first test section, these inhomogeneities can no more be detected for any flame. The jet boundary lines are also presented. It can be seen in the figures that the jets are spreading out until reaching the refractories. Experiments showed that the radial expansion is more significant in the long flame, in which case a greater proportion of the overall heat release

realizes in the combustion chamber than for the short flame.

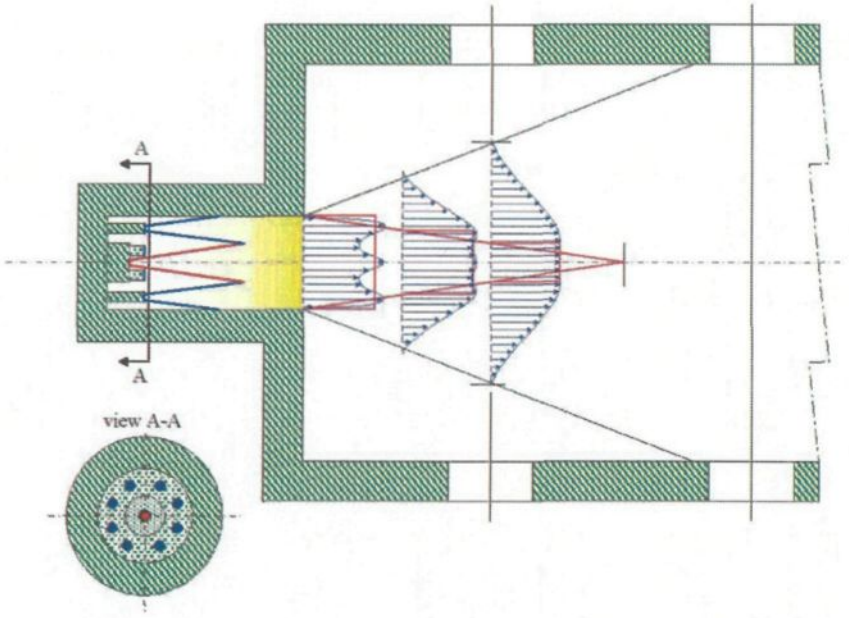

Figure 3.51 Velocity profiles of the long flame in the combustion chamber

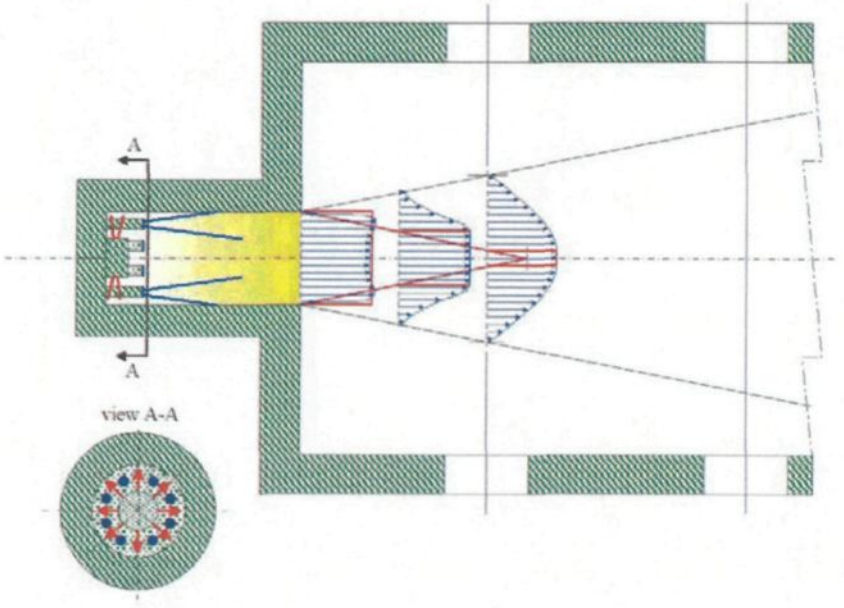

Figure 3.52 Velocity profiles of the short flame in the combustion chamber

TRADITIONAL BURNER				
	short flame		long flame	
	parallel firing	impingement	parallel firing	impingement
T_{inlet} [K]	1705	1705	1360	1360
T_{inf} [K]	873	1273	1073	1273
v_{inlet} [m/s]	17	17	13.5	13.5
d_{nozzle} [m]	0.118	0.118	0.118	0.118
X_v (experimental)	2.372	2.372	3.419	3.419
l_v [m] (exp.)	0.280	0.280	0.403	0.403
Re_{outlet} [-]	6713	6713	7722	7722

Table 3.5 Nozzle exit parameters in the short and long flames

3.6.2. Longitudinal velocity distribution in the short and long flames

The inverse of the axial velocity decay as a function of the dimensionless distance from the burner nozzle is presented in Figure 3.53 and Figure 3.54 for the short and long flames. For easier comparison, the diagrams have the same scalling as it was used for the high velocity and envelope flames in Figure 3.25, and Figure 3.39. The stars and the triangles are both experimental results taken in impingement and parallel firing configurations respectively. The solid lines are the computed values using Eq. 1.7 given by Hinze and van der Hegge Zijnen[3] for constant density systems. The computed lines for non-constant density systems with the concept of the equivalent nozzle diameter (Eq. 1.9) are represented with dotted lines. In the case of the short and long flames, neither the constant nor the non-constant density approach is applicable.

As it was discussed in section 1.1.4, according to Hinze and van der Hegge Zijnen[3], the length of the mixing region is about 7 d_n. If this statement would be accurate in the case of the short and long flames, the potential core should extend even until the third

measurement section. On the contrary, the measurements have shown that the critical point is at the distance of $X_v = 2.37$ and $X_v = 3.42$ for the short and long flames respectively (see Table 3.5). However, these experimental results are closer to the conclusions of Beér and Chigier[2] or the results of Forstall[7]. They predicted the potential core length to 4-nozzle diameter. Beér and Chigier[2] made their experiments using a burner with concentric tubes. The town gas was injected through the tube in the middle while the air was issued around, via the annular section of the concentric tube. However, this gas inlet is not absolutely the same as that for the long flame of the present study, but in fluid dynamic sense, the two inlets are similar. Contrary to the flame studied by Beér and Chigier[2] the long flame is a confined flame, the potential core lengths in the two cases are comparable. In conclusion, the burner geometry has probably an important influence to the developpement of the potential core.

In the case of the short flame, the fourth measurement point is out of the displayed range in Figure 3.53, for both impingement and parallel firing arrangements. This is due to the very low velocities, which are close to the detectability threshold. The results at the third test section are also interesting in the case of the short flame, because the deceleration of the gas flow at parallel firing arrangement is greather than that of impingement configuration. However, at the impingement arrangement, the flame is affected by the elevated furnace hearth. The only explanation might be the conduit effect. If the flame is so much expanded that all the accessible space is occupied by the gas, the diminishing cross section causes velocity increase. Comparing to the long flame at impingement configuration, the velocity profile is much more spreaded out in the third measurement

section. This can be observed in Figure 3.13 and Figure 3.14.

In the case of the long flame, the reciprocal of the centerline velocity decay is regular. The velocities at the last furnace section are small, but already detectable. Similar to the high velocity and envelope flames, the gas flow decelerates more rapidly in the case of the impingement arrangement than for the parallel firing configuration.

The longitudinal velocity distribution in the centerline of the short and long flames for parallel firing and impingment configurations are shown in Figure 3.55. It is surprising that in spite of the considerable difference in the nozzle exit velocities, the curves are nearly identical in the decaying sections. In conclusion, the differences in the nozzle exit velocities as well as the dissimilarities in the potential core lengths neutralize each other.

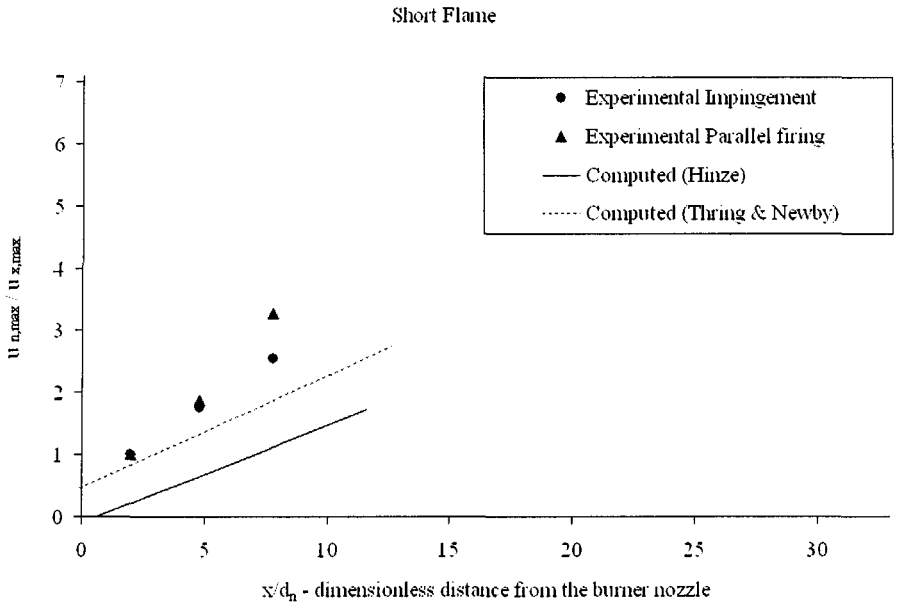

Figure 3.53. Short flame - reciprocal of the the centerline velocity decay as a function of the distance from the nozzle

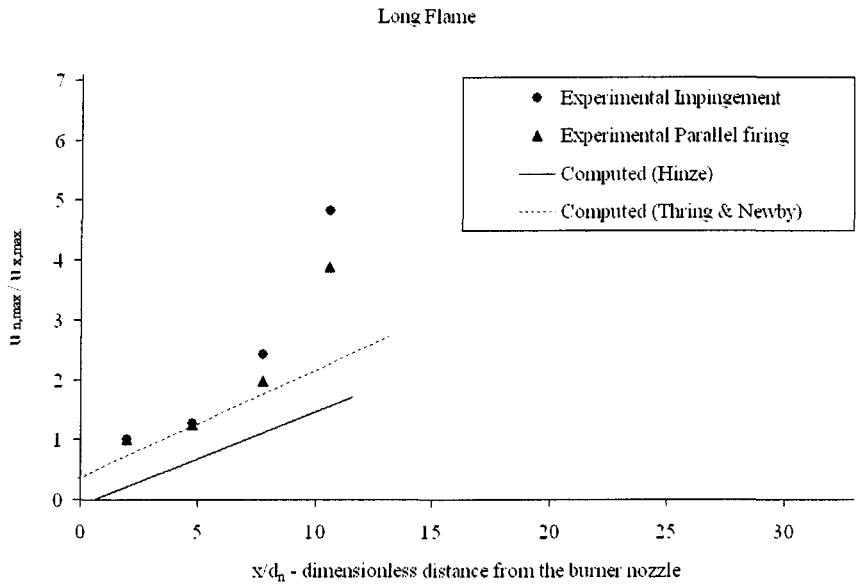

Figure 3.54 Long flame - reciprocal of the centerline velocity decay as a function of the distance from the nozzle

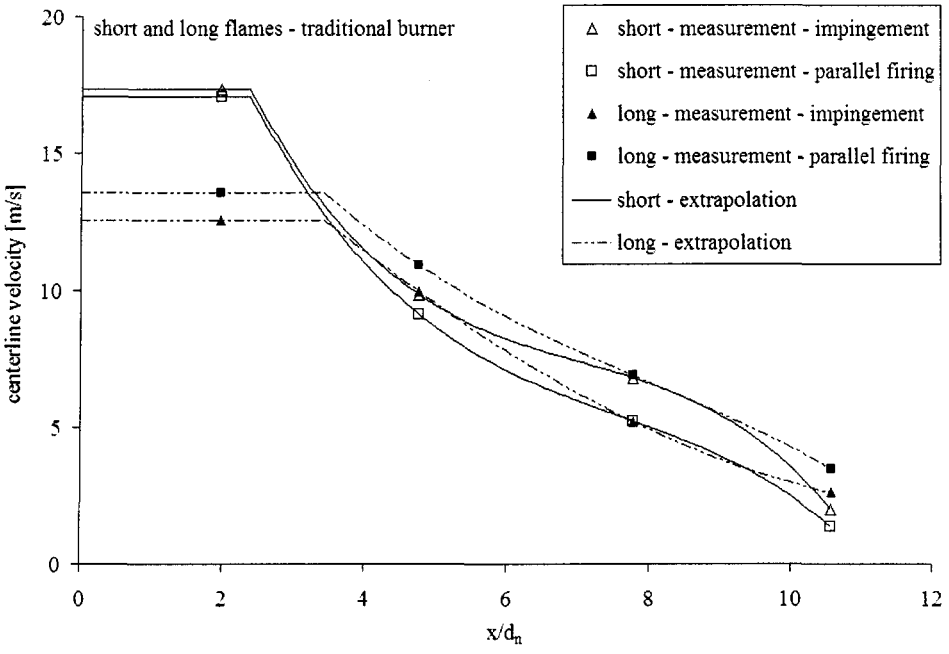

Figure 3.55. Longitudinal velocity distribution in the centerline of the short and long flames for parallel firing and impingment configurations

The radial velocity distribution described by Eq. 1.4 was also calculated. However, in the case of these confined flames, the similarity principle is not applicable at all. Therefore, the results are not presented here.

3.6.3. Longitudinal temperature distribution in the short and long flames

For the short and long flames, the longitudinal temperature distribution at the furnace centerline is shown in Figure 3.56 and Figure 3.57 respectively. The four marks on the diagrams are the measurement data in the four furnace sections. The temperatures at the nozzle exit are computed values discussed in section 3.6.1. The presented curves are the interpolations between the four measurement points and approximations between the nozzle exit parameters and the first measurement point. The scale of the diagrams is the same as it was used for the high velocity and envelope flames.

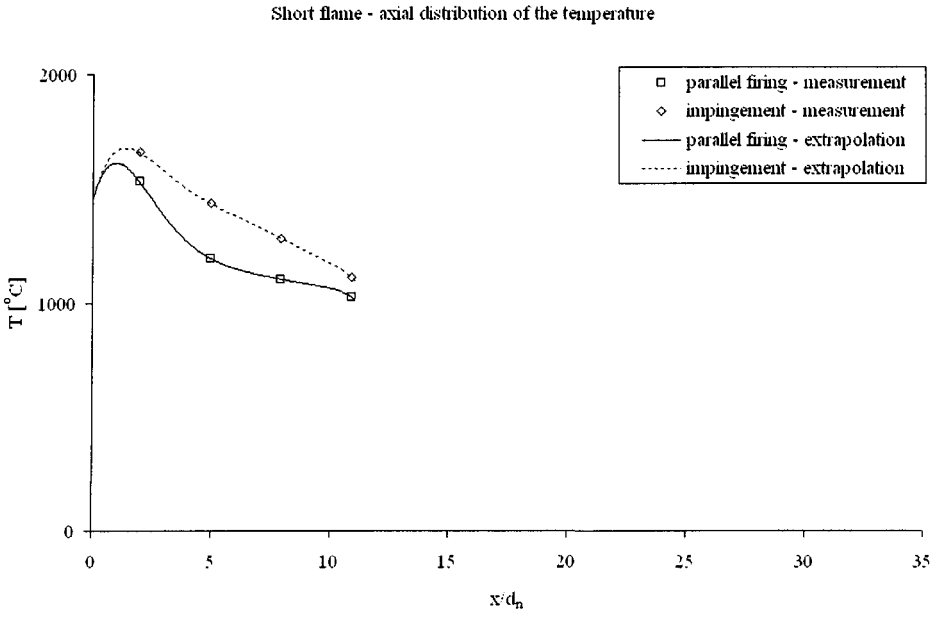

Figure 3.56. Longitudinal temperature distribution in the short flame

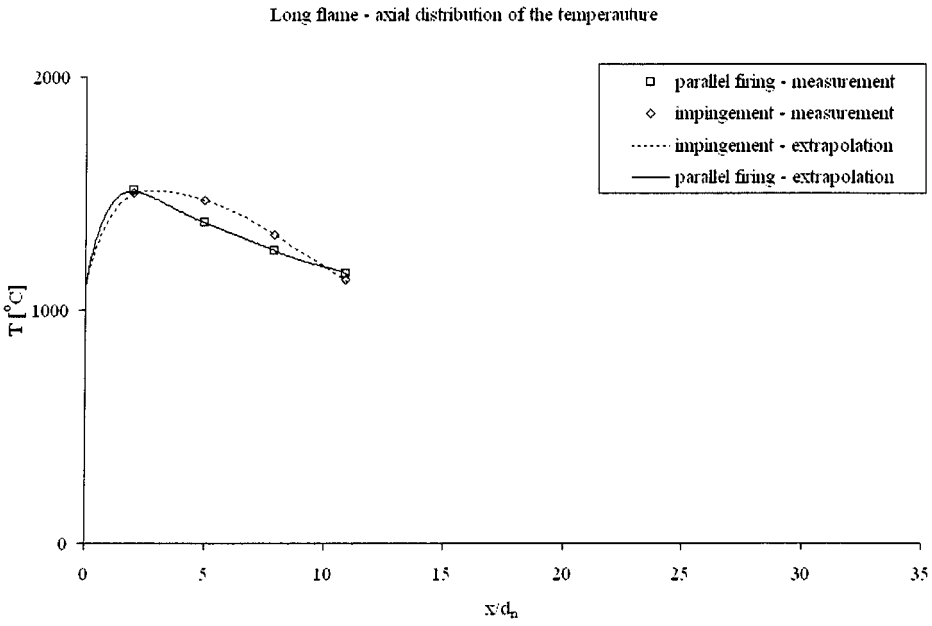

Figure 3.57. Longitudinal temperature distribution in the long flame

For the short flame, the gas temperatures are slightly higher for the impingement configuration in the entire furnace. On the contrary, for the long flame, the temperatures are only higher in the second and third furnace sections. However, as it will be discussed in the following section, the gas temperature curves depend very strongly on the refractory temperature. The latter depends on the operational conditions.

Finally, the gas temperature distributions in the centerline of the furnace are compared for the four studied flame types in Figure 3.58. These curves were captured in the impingement configuration. The differences in the characteristics of the temperature curves for the various flame types can be well distinghished in this figure. Comparing to the other flames, the axial temperature curve of the envelope flame is radically different.

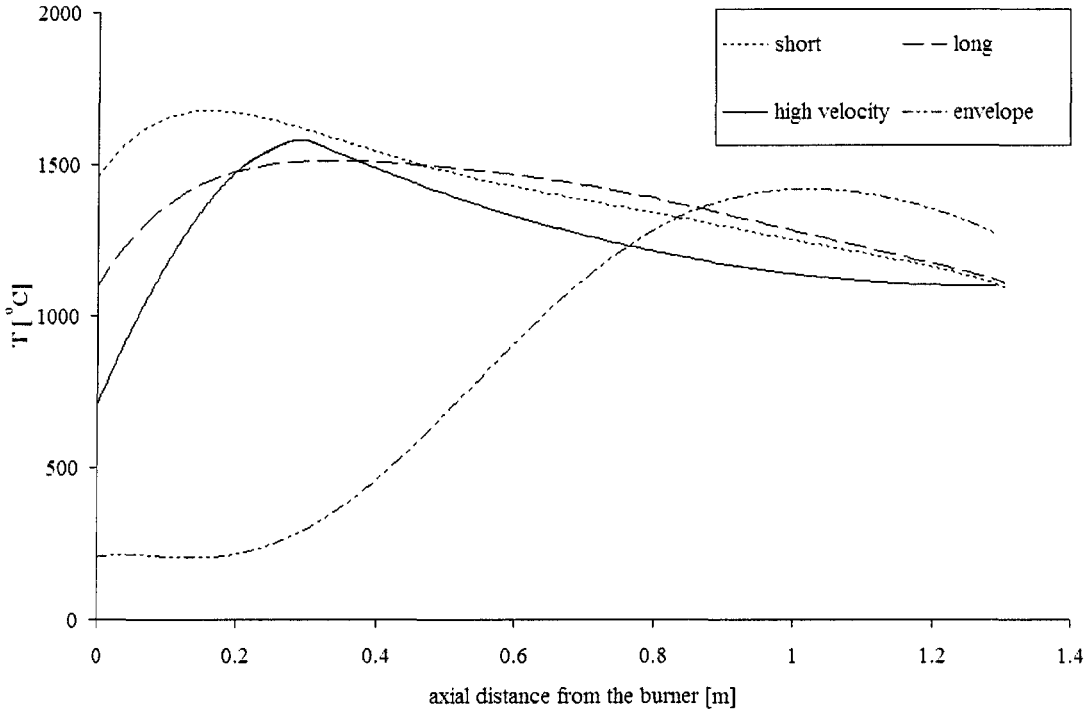

Figure 3.58 Comparison of the longitudinal temperature distributions in the furnace centerline for the four studied flame types at impingement configuration

3.7 Refractory temperatures

3.7.1. Objectives and methodology of the refractory temperature measurements

The heat flux results will be presented in the next chapter. It will be discussed there that a very important portion of the radiative heat flux (nearly 40%) arrives to the sensors from the refractory walls. Thus, for a detailed heat flux analysis, the refractory temperatures have to be analysed first. In this section, the refractory temperature distributions are compared for the four different flame types and for the three different flame-target configurations.

Figure 3.59 represents the refractory temperatures collected during a typical day of experimentation. It can be seen in this figure that even nine hours are not enough to the refractories to reach the steady state condition. Hence, the measured heat fluxes depend not only on the flame type and on the burner-target configuration but also on the actual state of the heating-up procedure.

During the heat flux experiments, we were not able to reach the steady state condition of the refractories. Therefore, we attempted to make the measurements in all cases at the same preheating period after the ignition of the burner. This period was determined by the envelope flame, which needs the longest preheating period because of the necessity adequately preheated refractories for safe operation (near to the steady state condition). In the case of the parallel firing and inclined configurations (see the plug-type heat-flux sensor concept in section 2.3.3.2), the heat-flux data acquisition was done simultaneously using 24 plug-type heat flux sensors embedded in the calorimetric plates. Data were acquiered continuously, in every 30 seconds, during the entire experimentatal day. Thus, for parallel and inclined burner-charge configurations, those heat flux data were simply selected which were recorded after the same time (8-10 hours) after burner ignition. tooken at the same preheating period after the burner ignition for each flame types. Because of the continous recording of the heat fluxes, by these arrangements the adequate heat flux values the heat-flux this was only a technical For these burner-target configurations, we accomplished the measurements at the same preheating period after the burner ignition as it was expected. Otherwise, this was easily feasible because we disposed of continuously acquisitioned data files over the entire experimental day. On the other hand, for impingement arrangement the

concept of the heat-flux sensor was modified (see the transformation of the furnace, plug-T-type heat flux sensors in section 2.3.4.2). The new plug-T-type sensors were not permanently installed in the calorimetric plates. Therefore, the heat-flux data acquisition in the entire furnace was realized using only two sensors, an absorptive black and a reflective bright one. Thus, in the case of the impingement configuration, a complete data scanning was a very time-consuming procedure (took approximately one and a half, two hours). During this long interval, the incident heat-flux can vary even in the same measurement point between the beginning and the end of the data acquisition. To evaluate as well as to compensate this effect, a reference measurement point was selected in the furnace to which we recurrently returned during the heat-flux measurement procedure. This method was applied for the heat-flux measurement of all flames types in the case of impingement arrangement. The selected reference point in all tests was the direct impingement point located in the furnace centerline on the vertical calorimetric plate.

The series of measurements were not executed at the same time (2001 and 2004 respectively). Thus, between the measurement series, the position of the thermocouples and the configuration of the data acquisition system were modified. The following (Figure 3.60 and Figure 3.61) show the exact positions of the thermocouples. The numbers given in the neighbourhood of the thermocouples between the brackets represent the immersion depth of the sensors in the refractory wall. All the thermocouples are of the type R (Pt/platinum-13%Rh/rhodium). The four furnace sections located between the burner and the stack in the middle row represent schematically the refractory ceiling. The two other rows, above and below, are the sidewalls of the furnace, folded up by 90 degree.

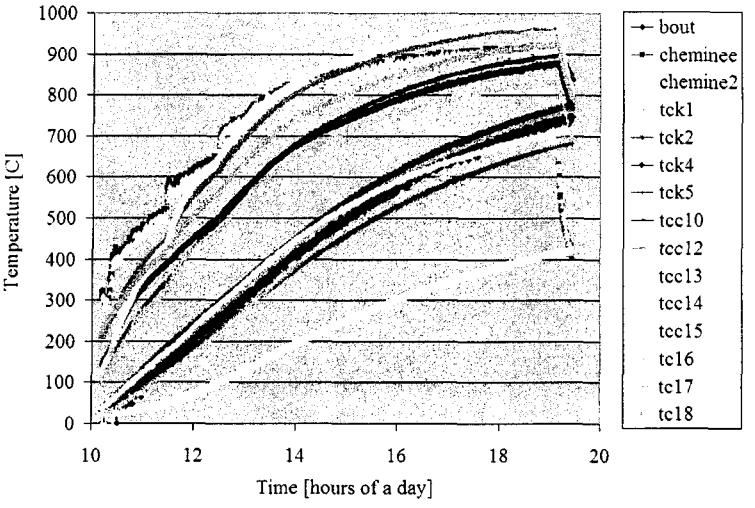

Figure 3.59. Temperature distribution in the refractory walls during a typical experimental day, as seen in Figure 3.61

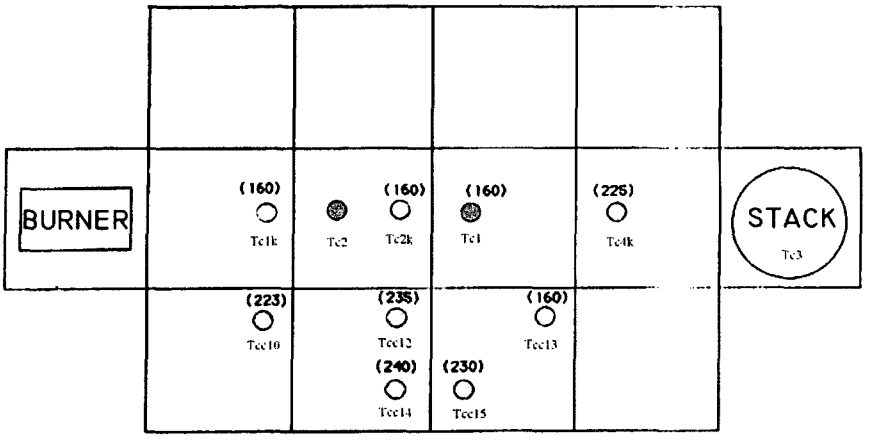

Figure 3.60. Position of the thermocouples in the refractory walls during experiments for parallel firing and inclined arrangements (the numbers between brackets are the penetration depth of thermocouples in millimetres)

In Figure 3.61, the impingement zone is marked with crossed rectangles. The presence of water-cooled calorimetric-plates in this refractory zone deviates the heat flux, otherwise normal to the plane of the wall. Namely, the temperature gradient becomes parallel to the faces of the wall, thus the thermocouple placed in this zone (tcc15) cannot be used for

further analysis.

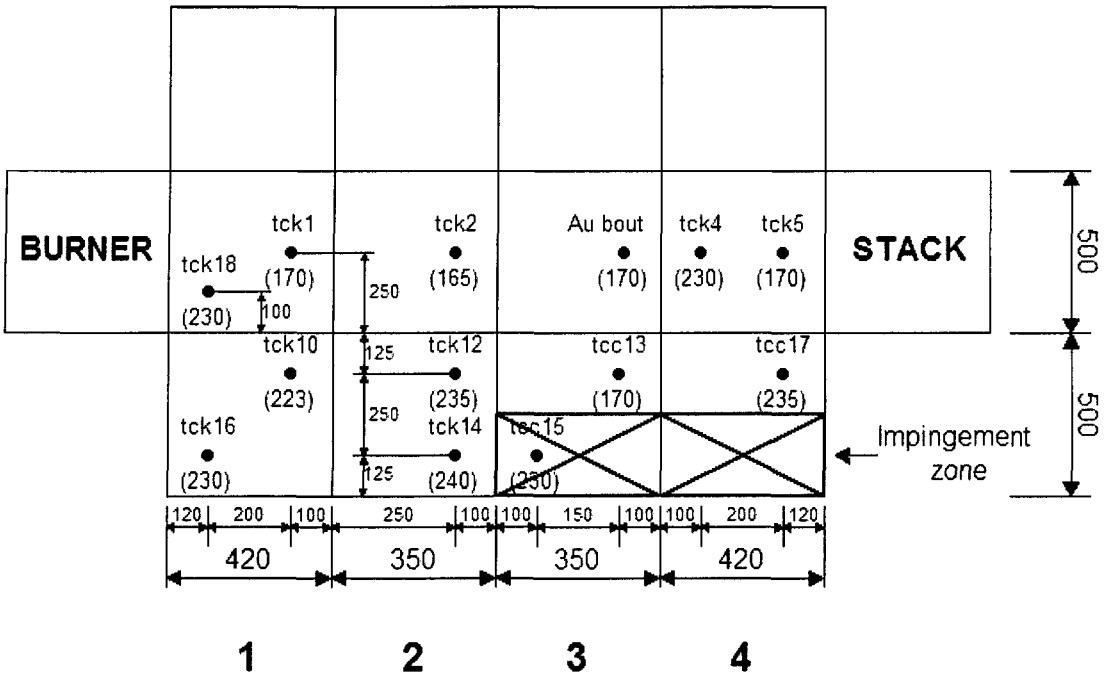

Figure 3.61 Position of the thermocouples in the refractory walls during the experiments for impingement arrangements (the numbers between brackets are the penetration depth of thermocouples in millimetres)

The total thickness of the refractory is 250 mm. The distribution of the temperature on the internal surface represents crucial information for the radiation analysis. Unfortunatelly, this cannot be measured directly. However, it can be determined by the extrapolation using the temperature values measured with thermocouples inside the refractory and at the external surface of the furnace. The one-dimensional heat conduction equation of Fourier was used:

$$q = -k\frac{dT}{dx}$$

Eq. 3.8

If it is assumed that the refractories of the experimental furnace are homogenous (k=const.)

and independent of temperature, the internal surface temperature of the refractory for an arbitrary chosen thermocouple can be extrapolated using the following formula:

$$T_{s,\text{int}} = \frac{0.25}{k}\left[\frac{k \cdot T_{tc}}{x_{tc}} - \frac{k \cdot T_{s,ext}}{x_{tc}} + \frac{k \cdot T_{s,ext}}{0.25}\right] = \frac{0.25}{x_{tc}}\left(T_{tc} - T_{s,ext}\right) + T_{s,ext}$$

Eq. 3.9

where $T_{s,\text{int}}$ and $T_{s,ext}$ are the internal and external surface temperatures of the refractories respectively. T_{tc} is the temperature measured by the thermocouple at the depth x_{tc} in the wall from the outer surface. k represents the thermal conductivity of the refractory wall. Eq. 3.9 shows that the internal surface temperature depends on a linear equation. The variation of the external surface temperature between 25-80°C can be neglected compared to the rise of the temperature at the internal surface, from 25 to 1300°C. For this reason, instead of following countinously the external variation, a representative average value of 60°C was chosen. On the contrary, small displacements of the positions of the thermocouples in the measurements holes cause important errors. This can happen for exemple, when the sensor is not inserted completely to the bottom of the hole.

As an additional benefit, the information obtained with thermocouples is used to assure a safe operation of the furnace. For exemple, the envelope flame cannot be started before 800°C were not reached everywhere in the furnace. The distributions of the refractory temperature are presented in the following sections for the different flame-object configurations and the various flame types.

3.7.2. Refractory temperatures during the heat flux measurements - comparative diagrams

The thermocouples, presented in Figure 3.60 and Figure 3.61, were divided into two groups: thermocouples located at the refractory ceiling and thermocouples inside the sidewalls.

First, the refractory ceiling temperatures are compared for the different burner-target configurations in the diagrams in Figure 3.62, where the longitudinal distances from the burner exit are plotted versus the internal surface temperatures. The solid-lines, the dotted lines and the dots-and-dashes represent the impingement, the inclined and the parallel firing configurations respectively. In the cases of the parallel firing and inclined burner-target configurations (Figure 3.60), all the five thermocouples in the refractory ceiling were used for the analysis. In the case of the impingement arrangement (Figure 3.61), the following four ceiling thermocouples were considered: tck1, tck2, "Au bout", tck5. The results of the two remaining thermocouples were not taken into account, because thermocouple tck18 is not in the centerline and the behaviour of thermocouple tck4 was not reliable.

Secondly, the sidewall temperatures are presented in Figure 3.63. In the case of the parallel firing and inclined arrangements, only the three upper thermocouples are considered (Tcc10, Tcc12, Tcc13). The responses of the two lower sensors (Tcc14, Tcc15) are similar to that of the thermocouple Tcc12. However, for the impingement configuration, all the uppers (tck10, tck12, tcc13 and tcc17) and one of the lower (tck16) thermocouple were taken into account. The response of the thermocouple at the bottom of the furnace, close to the cooled calorimetric plates (tck16), is the first points in the curves.

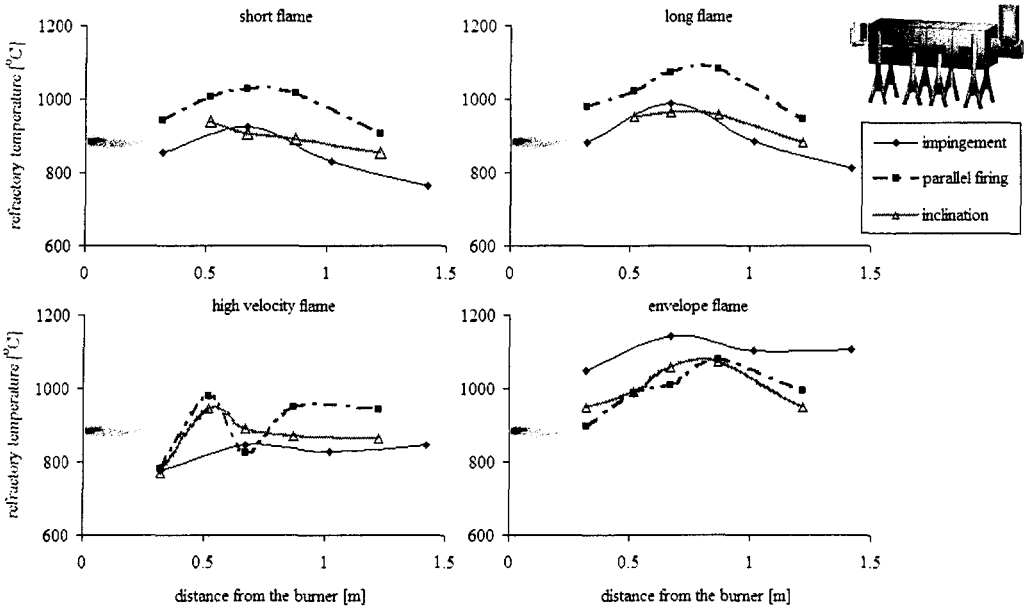

Figure 3.62 Comparison of the wall temperatures in the refractory ceiling between the three different flame-target arrangements for the four flame types

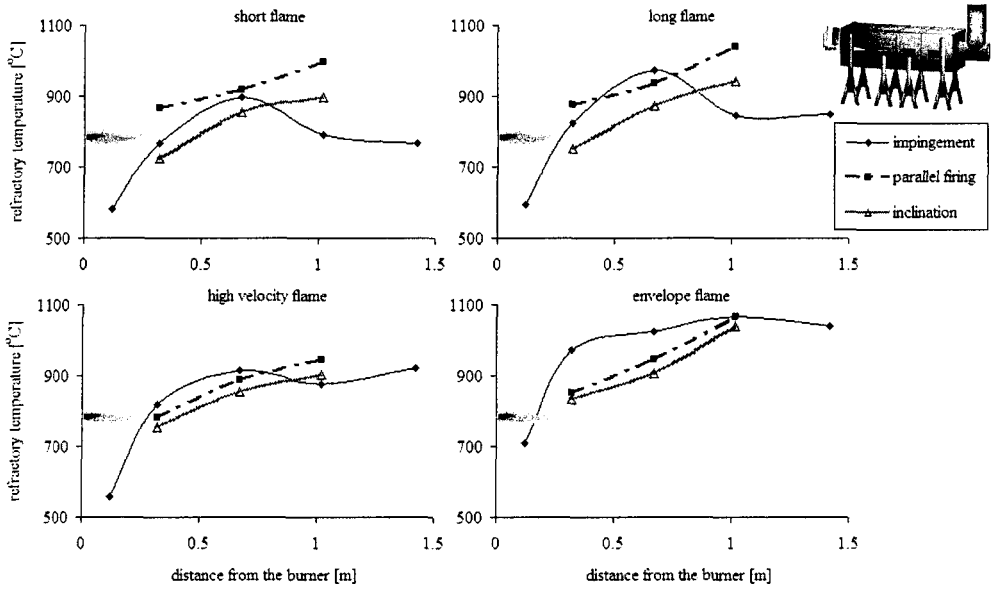

Figure 3.63 Comparison of the wall temperatures in the refractory sidewalls between the three different flame-target arrangements for the four flame types

Incidentally, due to the proximity of this thermocouple to the water-cooled

calorimetric plates, these points are the coldest temperatures in each diagram. The other two thermocouples are not included in the diagrams because thermocouple tck14 has similar values than that of tck12 and thermocouple tcc15 is located below the water cooled calorimetric plates.

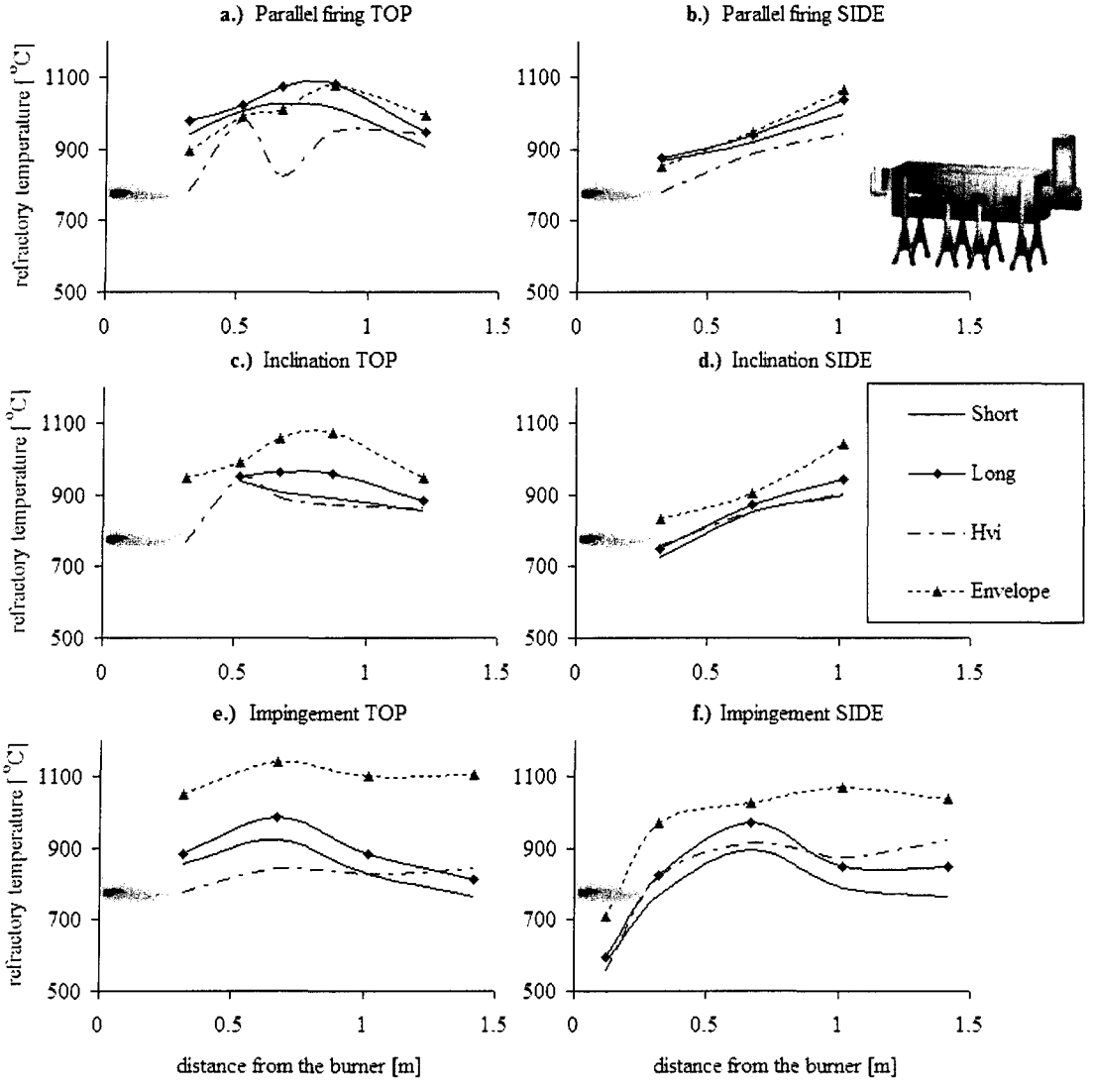

Figure 3.64. Comparison of the wall temperatures in the refractory sidewalls and ceiling between the four different flame types for parallel firing, inclined and impingement configurations

While Figure 3.62 and Figure 3.63 accentuate the differences between configurations, Figure 3.64 emphasizes the differences between the various flame types. In the first, second and third rows the parallel firing, the inclined and the impingement arrangements are presented respectively. The first column represents the wall temperatures in the refractory ceiling while the second one demonstrates the results in the sidewalls. The solid lines in the figures with and without markers correspond to the short and long flames respectively and the dotted lines with and without markers represent the high velocity and envelope flames.

3.7.3. Discussion and conclusions of the refractory temperature measurements

Analysing Figure 3.62 and Figure 3.63, the first eye-catching particularity is the similarity between the characteristics of both the ceiling and the sidewall temperatures of the short and long flames for all the studied configurations. On the contrary, the differences between the high velocity and the envelope flames are significant.

For the short, the long and the high velocity flames, the ceiling was the most intensively heated at parallel firing arrangement. This seems to be logic, as both burner tilting and direct flame-object impingement amplify the heat transfer toward the water-cooled calorimetric plates. On the other hand, in the case of the envelope flame the highest ceiling temperature occured in the impingement arrangement. It can also be mentioned that for this flame type the burner tilting had less influence on the wall temperature distribution compared to the parallel-firing configuration.

In the impingement configuration, the peak temperature in the ceiling is located in the first half of the furnace for the short and long flames. For the high velocity and envelope

flames a quasi-flat platform is observable in the rear half of the furnace after a moderate increase in the first half of the furnace.

The sidewall temperatures at the parallel-firing and inclined arrangements are approximately similar for all the four flame types. The curves increase continuously toward the chimney. The only difference is whether the curves are concave or convex.

In the case of impingement arrangement, the form of the curves for the short and long flames is almost identical. The only small difference can be observed in the last measurement point. However, the temperature values are higher for the long flame. The maximum temperature, identically to the refractory ceiling, is located in the first half of the furnace, close to the middle. For the envelope flame, the sidewall temperatures are very high in all the upper measurement points. The maximum value is situated in the rear part of the furnace, similarily to the the ceiling. The refractory temperature distribution for the high velocity flame seems to be a transition between the short or long and the envelope flames.

So far, the characteristics of the curves were compared in Figure 3.62 and Figure 3.63. However, the analysis of the Figure 3.64 permits to differentiate the temperature levels for different flame types and various configurations. The first obvious remark in the characteristic of the curves is the much higher wall temperatures for the envelope flame at inclined and impingement configurations. On the contrary, at parallel-firing arrangement, the refractory temperature curves, both in the ceiling and in the sidewalls, are comparable for all the four flame types. In the impingement configuration, this difference is up to 300°C between the envelope flame and the other flame types.

There are several reasons of these important differences. As it was mentioned above,

the burner-target orientation has less influence on the envelope flame. On the contrary, in the case of the other flame types, the flame was oriented toward the water-cooled calorimetric plates. Thus, the ceiling was less heated. In addition, the object inserted in the flame at impingement configuration modified the mixing pattern of the oxidizer and reactants in the envelope flame. This provoked most intensive chemical reaction in the rear half of the furnace, which caused very high refractory ceiling temperatures.

The refractory temperatures, both in the sidewalls and ceilings, are higher for the long flame than for the short one. This is a very important observation from the point of view of the radiative heat transfer.

Finally, the reason of the fluctuation in the ceiling temperature curve for the high velocity flame at parallel firing arrangement is not known. A little difference is also observable in the same point for the short and envelope flames. Unfortunately, the refractory thermocouples were not checked right after the experiments. Actually, the only possible assumption is that the tip of the thermocouple was not perfectly imbedded in the hole.

3.7.4. Correction of the gas temperatures based on the refractory temperature level

As it is well known from the literature, the refractory temperature influences significantly the temperature of the combustion products and slightly the flame temperature. Two gas temperature profiles are presented in Figure 3.65, to demonstrate this effect. The measurements were taken in the long flame at the first furnace section (closest

position to the burner nozzle) using the suction pyrometer. The only difference is in the refractory temperatures. It is higher for the test made on 30 November (solid-line). As it can be seen on the diagram, the differences are negligible in the centerline where the active combustion zone is located. On the contrary, the difference is important close to the refractories. The differences of the refractory temperatures influence the rate of the cooling of the hot combustion products as well as the entrained surrounding gas temperature.

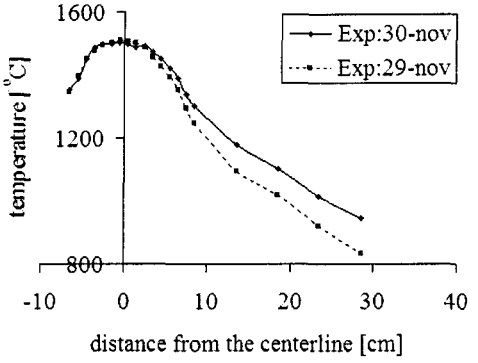

Figure 3.65. Comparison of two temperature profiles for different refractory temperatures

As it was mentioned above, it was attempted to make the heat flux measurements for all flame types after the same heating up period of the refractory. On the contrary, this consideration was not respected during the gas temperature measurements using the suction pyrometer. However, if the refractory temperatures are known, the measured gas temperatures can be corrected for the heat flux experiments.

Figure 3.66 represent the measured and the corrected temperature curves in the centerline of the furnace. The correction was made to the heat flux measurements in the impingement configuration. The heat-flux measurements will be presented in details, in CHAPTER 4. Centerline temperature curves belonging to the impingement configuration

are compared for the four studied flame types in Figure 3.67. The straight line at 1500°C represents the approximative temperature limit of the thermal NO_x formation.

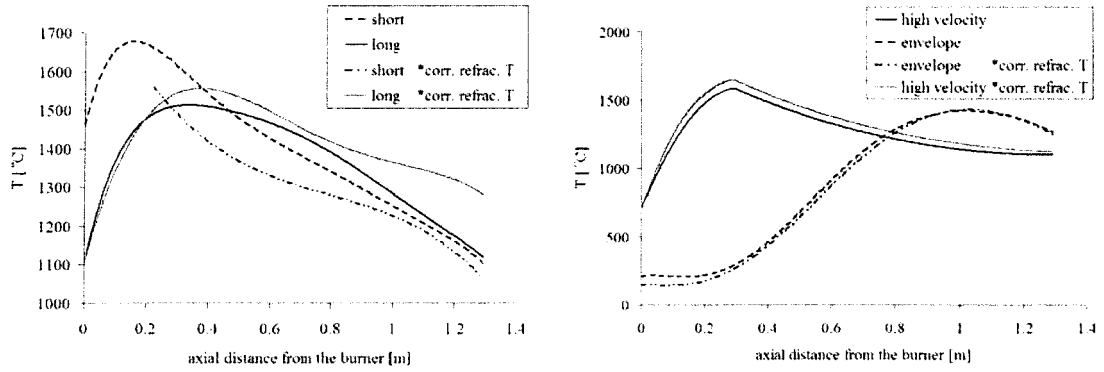

(a) (b)

Figure 3.66. Measured and corrected temperature curves in the centerline of the furnace for the (a) short and long (b) high velocity and envelope flames. Temperatures were corrected for the heat flux measurements in the impingement configuration.

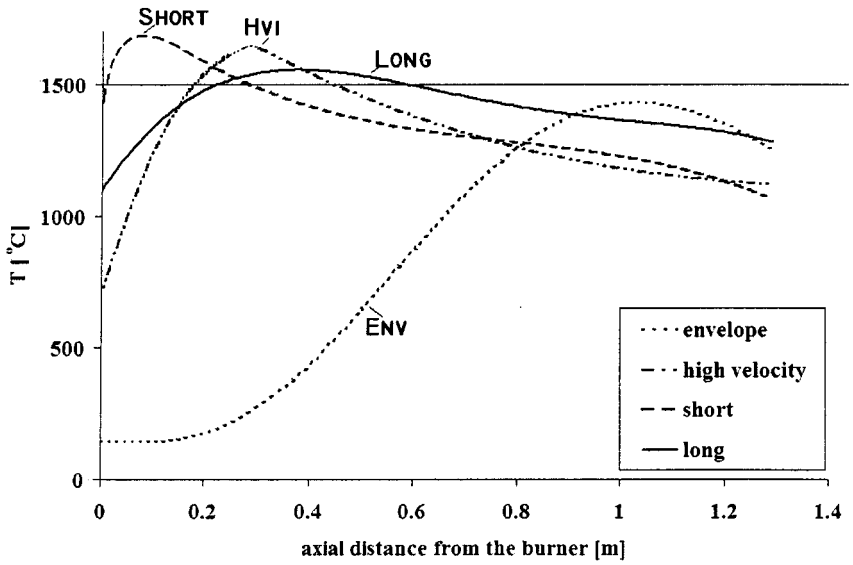

Figure 3.67 Comparison of the centerline-temperature curves of the four studied flame types corrected for the heat flux experiments in the impingement configuration.

3.8 NO_x formation

3.8.1. Analysis and discussion of the experimental results

The gas compositions for various flame types and different burner-target orientations were presented above in this chapter (section 3.4). All the nominative values of the NO_x emission rates given by the burner fabricants refer to the full power mode. Similarly, the measured pollutant emission rates presented in Table 3.1 apply to operations at 100% burner power.

However, the NO_x emission rates were not consequently analyzed at reduced burner powers, some tendencies were observed. For the high velocity flame, the NO_x emission is significantly higher at reduced burner power. After the detailed analysis of the velocity and temperature fields (see section 3.5, see Figure 3.23), the differences in the NO_x formation can be explained. As it was discussed above, the two basic factors that influence the thermal NO_x formation are the flame temperature and the residence time. By reduced burner power, both these factors change to promote the formation of the NO_x in the high velocity flame.

At full burner power, as it is shown in Table 3.1, the highest NO_x emission occurred in the case of the long flame for all flame-target configurations. On the average, the short flame emitted only 80% of the NO_x, produced by the long flame. Although, the maximum temperature is higher in the case of the short flame (Figure 3.67), the difference can be attributed to the smaller flow velocities in the long flame (Figure 3.55). Therefore, the residence time of the dissociated gases in the high temperature zones for the long flame is

longer. In addition, the centerline temperature in the short flame is higher only in the first furnace section (Figure 3.67).

In spite of the higher maximum temperature, the high velocity flame produced only 36% of the NO_x emitted by the long flame. This is again due to the shorter residence time of the gas in the high temperature zone. As it can be seen in Figure 3.12, the nozzle exit velocity in the high velocity flame is more than six times higher than that in the long flame. Finally, the envelope flame produced the less NO_x, only 6% that of formed in the long flame which had the maximal emission in our study. That reason is the low temperature maximum in this flame. Due to the largely expanded volume, as its name indicates, the combustion is less concentrated in the envelope flame. As it can be seen in Figure 3.67, the temperature in the envelope flame never exceeds 1500°C. (see also Figure D.1 in Appendix D)

3.8.2. Numerical calculation of the thermal NO_x formation in the envelope flame

To execute numerical NO_x formation calculations, both the velocity and temperature distributions have to be known. The envelope flame is the only flame where the heat release occurs in the zone, which is accessible for the measurements. Therefore, these numerical computations were only done for the envelope flame using the experimental results obtained in the impingement arrangement. The numerical model is presented in this section.

As it was presented before (Table I.1 in Appendix I.), the natural gas used in the

experiments is composed of more than 95% of methane. Assuming that the composition is 100% of methane, the simplified combustion equation of methane–air mixture with 10% excess air ratio (equivalence ratio $\phi = 0.91$) can be written as follows:

$$CH_4 + 2.2O_2 + 8.27N_2 \longrightarrow CO_2 + 2H_2O + 8.27N_2 + 0.2O_2$$

Eq. 3.10

Evidently, the nitrogen and excess oxygen do not participate in the reaction, they only dilute the reactives. For 1 mole fuel, the overall number of moles of all species in the reactions is: $n_s = 11.47mol$. From the point of view of the thermal NO_x formation, the oxygen and the nitrogen contents are important. This species are present in the following quantities: $n_{O_2} = 0.2mol$, and $n_{N_2} = 8.27mol$.

The general NO_x formation mechanisms are discussed in Appendix D. In our case, only the thermal mechanism is significant, which is also presented in detail in section D.2 of Appendix D. The formation of thermal NO_x is determined by the Zeldovich reaction, according to Eq. D.1, Eq. D.2 and Eq. D.3. Due to the simplifications described in section D.2, it is sufficient to consider only Eq. D.1, which is the rate limiting reaction. If reaction of Eq. D.1 occurs, then two NO molecules will be formed. Thus, the thermal NO formation rate is given by Eq. D.10 as:

$$\frac{d[NO]}{dt} = 2k_{1f}[N_2][O]$$

Eq. 3.11

The kinetics of the thermal NO_x formation rate is much slower than the main hydrocarbon oxidation rate, so most of the thermal NO_x is formed after completion of combustion. Therefore, the thermal NO_x formation process can often be decoupled from the

main combustion reaction mechanism and the NO_x formation rate can be calculated by assuming equilibrium of the combustion reactions. Using this approach the calculation of the thermal NO_x formation rate is considerably simplified. The assumption of equilibrium can be justified by a reduction in the importance of radical overshoots at higher flame temperature[78]. According to Westenberg[79], the equilibrium O-atom concentration can be obtained from the expression:

$$[O] = K[O_2]^{\frac{1}{2}}$$

Eq. 3.12

Substituted K into Eq. 3.12, this expression becomes:

$$[O] = 3.97 \cdot 10^5 \cdot T^{-\frac{1}{2}} \cdot [O_2]^{\frac{1}{2}} \cdot e^{-\frac{31090}{T}} \ [\text{mol/m}^3]$$

Eq. 3.13

where T is in Kelvin.

The mole fraction (molar density) of species i is defined by $X_i = \frac{n_i}{n_s}$. Assuming that the injected excess air is perfectly distributed in the combustion chamber after the combustion is completed, one obtains $X_{O_2} = 0{,}01743$, and $X_{N_2} = 0{,}72106$. Thus, the molar concentrations of nitrogen $[N_2]$ and oxygen $[O_2]$ can be calculated as follows:

$$[N_2] = \frac{X_{N_2} \cdot p}{\Re T}\left[\frac{mol}{m^3}\right]$$

Eq. 3.14

$$[O_2] = \frac{X_{O_2} \cdot p}{\Re T}\left[\frac{mol}{m^3}\right]$$

Eq. 3.15

where p is the absolute pressure. As the furnace is an atmospheric device, p = 101325 Pa.

$\Re$ is the universal gas constant ($\Re$=8314.41 J/(mol K)) and T is the gas temperature in Kelvin.

In the calculation, the temporal fluctuation in species concentration and temperature due to the turbulent mixing were not taken into account.

A computational module was developed to calculate the thermal NO_x formation in the $1cm^3$ size cells. The numerical result is graphically represented in Figure 3.68. On the x-axis, the longitudinal position is represented between the first and last test sections. On the y-axis, the radial distance from the centerline is shown. In the z-axis, the NO concentration is given in the cellules. The sharp, non-linear increase in the NO concentration is very interesting. The values are given in ppm x 10^3. Integration of the results over the entire plane yields to 0.65 ppm. Although the perfect rotational symmetry is disputable, the results were also integrated for a cylindrical volume, as it should be a conventional, rotation-symmetric flame in a non-disturbed space. This gives a result of 11.04 ppm. Recall that the measured concentration was 16 ppm for the same flame at the same configuration. It has to be mentioned again that the envelope flame is not rotationally symmetric and the impingement caused important perturbation.

Correlation between the temperature distribution and the thermal NO_x formation rate in the envelope flame can be observed in Figure 3.69. It can be seen, how strongly the NO_x formation is concentrated in the high temperature zone.

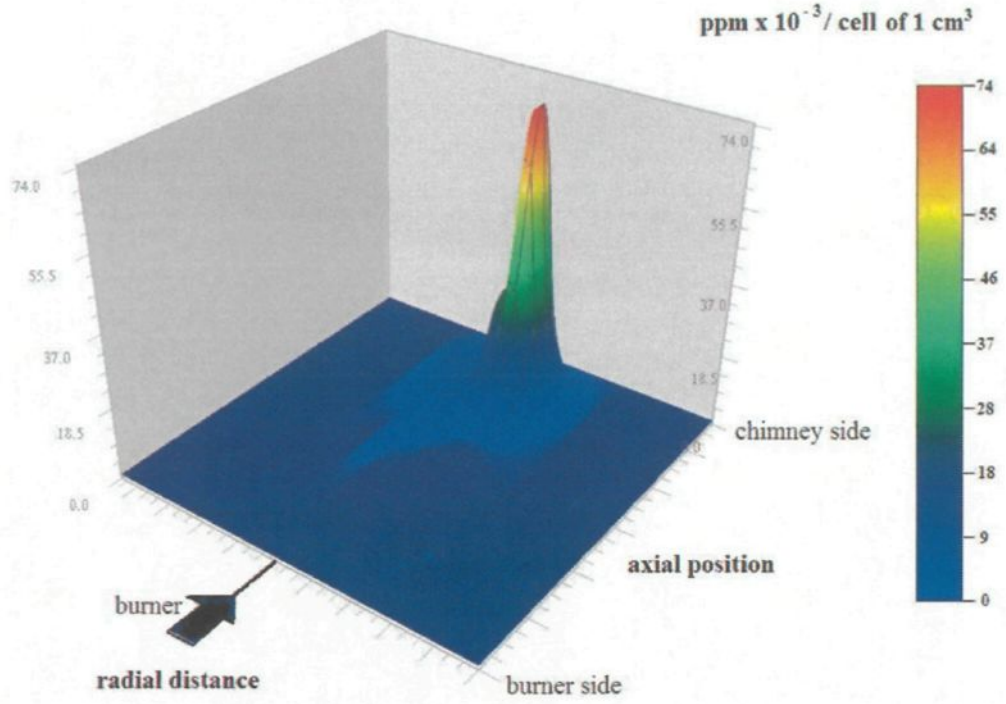

Figure 3.68 Thermal NO_x formation in the envelope flame

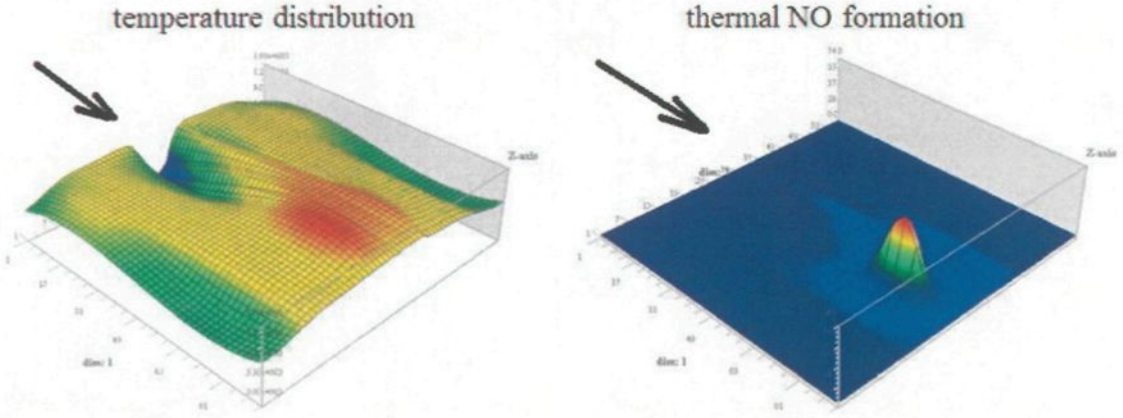

Figure 3.69 Correlation between the temperature distribution and the thermal NO_x formation rate in the envelope flame

In conclusion, the NO_x measurements have shown that the flames produced by the LNI burner produce considerably less NO_x. However, at partial burner power, important

deviations occur. The measured NO_x formation values for all the four studied flame types were validated by the help of the temperature and velocity distributions.

A simplified numerical model was also solved to calculate the thermal NO_x concentration. Sufficient measurement data was only available in the case of the envelope flame. Even in this case, the temperature and velocity distribution have to be known in the entire furnace for more accurate calculations. To compensate turbulence effect, turbulence intensity measurements are also necessary. Still, by the help of this simplified numerical model, the essential tendencies of the NO_x formation can be well seen.

CHAPTER 4.
PRESENTATION AND ANALYSIS OF THE HEAT FLUX MEASUREMENTS

4.1 General overview

In the first section of this chapter, the average heat-flux measurements by the calorimetric method are presented. This section includes the discussion of the energy balance of the furnace in the preheating period and later in quasi-steady state conditions. The results are compared with the predictions of the Sankey diagram.

Subsequently, in sections 4.3, 4.4 and 4.5, the heat flux measurements are presented for the four studied flame types in the parallel firing, inclined and impingement configurations.

Finally, empirical and semianalytical heat transfer calculations are discussed. Calculated results are compared with measurements made in impingement configuration.

4.2 Average heat flux measurements with calorimetry

As it was discussed in the chapter of experimental procedures, an additional insulation had to be applied on the top surface of the calorimetric plates to insure the stability of the envelope flame. With this modification, the ability to measure a very accurate and reliable

average total heat flux data was lost. On the other hand, there are some experimental data available obtained at partial power for the short and long flames from the period when the Fibreflex insulation was not yet installed. Using these data, the overall energy balance of the furnace as well as the verification of the prediction of the Sankey diagram can be made.

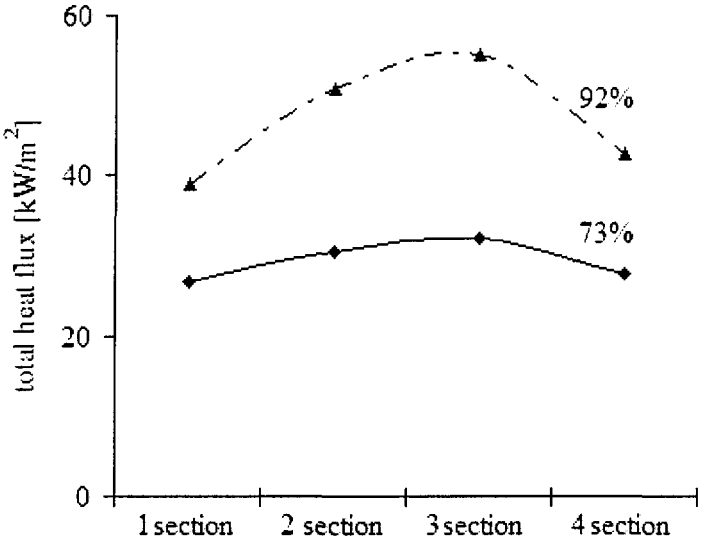

Figure 4.1 Average values per furnace section of the incident total heat fluxes for the long flame at different furnace powers

These results at partial burner power were obtained during the heating-up procedure of the long flame. In this early experiment, the stack-gas temperature was not simultaneously measured. Later, to have an approximate idea of the variation of the stack gas temperatures as a function of the burner power in the heating-up period, all available stack gas data at the given burner power was compared. We were able to establish a linear equation, which correlated the data with a precision of about 20%.

The approximative stack gas temperature as a function of the furnace power is listed in Table 4.1. The firing rate for natural gas is also presented here. Knowing the stack gas

composition, its temperature and the overall flow rate, the heat loss through the chimney can be calculated. The column of Q_{net} is the sum of the incident heat to the load and refractories. This can be obtained by substracting the stack loss from the firing rate. Wall losses were not measured. In the two cases (at 73% and 92% burner power) when calorimetry data are available the wall losses can be calculated. The stack loss, wall loss and effective heat flow results are also presented in percentage relative to the firing rate. In the case of 100% burner power, an almost steady state result is also presented in the last row of this table. As the Sankey diagram (Figure 1.8) is only valid in steady state condition, the data in the last row will be used for comparison.

As it can be seen from the table, when the furnace is already in the heating-up period, the heat removal by the refractories is higher. This is because of the significant heat capacity of the refractories. At nearly steady state condition, the wall loss is about 10%, as it is predicted by the Sankey diagram. However, the effective heat to the load is slightly higher than the prediction of the Sankey diagram. Comparing to a metallurgical furnace, the black painted and very intensively cooled calorimetric plates extract more heat like for example a gray, non-cooled mass of metal scrap.

real furnace power [%]	$T_{stack\ gas}$ [°C]	firing rate [kW]	$Q_{stack\ loss}$ [kW]	Q_{net} [kW]	Q_{load} [kW]	$Q_{refrac.}$ [kW]	stack loss [%]	effective heat to the load [%]	wall loss [%]
47%	535	32.8	7.8	24.97			23.79%		
49%	549	34.1	8.4	25.75			24.50%		
50%	556	34.8	8.6	26.12			24.85%		
53%	583	37.3	9.8	27.50			26.20%		
57%	615	40.2	11.2	29.02			27.80%		
65%	674	45.6	14.1	31.59			30.79%		
73%	730	50.8	17.1	33.70	19.80	13.90	33.65%	39.0%	27.4%
80%	783	55.8	20.3	35.44			36.44%		
83%	809	58.2	22.0	36.18			37.80%		
86%	834	60.5	23.7	36.83			39.13%		
90%	858	62.7	25.3	37.38			40.39%		
92%	880	64.7	26.9	37.83	31.67	6.17	41.56%	48.9%	9.5%
97%	916	68.1	29.6	38.47			43.48%		
100%	937	70.0	31.2	38.78			44.60%		
100%	1000	70.0	33.6	36.39			48.01%		

Table 4.1. Energy distribution in the combustion system during the heating up period and in steady state condition

4.3 Heat transfer at parallel firing arrangement

4.3.1. Presentation and discussion of the results

The results of the heat flux measurements for parallel firing arrangement are presented below in Figure 4.2 to Figure 4.5. The upper curves are the total heat flux distributions while the lower ones represent the convective contribution to the total heat transfer.

There are certain common features in the four graphs. The convective part of the total

heat transfer is between 15-20 % for all the tested flames. Neither the geometric characterization of the flames as "short" or "long", nor their flow properties like "high-velocity" influence significantly the contribution to the total heat transfer by direct flame-to-object convection.

The second important feature is that the amount of the total heat transfer as well as the character of its longitudinal distribution does not vary much. The character of the heat flux distribution is more characteristic to the burners than to the flames. This was a surprising discovery, considering that the traditional burner produced a short and a long flame that were visually different. The visual difference between the two flames is also distinct in the case of the LNI burner: the jet of the hot combustion gases can be seen very well in the high-velocity setting, while the envelope flame in the injection mode is hardly visible.

The visible difference between the two flames produced by the conventional burner is even more pronounced than in the case of the LNI burner. In the long-flame setting a long, intensive yellow luminous zone can be seen, while the luminosity of the short flame is practically negligible. The discrepancies, as it was presented in the previous chapter, can be attributed to the dissimilar mixing conditions, caused by the differencies in the gas inlet geometry.

We could not find a convincing result to demonstrate the effect of the luminosity of a flame and its total radiative power. Our measurements of the visible radiation were not conclusive as we were not able to effectively suppress the background radiation and measurement noise. Further efforts are needed to obtain reliable quantitative results, but we do not expect to find very important differences among the radiation power of the four

already studied flames. It is very likely that for a sensible increase of the emissivity of the flames one must increase drastically the solid particle content in comparison to the present levels.

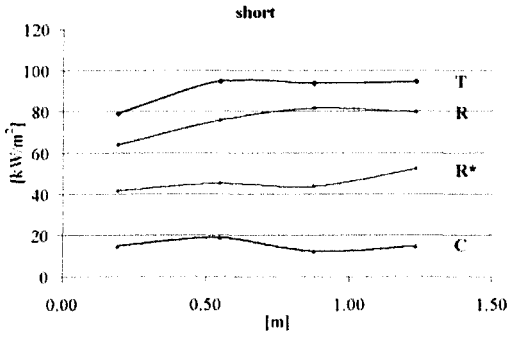

Figure 4.2 Longitudinal distribution of the total, radiative and convective heat fluxes under a so-called "short-flame"

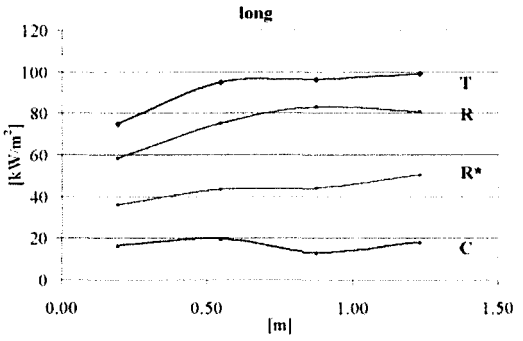

Figure 4.3 Longitudinal distribution of the total, radiative and convective heat fluxes under a long, luminous flame

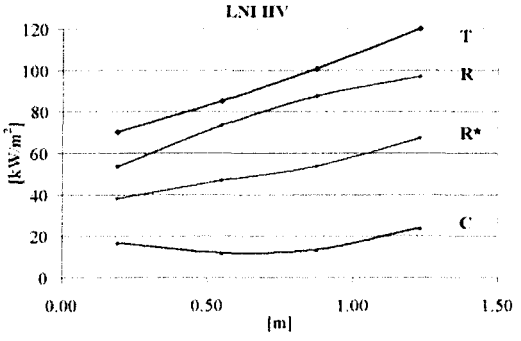

Figure 4.4 Longitudinal distribution of the total, radiative and convective heat fluxes under a low-NO_x burner in high-velocity mode.

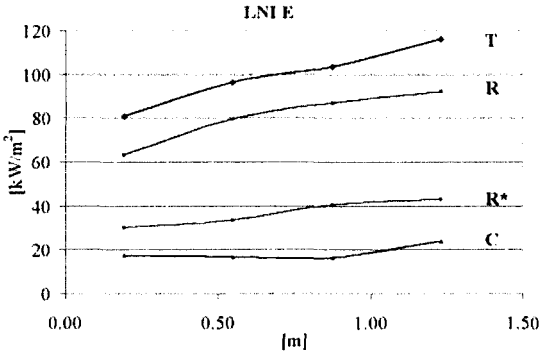

Figure 4.5 Longitudinal distribution of the total, radiative and convective heat fluxes under a low-NO_x burner in injection mode (envelope flame).

As it was discussed above (see Figure 1.7), the radiative heat transfer toward the cooled bottom of the furnace has a direct flame-object component and another indirect one from the refractory. In the Figure 4.2 to Figure 4.5, two radiative flux profiles are given: the

upper curve (marked R) represents the total radiation, while the lower one, marked R*, represents the direct flame-object radiative transfer. It must be noted that the indirect radiation is function of the temperature level inside the furnace so it depends on the operating conditions. The splitting of the total radiation into direct and indirect components by the simple experimental tests and calculations we used has an approximate character (see section E.3.3 of Appendix E). The common tendency is that under the given experimental conditions, the direct radiation from the flames is responsible roughly for about half of the total radiative heat transfer toward the target.

In order to emphasize more strongly the character of the variation of the heat flux components along the length of the furnace, we have normalized the distributions and plotted them in Figure 4.6 to Figure 4.8. The differences among the convective heating patterns produced by the different flames cannot be seen very well in the diagrams in Figure 4.2 to Figure 4.5 as their absolute value is very small within the total flux. By projecting all components of the heat flux to the same scale between 0-1.0 by normalizing them with respect of their own maximum value along the length, the individual differences can be easier detected.

The first important feature is that there is a similarity between the flames produced by the same burner. The character of the curves of the total, radiative and convective fluxes shows similar trends for the short and long flames (conventional burner) and for the high-velocity and envelope flames (LNI burner).

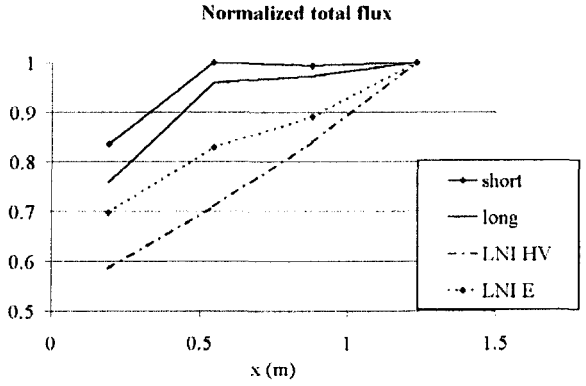

Figure 4.6 Total heat flux normalized by the maximal value along the length

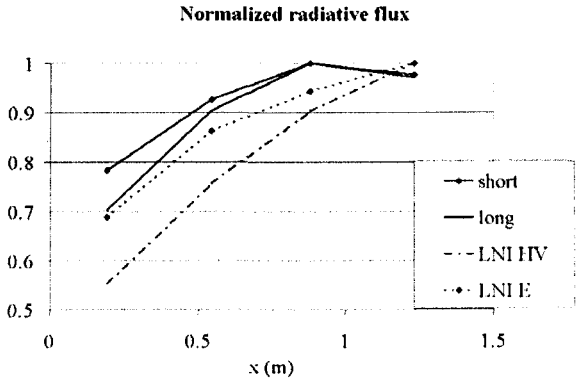

Figure 4.7 Distribution of the normalized total radiative flux along the length

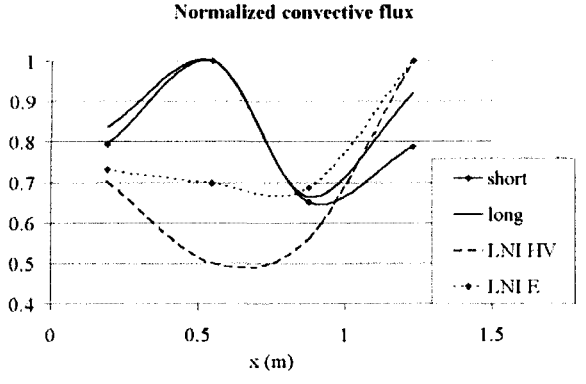

Figure 4.8 Distribution of the normalized convective flux along the length

The differences are the most pronounced between the shapes of the convection profiles

of the two burners. We explain the local maximum at first third of the furnace length in the case of the conventional burner by the presence of a recirculation zone there (see section 1.1.2). The spatial resolution of the heat flux measurements is low; we obtained only four points along the total length. For this reason, the apparent coincidence of the maximal convection rate for the short and long burner can be merely a result of curve fitting.

However it can be determined that both flames produce the most intensive convection in the first half of the furnace while the high-velocity and envelope flames have their maximum at the end of the furnace. Both flames from the LNI burner are very much elongated and they produce a swirling back flow at the zone of flue exit.

Another feature of the convective heat flux pattern requires further explanation. One argument for promoting of the high-velocity flame technology is that it increases convective heat transfer. However as Figure 4.4, Figure 4.5 and Figure 4.8 show, both the absolute values and the normalized, relative values demonstrate that the high-velocity mode produces less convection than the envelope mode. The explanation is that while it is true that there is a high velocity gas stream along the centerline of the burner, that high velocity zone is relatively far from the surface of target – the floor of the experimental furnace – and the movement is parallel and relatively ordered. This ordered, parallel movement produces less energy transport toward the surface to be heated than the randomly fluctuating, highly turbulent gas in the envelope flame. Also, the heat source is localized into the narrow jet in the case of the high velocity burner while it is nearly uniformly distributed in the whole volume of the envelope flame. All that said, it must be noted that the role of convection is too weak in all four cases to serve as a base of comparison for the overall heating

performance of the flames.

The overall heat transfer toward the horizontal target was nearly identical for the flames except the envelope flame that transferred about 8-10 % more energy to the object than the others. Although the differences between the other three flames were within the zone of measurement uncertainty, the short flame produced consequently the lowest heat transfer rate.

4.3.2. Conclusion of the results at parallel firing configuration

The conclusions of the experiments at parallel firing configuration are listed next:

1.) In the tests performed in the reverbatory-type experimental furnace, the differences in the heating patterns of the four flame types are minimal. The refractory lining has an equalizing effect, ironing out small variations in the distribution of the direct convective and radiative fluxes.

2.) For all flame types tested, the radiative heat flux represented about 80 % or slightly more of the total heat flux, the convective portion representing maximum 20 %.

3.) Within the radiative flux, the direct portion between flame and object is roughly equal to the indirect radiation from the refractory walls.

4.) In comparison to the other flames in the study, the envelope flame increased the total heat flux slightly. The increase is about 8-10 % over the normal short medium velocity type flame.

The majority of energy transferred to the charge is radiative energy and adjustments to

the velocity of the gases exiting the burner are limited to variations on the convective portion of the heat transfer that has a minor effect on the overall energy transfer over the melt operation.

The 4th conclusion supports anecdotal and preliminary test results of new direct fired melting furnaces in which envelope flame type burners with regenerative burner technology have been installed. It must be pointed out that the envelope type flame was in fact developed to reduce the NOx formation while maintaining the benefit of very high temperature preheated combustion air. The benefit of high air temperature preheating on energy conservation would have been lost if the NOx emission standards were to be met.

4.4 Heat transfer at burner inclination

4.4.1. Presentation and analysis of the results

In this experimental series, the burner was tilted at 11.4° downward from horizontal, as shown in the Figure 2.1. As it can be observed in the figure, the flame hits the calorimetric plates. This flame-object impingement point is located about the centerline of the furnace, between the second and third furnace sections. Unfortunately, the distance of the neighbouring sensors to this impingement zone is relatively large, due to the low spatial resolution of the heat-flux measurement points.

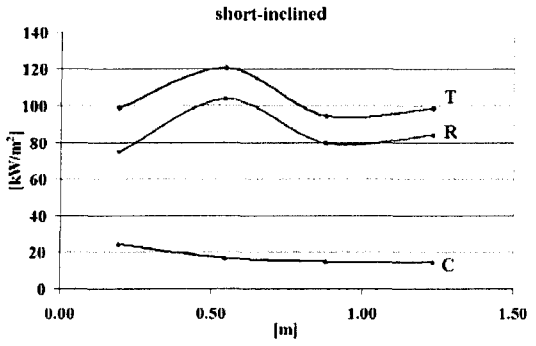

Figure 4.9 Distribution of the total, radiative and convective heat fluxes under the short-flame, by inclined burner setup.

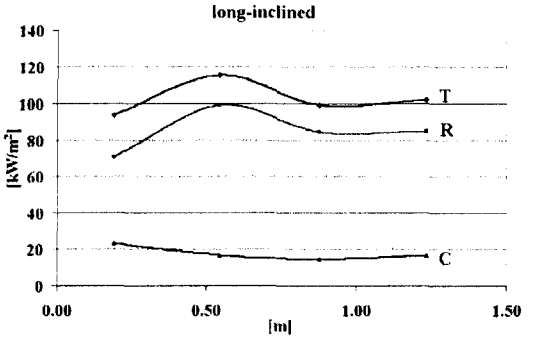

Figure 4.10 Distribution of the total, radiative and convective heat fluxes under the long flame by inclined burner setup.

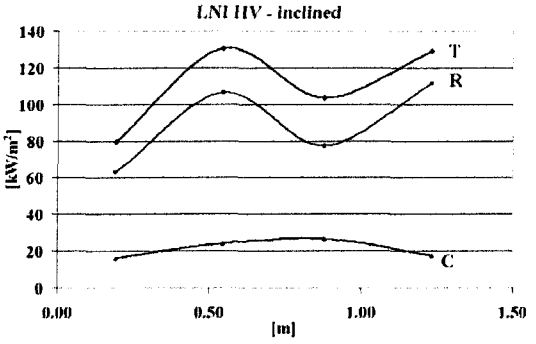

Figure 4.11. Distribution of the total, radiative and convective heat fluxes under the high-velocity flame produced by the LNI burner for inclined burner configuration

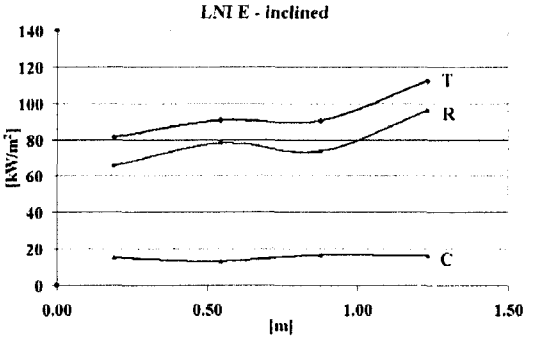

Figure 4.12. Distribution of the total, radiative and convective heat fluxes under the envelope flame produced by the LNI burner in injection mode for inclined burner configuration

The results of the heat flux measurements by inclined burner setup are presented above in Figure 4.9 to Figure 4.12. As it was concluded above for parallel firing configuration, the character of the heat flux distribution is more characteristic to the burners than to the flames. This is also justified by the inclined results in the case of the short and long flames. Observing the longitudinal heat-flux distribution under these flames produced by the conventional burner (Figure 4.9 and Figure 4.10) the similarity is obvious. On the other

hand, the differences between the measured heat fluxes under the high velocity and envelope flames are more pronounced at inclined burner setup. These two flame types are so much dissimilar that the differences in heat fluxes were expected. As it was discussed in section 3.5, the LNI burner in high velocity mode produces an ordered, high-speed gas jet along the centerline of the burner, which strikes at the calorimetric plates. On the contrary, the same burner in injection mode produces the so-called envelope flame, which does not have a definite orientation. Thus, the burner configuration does not influence significantly the heat-flux distribution.

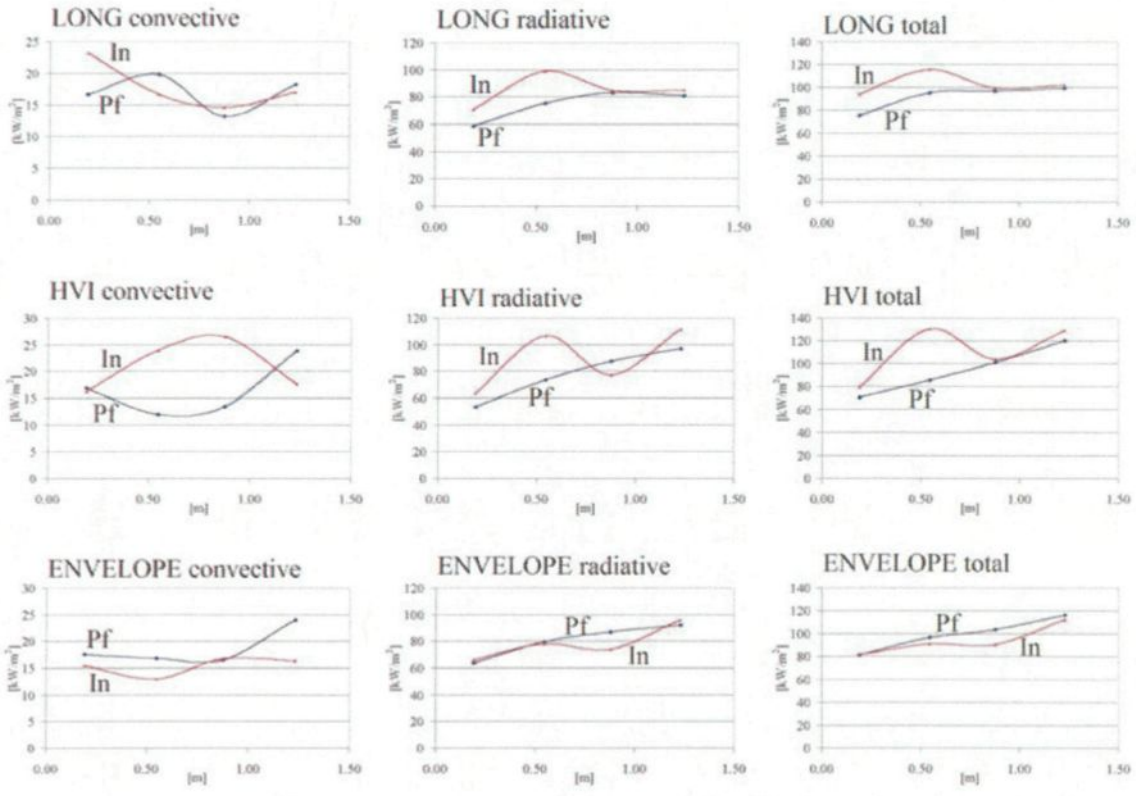

Figure 4.13. Comparison of the convective, radiative and total heat flux curves along the furnace centerline under the long, the high velocity and the envelope flames for parallel firing (Pf) and inclined burner position (In)

The comparaison of the heat flux curves between the parallel firing and inclined arrangements are shown in Figure 4.13 for the long, the high velocity and the envelope flames. In this figure, only the long flame among those produced by the conventional burner is presented because the heat flux distribution of the short and long flames resemble each other very nearly for both parallel firing and inclined configurations.

As presented in Figure 4.13, in the case of the short and long flames at inclined burner setup the convective heat flux is slightly higher in the first section of the furnace. The radiative and total heat fluxes are higher in the entire first half of the furnace (1 and 2 sections). On the other hand, in the rear half of the furnace, the differences in the heat fluxes between the various configurations are negligible for all heat flux components. In effect, for inclined configuration, the energy-transfer toward the charge raised by as much as 20% in the first half of the furnace. On the contrary, no significant variation can be detected in the rear half of the furnace.

At inclined burner setup, in the case of the high velocity flame, the convective heat flux increased by 100% in the central furnace sections. In the second furnace section, the radiative heat flux has also change significantly. Finally, as a result, the total heat flux at inclined configuration was higher in the second furnace section by as much as 50%. On the contrary, the total heat flux does not change at all in the other furnace sections.

The burner tilting has less influence on the envelope flame. The total heat flux distribution has changed only slightly, by 10% in the third section of the furnace. However, in all the cases discussed previousely, burner tilting intensified the heat transfer toward the target, while in the case of the envelope flame the transferred energy decreased.

4.4.2. Conclusions of the burner tilting

The conclusions of the experiments at inclined burner setup are listed next:

1.) Burner tilting resulted in higher convective and total fluxes in the impingement zone. The effect was intensified with higher flame velocities.

2.) The inclination practically did not effect the heat flux distribution for the envelope type flame.

3.) Burner inclination resulted in 100% higher convective heat fluxes in the proximity of the direct impingement point for the high velocity flame.

4.5 Heat transfer with the step- impingement arrangement

While the only difference between the parallel firing and inclined configurations was the burner tilting, the impingement arrangement has important differences in comparison to the first two configurations. Beyond the well-seen modification in the geometric configuration of the calorimetric plates, also the material of the plates, the concept of their water cooling channels, the position of the heat-flux sensors, the thickness of the Fiberfrax insulation on the plates as well as the concept of the heat-flux sensors were modified. The details of these devices, the reasons and advantages of the effectuated modifications were all presented in the section 2.3.4 (Transformation of the experimental furnace) in CHAPTER 2. The sketch of the transformed furnace and the technical design of the new plates were presented in Figure 2.2 and in Appendix L.

The measured total, radiative and convective heat fluxes for the four studied flame types in the impingement arrangement are presented in Figure 4.14 to Figure 4.17. The

thick solid lines represent the total heat flux distributions, while the thin solid lines and the dashed lines show the radiative and convective contributions to the total heat transfer respectively.

The split in the curves corresponds to the vertical step formed by the calorimetric plates 0.7 m from the burner mouth. The left part of the curves - between 0 and 0.7 m – show the sensor readings on the hearth (first and second calorimetric plates) except the last point which is already on the vertical plate at the height of 108 mm. The last point is also rotated by 90° from the horizontal. The right side of the curves between 0.7 and 1.4 m includes the results of the sensors along the calorimetric plates at the elevated position (height of 244 mm from the bottom – third and fourth plates) except the direct impingement point which is on the chamfered edge of the vertical plate. This point is rotated by 45° from the horizontal.

4.5.1. Comparison of the measured heat fluxes at the stagnation point

The experimental heat flux data in the impingement point are presented in Table 4.2, and the heat flux curves are shown in Figure 4.14 to Figure 4.17.

The total and radiative heat flux curves have prominent peaks at the impingement point for all the flames studied. The convective heat flux has its maximum in the impingement point for the flame with high impact velocity like the high velocity flame, while the increase of the local convective exchange is less for the short and long flames and it is practically non-detectable in the case of the envelope flame. As we have already seen above, the distributed character of the combustion zone in the volume of the furnace and

the nearly isotropic velocity fluctuations do give rise to a concentrated and well-directed convective transfer.

In the impingement point, there is a direct contact between the flame and the object. Because the impingement occurs at the corner of the solid charge, the flame bifurcates into two separate streams. The lower half of the stream turns downwards along the vertical plate then it is redirected toward the burner where it meets the hot combustion products. The second half of the separated stream continues its horizontal travel along the horizontal upper surface of the calorimetric plates in elevated position in the rear sections of the furnace. A boundary layer develops as the hot gas slows and cools down in the proximity of the surface. As a general tendency, the heat flux curves show a decreasing character both forwards and backwards* from the impingement point.

The highest value of the total heat flux for the whole range of the studied cases occurred for the high velocity flame (Figure 4.16 and Table 4.2) at the impingement point with the value of 226 kW/m^2. It is very interesting that in the direct impingement point of the high velocity jet flame, the radiative contribution to the total heat flux is greater than the convective part. Furthermore, it occurs also in this point that the relative contribution of the convective heat flux to the total is the smallest, with a percentage of 46 %. Even so, it was the absolute highest measured convective heat flux for all cases studied (104 kW/m^2).

The fact that besides the convective heat transfer rate, the radiative flux also shows a

---

* forwards and backwards means in the axial direction from the burner that corresponds to right and leftward in Figure 4.14 to Figure 4.17; backward flow: recirculation, counter moving under the main stream toward the burner at the bottom of the furnace

maximum in the impingement point needs explanation. The impingement point was represented in the setup by a 45° narrow flat surface (chamfer) looking simultaneously toward the hot refractory ceiling (Figure 3.64.e) and the hottest gas mass in the flame. This way both the direct flame-object radiation and the indirect radiation contribute to the radiative sensor readings in that point.

The envelope flame (Figure 4.17 and Table 4.2) has a total heat flux of 186 kW/m^2 and the convective part is the smallest among the four flames, only 38 %. As already shown above, this flame does not produce a convective peak in the impingement point. There are non-monotonic variations in both the convective and radiative heat flux curves. However, the intensity of the distribution of convection is not far from uniform as a consequence of the nearly homogeneous velocity field and isotropic fluctuations.

Flame type	sensor position	axial distance from the burner nozzle [m]	x/dn	convective heat flux [kW/m2]	radiative heat flux [kW/m2]	total heat flux [kW/m2]
high velocity flame	impingement point	0.775	20.39	104.03	121.87	225.90
envelope flame			20.39	71.37	114.75	186.12
short flame			6.57	77.15	88.37	165.52
long flame			6.57	73.50	109.04	182.54

Table 4.2 Experimentally measured heat fluxes in the impingement point

In the case of the short (Figure 4.14 and Table 4.2) and long (Figure 4.15) flames, the total heat flux in the impingement point is 166 kW/m^2 and 183 kW/m^2 respectively. Their convective contributions amount to 46.6 % and 40 % respectively. Both the radiative and convective curves have a noticeable peak in the impingement point. Comparing the general character of the curves of the short and long flames, the similarity is eye-catching; on the

other hand, there are differences in the proportions of the convective and radiative fluxes.

If the conception of the "relative peak" is introduced, the heat flux peak in the impingement point can sensibly be compared. Under "relative peak", the prominence of the heat flux curves at the impingement point in comparison of the neighbouring values is meant. For determining the average heat flux of the neighbouring sensors, we do not count the resulting heat flux of the sensor on the vertical plate at the height of 108 mm rotated by 90° from the horizontal.

In the case of the short flame, the relative peak in the radiative curve is almost three times higher than the peak in the convective one. The comparative values are given in Table 4.3 for all the four different flame types. In the case of the long flame, the relative radiative peak is less important as it was for the short flame; it is slightly more than 2 times as high as for the convective curve. The relative peak of the convective heat flux in the impingement point is 28 kW/m^2. This is two times as high as the second highest value, which occurs in the case of the long flame. The relative convective heat flux peak is close to zero for the envelope flame (Table 4.3). Negative heat-flux peaks could be measured in the case of impinging cold air jet, while positive peaks could denote the presence of active combustion zones.

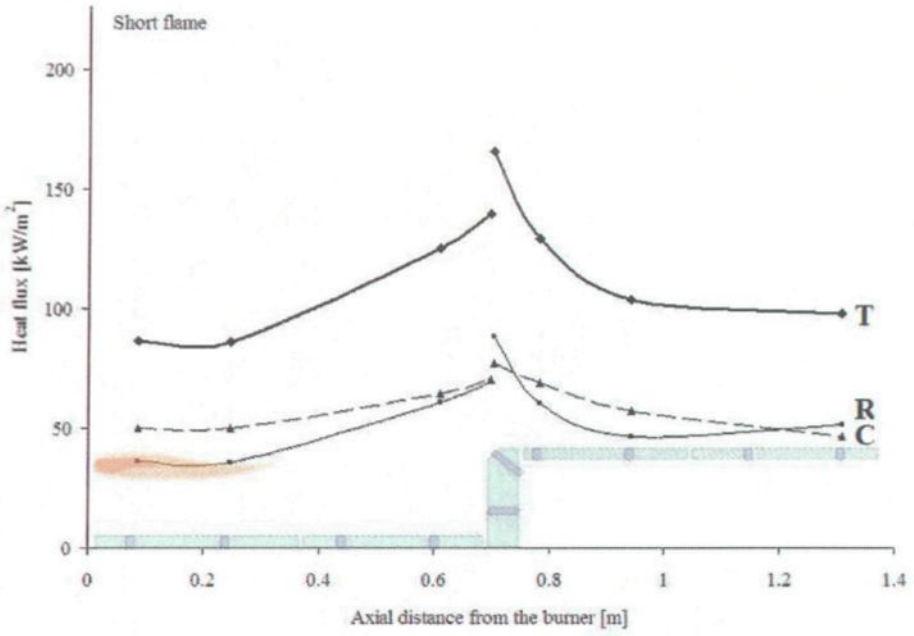

Figure 4.14 Total, radiative and convective heat flux under the short flame at impingement configuration; (T) total, (R) radiative, (C) convective heat fluxes

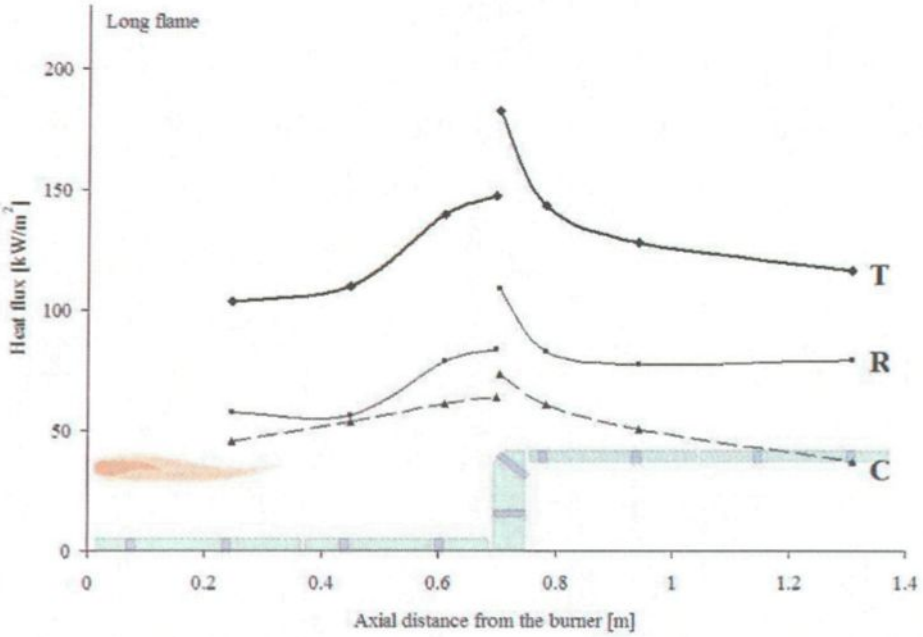

Figure 4.15 Total, radiative and convective heat flux under the long flame at impingement configuration

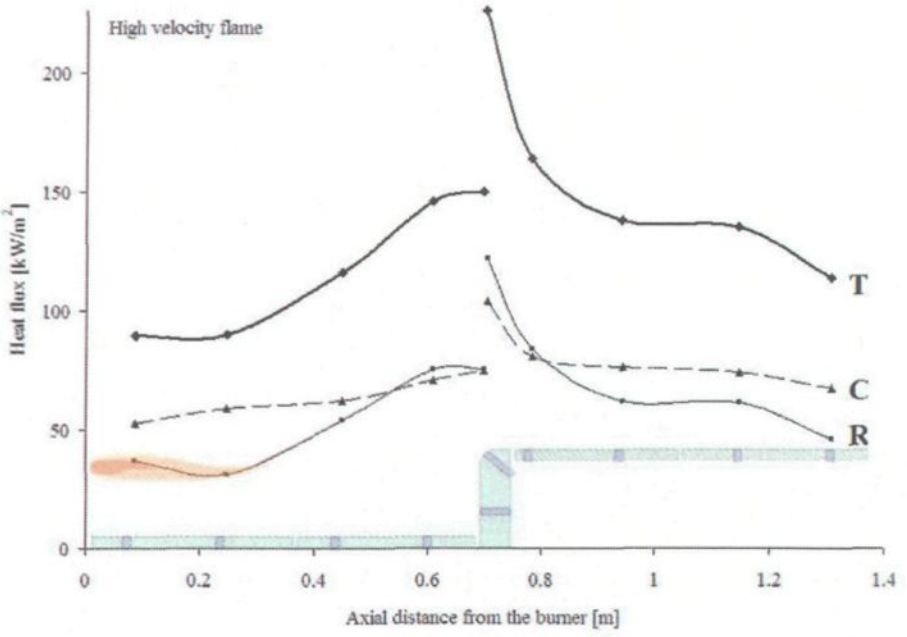

Figure 4.16 Total, radiative and convective heat flux under the high velocity flame at impingement configuration

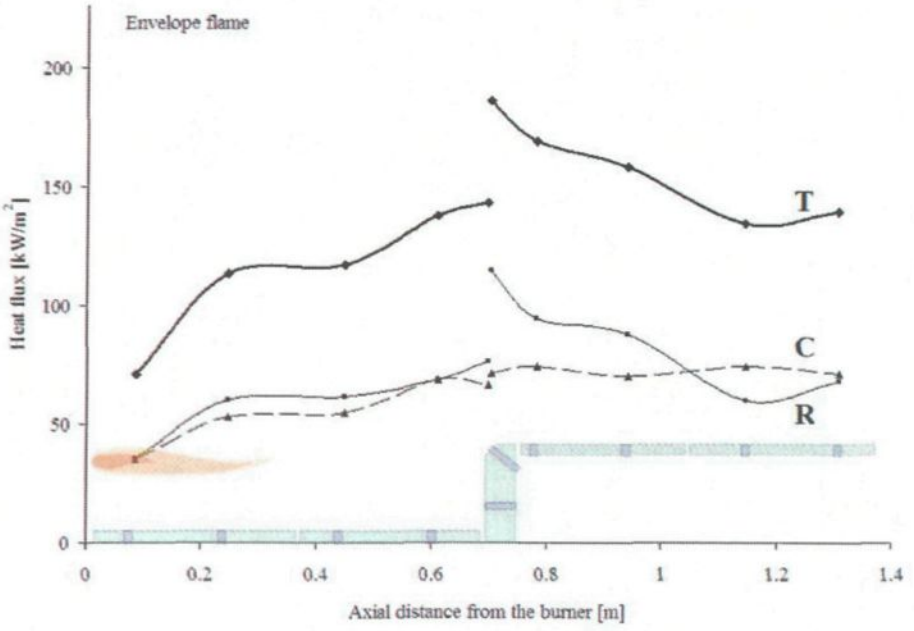

Figure 4.17 Total, radiative and convective heat flux under the envelope flame at impingement configuration

heat flux [kW/m^2] / flame types	relative peaks on the convective heat flux curves in the impingement point	relative peaks on the radiative heat flux curves in the impingement point	relative peaks on the total heat flux curves in the impingement point
short flame	10.61	27.78	38.39
long flame	12.65	28.40	41.05
high velocity flame	28.48	42.36	70.84
envelope flame	-0.14	32.99	32.86

Table 4.3 Prominence of the convective, radiative and total heat fluxes at the impingement point from the two neighbouring measurement points, not counting the results of the vertical plate.

4.5.2. Comparison of the measured heat fluxes along the centerline of the furnace

In Figure 4.18, Figure 4.19 and Figure 4.20 the convective, radiative and total heat fluxes are compared for the four flame types. The solid lines without and with markers are the short and the long flames respectively produced by the traditional burner. The dotted lines without and with markers are the high velocity and the envelope flames respectively, produced by the LNI burner. It is well seen in Figure 4.18, that the highest convective heat flux is produced by the high velocity jet flame everywhere in the furnace and its peak in the impingement point is outstanding. In the case of the envelope flame, it is remarkable that in the rear furnace sections the convective heat flux is not decreasing toward the chimney as it happens with the other flames. Except the peak in the impingement point, the high velocity jet flame and the envelope flame give similarly high convective rates. However the mechanisms are different. In the envelope flame, the gas temperature increases steadily in this active combustion zone, as it is presented in Figure 3.66(b) or in Figure 3.67. The elevated gas temperature together with the intense random fluctuations results in the high

average convective heat fluxes.

For the short and long flames, the convective heat transfer is less important than for the two flames produced by the LNI burner. The similar characteristics of their convective heat flux curves can be observed again.

The average values of the convective contributions to the total heat flux for all the measurement points in the furnace centerline are given in Table 4.4. The highest proportion, 54 %, belongs to the high velocity flame. In the light of the differences in the fluid dynamics between the studied flame types, this result could be easily expected. The average values for the short, envelope and long flames are respectively 52 %, 47 % and 41 %. From these results, we can conclude that the most intensely radiating flame is the long luminous flame while the second one is the envelope flame (Figure 4.19). The visible difference between these two flame types is very characteristic: the long flame is a very luminous flame while the envelope flame is hardly or never visible. Analyzing the refractory temperatures in Figure 3.64.e. and f, one can see the remarkable differences between the two flame types. The envelope flame produces 200-300°C higher refractory ceiling temperatures and even for the side walls (not shown here) the difference is about 50 to 150°C. The conclusion is that in the case of the envelope flame, the important radiative contribution is owing to the refractory, while in the case of the long luminous flame, this is the effect of the elevated gas radiation

It is surprising how the total heat flux curves iron out the particular details of the convective and radiative curves. In almost every case, an elevated radiative transfer is associated with less convective contribution in the same axial position and vice-versa.

Therefore, the differences existing in either the convective or the radiative heat flux are finally attenuated in the total heat flux curves.

	average convective heat flux [kW/m^2]	average radiative heat flux [kW/m^2]	average total heat flux [kW/m^2]	average convective contribution to the total heat flux [%]	average radiative contribution to the total heat flux [%]
short flame	60.52	56.06	116.57	52.59%	47.41%
long flame	55.67	78.09	133.76	41.70%	58.30%
high velocity flame	72.07	64.69	136.76	54.04%	45.96%
envelope flame	64.03	72.80	136.83	47.35%	52.65%

Table 4.4 Statistics of the average heat fluxes in the furnace centerline and their average contribution to the total heat flux in percent by impingement arrangement

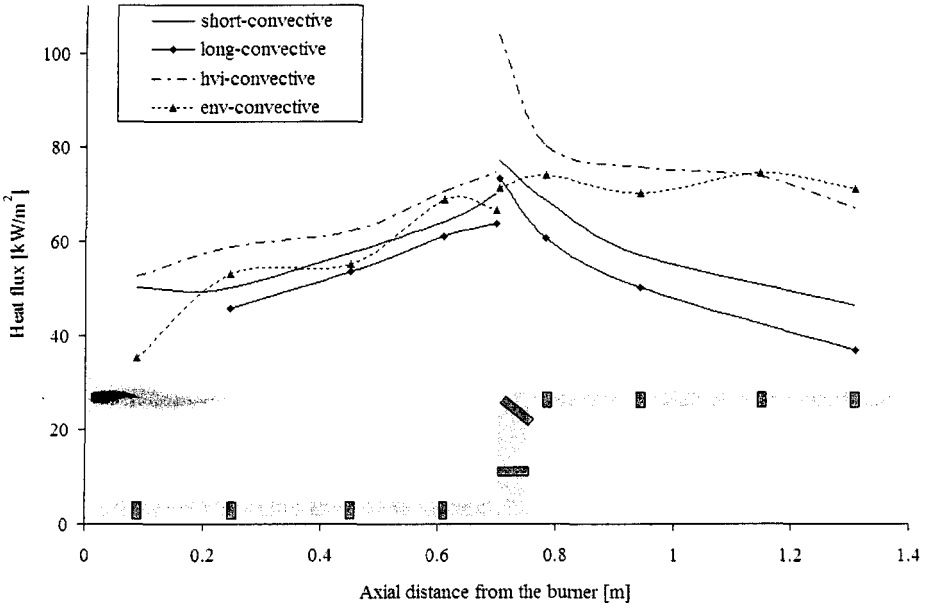

Figure 4.18. Measured convective heat fluxes under the four studied flame types at impingement arrangement

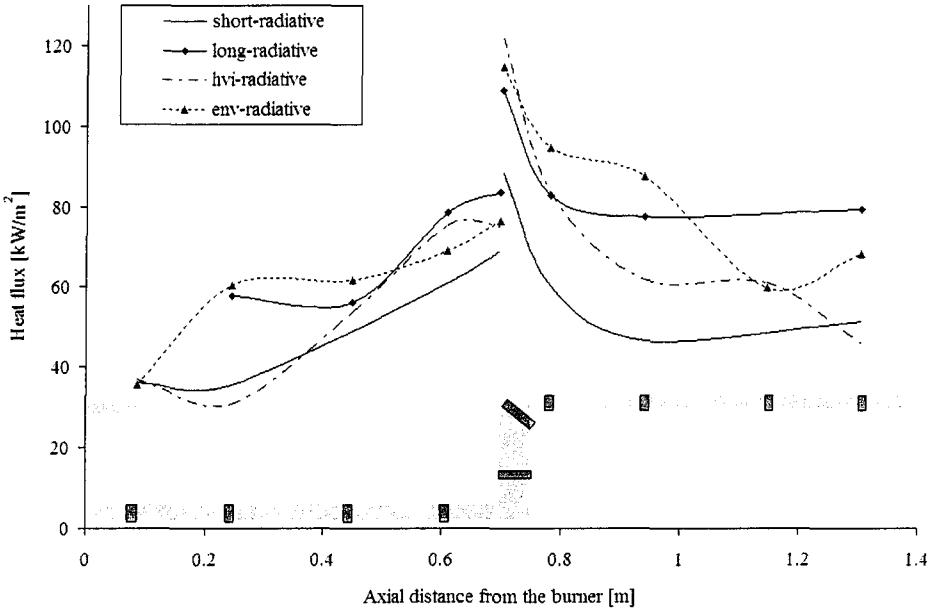

Figure 4.19. Measured radiative heat fluxes under the four studied flame types at impingement arrangement

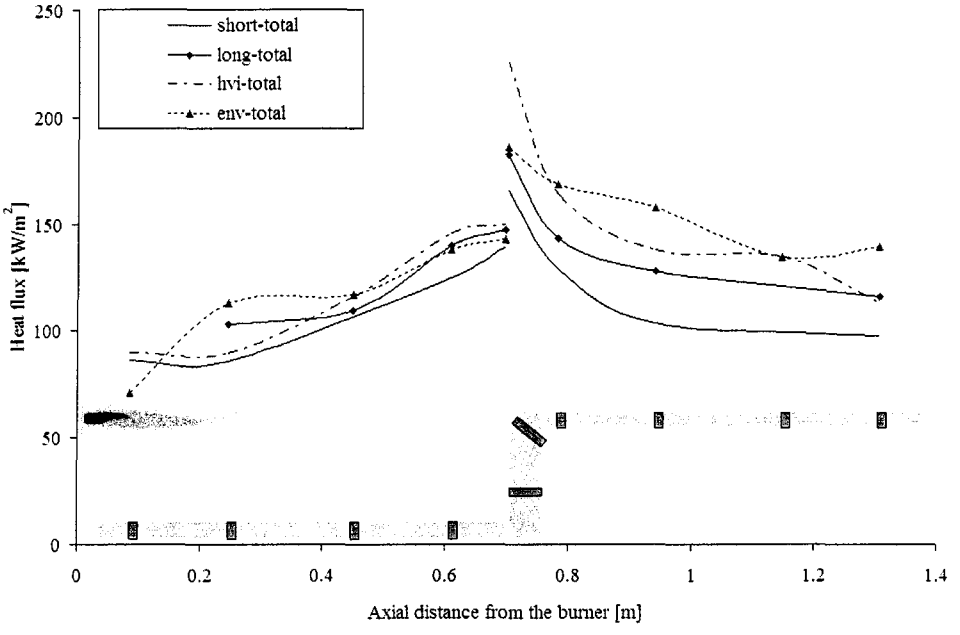

Figure 4.20. Measured total heat fluxes under the four studied flame types at impingement arrangement

4.5.3. Comparison of the heat fluxes between the impingement and the parallel firing configurations

In Figure 4.21 to Figure 4.24, the above presented heat flux results are compared with the results for parallel firing configurations and for the same four flame types. The thick solid lines, the thin straight lines as well as the dashed lines are the total, radiative, and convective heat fluxes respectively; the lines with markers show the impingement results while the curves without marker correspond to the parallel firing.

The increase of the convective contribution to the total heat flux, compared with the parallel firing results, is very significant for all the tested flames. While in the case of the parallel firing arrangement, the convective contribution is between 15-20 %, in the case of impingement configuration this contribution lies in the range of 30 to 66 %.

Comparing to the parallel firing arrangement, the total heat fluxes are increased significantly around the vertical plate (impingement zone) for all flame types. The smallest change in the total heat flux curve occurs for the short flame. The general tendency is an increase in convective heat fluxes and a decrease in the radiative ones. However, the increase in the convective heat fluxes is more important than the reduction in the radiative heat flux.

An important finding is that the convective transfer for the short and high velocity flames (with few exceptions like the impingement point and the rear furnace section for the short flame) slightly exceeds the radiative part Figure 4.21 to Figure 4.24). This is a very important difference in the heat flux distributions between the parallel firing and impingement configurations. Contrarily to the short and high velocity flames, in the case of

the long luminous flame, the radiative part of the total heat flux remains dominant along the whole furnace length (Figure 4.15), however the partition of the convective and radiative fluxes changed from 20–80 % to 40 – 60 %. In the case of the envelope flame, the convective contribution is also increased. In the first furnace section, the convective and radiative contributions share 50% - 50%, however, excepting one measurement point the radiative part remained most important in the rear furnace sections.

When analyzing our results for the parallel firing arrangement, we arrived to drastically different conclusions. There we found that in spite of the visual difference between the short and the long luminous flames, the radiative transfer is similar. It must be noted that in the case of the parallel firing configuration due to the relatively greater distance between the flame and the object, the structural differences between the various flame types were not so much noticeable in the heat exchange. The distant parallel movement was far from the calorimetric plates located at the furnace hearth to influence significantly (more than the proportion of 20%) the convective heat transfer just above the sensors.

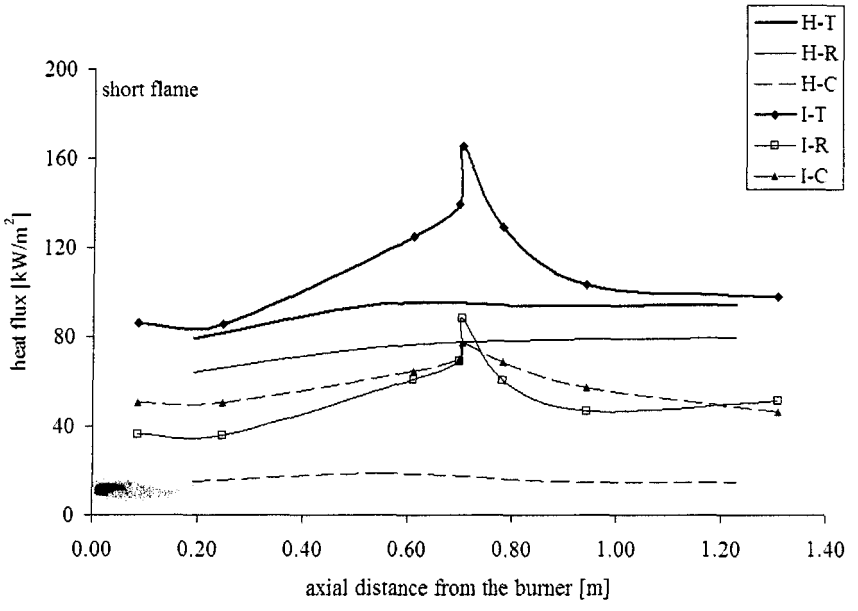

Figure 4.21. Comparison of the measured heat fluxes between the parallel firing and impingement configurations for the short flame; (H) parallel firing, (I) impingement; (T) total, (R) radiative, (C) convectiv

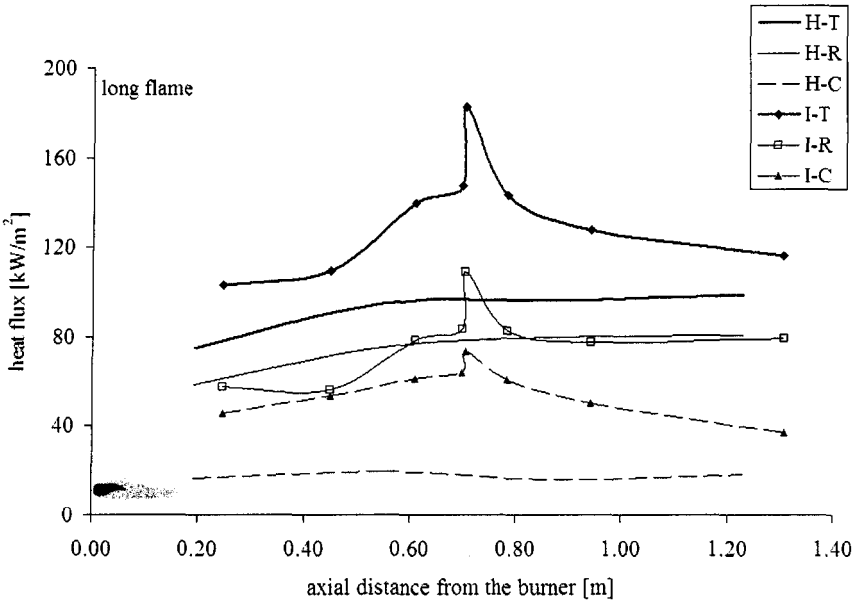

Figure 4.22 Comparison of the measured heat fluxes between the parallel firing and impingement configurations for the long flame

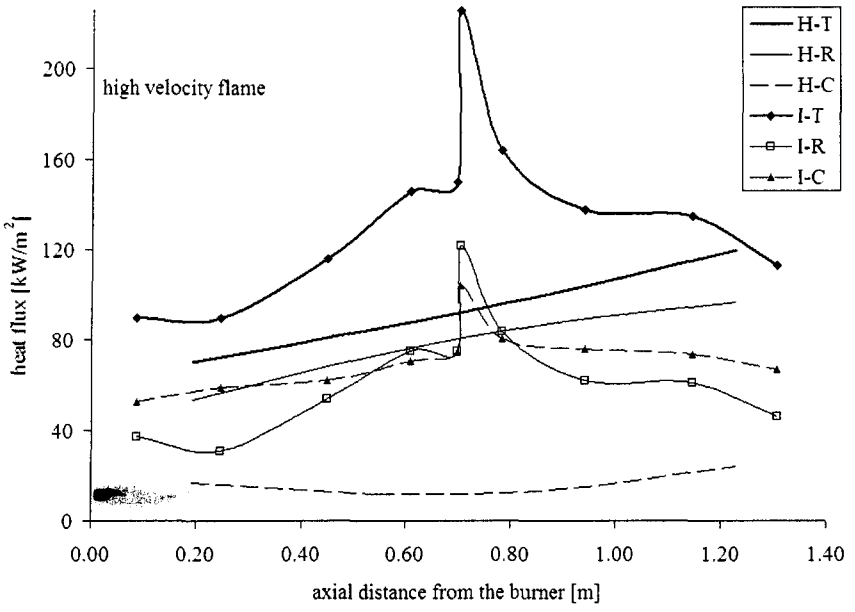

Figure 4.23 Comparison of the measured heat fluxes between the parallel firing and impingement configurations for the high velocity flame

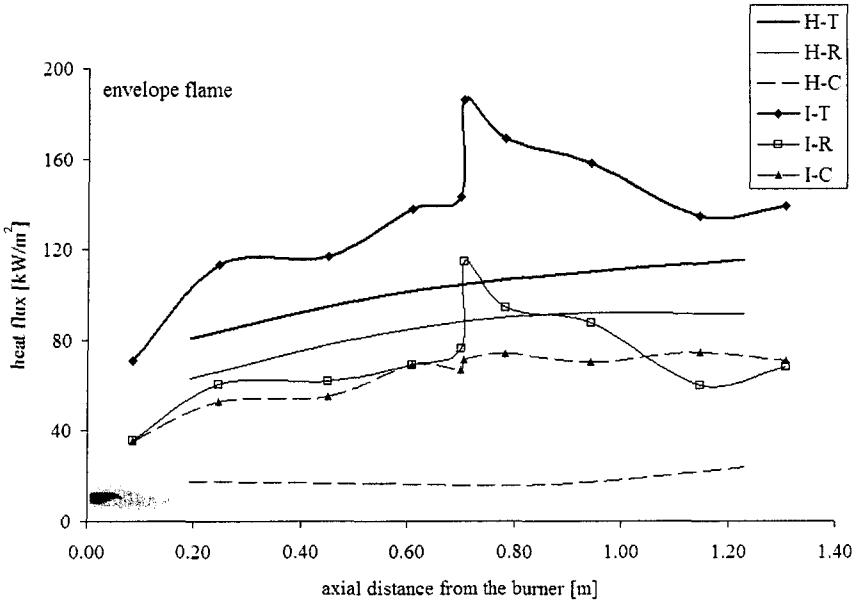

Figure 4.24 Comparison of the measured heat fluxes between the parallel firing and impingement configurations for the envelope flame

4.5.4. Measured heat fluxes in the lateral measurement points of the furnace

In the above sections, the heat flux distributions were presented along the centerline of the furnace. As it was presented in CHAPTER 2, the calorimetric plates have also measurement holes at the distance of ±120 mm parallel to the centerline (leftside and rightside). In all the other (presented above) test series we repeated the experiments at least twice for every flame types, counting neither the preliminary experiments nor those where technical difficulties arose. On the contrary, the measurement series at the lateral measurement points (except the point on the chamfered corner – right from the direct impingement point) were made just once and only for the high velocity and envelope flames. Thus, the reliability of these results is questionable.

The longitudinal convective, radiative and total heat flux curves measured in the centerline and in the two lateral measurement locations are presented in Figure 4.25, for the high velocity and envelope flames. The solid lines are the heat flux curves at the centerline and the discontinous lines are the lateral heat flux curves.

The first important feature is the similarity between the centerline and the lateral heat flux curves. For the high velocity flame, the only significant difference occurs in the stagnation zone. On the other hand, in the case of the envelope flame, countinous fluctuation can be observed in both, the convective and the radiative curves. The highest instability occurs at the first section of the furnace.

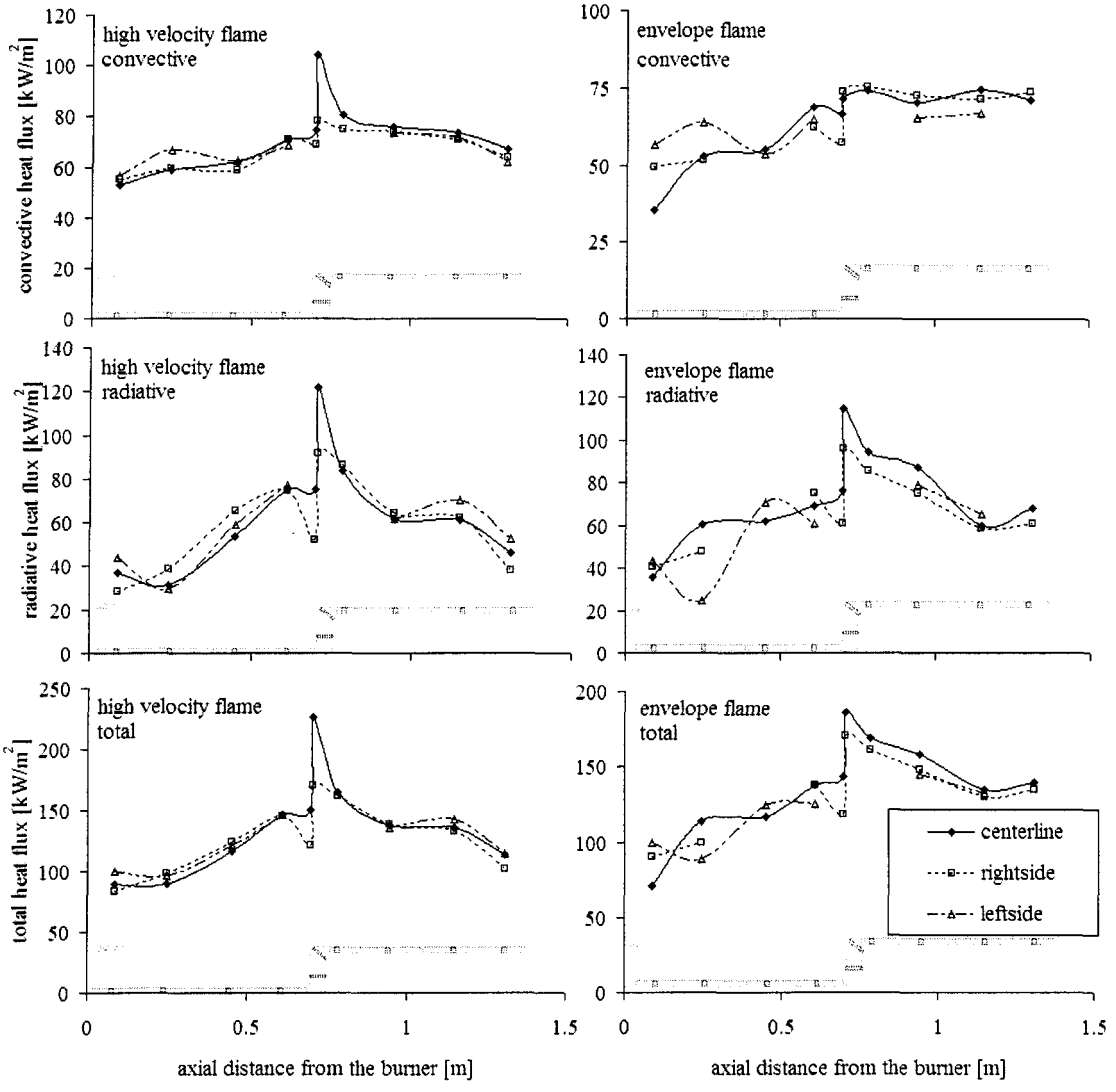

Figure 4.25 Longitudinal convective, radiative and total heat flux curves measured in the centerline and in the two lateral measurement locations for the high velocity and envelope flames.

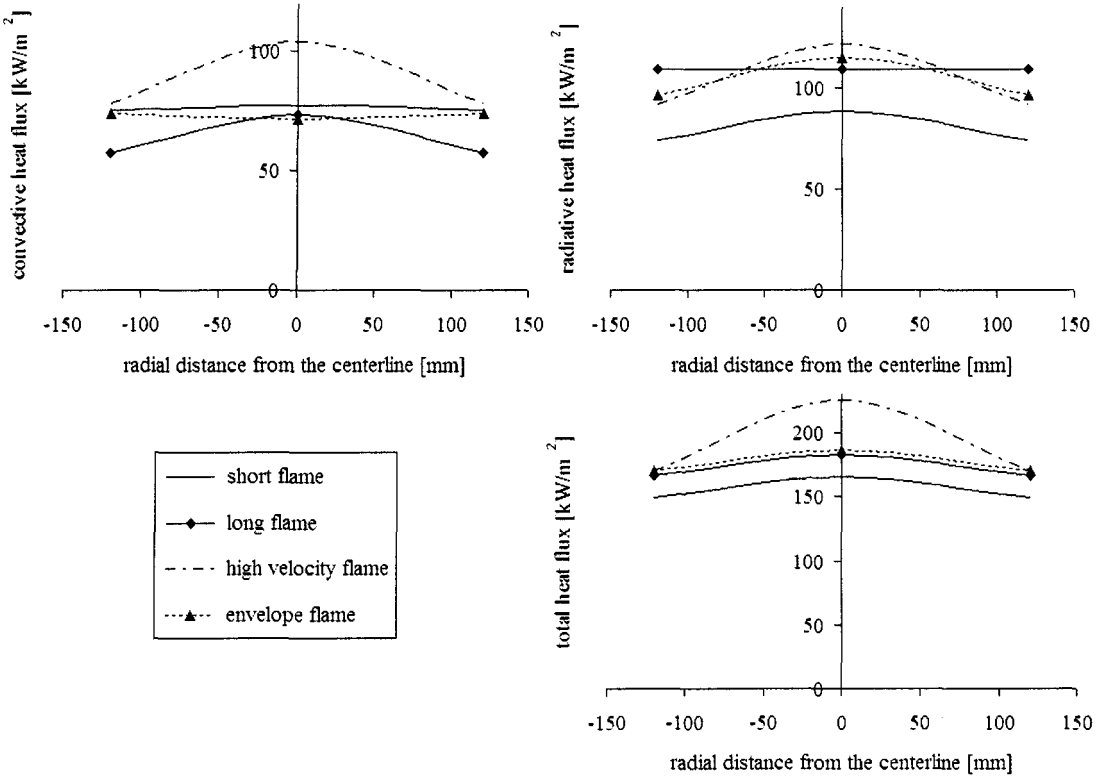

Figure 4.26 Measured heat fluxes in the central and lateral impingement points

The differences between the centerline (stagnation point) and the lateral measurement point at the chamfered corner of the vertical calorimetric plate are additionally presented in Figure 4.26. Only one of the lateral points was measured, while the other point on the figure is simply mirrored.

The total heat flux curves have peak values in the centerline for all flame types. On the other hand, it is a surprising feature that only the high velocity and the long flames have notable peaks in their convective curves at the centerline. In the case of the short flame, the central and lateral heat fluxes are almost identical. In addition, the heat fluxes are slightly higher in the lateral measurement points than in the centerlines for the envelope flame. This

latter can be easily understood by observing the temperature contours in the envelope flame in Figure 3.4. At the distance of the vertical plate (700 mm), the temperature is almost 200°C lower at the centerline than the gas temperature at the lateral measurement location (120 mm). On the contrary, for an accurate explanation in the case of the short flame, further measurements have to be done. The impingement zone is located between the second and third measurement sections of the experimental furnace, so it is not directly accessible for measurements.

In the case of the radiative heat fluxes, the high velocity, the envelope and the short flames have significant peak heat-fluxes at the furnace centerline. The only flame, which has no radiative heat-flux peak in the furnace centerline, is the long one. The two possible explanations are the flame luminosity and the jet spreading. As it was discussed above, the long flame is a very luminous, bright, yellow flame. Thus, the direct radiative heat flux arriving from the flame is more significant than for other flame types. Secondly, as it was presented in Figure 3.51, the long flame is the mostly expanded flame. Therefore, the visible flame volume of the lateral sensors should be similar to that of the centerline sensors.

4.5.5. Summary and conclusion of the impingement experiments

The flame-object heat transfer was analyzed experimentally using four different flames and a half-raised solid block in a reverbatory type laboratory furnace. The measured velocity and temperature profiles helped greatly the interpretation of the differences in the measured heat flux distributions. The following general conclusions can be drawn:

1.) All flames produce a strong peak of the radiative and total heat fluxes at the impingement point.

2.) There is a marked difference between the so-called envelope flame and the other three flames in the distribution of the convective heat flux. The distribution of the convective flux along the surface of the object is the most uniform for the envelope flame.

3.) The high velocity flame transfers 54% of the total heat exchange by convection in the impingement arrangement. This behavior is very different from that in parallel firing.

4.) The details of the variations in the convective and radiative flux distributions are less visible in the total heat flux curves.

5.) The total heat exchange rates as well as the convective fluxes are higher in the impingement arrangement than in the case of parallel firing.

6.) An increased radiation was found for the long luminous flame in the impingement arrangement while that effect was undetectable in parallel firing.

7.) Comparing to the lateral measurement point, in the centerline of the chamfered impingement corner of the vertical plate, uniquely the high velocity flame produces both radiative and convective heat flux peaks.

4.6 Heat transfer calculations for the direct impingement point

The four commonly investigated configurations in the flame impingement studies were presented in Figure 1.11. The flame-target arrangement analysed in the present work was

not a common configuration and it was not previousely studied anywhere. Nevertheless, we attempted to adapt the correlations presented in the literature to the geometrical arrangement of the present study. The supplementary objective was to compare the given correlations to each other for estimating the possible error percentage of these formulas.

First, the heat flux results are compared with the predictions of some semianalytical equations. Subsequently, the same results are compared with the predictions of empirical correlations for flames impinging normal to a plane surface, for flames impinging to a cylinder in cross flow and for flames impinging to a hemi-nosed cylinder. Finally, a short conlusion is given.

4.6.1. Comparison of the measured heat flux results in the impingement point with the predictions of some semianalytical equations

The heat flux equations using semianalytical solution were presented in section 1.2.3.5. These equations were calculated for the four different flame types. The predicted heat flux values are compared with the measurements in Table 4.5.

In the first four rows, the early semianalytical solutions of Sibulkin as well as of Fay and Riddell are given for the heat transfer in stagnation flows. Sibulkin's result is calculated for three different stagnation body shapes, so the velocity gradient, β, in Eq. 1.17 is replaced by Eq. 1.30, Eq. 1.32 and Eq. 1.33 respectively. However, the solution of Fay and Riddell in Eq. 1.34 is only calculated for flame impingement normal to a disk using the velocity gradient given in Eq. 1.32., because, as seen in the table, the difference in comparison to the solution of Sibulkin is negligible.

Reference	Equation No.	Impingement target	Flow type at the nozzle exit	Heat flux component	Predicted heat flux [kW/m^2]			
					short flame	long flame	HVI flame	envelope flame
Sibulkin[46]	Eq. 1.17	cylinder in cross flow	laminar	q''_s	190	186	326	266
	Eq. 1.17	disk	laminar	q''_s	107	105	184	150
	Eq. 1.17	flat plate	laminar	q''_s	21	20	43	N.A
Fay and Riddell[52]	Eq. 1.34	disk	laminar	q''_s	118	116	204	166
Horsley et al.[50]	Eq. 1.35	flat plate	turbulent	q''_s	79	69	135	N.A
Hargrave et al.[51]	Eq. 1.36	hemi-nosed cylinder	turbulent	q''_s	195	192	333	272
Hemeson et al.[48]	Eq. 1.37 (a)	cylinder in cross flow	turbulent	q''_s	81	71	138	N.A
	Eq. 1.37 (b)	hemi-nosed cylinder	turbulent	q''_s	99	87	170	N.A
van der Meer[49]	Eq. 1.38	flat plate	turbulent	q''_s	135	130	239	186
					Measured heat flux [kW/m^2]			
present work	-	45° circular sensor	turbulent	$q''_{conv,measured}$	77	74	104	71

Table 4.5 Comparison between the measured heat fluxes in the present work and the predicted heat fluxes using some semianalytical equations

The other equations are the experimental results compared with some form of semianalytical solution. All the applied formulas are based on Eq. 1.17. Little differences are in the driving forces, in the constants and in the references to some thermophysical properties, however the velocity gradients are individually given in each correlation. The experimental conditions as well as the formulas to calculate the velocity gradients are given in Table 1.1 and Table 1.2.

Finally, in the last row, the experimentally measured convective heat fluxes of the present work are given in Table 4.5.

The calculated results generally overpredict the experimental data. The only exception when the measurements are underpredicted by 58% up to 73% is for Eq. 1.17 given by Sibulkin for impingement normal to a flat plate. There are good agreements with the experimental data of the short and long flames for Eq. 1.35 and Eq. 1.37 (a) given by Horsley et al.[50] and Hemeson et al.[48] respectively. On the other hand, in both cases, the experimental data of the high velocity flame are overpredicted by 30% and the results are not interpretable for the envelope flame. For the long and short flames, Eq. 1.37 (b) overpredicted the results by only 20% as well as 30% respectively. The difference between the two equations of Hemeson, Eq. 1.37 (a) and (b), is only in the velocity gradient, β, which is calculated differently for the two configurations. In all other cases, the measured heat fluxes are overpredicted by 40% up to 280%.

The coincidence of the best matching and underpredicted results with those, which cannot be interpreted for the envelope flame, is obvious. The reason is that the velocity gradient in these semianalytical solutions has to be calculated using either the radius $r_{0.5t}$ or the diameter d_j. These parameters are, both, characteristic properties related to a jet flame. In all other equations that significantly overpredict the experiments, the characteristic length depends on the target size and not on the flow conditions.

The radius $r_{0.5t}$, at which the measured gas temperature is halfway between the maximum and the ambient at a given axial location, cannot be interpreted for the envelope flame. The temperature distribution is very different for the envelope flame in comparison

to a traditional flame. As a reminder, cold ambient air is entering in the furnace centerline, which is surrounded in the proximity of the refractories by randomly ignited flame packages and by the mixture of hot combustion products.

Mention must be made here, that approximately 95 percent of the general known experimental methods are not suitable for testing the envelope type flame. The reason is that this flame type cannot operate in ambient conditions; the flame must be surrounded by refractory lining! Except the present work, none of the experiments in Table 4.5 was made in a furnace. In addition, among the more than one-hundred various experimental programs in the overall flame impingement field, only six were performed inside a furnace.

4.6.2. Comparison of the measured heat flux results at the impingement point with the predictions of empirical heat transfer correlations

The empirical heat transfer correlations were presented in section 1.2.3.6 for flames impinging normal to a plane surface, in section 1.2.3.7 for flames impinging to a cylinder in cross flow and in section 1.2.3.8 for flames impinging to a hemi-nosed cylinder. The experimental conditions in the related configurations are tabulated in Table 1.3, Table 1.4 and Table 1.5. The predicted heat flux results for the three above-mentioned configurations are compared with the measured heat flux in the impingement point of our experiments. These results are presented in Table 4.6, Table 4.7 and Table 4.8.

4.6.2.1. Flames impinging normal to a plane surface

The calculated heat flux results in Table 4.6 for flames impinging normal to a plane surface are generally local convection heat transfer values ($q''_{s,conv}$) related to the stagnation

point. The only exception is the correlation of You[56] in Eq. 1.45 and Eq. 1.46, where the average convective heat flux ($q''_{b,conv}$) is given as a function of the distance from the stagnation point.

Reference	Equation No.	Impingement target	Flow type at the nozzle exit	Heat flux component	Predicted heat flux [kW/m^2]			
					short flame	long flame	HVI flame	envelope flame
Hoogendoorn et al.[45] and Popiel et al.[13]	Eq. 1.39	flat plate	laminar	$q''_{s,conv}$	62	61	339	282
	Eq. 1.40	flat plate	laminar	$q''_{s,conv}$	53	51	123	92
	Eq. 1.41	flat plate	laminar	$q''_{s,conv}$	44	44	74	61
	Eq. 1.42	flat plate	laminar	$q''_{s,conv}$	62	61	124	98
Kataoka et al.[54]	Eq. 1.43	flat plate	laminar	$q''_{s,conv}$	72	68	156	97
You[56]	Eq. 1.45	flat plate	laminar	$q''_{b,conv}$	70	71	65	66
Shorin and Pechurkin[35]	Eq. 1.47	flat plate	turbulent	$q''_{s,conv}$	18	18	49	46
	Eq. 1.48	flat plate	turbulent	$q''_{s,conv}$	264	402	16	37
Buhr et al.[58, 59] Kremer et al.[57]	Eq. 1.49	flat plate	turbulent	$q''_{s,conv}$	128	115	451	291
Matsuo et al.[55]	Eq. 1.50	flat plate	turbulent	$q''_{s,conv}$	64	66	18	18
					Measured heat flux [kW/m^2]			
present work	-	45° circular sensor	turbulent	$q''_{conv,measured}$	77	74	104	71

Table 4.6 Comparison of the measured heat flux of the present work with the predicted heat flux using empirical heat transfer correlations for flames impinging normal to a plane surface

The predictions for turbulent flows are expected to match better the experimental results better than the correlations for laminar flow conditions. In addition, the heat-flux sensors are located to some distance from the hypothetical stagnation point. Therefore, the measured heat fluxes are not the maximum values. Nevertheless, the main objective of this

analysis is the comparison of the tendencies and relative results of the correlations available in the literature with each other and with the measured heat fluxes in our experiments. We attempt to find those parameters, which must be included in the correlations to be able to distinguish between the flames having different flow structures.

The first four equations given by Hoogendoorn et al[45] and Popiel et al[13] represent very well the importance of the burner-target distance, which is L=6.6 for the short and long flames and L=20.4 for the high velocity and envelope flames. Eq. 1.39 is valid in the range of $2 \leq L \leq 5$, so the calculated results underpredict the experimental data by only 20% for the short and long flames while for the high velocity and envelope flames the experimental data are overpredicted by as much as 230% and 300%. However, Eq. 1.40 is valid for $L > 12$, so in the case of the short and long flames, the results are underpredicted by 30%, but on the other hand, the high velocity and envelope flames are only overpredicted by 20% and 30% respectively. As Baukal stated, the modified correlation (Eq. 1.41), valid in the range of $8 \leq L \leq 20$, really underpredicts the data. However, Eq. 1.42, which is additionally modified to include free jet turbulence, yields approximately to the same results as Eq. 1.39 for the short and long and Eq. 1.40 for the high velocity and envelope flames.

In spite of the significant differences (average 50%) of the experimental data compared to the predicted results of Eq. 1.43 given by Kataoka, this correlation reflects most of convective heat flux proportions in between the four flame types. In this equation, the distance of the critical point, the burner-target distance, the parameters related to the jet are all included.

The correlation given by You[56] is based on very low speed flows, where buoyancy

effects have important contribution to the flow structure. The low heat flux in the case of the high velocity flame is attributed to this effect.

Eq. 1.47 of Shorin and Pechurkin[35] is valid for $L \leq X_v$. The results of this equation underpredicted the data by 36% up to 76%. Their second proposed equation, Eq. 1.48, is valid in the range of $L > X_v > 14$. For flames impinging normal to a plane surface, this is the only equation where the heat transfer rate is given as a function of the distance from the stagnation point. Therefore, Eq. 1.48 was a point of origin in the heat transfer analysis. Many efforts were made to match the results of our geometry to the different impingement arrangement found in the literature. As a preliminary solution, the stagnation point was supposed to be in the center point of the heat flux sensor. Eq. 1.48 was numerically integrated to the entire circular surface of the sensors. Enormous heat fluxes arose for the short and long flames. Then, a computational module was created which numerically integrates the convective heat fluxes on the sensor surface for any stagnation point location in the axial direction (without radial offset). Results in Table 4.6 were calculated using this module for the later hypothetical stagnation point determined. For flames impinging parallel to plane surfaces, Eq. 1.67 of Pohlhausen[28], Eq. 1.68 of Eckert[30] and Eq. 1.69 of Beér and Chigier[4] was further added to the computational module. In all these equations, the heat flux is calculated as a function of the distance from the leading edge. The obtained results are discussed in the following section. Returning to the solution of Eq. 1.48 by Shorin and Pechurkin, the results seriously overpredict the experimental data for the short and long flames. On the contrary, for the high velocity and envelope flames the experiments are underpredicted.

The results of Buhr et al.[58, 59] and Kremer et al.[57] overpredict the experimental data up to 334%.

Notwithstanding that Matsou et al[55] made experiments in a furnace, the given correlation is related to the firing rate, target distance and temperature difference. The particularities in the fluid dynamics of the flames are not taken into account. The calculated results do not follow at all the heat flux characteristic of the experimentally studied flames.

4.6.2.2. Flames impinging normal to a cylinder in cross-flow

The second group of heat transfer correlations are those studies, which were made for flames impinging normal to a cylinder in cross flow. The heat flux predictions are classified for the related solutions in Table 4.7. In two studies, the local, forced convection heat transfer rate, $q''_{s,conv}$, is given at the stagnation point. In these cases, the predicted heat flux is expected to be greater than our measurements data. In the other studies, the predicted average forced convection, $q''_{b,conv}$, the average radiation, $q''_{b,rad}$, and the total $q''_{\max,conv+rad}$ heat transfer rates are given. The experimental conditions are presented in Table 1.4.

As it was discussed in section 1.2.3.7, Hustad et al.[42, 43, 60] studied a wide range of experimental conditions. The local convection heat-transfer values of Eq. 1.51 match the experimental results within 10% for the short and long flames, however for the high velocity and envelope flames the data are overpredicted as much as 60% and 80% respectively. The average convection heat-transfer results (Eq. 1.52) underpredict the experimental data by 40% for the short and long flames, by 10% for the high velocity flame and match the data for the envelope flame.

Eq. 1.53 and Eq. 1.54 are referring to the radiative heat transfer rate for CH_4 and C_3H_8 flames respectively. Only the results of Eq. 1.53 are discussed. The average radiation heat-transfer rate is underpredicted by 90% to 95%. There are several reasons of such significant deviations. Contrary to the experiments of Hustad, our experiments were made in a combustion chamber surrounded with hot refractory bricks. During the radiative heat flux measurements, the background radiation was not suppressed and the refractory temperature was as high as about 1000°C. As opposed to pure diffusion flames, the combustion is mostly completed for premixed flames at the distance of the impingement point. Therefore, above the impingement point, hot combustion gases are present. Approximate calculations based on the temperature levels, partial pressures and mean path length resulted in a total emissivity value of about $\varepsilon = 0.1035$ for the mixture of combustion products (see section E.3.1 of Appendix E.). The third effect is the difference in the flow structure. In our experiments, a significant amount of the main stream recirculates and a secondary flow is continuously swirling around the main stream enlarging the visible, radiating volume of the hot gases above the impingement point. The combination of these effects leads to significantly higher radiative heat fluxes.

Finally, Eq. 1.55 by Hustad et al[61] leads to approximative total heat-flux values based only on the firing rates. As for as the differences in the various flames are not considered at all, the results overpredict the data by 25% up to 72%. The lower deviation occurs for the high velocity flame.

Reference	Equation No.	Impingement target	Flow type at the nozzle exit	Heat flux component	Predicted heat flux [kW/m^2]			
					short flame	long flame	HVI flame	envelope flame
Hustad et al.[42, 43, 60]	Eq. 1.51	cylinder c.f.	lam. & turb.	$q''_{s,conv}$	83	80	164	127
	Eq. 1.52	cylinder c.f.	lam. & turb.	$q''_{b,conv}$	46	45	92	71
	Eq. 1.53	cylinder c.f.	lam. & turb.	$q''_{b,rad}$	8	8	8	6
	Eq. 1.54	cylinder c.f.	lam. & turb.	$q''_{b,rad}$	25	25	25	20
	Eq. 1.55	cylinder c.f.	turbulent	$q''_{max,conv+rad}$	284	284	284	284
Hargrave et al.[61]	Eq. 1.56	cylinder c.f.	turbulent	$q''_{s,conv}$	224	217	440	346
Kilham[40]	Eq. 1.57	cylinder c.f.	laminar	$q''_{b,conv}$	69	68	121	98
Jackson & Kilham [41]	Eq. 1.58	cylinder c.f.	laminar	$q''_{b,conv}$	74	72	129	105
Fells and Harker[62]	Eq. 1.59	cylinder c.f.	unspecified	$q''_{b,conv}$	81	80	138	112
Davies[63, 44]	Eq. 1.60	cylinder c.f.	unspecified	$q''_{b,conv}$	162	159	278	227
	Eq. 1.61	cylinder c.f.	unspecified	$q''_{b,conv+TCHR}$	69	68	112	93
					Measured heat flux [kW/m^2]			
present work	-	45° circular sensor	turbulent	$q''_{conv,measured}$	77	74	104	71
				$q''_{rad,measured}$	88	109	122	115
				$q''_{total,measured}$	166	183	226	186

Table 4.7 Comparison of the measured heat flux of the present work with the predicted heat flux using empirical heat transfer correlations for flames impinging (perpendicular) to a cylinder in cross flow

Eq. 1.56 (Hargrave et al[61]) is a correlation for the local, forced convection heat-transfer rate in the stagnation point. The results overpredict the experimental data by 190% and 195% for the short and long flames as well as by 322% and 384% for the high velocity and envelope flames.

Eq. 1.57 and Eq. 1.58, by Kilham[40] and Jackson & Kilham[41] match the experimental data within 10% as well as within 4% for the short and long flames respectively. The target

distance, L, is in the measured range. For the high velocity flame, these equations overpredict the experimental data by 16% and 24% as well as for the envelope flame by 37% and 46%. The target distance was out of the measured range. Although the flow condition was termed laminar, the author did not specifiy the Reynolds number at the nozzle exit.

The results of Eq. 1.59 of Fells and Harker[62] for an unspecified flow type correlated the experimental data within 8% for the short and long flames. The target distance, L, was in the measured range. For the high velocity and envelope flames the experiments were overpredicted by 32% and 58% respectively, however the target distance was largely out of the measured range.

The results of Eq. 1.60 by Davies[63] seriously overpredict the experimental data (by 110% up to 220%). On the other hand, the predictions of Eq. 1.61 by Davies[44], correlate the experimental data within 10% for the short, the long and the high velocity flames. For the envelope flame, the result overpredicts the experiments by 30%. The target was located in the point of maximum heat release in the case of Eq. 1.60. On the other hand, for Eq. 1.61, the target was placed very close to the burner (L=0.5). The flow conditions are unspecified in both cases.

4.6.2.3. Flames impinging normal to a hemi-nosed cylinder

Finally, the third group of heat transfer correlations is the experiments made for flames impinging normal to a hemi-nosed cylinder. The calculated heat flux results are presented for the related correlations in Table 4.8. In all studies, the local, forced convection heat-transfer rate at the stagnation point is the resulting solution. These results overpredict

seriously, by 146% up to 470%, the experimental data.

Hargrave et al.[61] (Eq. 1.56) made experiments also for flames impinging normal to a cylinder in cross flow using the same experimental conditions. The results were presented above. The results of Eq. 1.66 overpredict the experimental data by 210% for the short and long flames, and by 432% and 470% for the high velocity and envelope flames. Comparing the two configurations, the overprediction of the correlation for hemi-nosed cylinders is more by 20% in the case of the short and long flames and by 90% for the high velocity and envelope flames.

Reference	Equation No.	Impingement target	Flow type at the nozzle exit	Heat flux component	Predicted heat flux [kW/m^2]			
					short flame	long flame	HVI flame	envelope flame
Galloway and Sage[64]	Eq. 1.64	hemi-nosed cylinder	laminar and turbulent	$q''_{s,conv}$	189	185	336	271
Fairweather et al.[65]	Eq. 1.65	hemi-nosed cylinder	laminar and turbulent	$q''_{s,conv}$	215	210	381	307
Hargrave et al.[61]	Eq. 1.66	hemi-nosed cylinder	turbulent	$q''_{s,conv}$	240	230	553	405
					Measured heat flux [kW/m^2]			
present work	-	45° circular sensor	turbulent	$q''_{conv,measured}$	77	74	104	71

Table 4.8 Comparison of the measured heat flux of the present work with the predicted heat flux using empirical heat transfer correlations for flames impinging to a hemi-nosed cylinder

4.6.3. Conclusions

It was found, analysing the semianalytical solutions that the best correspondence between the measured and computed results arose when the characteristic properties that

are related to the gas flow were used (either the radius $r_{0.5t}$ or the diameter d_j). In the equations, where the characteristic length depends on the target size and not on the flow conditions, the calculations significantly overpredicted the experiments.

The importance of the burner-target distance was well represented by the different correlations of Hoogendoorn et al[45] and Popiel et al[13].

Although the heat-flux values were not exactly reproduced in the predictions, the relative tendencies of the measured and predicted heat fluxes for the short, the long and the high velocity flames were well expected for flames impinging normal to a cylinder in cross flow and for flames impinging normal to a hemi-nosed cylinder. On the contrary, for flames impinging normal to a plane surface, the calculated and measured tendencies were not matching in the case of Matsuo et al. [55] (Eq. 1.50), You[56] (Eq. 1.45) and Shorin and Pechurkin[35] (Eq. 1.47 and Eq. 1.48). In addition, the tendencies of the measured and calculated heat fluxes for the envelope flame relative to the other flame types were never coincident in any configurations.

Despite the good tendencies, the calculations overpredicted seriously the experimental data for the configuration when the flame impinges to a hemi-nosed cylinder.

Summarizing, the smallest errors and the best tendencies relative to the different flame types arose for the configuration where the flame is impinging normal to a cylinder in cross flow. Otherwise, this is the geometrical arrangement which corresponds the most to the 45° chamfered corner at the top of the vertical plate. The target distance seems to be a very important parameter in impingement heat transfer. Equations basing only on general parameters, as for example the firing rate, have significant deviation from measurement

data. None of the correlations gives reliable prediction for the envelope flame.

Above analysis support well the contestation of Baukal[6] that in spite of the large amount of studies, in many cases, the heat transfer distribution can only be approximated very roughly. Therefore, caution must be used in the absence of any experimental data.

4.7 Comparison of the measured heat flux results with the predictions of empirical heat transfer correlations over the elevated furnace hearth

The measured convective heat fluxes over the elevated furnace hearth are compared with the computed results using Eq. 1.68 after Eckert in Figure 4.27. The thick, solid lines are the experimental curves while the dotted lines are the calculated curves.

In the case of the short and long flames, the experimental data are significantly underpredicted along the entire furnace length. For the high velocity flame, although the experimental data in the impingement point is radially overpredicted, the computed points correlate well the experimental data further downstream. In the case of the envelope flame, the experimental data in the impingement point are overpredicted. On the contrary, further downstream, the measured data are significantly underpredicted.

In the case of the short, the long and the high velocity flame, the decreasing tendencies of the curves are similar to the predictions. On the other hand, the measured heat fluxes in the case of the envelope flames are increasing further downstream, unlike to all other flame types and predictions.

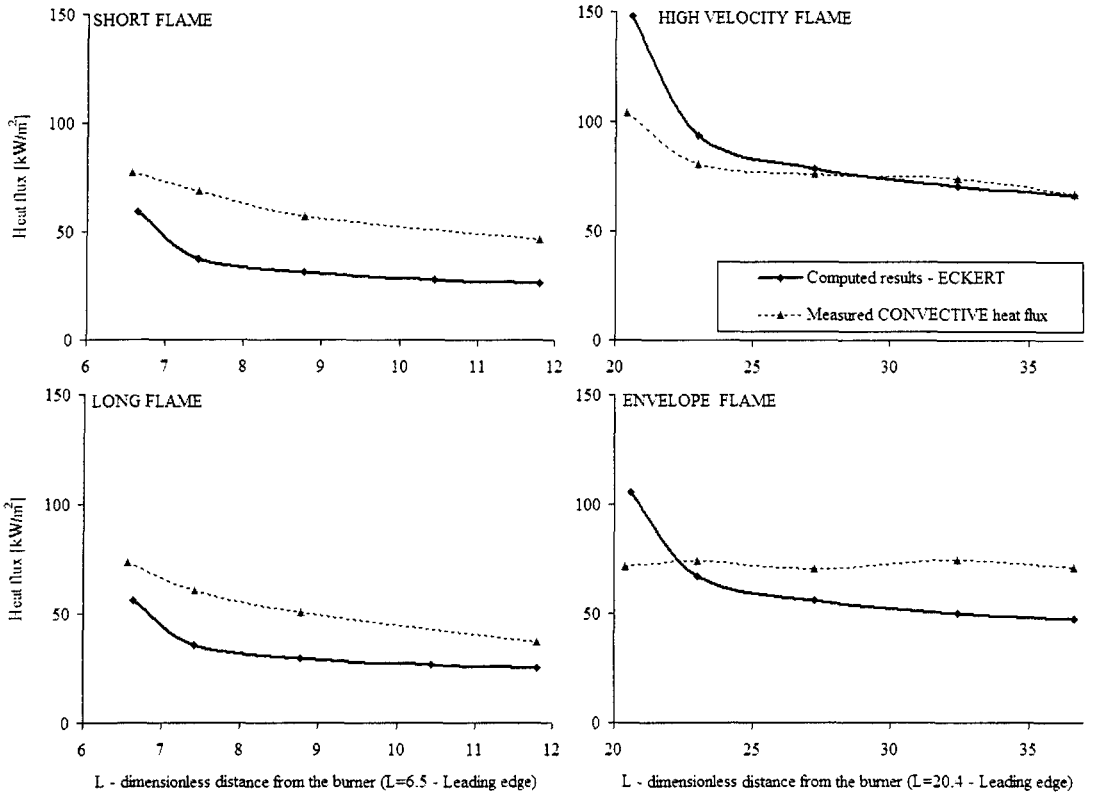

Figure 4.27 Comparison of the predicted convective heat flux curves of Eq. 1.68 after Eckert with the experimental data of the present work measured over the elevated calorimetric plates for the four flame types

In Figure 4.28, the measured total heat fluxes over the elevated furnace hearth are compared with the predictions of Eq. 1.69 after Beér and Chigier. As it was discussed earlier, the velocity in the Reynolds number is always the maximum velocity at any one axial station in Eq. 1.69. Similarly, all the thermophysical properties are evaluated taking the maximum temperatures at any axial station. Contrary to Eq. 1.68 by Eckert, Eq. 1.69 after Beér and Chigier predicts the total heat fluxes.

The general tendencies are about the same as for the correlation of Eckert. For the short and long flames, the experimental data are seriously underpredicted. In the case of the

high velocity and envelope flames, the impingement point is the most overpredicted. Further downstream, the calculated curves intersect the experimental ones. In the rear section of the furnace, the measurement data are underpredicted. The important discrepancy of the envelope flame is attenuated in the total heat flux curves. In Figure 4.28, the most eye-catching feature is the difference between the prediction and the measurement for the short and long flames.

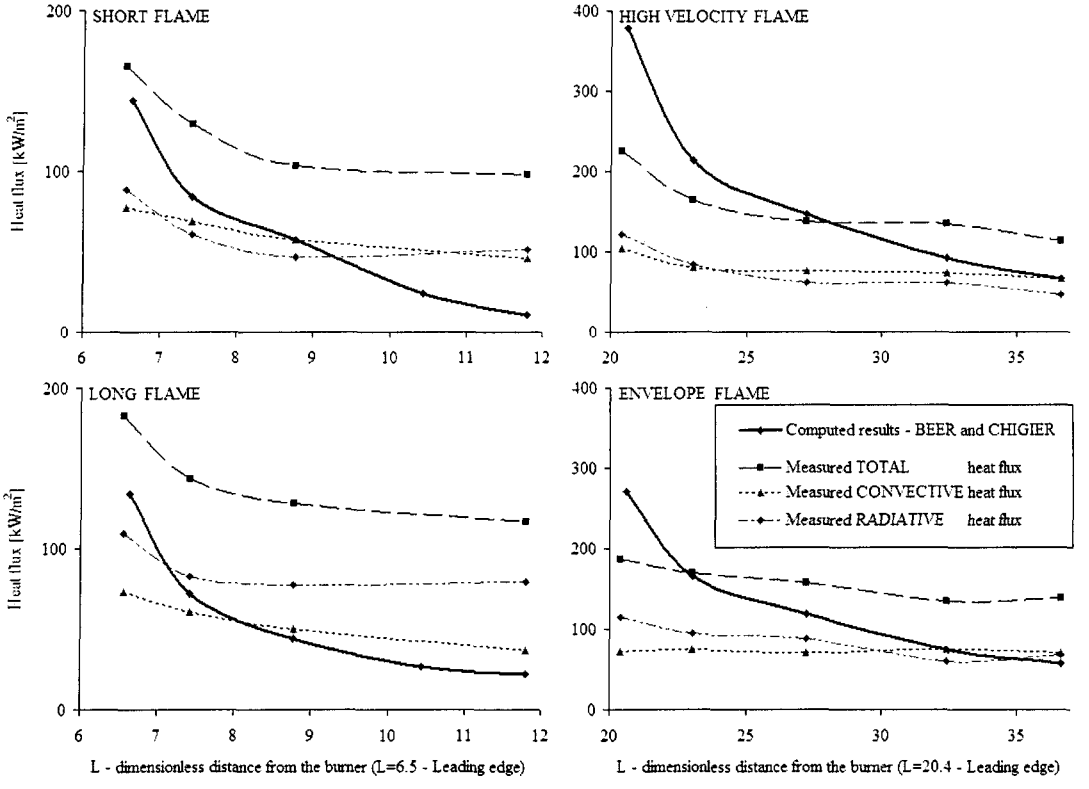

Figure 4.28. Comparison of the predicted heat flux curves of Eq. 1.69 after Beér and Chigier with the experimental data measured at UQAC for the four flame types over the elevated calorimetric plates

4.7.1. Establishment of empirical heat transfer correlations over the elevated furnace hearth using the experimental data of the present work

Over the calorimetric plates at raised position (rear furnace sections), not only the heat fluxes were measured but also the temperature and velocity distributions near the heat flux measurement points. The large amounts of available data permit the establishment of empirical heat transfer correlations. In these furnace sections, the flame is parallel to the horizontal surface of the calorimetric plates. The five heat-flux sensor data in the centerline were used. The solution was searched in the following forms:

$$q''_{x,conv} = \frac{k_{x,\max}}{x}\left\{a\,\mathrm{Re}^{b}_{x,\max}\right\}\left(t_{x,\max} - t_w\right) \qquad \text{Eq. 4.1}$$

$$q''_{x,conv} = \frac{\overline{k_x}}{x}\left\{a\,\mathrm{Re}^{b}_{x,\max}\right\}\left(t_{x,\max} - t_w\right) \qquad \text{Eq. 4.2}$$

$$q''_{x,conv} = \frac{\overline{\overline{k_x}}}{x}\left\{a\,\mathrm{Re}^{b}_{x,\max}\right\}\left(t_{x,\max} - t_w\right) \qquad \text{Eq. 4.3}$$

where a and b are constants. Correlations were formed for the short, the long, the high velocity and the envelope flames separately, for the flames produced by the traditional burner and for all flame types together.

It was found that the solutions of the form of Eq. 4.1 predict better the experimental data. The equations for the short and long flames as well as the common formula for these two flames correlate the experimental data within 15%. However, the correlation of the high velocity flame matches the data only within 27%. For the envelope flame, no good

solution was found in the given forms. Even the result of the best fitting curve underpredicts the data in certain locations by as much us 60%. The differences among the various flame types are amplified in the common solution and even the best matching curve correlates the data on an average within 44%. However, the last curve underpredicts the data by up to 90% at certain locations.

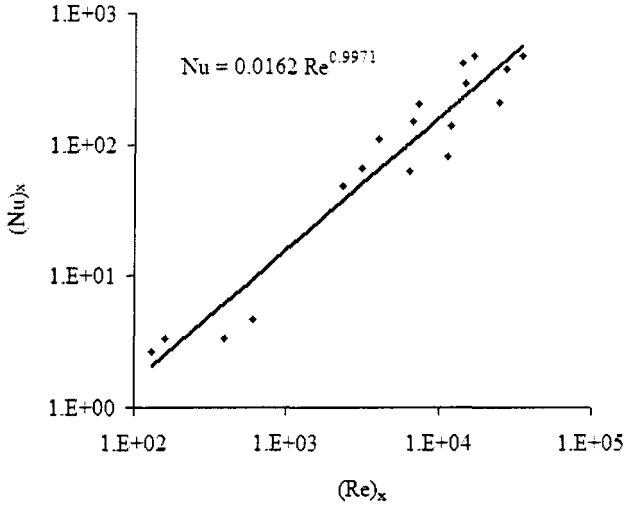

Figure 4.29 The Nusselt-Reynolds relationship along the axis of the elevated furnace hearth for all flame types studied

The general empirical heat transfer correlation parallel to the elevated calorimetric plates for all flame types is:

$$q''_{x,conv} = \frac{k_{x,\max}}{x}\left\{0.0162\,\mathrm{Re}_{x,\max}^{0.9971}\right\}\left(t_{x,\max} - t_w\right)$$

Eq. 4.4

where the characteristic length (x) is the distance from the leading edge. All the thermophysical properties are evaluetad at the maximum temperature at any one axial location. Similarly, the flow velocity in the Reynolds number is also the maximum velocity

at any one axial station. The Nusselt-Reynolds relationship along the centerline over the elevated furnace hearth is represented in Figure 4.29.

The common solution for the flames produced by the traditional burner (short and long flames) is defined as:

$$q''_{x,conv} = \frac{k_{x,\max}}{x}\left\{0.0150\,\mathrm{Re}_{x,\max}^{1.0582}\right\}\left(t_{x,\max} - t_w\right)$$

Eq. 4.5

The Nusselt-Reynolds relationship for these flame types is shown in Figure 4.30. This correlation matches the experimental data within 14%. For each correlations, the constants (a, b) are given in Table 4.9.

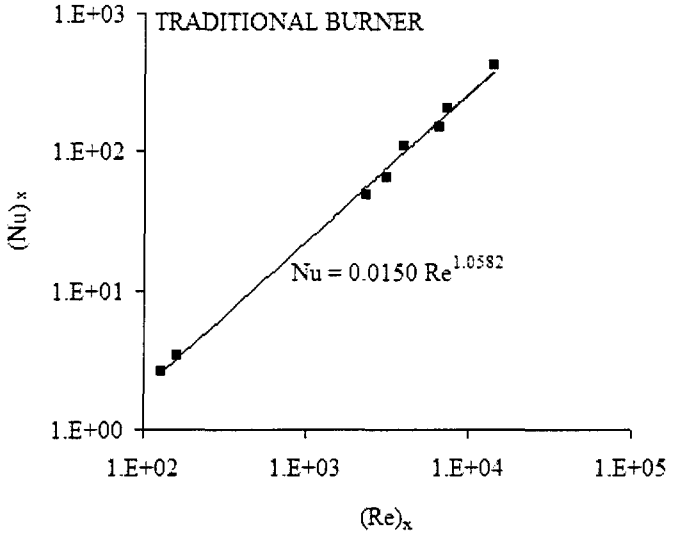

Figure 4.30 The Nusselt-Reynolds relationship along the axis of the elevated furnace hearth for the short and long flames produced by the traditional burner

Form of equation : $q''_{x,conv} = \frac{k_{x,\max}}{x}\left\{a\,\mathrm{Re}^{b}_{x,\max}\right\}\left(t_{x,\max} - t_w\right)$		
correlation given for:	Constants	
	a	b
short flame	0.01527	1.0523
long flame	0.01408	1.0698
high velocity flame	0.00364	1.1044
envelope flame	0.00207	1.2182
traditional burner	0.01496	1.0582
all flame types	0.01619	0.9971

Table 4.9 Established empirical heat transfer correlations for flames impinging parallel to a plane surface

4.8 Summary of the heat transfer calculations

A detailed analysis was made concerning the convective heat exchange at the impingement point. The measured convective heat fluxes were compared with computed results obtained using numerous empirical heat transfer correlations published in the literature. Neither the formulas for flames impinging normal to a plane surface (Figure 1.11.c) nor those for flames parallel to a plane surface (Figure 1.11.d) yielded to acceptable results. The best correspondence with our measurement results was found by comparing them with the case of flames impinging normal to a cylinder (see Figure 1.11.a). The results of Kilham and Jackson [40, 41], and Hustad et al.[60] are close to our measurements for all flame types.

Flame impingement correlations parallel to a plane surface were compared with measurement data over the elevated furnace hearth. The increasing tendency of the measured convective heat flux downstream the leading edge in the case of the envelope

flame cannot be described by any existing heat transfer correlation. In addition, the best fitting curve in the searched form deviated by as much as 60% from the measurements. On the contrary, in the case of the short and long flames (traditional burner) and for the high velocity flame, the formula found in the present study matches acceptably the experimental data.

CHAPTER 5.
CONCLUSIONS AND SUGGESTED FUTURE WORK

5.1 Conclusions

5.1.1. Fluid dynamics of the flames

As it was presented above in section 1.1.5.2, Popiel, van der Meer and Hoogendoorn[13] studied convective heat transfer in impinging flame jets. In their work, the centerline velocity distribution was compared with many other experimental results. The novelty in their work was the extension of the validity of Eq. 1.4 by Hinze and van der Hegge Zijnen and Eq. 1.9 by Thing and Newby for cases, where the density ratio ρ_∞ / ρ_n is as high as 7.6. In the present work, a high velocity jet flame and a so-called envelope type flame were tested. The measurement data are compared with those of other works in Figure 3.46. In the case of the high velocity flame, the density ratio is nearly one. However, for the envelope flame the density ratio was about 0.36. Although it was not mentioned in the original sources, it can be seen in Figure 3.46 that Eq. 1.4 and Eq. 1.9 are also valid for density ratios less than one.

For the correlation, which describes the velocity distribution we identified a constant

of 0.022 in our work, while Popiel, van der Meer and Hoogendoorn[13] proposed a slightly different value of 0.02088. None of these values are valid for a flame where the active combustion zone extends over the whole furnace length, in the case of the envelope flame. In these cases, the recommended value is 0.040 (see section 3.5.4).

5.1.2. Flame object heat transfer

When the flame and charge are not in close contact, the particularities of the different flames are less pronounced in the flame-object heat transfer. The more closely the object is placed to the flame, the more the individual differences are emphasized.

The conclusions of the experiments at parallel firing configuration are listed next:

1.) In the tests performed in the reverbatory-type experimental furnace, the differences in the heating patterns of the four flame types are minimal. The refractory lining has an equalizing effect, ironing out small variations in the distribution of the direct convective and radiative fluxes.

2.) For all flame types tested, the radiative heat flux represented about 80 % or slightly more of the total heat flux, the convective portion representing maximum 20 %.

3.) Within the radiative flux, the direct portion between flame and object is roughly equal to the indirect radiation from the refractory walls.

4.) In comparison to the other flames in the study, the envelope flame increased the total heat flux slightly. The increase is about 8-10 % over the normal short medium velocity type flame.

The conclusions of the experiments at inclined burner setup are listed next:

5.) Burner tilting resulted in higher convective and total fluxes in the impingement zone. The effect was intensified with higher flame velocities.

6.) The inclination practically did not effect the heat flux distribution for the envelope type flame.

7.) Burner inclination resulted in 100% higher convective heat fluxes in the proximity of the direct impingement point for the high velocity flame.

The following general conclusions can be drawn for flame impingement on a corner of a half-raised solid block:

8.) All flames produce a strong peak of the radiative and total heat fluxes at the impingement point.

9.) There is a marked difference between the so-called envelope flame and the other three flames regarding the distribution of the convective heat flux. The distribution of the convective flux along the surface of the object is the most uniform for the envelope flame.

10.) The high velocity flame transfers 54% of the total heat exchange by convection in the impingement arrangement. This behavior is very different from that in parallel firing.

11.) The details of the variations in the convective and radiative flux distributions are less visible in the total heat flux curves.

12.) The total heat exchange rates as well as the convective fluxes are higher in the impingement arrangement than in the case of parallel firing.

13.) An increased radiation was found for the long luminous flame in the impingement arrangement while that effect was undetectable in parallel firing.

14.) From the point of view of hot-spot formation on the heated object, the high velocity flame poses the highest risk. This flame produced the most concentrated convective and radiative heat flux in the direct impingement point.

Generally, we found that there are bigger differences between the two burners than between the two flames produced by the same burner. Likewise, as it was shown in parallel firing mode, the temperature distributions in the refractories are similar for the flames produced by the same burner. The refractories were not in close contact with the flames, so similarly to the distant objects, the details of the flame structure do not exert detectable influence on them.

It was found, analysing the semianalytical solutions for impingement heat transfer that the best correspondence between the measured and computed results occurs when the characteristic properties related to the gas flow were used (see section 4.6.1). In the equations, where the characteristic length depends on the target size and not on the flow conditions, the calculations significantly overpredicted the experimental results.

The importance of the burner-target distance was well represented by the different correlations of Hoogendoorn et al[45] and Popiel et al[13] (see section 4.6.2.1).

Although our experimental arrangement did not correspond exactly to the conditions of the predictive models, the tendencies of the measured heat fluxes for the short, the long and the high velocity flames were close to the predictions given by the models for

impingement normal to a cylinder in cross flow and for flame impingement normal to a hemi-nosed cylinder. Contrarily, for flames impinging normal to a plane surface, the measured tendencies did not match the calculated results based on the model of Matsuo et al. [55] (Eq. 1.50), You[56] (Eq. 1.45) and Shorin and Pechurkin[35] (Eq. 1.47 and Eq. 1.48). In addition, none of the published semi-empirical correlations could describe the measured tendencies for the envelope flame in any configuration.

Despite the correct tendencies, the calculations overpredicted seriously the experimental data for the configuration when the flame impinges to a hemi-nosed cylinder.

Summarizing, the best fit between theoretical prediction and our measurement results was found when using the models for impingement on cylinders in cross flow. Furthermore, this geometrical arrangement corresponds the most to the 45° chamfered corner at the top of the vertical plate. The target distance seems to be a very important parameter in impingement heat transfer. Equations based only on general parameters, as for example the firing rate, have significant deviations from measurement data (Hustad et al.[42, 43, 60] see Eq. 1.55). None of the correlations gives reliable prediction for the envelope flame.

Heat transfer correlation for solid plates inserted in the flames, parallel to the flow direction, were compared with our results obtained for the calorimetric plates in the elevated position inside our furnace. It was possible to cast the heat transfer correlations into a power-law form (Eq. 4.1 to Eq. 4.3) very well for the short and long flames, and with a maximum uncertenity of 27% for the high velocity jet flame. On the other hand, the envelope flame does not fit into the group at all. The increasing tendency of the measured convective heat flux downstream the leading edge cannot be described by the same type of

heat transfer correlation.

An overwhelming majority of the impingement studies were performed in large unbounded space. As the envelope flame exsist only in a confined space with hot internal walls, those methods are not applicable. According to our best knowledge, our experimental study is the first in the open literature that tackled the heat transfer between an envelope flame and solid charge under impingement conditions.

The above analysis supports well the conclusion of Baukal[6] that in spite of the large number of studies, in many cases the heat transfer distribution can only be approximated very roughly by using the references published in the literature. Therefore, caution must be used in the absence of any experimental data.

5.1.3. Pollutant formation

The NO_x measurements have shown that the flames produced by the LNI burner produce considerably less NO_x than the others. However, at partial burner power, important deviations can occur. The recorded NO_x formation values for all the four studied flame-types were validated by calculations based on the measured temperature and velocity distributions.

A simplified numerical model was also solved to calculate the thermal NO_x formation. Sufficient measurement data were only available in the case of the envelope flame. Even in this case, the temperature and velocity distribution have to be known in the entire furnace for an accurate calculation. Although the turbulence intensity was not measured, the simplified numerical model gave the essential tendencies of the NO_x formation correctly.

5.2 Some suggested future works

The developed methodology permits the testing of virtually any type of gas-fuelled burners up to 150 kW nominal power. This offers the potential to extend the applicability of the results presented here to other burner and flame types.

Using the actually available two burners, experimental tests at 50% burner power for the impingement arrangement were not performed. The performance of reduced power tests could be useful to check the differences in the convective and radiative heat fluxes at the impingement point. Reduced power tests can also be made by cold refractory conditions, directly after burner start, to suppress the indirect radiation.

After Kataoka et al.[8] the maximal heat fluxes in direct flame impingement are produced in the critical point. In the case of the high velocity flame, this is located just before the first viewing port. On the contrary, in the case of the long, the short and the envelope flames, the critical point falls about between the first and second furnace sections. Thus, with a little transformation of the furnace, namely by placing the vertical calorimetric plates just after the first horizontal plate, the incident heat flux for all flames could be increased significantly.

REFERENCES

1 Daily, J.W., Harleman, D.R.F., Fluid Dynamics, Addison-Wesley Publishing Company, Inc. (Canada) Limited, Don Mills, Ontario, 1966.

2 Beér, J.M., Chigier, N.A., Combustion Aerodynamics, Halsted Press Division John Wiley & Sons, Inc. New York,1972.

3 Hinze, J.O., Turbulence, An Introduction to Its Mechanism and Theory, McGraw-Hill Book Co., New York, 1959.

4 Beér, J.M., Chigier N.A., Impinging Jet Flames, Combustion and Flame, Volume 12, Issue 6, December 1968, Pages 575-586

5 Abramovich, G.N., The Theory of Turbulent Jets, The M.I.T. Press, Cambridge, Mass., 1963

6 Baukal, C.E.(Jr.) John Zink Company LLC Tulsa, Oklahoma, Heat Transfer in Industrial Combustion, CRC Press, New York, 2000

7 Forstall, W.Jr., Material and Momentum Transfer in Coaxial Gas Streams, PhD. Thesis, M.I.T. Cambridge, 1949.

8 Kataoka, K., Optimal nozzle-to-plate spacing for convective heat transfer in nonisothermal, variable-density impinging jets. Drying Tech., 3, 235-254, 1985.

9 Hinze, J.O., van der Hegge Zijnen, B.G., Appl. Sci. Research, 1A, 435 (1949)

10 Thring, M.W., Newby, M.P., 4th Symposium on Combustion, p.789, Cambridge, Mass., 1952.

11 Mathieu, J., « Contribution à l'étude aérothermique d'un jet plan évoluant en présence d'une paroi », Publication Scientifiques et Techniques du Ministère de l'Air, No. 374, Paris (1961)

12 Fox, R.W., McDonald, A.T., Introduction to Fluid Mechanics, 4th Edition, J.Wiley, c1992, New York, Toronto p.342-344

13 Popiel, Cz.O., van der Meer, Th.H, Hoogendoorn, C.J., Convective Heat Transfer on a plate in an impinging roung hot gas jet of low Reynolds number, Int.J.Heat Mass Transfer, Vol.23, pp.1055-1068, Pergamon Press Ltd 1980.

14 Schlichting, H. Boundary layer theory, 4th Ed. McGraw Hill Book Co.Inc. – New York 1962. p.590-614.

15 Hottel, H.C., Hawthorne, W.R., Third Symposium on Combustion, p.254, Williams and Wilkins, 1949.

16 Reichardt, H., Impuls und Wärmeaustausch in freier Turbulenz. ZAMM 24 268 (1944)

17 Martin, H., Heat and mass transfer between impinging gas jets and solid surfaces, Adv. Heat Transf. 13, 1-60 (1977)
18 Hinze, J.O., van der Hegge Zijnen, B.G., Transfer of heat and matter in the turbulent mixing zone of an axially symmetric jet. Proc. 7th Intern. Congr. Appl. Mech. 2, Part I, 286-299 (1948)
19 Corrsin, S., Uberoi, M.S., Further experiments on the flow and heat transfer in a heated turbulent air jet. NACA TN 998 (1950)
20 Keagy, W.R., Weller, A.E., Proc. Heat Transfer and Fluid Mechanics Inst., Berkeley Calif., 1949, p.89.
21 Sunavala, P.D., Hulse, C., Thring, M.W., Combustion and Flame, 1, 179 (1957).
22 Anderson, J.E., Stresino, E.F., Heat Transfer from flames impinging on flat and cylindrical surfaces, J. Heat Transfer 85(1), 49-54, 1963.
23 Woodruff, L.W., Giedt, W.H., Heat transfer measurements from a partially dissociated gas with high lewis number, J. Heat Transf., 88, 415-420, 1966.
24 Fay, R.H., Heat transfer from fuel gas flames, Welding J., Research Supplement, 380s-383s, 1967.
25 Reed, T.B., Heat transfer intensity from induction plasma flames and oxy-hydrogen flames, J. Appl. Phys., 34(8), 2266-2269, 1963.
26 Baukal, C.E., Heat transfer in industrial combustion, CRC Press, New York, 2000
27 Hottel, H.C., The Melchett Lecture for 1960: Radiative transfer in combustion chambers, J. Inst. Fuel, 34, 220-234, 1961.
28 Pohlhausen, E.Z., Angewandte Math. Mech., 1. 115, 1921.
29 Incropera, F.P., Dewitt, D.P., Introduction to heat transfer, 4th Edition, John Wiley and Sons, New York 2002.
30 Eckert, E.R.G., Engineering relations for heat transfer and friction in high-velocity laminar and turbulent boundary-layer flow over surfaces with constant pressure and temperature, J. Heat Trans., 78, 1273-1283, 1956
31 Giedt, W.H., Cobb, L.L., Russ, E.J., Effect of hydrogen recombination on turbulent flow heat transfer, ASME Paper 60-WA-256, New York, 1960.
32 Martin, H., Heat and mass transfer between impinging gas jets and solid surfaces - in J.P. Hartnett and T.F. Irvine, Jr., Eds., Advances in heat transfer, Vol 13, Academic Press, New York, 1977.
33 Popiel, Cz.O., and Bogusiawski, L., Mass or heat transfer in impinging single round jets emitted by a bell-shaped nozzle and sharp-ended orifice, in gas jets and solid surfaces – in C.L.Tien, V.P.Carey, and L.K.Ferrel, Eds., Heat transfer 1986, Vol 3, Hemisphere Publishing, New York, 1986.
34 Goldstein, R.J. and J.F. Timmers, Int. J. Heat Mass Transfer, 25, 1857, 1982.
35 Shorin, S.N., Pechurkin, V.A., Effectivnost teploperenosa na poverkhnost plity ot vysokotemperaturnoi strui produktov sjoraniya razlichnykh gazov, Teoriya I Praktika Szhiganiya Gaza, 4, 134-143, 1968.
36 Vizioz, J.P., Lowes, T.M., Convective heat transfer from impinging flame jets, Int'l Flame Research Found, Report F 35/a/6, IJmuiden, The Netherlands, 1971.
37 Smith, R.B., Lowes, T.M., Convective heat transfer from impinging tunnel burner flames, - A short report on the NG-4 trials, Int'l Flame Research Found, Report F

35/a/9, IJmuiden, The Netherlands, 1974.
38 Ivernel, A., Vernotte, P., Étude expérimentale de l'amélioration des transferts convectifs dans les fours par suroxygénisation du comburant, Rev. Gén. Therm., Fr., (210-211), 375-391, 1979.
39 Blasius, H.Z., Math. Phys., 56, 1, 1908. English translation in National Advisory Committee for Aeronautics Technical Memo No. 1256.
40 Kilham, J.K., Energy transfer from flame gases to solids, Third Symposium on Combustion and Flame and Explosion Phenomena, Williams and Wilkins, Baltimore, MD, 1949, 733-740
41 Jackson, E.G., and Kilham, J.K., Heat transfer from combustion products by forced convection, Ind. Eng. Chem., 48(11), 2077-2079, 1956.
42 Hustad, J.E., Sonju, O.K., Heat transfer to pipes submerged in turbulent jet diffusion flames, Heat Transfer in Radiating and Combusting Systems, Springer Verlag, Berlin, 1991, 474-490
43 Hustad, J.E., Rokke, N.A., Sonju, O.K., Heat transfer to pipes submerged in lifted buoyant diffusion flames, Experimental Heat Transfer, Fluid Mechanics and Thermodynamics, 1991, J.F.Keffer et al., Eds., Elsevier, New York, 1991, 567-574.
44 Davis, R.M., Heat transfer measurements on electrically boosted flames, Tenth Symposium (Intl.) on Combustion, The Combustion Institute, Pittsburgh, PA, 1965, 755-766.
45 Hoogendoorn, C.J., Popiel, C.O., van der Meer, T.H., Turbulent heat transfer on a plane surface in impingement round premixed flame jets, Proc. of 6th Int. Heat Trans., 23, 1055-1068, 1980.
46 Sibulkin, M., Heat transfer near the forward stagnation point of a body of revolution, J. Aero. Sci., 19, 570-571, 1952.
47 Baukal C.E., Gebhart, B., A review of semi-analytic solutions for flame impingement heat transfer, Int. J. Heat and Mass Trans., 39(14), 2989-3002, 1996.
48 Hemeson, A.O., Horsley M.E., Purvis, M.R.I., Tariq, A.S., Heat transfer from flames to convex surfaces, Inst. of Chem. Eng. Symp. Series, 2(86), 969-978. Publ. by Inst. of Chem. Eng., Rugby. U.K., 1984.
49 Van der Meer, T.H., Stagnation point heat transfer from turbulent low Reynolds number jets and flames jets, Exper. Ther. Fluid Sci., 4, 115-126, 1991.
50 Horsley M.E., Purvis, M.R.I., Tariq, A.S., Convective heat transfer from laminar and turbulent premixed flames, in Heat Transfer 1982., U Grigull, E. Hahne, K. Stephan, and J. Straub, Eds., Hemisphere, Washington, D.C., 3, 409-415, 1982.
51 Hargrave, G.K., Kilham, J.K., The effect of turbulent intensity on convective heat transfer from premixed methane-air flames, Inst. Chem. Eng. Symp. Ser., 2(86), 1025-1034, 1984.
52 Fay, J.A., Riddell, F.R., Theory of stagnation point heat transfer in dissociated air, J. Aero. Sci., 25, 73-85, 1958.
53 Baukal C.E., Gebhart, B., A review of flame impingement heat transfer studies, 1. Experimental conditions, Comb. Sci. Tech. 104, 339-357, 1995.
54 Kataoka, K., Shundoh, H., Matsuo H, Convective heat transfer between a flat plate and a jet of hot gas impinging on it, in Drying '84, A.S., Majumdar, Ed.,

Hemisphere/Springer Verlag, New York, 1984, 218-227.
55 Matsuo, M., Hattori, M., Ohta, T., Kishimoto, S., The experimental results of the heat transfer by flame impingement, Intl. Flame Research Found. Report F29/1a/1, Ijmuiden, The Netherlands, 1978.
56 You, H.-Z., Investigation of fire impingement on a horizontal ceiling. 2. Impingement and ceiling-jet regions, Fire & Materials, 9(1), 46-56, 1985.
57 Kremer, H., Buhr, E., Haupt, R., Heat transfer from turbulent free-jet flames to plane surfaces, in Heat Transfer in Flames, N.H.Afgan, J.M.Beér, Eds., Scripta Book Company, Washington, D.C., 1974, 463-472.
58 Buhr, E., Haupt, G., Kremer, H., Heat transfer from impinging turbulent jet flames to plane surfaces, in Combustion Institute European Symposium 1973, F.J.Weinberg, Ed., Academic Press, New York, 1973, 607-612.
59 Buhr, E., Über den Wärmeflub in Staupunkten von turbulenter Freistrahl-Flammen an gekühlten platten, PhD. Thesis, University of Trier-Kaiserslautern, Kaiserslautern, Germany, 1969.
60 Hustad, J.E., Jacobsen, M., Sonju, O.K., Radiation and heat transfer in oil/propane jet diffusion flames, Inst. Chem. Eng. Symp. Series, 10(129), 657-663, 1992.
61 Hargrave, G.K., Fairweather, M., Kilham, J.K., Forced convective heat transfer from premixed flames. 2. Impingement heat transfer, Int. J. Heat Fluid Flow, 8(2), 132-138, 1987.
62 Fells, I., Harker, J.H., An investigation into heat transfer from unseeded propane-air flames augmented with D.C. electrical power, Comb. Flame, 12, 587-596. 1968.
63 Davies, D.R., Heat transfer from working flame burners. B.S. thesis, Univ. of Salford, Salford, U.K. 1979.
64 Galloway, T.R., Sage, B.H., Thermal and material transfer from spheres, prediction of local transport, Int. J. Heat Mass Trans., 13, 1382-1386, 1970.
65 Fairweather, M., Kilham, J.K., Nawaz, S., Stagnation point heat transfer from laminar, high temperature methane flames, Int. J. Heat Fluid Flow, 5(1), 21-27, 1984.
66 Thring, M.W., Newby, M.P., Combustion length of enclosed turbulent jet flames, Fourth Symposium on Combustion, pp. 789-796, Williams and Wilkins, Baltimore, 1953.
67 Craya, A., Curtet, R., Compt. Rend. 1955, 241, 1, pp. 621-622.
68 Barchilon, M., Curtet, R., J. Basic Eng. (Trans. ASME) 1964. p.777.
69 Marinov, N. M., Pitz, W. J., Westbrook, C. K., Vincitore, A. M., Castaldi, M. J., Senkan, S. M. "Aromatic and Polycyclic Aromatic Hydrocarbon Formation in a Laminar Premixed n-Butane Flame" Combustion and Flame 114 192-213 (1998). UCRL-WEB-204236 Review and release date: May 19, 2004.
70 Rhine, J.M., Tucker, R.J., Modelling of gas-fired furnaces and boilers, British Gas, McGraw-Hill Book Co. New York, 1991.
71 AEA Technology, 2001, CFX-TASCflow and CFX-5 Documentation.
72 Lockwood, F.C., Romo-Millanes, C.A., Mathematical Modelling of Fuel - NO Emissions From PF Burners. J. Int. Energy, 65:144-152, September 1992.
73 Smoot, L.D., Smith, P.J., NOx Pollutant Formation in a Turbulent Coal System. In Coal Combustion and Gasification, page 373, Plenum, Plenum, NY, 1985.

74 Levy, J.M., Chen, L.K., Sarofim, A.F., and Beer, J.M., NO/Char Reactions at Pulverized Coal Flame Conditions. In 18th Symp. (Int'l.) on Combustion. The Combustion Institute, 1981.
75 De Soete, G.G., Overall Reaction Rates of NO and N_2 Formation from Fuel Nitrogen. In 15th Symp. (Int'l.) on Combustion, page 1093. The Combustion Institute, 1975.
76 Dugué, J., Saponaro, A., and Weber, R., Development of Multi-Fuel Low NO_x Burner Technology IFRF - Ijmuiden, April 1991. Phase One: Natural Gas Burner
77 Takahashi, Y. et al. Development of Mitsubishi "MACT" in furnace NO_x removal process. Presented at US-Japan NO_x information exchange, Tokyo, May 25-30, 1981
78 Drake, M.C., Correa, S.M., Pitz, R.W., Shyy, W., and Fenimore, C.P., Superequilibrium and Thermal Nitric Oxide Formation in Turbulent Diffusion Flames. Combustion and Flame, 69:347-365, 1987.
79 Westenberg, A.A., Comb. Sci. Tech., 4:59, 1971.
80 Fluent 6.0, Documentation Fluent Inc 2001-11-29
81 Fenimore, C.P., Formation of Nitric Oxide in Premixed Hydrocarbon Flames. In 13th Symp. (Int'l.) on Combustion, page 373. The Combustion Institute, 1971.
82 Barnes, F.J., Bromly, J.H., Edwards, T.J., Madngezewsky, R., NOx Emissions from Radiant Gas Burners. Journal of the Institute of Energy, 155:184-188, 1988.
83 Hanson, R.K., Salimian, S., Survey of Rate Constants in H/N/O Systems. In W. C. Gardiner, editor, Combustion Chemistry, page 361, 1984.
84 Siegel, R., Howell, J., Thermal radiation heat transfer, 4ed., Taylor and Francis, New York, 2002,
85 Környei, T., Hőátvitel, Budapesti Műszaki Egyetem, 1999.
86 Hirschfelder, J.O., Curtiss, C.F., Bird, R.B., Molecular theory of gases and liquids, John Wiley and Sons, Inc. New York, 1954.
87 Hottel, H.C., Sarofim, A.F., Radiative Transfer, McGraw-Hill, New York, 1967.
88 Eckert, E.R.G., Drake, R.M.Jr., Heat and Mass Transfer, 2d. Ed., McGraw-Hill, New York, 1959.
89 Sato, T., Matsumoto, R., Radiant heat transfer from luminous flame, Int. Develop. Heat Transfer, ASME, pp. 804-811, 1963.
90 Leckner, B., Spectral and total emissivity of water vapor and carbon dioxide, Comb.Flame, 19, 33-48, 1972.
91 Echigo, R., Nishiwaki, R., Hirata, M., A study on the radiation of luminous flames, Eleventh Symposium International on Combustion, The Combustion Institute, Pittsburgh, PA., 1967, 381-389.
92 Talmor, E., Combustion hot spot analysis for fired process heaters, Gulf Publishing, Houston, TX, 1982.
93 Monchick, L., Mason, E.A., Transport properties of polar gases, J. Chem. Phys., 35, p. 1676. 1961.
94 Warnatz, J., Influence of transport models and boundary conditions on flame structure, Numerical methods in flame propagation, Eds. N. Peters and J. Warnatz, Friedr. Vieweg and Sohn, Wiesbaden
95 Parker, J.G., Rotational and vibrational relaxation in diatomic gases, Phys. of fluids, 2.p.449, 1959.

96 Brau, C.C., Jonkman, R.M., Classical theory of rotational relaxation in diatomic gases, J. Chem. Phys., 52. p. 447., 1970.
97 Chedaille, J., and Brand, Y., Industrial Flames, Vol. I. - Measurements in Flames, edited by J. M. Beér and M. W. Thring, Crane, Russak, New York, 1972.
98 Kaskan, W. E., "The Dependence of Flame Temperature on Mass Burning Velocity' Sixth Symposium (International) on Combustion, Reinhold, New York, 1957, pp. 134-143.
99 Bilger, R. W., "Probe Measurements in Turbulent Combustion" published elsewhere in this volume.
100 Warshawsky, I., Kuhns, P. W., "Review of the Pneumatic-Probe Thermometer" pp. 573-586 - Dahl, A. I. (ed.) Temperature – Its Measurements and Control in Science and Industry, Vol. 3, Part 2, Reinhold, New York, 1962.
101 Bowman, C. T., and Cohen, L. S., "Influence of Aerodynamic Phenomena in Pollutant Formation in Combustion" Rept. EPA-650/2-75-061a, July 1975, Environmental Protection Agency.
102 Glave, G. E., Johnson, R. C., and Krause, L. N., "Intercomparison of Several Pyrometers in a High Temperature Gas Stream" pp. 601-605 - Dahl, A. I. (ed.) Temperature – Its Measurements and Control in Science and Industry, Vol. 3, Part 2, Reinhold, New York, 1962
103 Bowman, C. T. - Probe Measurements in Flames (1976) Stanford University, California – Progress in Astronautics and Aeronautics, Vol.53.
104 Takeshi Kunitomo – Kyoto University, Japan - Measurement Techniques in Combustion Engineering
105 Fingerson, L. M., Adrian, R. J., and Kaufman, S. L., "Laser Doppler Velocimetry: Theory, Application, and Techniques," TSI LDV Course Text, 1990.
106 Becker, H. A., Physical Probes for Combustion - Technical Report CAGCT.TR.001. Centre for Advanced Gas Combustion Technology – Queens University at Kingston 1991.
107 Becker, H. A., and Brown, A. P. G., Twelfth Symposium (International) on Combustion, p. 1059, The Combustion Institute – 1974.
108 Cho, S. H., and Becker, H. A., Experiments in Fluids 3, 93 - 1985.
109 Pankhurst, R. C., Holder, D. W., 1952. Wind-Tunnel Technique, Pitman
110 Becker, H. A., and Brown, A. P. G., 1974. Pitot Response Functions for Turbulent Flows, Rept. No. 2-72, Thermal and Fluid Sciences Group, Dept. of Chem. Engrg., Queens University, Kingston, Canada
111 BACHARACH Inc. – www.bacharach-inc.com, 625. Alpha Drive, Pittsburgh, PA.
112 Kiss L.I., Charette, A., Bui, R.T., "The Determination of Thermal Boundary and Coupling Conditions on Furnace Walls", Proc. Intl. Conf. Num. Exp. Methods in Heat Transfer, ed. P. Brebbia, 1991, 256-267.
113 Walter G., Hagyományos és alacsony NO_x emissziójú gázégők összehasonlító vizsgálata (in Hungarian) – MSc Thesis, BME – Budapest, 2000.
114 Versteeg, H.K., Malalasekera, W., An introduction to computational fluid dynamics, The finite volume method, 1995.

APPENDIX A
CALCULATION OF THE TRANSPORT AND THERMODYNAMICAL PROPERTIES USING THE CHEMKIN DATABASE

A.1 The transport properties of single components

The transport and thermodynamical properties are evaluated using the CHEMKIN[69] database. The single component viscosities are given by the standard kinetic theory expression by Hirschfelder et al.[86]:

$$\mu_k = \frac{5}{16}\frac{\sqrt{\pi M_k k_B T / N_A}}{\pi \sigma_k^2 \Omega^{(2,2)*}}$$

Eq. A.1

where σ_k is the Lennard-Jones collision diameter, M_k is the molar mass, k_B is the Boltzmann constant, N_A is the Avogadro number and T is the temperature. The collision integral, $\Omega^{(2,2)*}$, is used to correct the electromagnetic interactions. It depends on the reduced temperature given by:

$$T_k^* = \frac{k_B T}{\varepsilon_k}$$

Eq. A.2

and the reduced dipole moment given by

$$\delta_k^* = \frac{1}{2}\frac{\lambda_k^2}{\varepsilon_k \sigma_k^3},$$

Eq. A.3

where ε_k is the Lennard-Jones potential well depth and λ_k is the dipole moment. In a first approximation, the collision integral was taken to unity according to the pool-balls model. Finally, in the developed model, the collision integral values were determined by a quadratic interpolation of the tables based on the Stockmayer potentials given in Monchick and Mason[93] (Table A.1 and Table A.2).

TABLE III (a). $\Omega^{(1,1)*}$.

T^* \ δ^*	−2.5	−2.0	−1.5	−1.0	−0.5	0	0.25	0.5	0.75	1.0	1.5	2.0	2.5
0.1	32.491	27.796	23.860	17.337	11.034	4.0079	2.5030	4.8195	7.0752	8.7831	11.683	14.223	16.042
0.2	20.231	17.334	14.250	10.858	7.0967	3.1300	1.8648	2.5558	4.1729	5.3663	7.2732	8.9026	10.378
0.3	15.325	13.141	10.815	8.2836	5.5257	2.6494	1.6049	1.8216	3.0004	3.9671	5.4825	6.7496	7.8875
0.4	12.581	10.796	8.8974	6.8508	4.6309	2.3144	1.4442	1.4983	2.3752	3.1825	4.4702	5.5351	6.4844
0.5	10.796	9.2718	7.6516	5.9160	4.0268	2.0661	1.3343	1.3208	1.9970	2.6795	3.8070	4.7390	5.5655
0.6	9.5286	8.1904	6.7712	5.2434	3.5795	1.8767	1.2556	1.2156	1.7489	2.3329	3.3346	4.1700	4.9086
0.7	8.5753	7.3764	6.1031	4.7278	3.2304	1.7293	1.1966	1.1462	1.5766	2.0795	2.9798	3.7400	4.4118
0.8	7.8277	6.7363	5.5738	4.3143	2.9491	1.6122	1.1509	1.0973	1.4514	1.8850	2.7031	3.4019	4.0205
0.9	7.2226	6.2159	5.1402	3.9730	2.7172	1.5175	1.1144	1.0609	1.3571	1.7411	2.4815	3.1284	3.7032
1.0	6.7201	5.7816	4.7758	3.6850	2.5231	1.4398	1.0845	1.0329	1.2839	1.6235	2.3001	2.9023	3.4399
1.2	5.9263	5.0899	4.1924	3.2244	2.2173	1.3204	1.0382	0.99162	1.1787	1.4496	2.0215	2.5495	3.0269
1.4	5.3195	4.5588	3.7421	2.8717	1.9888	1.2336	1.0038	0.96264	1.1070	1.3263	1.8185	2.2869	2.7165
1.6	4.8352	4.1326	3.3823	2.5932	1.8131	1.1679	0.97690	0.94058	1.0553	1.2394	1.6946	2.0838	2.4742
1.8	4.4363	3.7816	3.0880	2.3694	1.6745	1.1166	0.95503	0.92286	1.0161	1.1719	1.5445	1.9225	2.2797
2.0	4.1006	3.4873	2.8428	2.1852	1.5626	1.0753	0.93686	.90797	0.98537	1.1189	1.4484	1.7912	2.1199
2.5	3.4515	2.9229	2.3808	1.8463	1.3614	1.0006	0.90147	0.87918	0.93080	1.0261	1.2763	1.5509	1.8232
3.0	2.9827	2.5221	2.0594	1.6168	1.2286	0.95003	0.87520	0.85747	0.89424	0.96385	1.1630	1.3887	1.6188
3.5	2.6294	2.2243	1.8258	1.4531	1.1353	0.91311	0.85440	0.83989	0.86740	0.92332	1.0831	1.2724	1.4701
4.0	2.3546	1.9960	1.6495	1.3318	1.0662	0.88453	0.83720	0.82506	0.84668	0.89140	1.0239	1.1852	1.3573
5.0	1.9592	1.6729	1.4042	1.1650	0.97130	0.84277	0.80977	0.80067	0.81486	0.84594	0.94178	1.0637	1.1982
6.0	1.6916	1.4582	1.2435	1.0567	0.90894	0.81287	0.78837	0.78154	0.79143	0.81432	0.88729	0.98319	1.0916
7.0	1.5008	1.3070	1.1318	0.98147	0.86449	0.78976	0.77086	0.76543	0.77282	0.79045	0.84814	0.92586	1.0155
8.0	1.3595	1.1958	1.0494	0.92618	0.83109	0.77111	0.75694	0.75162	0.75737	0.77142	0.81835	0.88283	0.95847
9.0	1.2507	1.1110	0.98706	0.88364	0.80494	0.75553	0.74322	0.73954	0.74416	0.75565	0.79471	0.84923	0.91405
10.0	1.1636	1.0441	0.93615	0.84990	0.78360	0.74220	0.73191	0.72861	0.73262	0.74224	0.77533	0.82214	0.87844
12.0	1.0403	0.94699	0.86001	0.79581	0.75055	0.72092	0.71269	0.71042	0.71316	0.72023	0.74504	0.78084	0.82468
14.0	0.95392	0.87951	0.81546	0.76397	0.72575	0.70234	0.69678	0.69505	0.69714	0.70261	0.72202	0.75047	0.78576
16.0	0.89067	0.82589	0.77819	0.73667	0.70615	0.68776	0.68322	0.68187	0.68354	0.68793	0.70562	0.72688	0.75603
18.0	0.84280	0.78194	0.74929	0.71501	0.69007	0.67510	0.67144	0.67036	0.67174	0.67536	0.68838	0.70782	0.73240
20.0	0.80498	0.76209	0.72605	0.69726	0.67649	0.66405	0.66103	0.66015	0.66138	0.66439	0.67539	0.69194	0.71301
25.0	0.73865	0.70865	0.68355	0.66351	0.64973	0.64136	0.63938	0.63884	0.63970	0.64183	0.64958	0.66134	0.67647
30.0	0.69505	0.67267	0.65416	0.63977	0.62950	0.62350	0.62211	0.62175	0.62244	0.62404	0.62987	0.63873	0.65026
35.0	0.66372	0.64638	0.63216	0.62115	0.61331	0.60882	0.60780	0.60755	0.60814	0.60939	0.61398	0.62099	0.63011
40.0	0.63977	0.62598	0.61475	0.60603	0.59988	0.59640	0.59563	0.59544	0.59597	0.59698	0.60072	0.60642	0.61386
50.0	0.60473	0.59563	0.58819	0.58246	0.57848	0.57626	0.57578	0.57666	0.57612	0.57681	0.57946	0.58347	0.58871
75.0	0.55113	0.54806	0.54560	0.54378	0.54254	0.54186	0.54128	0.54138	0.54158	0.54206	0.54338	0.54532	0.54782
100.0	0.51718	0.51777	0.51829	0.51875	0.51915	0.51805	0.51795	0.51860	0.51820	0.51901	0.52064	0.52049	0.52153

L. MONCHICK AND E. A. MASON

Table A.1 Collision integrals of polar gases according to Monchick and Mason[93]

TABLE III (b). $\Omega^{(s,s)*}$.

T^* \ δ^*	−2.5	−2.0	−1.5	−1.0	−.5	0	0.25	0.5	0.75	1.0	1.5	2.0	2.5
0.1	29.139	25.148	20.830	16.015	10.451	4.1005	3.0142	6.4500	9.4870	11.699	15.508	18.860	21.923
0.2	18.420	15.917	13.211	10.225	6.8596	3.2626	2.1702	3.2515	5.6362	7.1946	9.6786	11.820	13.765
0.3	14.097	12.196	10.146	7.9029	5.4303	2.5399	1.8408	2.2186	4.0126	5.3309	7.3133	8.9737	10.471
0.4	11.668	10.106	8.4375	6.6083	4.6384	2.5310	1.6348	1.7708	3.1216	4.2632	5.9726	7.3682	8.6157
0.5	10.081	8.7416	7.3096	5.7737	4.1155	2.2837	1.4952	1.5375	2.5764	3.5654	5.0888	6.3144	7.4001
0.6	8.9498	7.7708	6.5189	5.1848	3.7272	2.0838	1.3966	1.3997	2.2184	3.0764	4.4541	5.5594	6.5307
0.7	8.0965	7.0416	5.9275	4.7397	3.4170	1.9220	1.3241	1.3105	1.9705	2.7178	3.9732	4.9867	5.8723
0.8	7.4276	6.4722	5.4661	4.3847	3.1585	1.7902	1.2691	1.2487	1.7914	2.4458	3.5951	4.5346	5.3528
0.9	6.8882	6.0142	5.0923	4.0903	2.9388	1.6823	1.2259	1.2034	1.6576	2.2341	3.2899	4.1672	4.9306
1.0	6.4427	5.6362	4.7810	3.8363	2.7488	1.5929	1.1913	1.1688	1.5544	2.0657	3.0384	3.8618	4.5794
1.2	5.7488	5.0427	4.2814	3.4239	2.4382	1.4551	1.1391	1.1192	1.4076	1.8169	2.6495	3.3822	4.0259
1.4	5.2280	4.5900	3.8897	3.0928	2.1967	1.3551	1.1012	1.0846	1.3091	1.6440	2.3638	3.0221	3.6074
1.6	4.8159	4.2254	3.5677	2.8214	2.0057	1.2800	1.0722	1.0587	1.2390	1.5182	2.1464	2.7446	3.2786
1.8	4.4774	3.9202	3.2965	2.5954	1.8522	1.2219	1.0492	1.0382	1.1865	1.4232	1.9762	2.5293	3.0131
2.0	4.1898	3.6589	3.0638	2.4045	1.7270	1.1757	1.0300	1.0212	1.1455	1.3492	1.8399	2.3341	2.7939
2.5	3.6210	3.1378	2.6058	2.0413	1.4995	1.0933	0.99537	0.98859	1.0748	1.2210	1.5960	1.9969	2.3838
3.0	3.1902	2.7466	2.2710	1.7851	1.3486	1.0388	0.96545	0.96415	1.0281	1.1391	1.4361	1.7683	2.0992
3.5	2.8502	2.4433	2.0194	1.6045	1.2430	0.99963	0.94519	0.94453	0.99448	1.0822	1.3240	1.6042	1.8910
4.0	2.5756	2.2032	1.8255	1.4672	1.1655	0.96988	0.92764	0.92808	0.96854	1.0400	1.2414	1.4814	1.7326
5.0	2.1635	1.8526	1.5510	1.2754	1.0605	0.92675	0.89963	0.90136	0.93011	0.98086	1.1281	1.3108	1.5089
6.0	1.8736	1.6134	1.3694	1.1566	0.99273	0.89616	0.87766	0.88005	0.90203	0.94049	1.0539	1.1985	1.3694
7.0	1.6622	1.4429	1.2426	1.0727	0.94537	0.87272	0.85956	0.86230	0.87996	0.91048	1.0012	1.1291	1.2529
8.0	1.5035	1.3169	1.1501	1.0115	0.91013	0.85379	0.84417	0.84709	0.86180	0.88654	0.96160	1.0600	1.1734
9.0	1.3806	1.2208	1.0801	0.96522	0.88269	0.83795	0.83079	0.83379	0.84637	0.86745	0.93046	1.0142	1.1118
10.0	1.2839	1.1456	1.0256	0.92892	0.86035	0.82435	0.81895	0.82198	0.83296	0.85108	0.90517	0.97754	1.0627
12.0	1.1421	1.0361	0.94529	0.87547	0.82651	0.80184	0.79874	0.80172	0.81047	0.82449	0.86609	0.92218	0.98904
14.0	1.0452	0.96153	0.89171	0.83772	0.80132	0.78363	0.78189	0.78478	0.79207	0.80342	0.83680	0.88107	0.93627
16.0	0.97494	0.90740	0.85178	0.80938	0.78137	0.76834	0.76747	0.77024	0.77650	0.78600	0.81365	0.85108	0.89633
18.0	0.92214	0.86654	0.82120	0.78711	0.76498	0.75518	0.75488	0.75753	0.76303	0.77117	0.79464	0.82637	0.86485
20.0	0.88115	0.83457	0.79693	0.76897	0.75112	0.74364	0.74372	0.74626	0.75117	0.75828	0.77859	0.80596	0.83923
25.0	0.81004	0.77827	0.75314	0.73492	0.72377	0.71982	0.72045	0.72270	0.72662	0.73195	0.74700	0.76707	0.79150
30.0	0.76376	0.74088	0.72306	0.71041	0.70302	0.70097	0.70183	0.70381	0.70718	0.71137	0.72317	0.73876	0.75770
35.0	0.73046	0.71348	0.70044	0.69140	0.68638	0.68545	0.68641	0.68813	0.69107	0.69450	0.70412	0.71669	0.73192
40.0	0.70459	0.69195	0.68238	0.67591	0.67256	0.67232	0.67331	0.67480	0.67746	0.68028	0.68832	0.69870	0.71121
50.0	0.66536	0.65902	0.65445	0.65164	0.65061	0.65099	0.65195	0.65314	0.65538	0.65733	0.66314	0.67045	0.67917
75.0	0.60030	0.60470	0.60849	0.61171	0.61438	0.61397	0.61475	0.61624	0.61708	0.61832	0.62067	0.62330	0.62620
100.0	0.55518	0.56301	0.57833	0.58620	0.59170	0.58870	0.58931	0.59240	0.59105	0.59291	0.59278	0.59207	0.59082

Table A.2 Collision integrals of polar gases according to Monchick and Mason[93]

The pure species thermal conductivities, according to Warnatz[94], are composed of translational, rotational and vibrational contributions:

$$k_k = \frac{\mu_k}{M_k}\left(f_{trans}C_{v,trans} + f_{rot}C_{v,rot} + f_{vib}C_{v,vib}\right)$$

Eq. A.4

where

$$f_{trans} = \frac{5}{2}\left(1 - \frac{2}{\pi}\frac{C_{v,rot}}{C_{v,trans}}\frac{A}{B}\right)$$

Eq. A.5

$$f_{rot} = \frac{\rho D_{kk}}{\mu_k}\left(1 + \frac{2}{\pi}\frac{A}{B}\right)$$

Eq. A.6

$$f_{vib} = \frac{\rho D_{kk}}{\mu_k}$$

Eq. A.7

$$A = \frac{5}{2} - \frac{\rho D_{kk}}{\mu_k}$$

Eq. A.8

$$B = Z_{rot} + \frac{2}{\pi}\left(\frac{5}{3}\frac{C_{v,rot}}{\Re} + \frac{\rho D_{kk}}{\mu_k}\right)$$

Eq. A.9

where D_{kk} is the self diffusion coefficient,

$$D_{kk} = \frac{3}{16}\frac{\sqrt{2\pi N_A k_B^3 T^3 / M_k}}{p\pi\sigma_k^2 \Omega^{(1,1)*}}$$

Eq. A.10

The density comes from the equation of state for a perfect gas,

$$\rho = \frac{pM_k}{\Re T}$$

Eq. A.11

Z_{rot} is the rotational relaxation collision number. In the CHEMKIN database, $Z_{rot}(298K)$ is given. It has a temperature dependence given in an expression by Parker[95], and Brau and Jonkman[96]:

$$Z_{rot}(T) = Z_{rot}(298)\frac{F(298)}{F(T)}$$

Eq. A.12

where

$$F(T) = 1 + \frac{\pi^{\frac{3}{2}}}{2}\left(\frac{\varepsilon/k_B}{T}\right)^{\frac{1}{2}} + \left(\frac{\pi^2}{4} + 2\right)\left(\frac{\varepsilon/k_B}{T}\right) + \pi^{\frac{3}{2}}\left(\frac{\varepsilon/k_B}{T}\right)^{\frac{3}{2}}$$

Eq. A.13

In the case of linear molecule, the molar heat capacity C_v relationships are the following:

$$\frac{C_{v,trans}}{\Re} = \frac{3}{2}$$

Eq. A.14

$$\frac{C_{v,rot}}{\Re} = 1$$

Eq. A.15

$$C_{v,vib} = c_v - \frac{5}{2}\Re$$

Eq. A.16

For non linear molecules:

$$\frac{C_{v,trans}}{\Re} = \frac{3}{2}$$

Eq. A.17

$$\frac{C_{v,rot}}{\Re} = \frac{3}{2}$$

Eq. A.18

$$C_{v,vib} = c_v - 3\Re$$

Eq. A.19

where c_v is the specific heat at constant volume of the molecule and $\Re$ is the universal gas constant.

A.2 The transport properties of gas mixtures

The dynamic viscosity and thermal conductivity of ideal gas mixtures at low pressure can be calculated as follows:

$$k^0 = \sum_{i=1}^{n} \frac{k_i^0 y_i}{\sum_{j=1}^{n} y_j \phi_{i,j}}, \qquad \mu^0 = \sum_{i=1}^{n} \frac{\mu_i^0 y_i}{\sum_{j=1}^{n} y_j \phi_{i,j}}, \qquad \phi_{i,j} = \frac{\left(1 + \sqrt{\mu_i^0 / \mu_j^0} \sqrt[4]{M_j / M_i}\right)^2}{\sqrt{8\left(1 + M_i / M_j\right)}}$$

Eq. A.20

where k^0 and μ^0 are the thermal conductivity and dynamic viscosity of the gas mixture at low pressure. $\phi_{i,j}$ is the interaction parameter of the component.

The thermal conductivity and dynamic viscosity on the real pressure can be calculated as follows:

$$k = k^0 + X / \left(\Gamma Z_{cm}^5\right), \qquad \mu = \mu^0 + Y / \varsigma$$

Eq. A.21

where X is the dimensionless correction for the thermal conductivity, Y is the dimensionless correction for the viscosity, Z_{cm} is the fictive real factor in the critical point. Γ and ς are the thermal conductivity and viscosity constants.[85]

APPENDIX B
DIFFERENCES IN THE TRANSPORT AND THERMODYNAMIC PROPERTIES BETWEEN THE BURNT AND UNBURNT GAS MIXTURES

During all the experiments, natural gas was used as fuel. The data about the gas composition was delivered by the local gas-company (Polygaz). Equivalence ratio (ϕ) of 0.91 was consequently used. The mole fractions of the species in the unburnt and burnt gas mixtures are given in Table B.1.

Composition of the unburnt mixture		Composition of the burnt mixture	
0,952	CH4	0,000	CH4
8,255	N2	8,255	N2
0,004	CO2	1,006	CO2
0,000	H2O	1,978	H2O
2,190	O2	0,199	O2
0,022	C2H6	0,000	C2H6
0,002	C3H8	0,000	C3H8
0,000	C4H10	0,000	C4H10

Table B.1 Composition of the unburnt and burnt gas mixtures

In Figure B.1 to Figure B.5 the density, the dynamic viscosity, the thermal conductivity, the specific heat at constant pressure and the Prandtl number are shown for the fuel and oxidizer mixture before and after combustion process takes place.

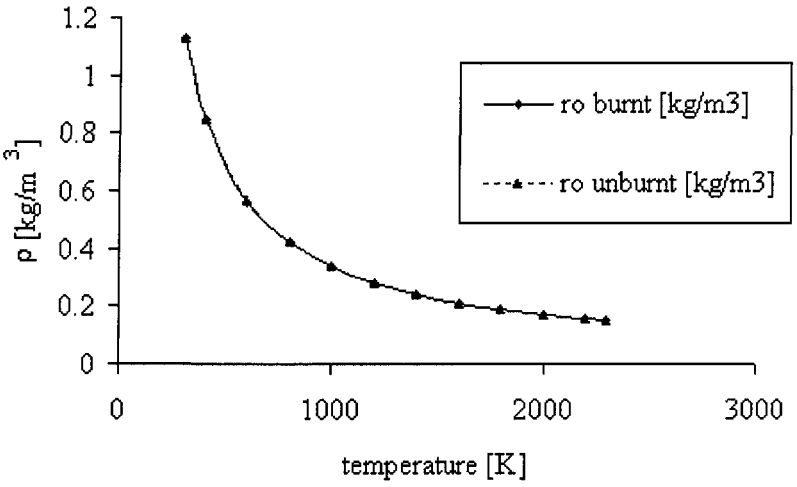

Figure B.1 Density of natural gas-air mixture ($\phi = 0.91$)

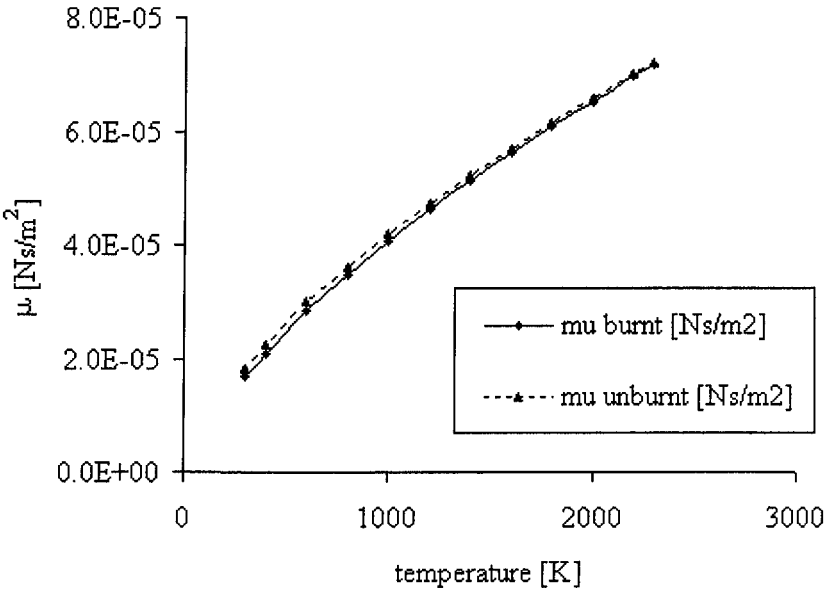

Figure B.2 Dynamic viscosity of natural gas-air mixture ($\phi = 0.91$)

APPENDIX C
3 DIMENSIONAL TEMPERATURE DIAGRAMS

All the interpolated diagrams presented here are based on experimental data which were measured using the suction pyrometer.

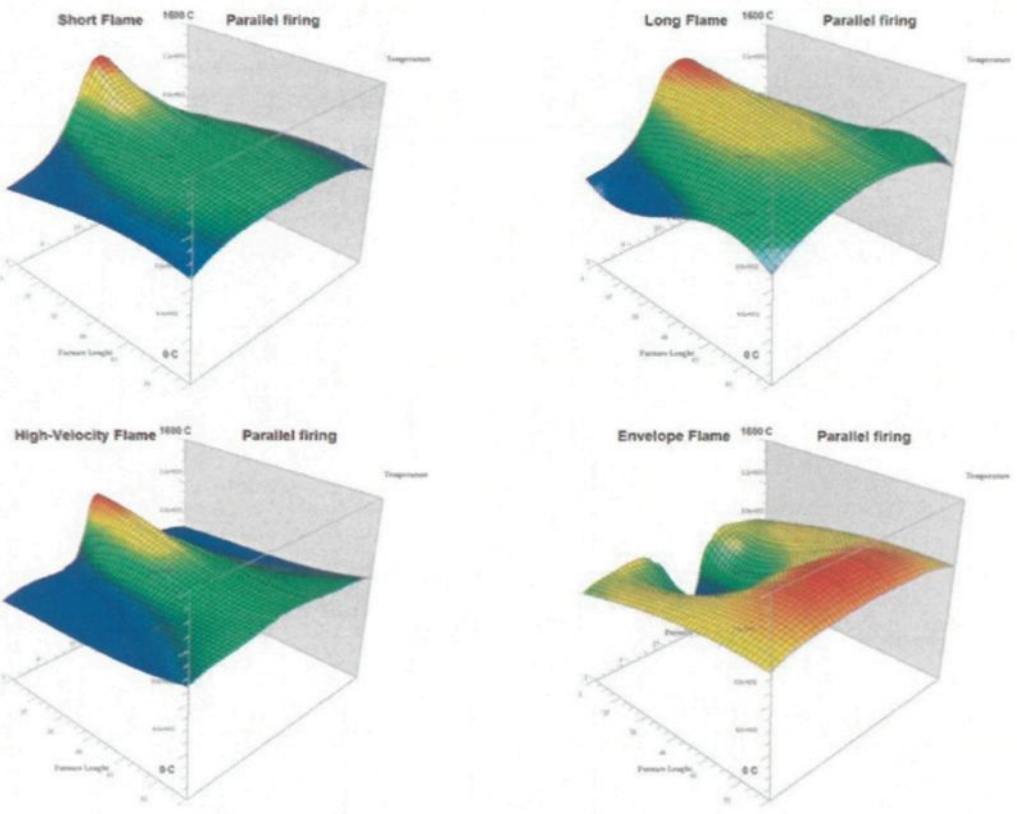

Figure C.1 – Temperature distribution (3D) for the four studied flame types at parallel firing arrangement – temperature range between 0-1600°C

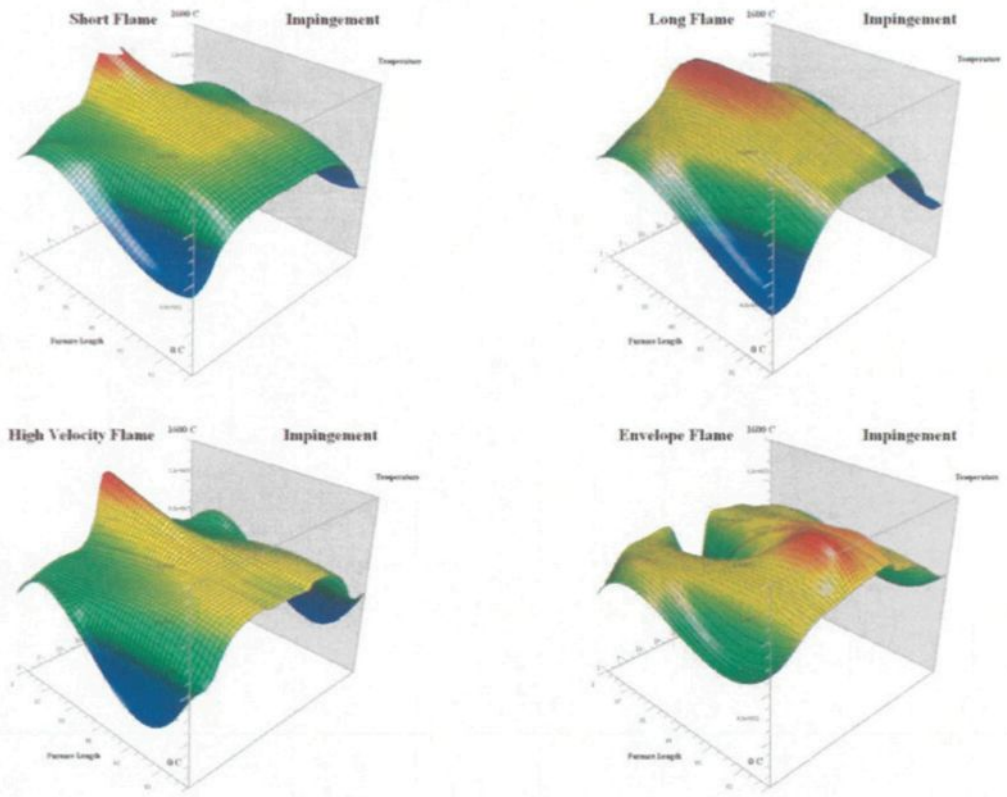

Figure C.2 – Temperature distribution (3D) for the four flame types studied at impingement arrangement – temperature range between 0-1600°C

Three dimensional temperature diagrams are presented for the four studied flame types at parallel firing and impingement configurations in Figure C.1 and Figure C.2 respectively. All the diagrams in the last two figures have the same scale, between 0-1600°C.

Three dimensional temperature diagrams are presented for the four studied flame types at parallel firing and impingement configurations also, in Figure C.3 and Figure C.4 respectively. In these cases, the temperature scale is the best adapted to each temperature distribution diagrams. This permits to compare better the particular character of the various flames.

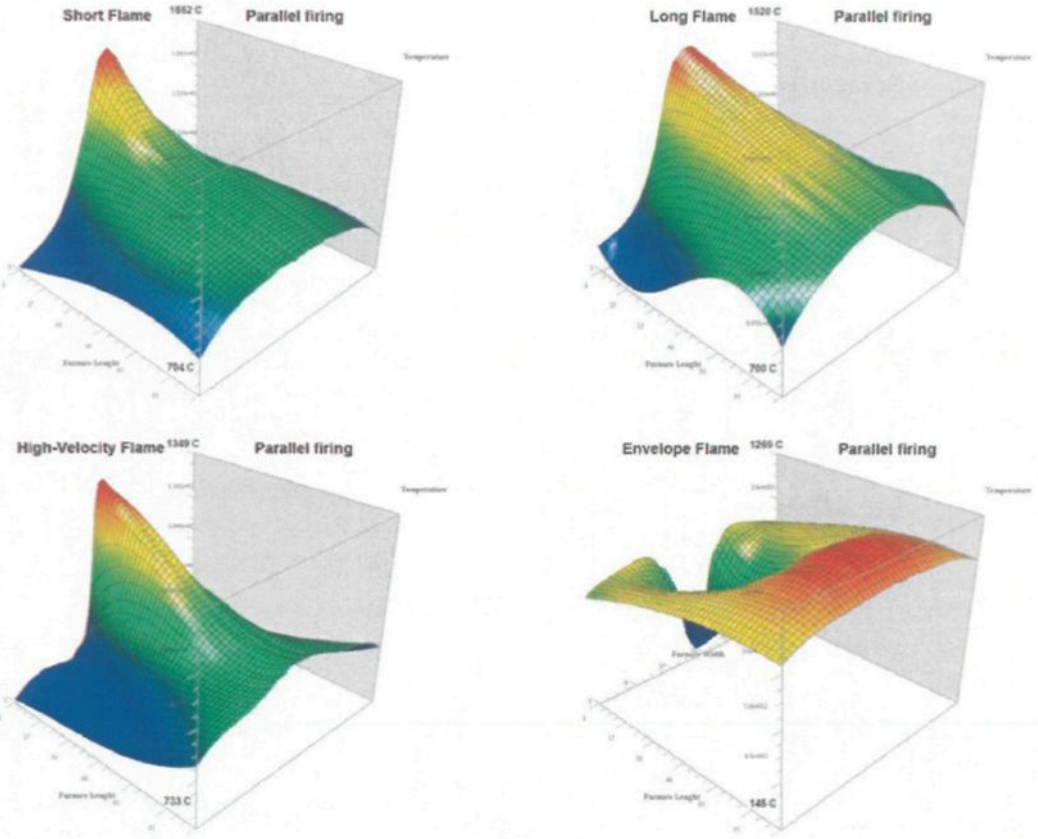

Figure C.3 Temperature distribution (3D) for the four studied flame types at parallel firing arrangement – best fitting temperature range

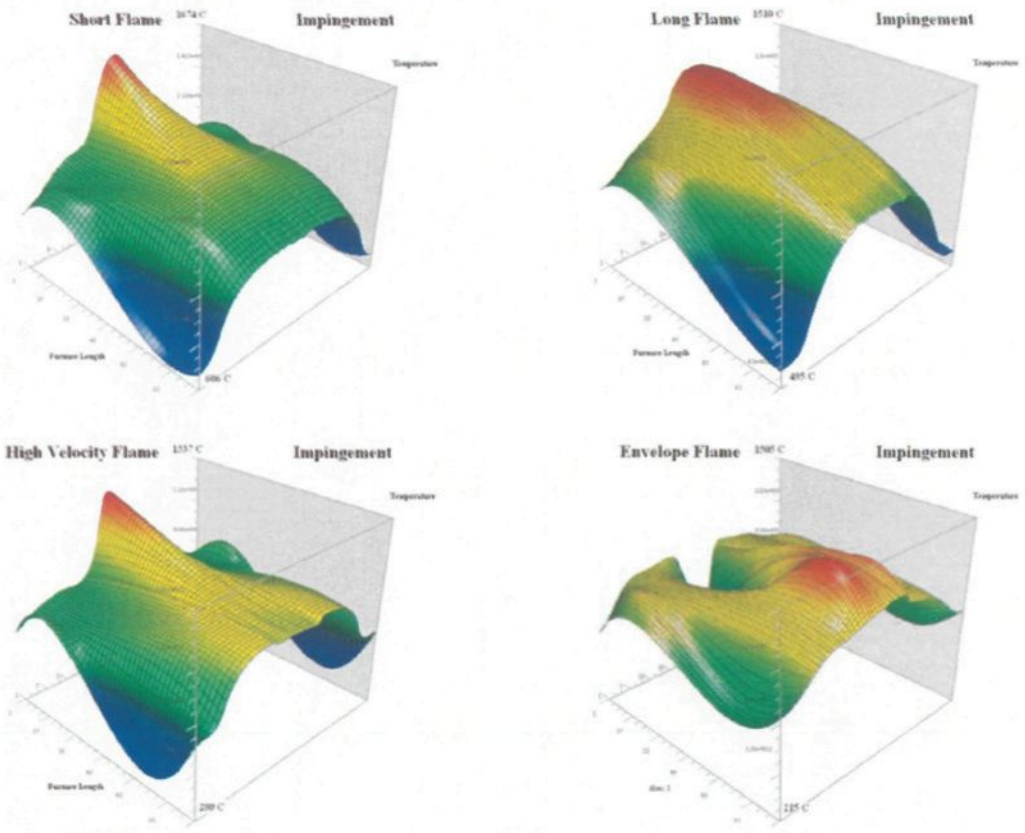

Figure C.4 Temperature distribution (3D) for the four studied flame types at impingement arrangement – best fitting temperature range

APPENDIX D
NO_x FORMATION

D.1 General formation mechanisms

In laminar flames, and at the molecular level within turbulent flames, the formation of NO_x can be attributed to four distinct chemical kinetic processes: thermal NO_x formation, prompt NO_x formation, fuel NO_x formation, and reburning. Thermal NO_x is formed by the oxidation of atmospheric nitrogen present in the combustion air. Prompt NO_x is produced by high-speed reactions at the flame front, and fuel NO_x is produced by oxidation of nitrogen contained in the fuel. The reburning mechanism reduces the total NO_x formation by accounting for the reaction of NO with hydrocarbons.

The formation of NO in natural gas flames proceeds only via thermal and prompt NO, since there is no fuel-bound nitrogen in natural gas. So, the fuel NO formation is no more discussed in this paper. Some basic reference works are [72], [73], [74] and [75].

The presence of a second mechanism leading to NO_x formation was first identified by Fenimore[81] and was termed "prompt NO_x". There is good evidence that prompt NO_x can be formed in a significant quantity in some combustion environments, such as in low-temperature, fuel-rich conditions and where residence times are short. Surface burners,

staged combustion systems, and gas turbines can create such conditions[82]. In stationary combustors, the majority of the NO_x comes from the thermal route, the amount of prompt NO formation being about an order of magnitude smaller than thermal NO. So, the calculation which will be presented below is based on the thermal formation of NO_x, while the prompt way is neglected.

It can be calculated that the initial rate of thermal NO formation is about 10 ppm/s at 1400°C. However, this rate can become very high at high temperature. The main way to control NO_x emissions in natural gas flames is to keep the peak flame temperature below 1500-1550°C. A more detailed theoretical background about the thermal NO_x formation is given below in this chapter.

As it was mentioned above, NO_x destruction reactions are also present in flames, in particular in staged flames. These reactions include for example recombination of NO_x with CX radicals resulting in complex nitrogen containing intermediates. These intermediates may be subsequently reduced to N_2. The reduction of NO_x by CX radicals occurs preferably in an oxygen lean environment. A second mechanism of NO reduction is via the reverse Zeldovich reaction. It is very temperature dependent and of little significance at temperatures below 1800K[76]. The application of reburning technology has been pioneered by Mitsubishi Heavy Industries with the MACT (Mitsubishi Advanced Combustion Technology) process[77].

In our case, the NO_x destruction reactions can always be neglected due to the reasons mentioned further down. Direct fuel staging has not been applied during the comparative study; the excess air ratio was always set up at the same level (about 10%). Apart from the

envelope flame, the three other flames (long, short and high velocity) are all well-mixed and ignited inside the burner nozzle. Thus, instead of fuel rich zones, oxygen rich zones are present in these flames. On the contrary, in the case of the envelope flame, the mixing takes place only later downstream in the combustion chamber. However, the injected gas and a separately injected air have low temperature downstream the nozzle exit. Therefore, in spite of the presence of an important fuel rich zone downstream the nozzle exit, the above mentioned NO_x formation reactions cannot be realized due to the high activation energy of these chemical reactions.

D.2 Thermal NO Formation

The formation of thermal NO_x is determined by a set of highly temperature-dependent chemical reactions known as the Zeldovich mechanism. The principal reactions governing the formation of thermal NO_x from molecular nitrogen are as follows:

$$O + N_2 \underset{k_{1b}}{\overset{k_{1f}}{\rightleftharpoons}} NO + N$$

Eq. D.1

$$N + O_2 \underset{k_{2b}}{\overset{k_{2f}}{\rightleftharpoons}} NO + O$$

Eq. D.2

In sub or near stoichiometric conditions, a third reaction may be important:

$$N + OH \underset{k_{3b}}{\overset{k_{3f}}{\rightleftharpoons}} H + NO$$

Eq. D.3

When this step is included with the first two, it is referred to as the extended Zeldovich mechanism. The expressions for the rate coefficients for reactions of Eq. D.1, Eq. D.2 and

Eq. D.3 are given below. These formulas were selected based on the evaluation of Hanson and Salimian[83].

$$k_{1f} = 1.8 \cdot 10^{8} \cdot e^{-\frac{38370}{T}} \left[\frac{m^3}{mol \cdot s} \right]$$

Eq. D.4

$$k_{1b} = 3.8 \cdot 10^{7} \cdot e^{-\frac{425}{T}} \left[\frac{m^3}{mol \cdot s} \right]$$

Eq. D.5

$$k_{2f} = 1.8 \cdot 10^{4} T \cdot e^{-\frac{4680}{T}} \left[\frac{m^3}{mol \cdot s} \right]$$

Eq. D.6

$$k_{2b} = 3.8 \cdot 10^{3} T \cdot e^{-\frac{20820}{T}} \left[\frac{m^3}{mol \cdot s} \right]$$

Eq. D.7

$$k_{3f} = 7.1 \cdot 10^{7} \cdot e^{-\frac{450}{T}} \left[\frac{m^3}{mol \cdot s} \right]$$

Eq. D.8

$$k_{3b} = 1.7 \cdot 10^{8} \cdot e^{-\frac{24560}{T}} \left[\frac{m^3}{mol \cdot s} \right]$$

Eq. D.9

The reverse reactions can be neglected and a steady state concentration of N can be assumed. As it was discussed above, in the experiments outlined at UQAC, super-stoichiometric conditions were set up, so the extended Zeldovich mechanism is also negligible. In the reactions Eq. D.1 and Eq. D.2, the first step tends to be rate limiting, producing both an NO and N radical species. The N radical is assumed to be oxidized by reaction Eq. D.2 in the Zeldovich mechanism. Either way, the second oxidation reaction is

assumed to be fast and if reaction Eq. D.1 occurs, then two NO molecules will be formed. The thermal NO formation rate can be written as follows:

$$\frac{d[NO]}{dt} = 2k_{1f}[N_2][O\ ]$$

Eq. D.10

The formation rate of NO is therefore a function of k_{1f} and the oxygen availability. The reaction constant k_{1f} is strongly dependent upon temperature because of its high activation energy. Figure D.1 presents the reaction rate of NO formation in function of temperature. The possible way of determining the oxygen radicals in the high temperature regions is presented below in this chapter accordingly to Westenberg[79].

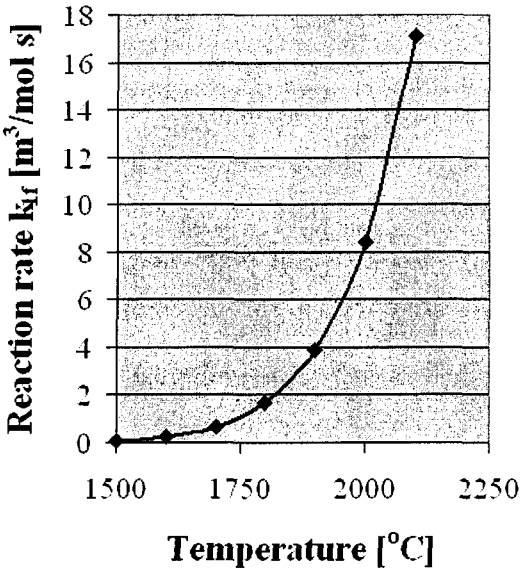

Figure D.1 The reaction rate of thermal NO formation as a function of the temperature

Consequently, all control strategies aimed at reducing thermal NO formation attempt to decrease peak flame temperatures and the residence time in the high temperature regions. The two flames produced by the LNI Burner used in our experimental test, are based on the

same principle. The high velocity flame traverses the elevated temperature region six times faster of than the flames produced by the traditional burner, thus reducing the residence time in the high temperature regions. On the other hand, the envelope flame has no temperature peaks above 1500°C.

APPENDIX E
RADIATION TRANSFER FROM SURFACES AND GASES

E.1 Radiation transfer from surfaces

Thermal radiation occurs within the ultraviolet, the visible and the infrared regions of the electromagnetic spectrum ($1 \cdot 10^{-7} \div 1 \cdot 10^{-4} m$). The monochromatic emissive power of a black surface (perfect emitter) was derived first by Planck, and it is given by:

$$E_{b,\lambda} = \frac{c_1 \lambda^{-5}}{\exp(c_2/(\lambda T)) - 1}$$

Eq. E.1

where $c_1 = 3.74 \cdot 10^{-8} \left[\frac{W \mu m^4}{m^2} \right]$ and $c_2 = 1.4388 \cdot 10^4 [\mu m K]$. λ is the wavelength in μm, T is the absolute temperature in Kelvin and $E_{b,\lambda}$ is in W m^{-2} μm^{-1}. At higher temperatures, the contribution from shorter wavelength radiation increases. The wavelength corresponding to the peak flux (λ_{max}) is inversely proportional to T and is given by Wien's displacement law:

$$\lambda_{max} T = 2897.8 \ \mu mK$$

Eq. E.2

Integration of equation Eq. E.1 over all wavelength leads to the well-known Stefan-Boltzmann equation:

$$E_b = \sigma T^4$$

Eq. E.3

where σ is the Stefan-Boltzmann constant ($5.67 \cdot 10^{-8}$ W m^{-2} K^{-4}). E_b is the total energy emission from a point on a black surface to all directions in the hemisphere above it (in 2π steradians of solid angle). However, when considering the energy transfer in a given direction (from a differential area on a plane, "black" surface) the concept of the black body total radiation intensity I_b of the beam must be introduced. The total emissive power of a black surface over a hemisphere is:

$$E_b = \pi \cdot I_b \ [\mathrm{W/m^2}]$$

Eq. E.4

The intensity of radiation, I, leaving a non-black surface, is also independent of direction if the surface emits isotropically. In this case, the directional flux from the surface at any angle η is simply equal to $I \cos\eta$. This is known as Lambert cosine law.

In the industrial furnaces, all surfaces emit, reflect and absorb radiation from their surroundings. Therefore, the knowledge of the emissivity of these surfaces is important in thermal design. The surface emissivity is the ratio of the measured radiant energy from a surface to that from a black body at the same temperature. It is a function of the surface properties as the material and physical structure of the surface. However, emissivity is also a function of the wavelength and direction of emitted radiation and of the surface temperature. An important class of surfaces are the grey Lambert surfaces where emissivity is assumed to be independent of both wavelength and direction. For these surfaces, $\varepsilon = \alpha = 1 - \rho$. For example, the surfaces of the furnace wall, the Fibreflex isolation, the black painted sensor surfaces and many other surfaces in industrial processes, approximate

these characteristics. The assumption that all participating surfaces behave as grey Lambert surfaces, greatly simplifies the analysis of radiation heat transfer.

The fraction of radiation, leaving one surface (1) that is incident on another surface (2) is known as the view or configuration factor (F_{12}). The view factor is dependent on the relative geometrical configuration of the two surfaces. The energy incident on surface 2 from black emitting surface 1 is given by

$$q_{1,2} = A_1 F_{12} E_{b,1}$$

Eq. E.5

The energy transfer between two grey Lambert surfaces of emissivities ε_1 and ε_2 is given by the equation:

$$q_{1,2} = \frac{E_{b,1} - E_{b,2}}{\frac{1}{A_1 \varepsilon_1} + \frac{1}{A_2}\left(\frac{1}{\varepsilon_2} - 1\right)}$$

Eq. E.6

where surface 1 is a convex surface fully enclosed by a concave surface 2. Two limiting cases can be derived form this. First, if the radii are large, the system approaches two parallel planes of equal area (A) and hence,

$$q_{1,2} = \frac{A\left(E_{b,1} - E_{b,2}\right)}{\frac{1}{\varepsilon_1} + \frac{1}{\varepsilon_2} - 1}$$

Eq. E.7

and, secondly, if $A_1 << A_2$, then the following approximation gives:

$$q_{1,2} = A_1 \varepsilon_1 \left(E_{b,1} - E_{b,2}\right)$$

Eq. E.8

This latter is true, when the enclosing surface is large compared to the enclosed surface, its emissivity does not influence the radiation interchange, and the surface behaves like a black cavity. More general analysis for enclosures containing an absorbing or emitting gas is described in many advanced radiation textbooks[84, 70].

E.2 Radiation transfer from gases

E.2.1 Nonluminous gaseous radiation

The inert gases (He, Ar, Kr, ...) as well as the molecules composed of two identical atoms (nonpolar gases) (e.g. H_2, O_2, N_2, etc.) do not contribute to thermal radiation. On the other hand, the molecules composed of two different atoms (polar gases), as for example the H_2O, CO_2, CH_4, emit and absorb over a wide temperature or wave length range. Gaseous radiation is a volumetric phenomenon and it is concentrated in specific wavelength bands.[85]

In oxygen rich combustion, the presence of methane can be neglected from the point of view of thermal radiation because, in general, methane is promptly burned. In the exceptional case of the envelope flame, when the chemical reaction takes place only further downstream in the combustion chamber, the methane is too cold to radiate significantly. Thus, the important gases leading to thermal radiation are the hot combustion products of water vapor and carbon dioxide. For a general case, the total emissivity and absorptivity are calculated in the next section. For a common experimental situation, the total emissivity and absorptivity of the gas mixture are calculated in section E.3.1.

E.2.1.1 Total emissivity and absorptivity of gas mixtures

The total emissivity can be calculated from Leckner[90]. The individual emissivity for polar gases is given by:

$$\varepsilon_i\left(p_aL,p,T_g\right)=\varepsilon_0\left(p_aL,T_g\right)\left(\frac{\varepsilon}{\varepsilon_0}\right)\left(p_aL,p,T_g\right)$$

Eq. E.9

where ε_i is the emissivity of the individual gas, p_a is the partial pressure of the gas, L is the gas mean beam length, T_g is the absolute temperature of the gas and ε_0 is the emissivity of the individual gas at a reference state. The first term in the above equation can be calculated using:

$$\varepsilon_0\left(p_aL,T_g\right)=\exp\left[\sum_{i=0}^{M}\sum_{j=0}^{N}c_{ij}\left(\frac{T_g}{T_0}\right)^j\left(\log_{10}\frac{p_aL}{\left(p_aL\right)_0}\right)^i\right]$$

Eq. E.10

where T_0 is the absolute reference temperature of the gas (1000K) and c_{ij} are constants. In Eq. E.9, the second term is calculated from:

$$\left(\frac{\varepsilon}{\varepsilon_0}\right)\left(p_aL,p,T_g\right)=\left\{1-\frac{(a-1)(1-P_E)}{a+b-1+P_E}\exp\left[-c\left(\log_{10}\frac{\left(p_aL\right)_m}{p_aL}\right)^2\right]\right\}$$

Eq. E.11

where a, b, c, P_E and $\left(p_aL\right)_m/p_aL$ are given in Table E.1. Graphical results for H_2O and CO_2 are shown in Figure E.1 and Figure E.2 respectively. The total emissivity is then calculated using:

$$\varepsilon_{CO_2+H_2O}=\varepsilon_{CO_2}+\varepsilon_{H_2O}-\Delta\varepsilon$$

Eq. E.12

where the $\Delta\varepsilon$ accounts for the overlap between the H_2O and CO_2 bands.

Gas	Water Vapor			Carbon Dioxide			
M, N	2,2			2,3			
c_{00} ⋯ c_{N1}	−2.2118	−1.1987	0.035596	−3.9893	2.7669	−2.1081	0.39163
⋮ ⋱ ⋮	0.85667	0.93048	−0.14391	1.2710	−1.1090	1.0195	−0.21897
c_{0M} ⋯ c_{NM}	−0.10838	−0.17156	0.045915	−0.23678	0.19731	−0.19544	0.044644

P_E	$(p + 2.56p_a/\sqrt{t})/p_0$	$(p + 0.28p_a)/p_0$
$(p_aL)_m/(p_aL)_0$	$13.2t^2$	$0.054/t^2$, $t < 0.7$ $0.225t^2$, $t > 0.7$
a	2.144, $t < 0.75$ $1.88 - 2.053 \log_{10} t$, $t > 0.75$	$1 + 0.1/t^{1.45}$
b	$1.10/t^{1.4}$	0.23
c	0.5	1.47

Note: T_0 = 1000 K, p_0 = 1 bar, $t = T/T_0$, $(p_a L)_0$ = 1 bar cm.

Source: From F. Kreith, Ed., CRC Handbook of Mechanical Engineering. CRC Press, Boca Raton, FL, 1998, 4-73.

Table E.1 Correlation constants for gas emissivity equations

It is calculated from:

$$\Delta\varepsilon = \left(\frac{\xi}{10.7 + 101\xi} - 0.0089\xi^{10.4}\right)\left(\log_{10}\frac{\left(p_{H_2O} + p_{CO_2}\right)L}{\left(p_aL\right)_0}\right)^{2.76}$$

Eq. E.13

where

$$\xi = \frac{p_{H_2O}}{p_{H_2O} + p_{CO_2}}$$

Eq. E.14

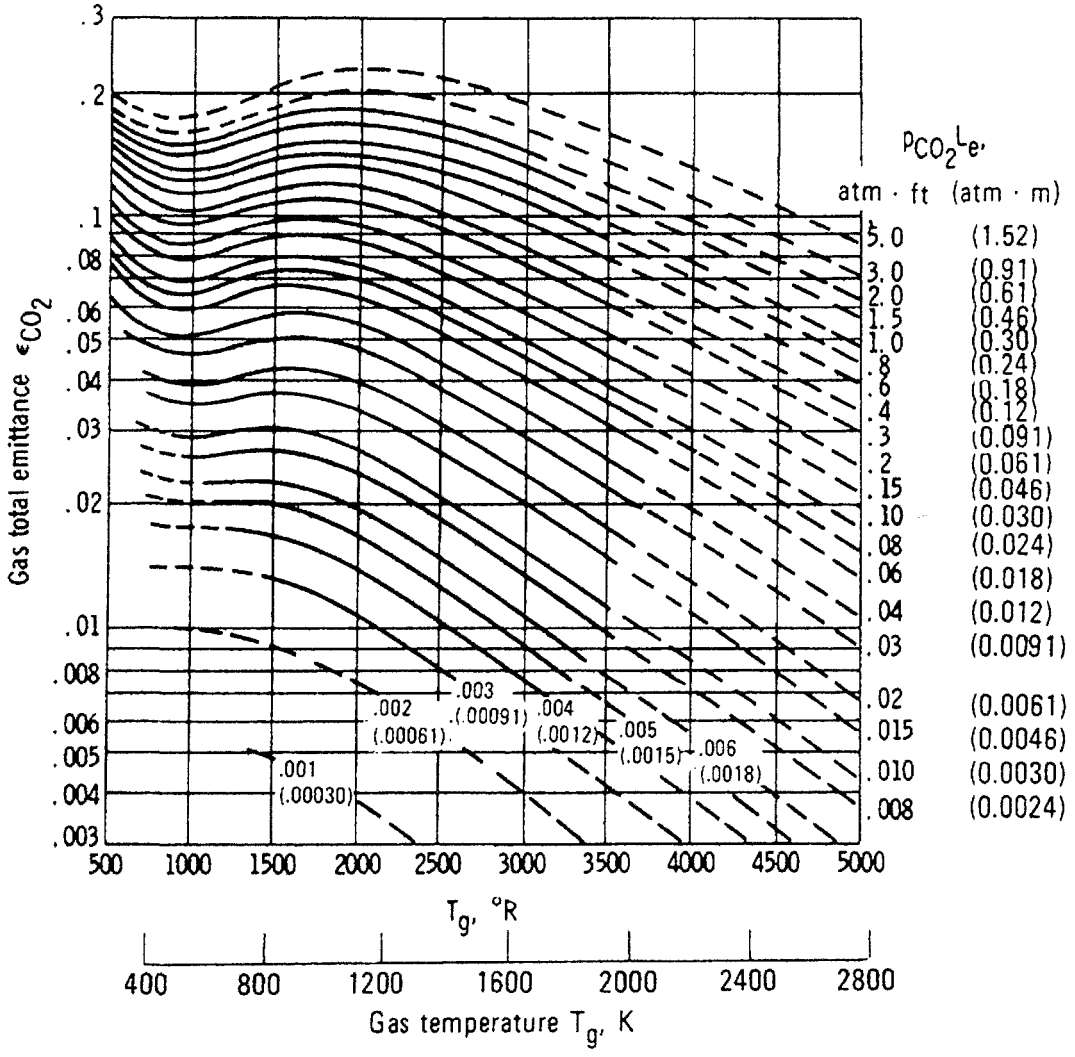

Figure E.1 Total emittance of carbon dioxide in a mixture having a total pressure P of 1 atm[89]

The absorptivity of H_2O and CO_2 can be calculated using:

$$\alpha\left(p_a L, p, T_g, T_s\right) = \left(\frac{T_g}{T_s}\right)^{1/2} \varepsilon\left(p_a L \frac{T_s}{T_g}, p, T_s\right)$$

Eq. E.15

where T_s is the surface temperature such as a furnace wall. The correction for the band overlap between H_2O and CO_2 can be calculated using:

$$\alpha_{CO_2+H_2O} = \alpha_{CO_2} + \alpha_{H_2O} - \Delta\varepsilon$$

Eq. E.16

where $\Delta\varepsilon$ is estimated with a pressure path length of $p_a LT_s/T_g$.

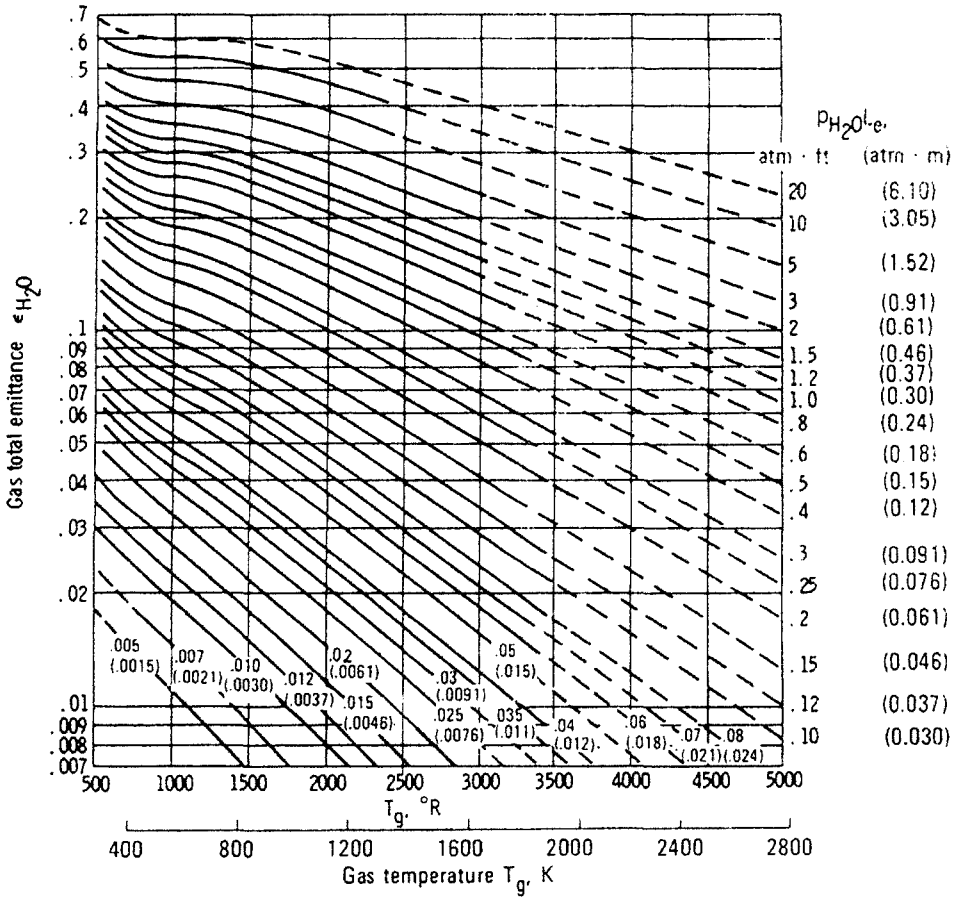

Figure E.2 Total emittance of water vapour in limit of zero partial pressure in a mixing having a total pressure P of 1 atm[89]

E.2.2 Luminous gaseous radiation

The continuous radiant emission of particles, such as soot, produces luminous flames. Soot approximately radiates as blackbodies. It forms at temperatures ranging from 1000 to 2500°C. Soot consists primarily of carbon, formed into long chains. The total amount of

soot formed is usually small in comparison to the amount of available carbon. However, according to the study of Echigo et al[91], a rigorous definition of luminous and nonluminous flames does not exist. The soot generated in a flame depends on several things. The most important is the fuel composition. Luminous radiation is usually important when solid and liquid fuels are used. For gaseous fuels, like natural gas, the luminous radiation is usually not significant. The determinant factor is the C:H weight ratio of the fuel. According to Talmor[92], for natural gas, the flame emissivity is about 0.22.

E.2.3 Total radiation exchange between entire medium volume and emitting boundary

In the case of significant wall emission, the average heat flux removed at the wall, to keep the wall at constant temperature, is the emission of the medium to the wall, which is all absorbed because the wall is assumed black, minus the average flux emitted from the wall that is absorbed by the medium[84]. An energy balance gives, for an enclosure with its entire boundary black and at T_w,

$$-\frac{q_w}{A} = \frac{q_g}{A} = \sigma\left[\varepsilon_g(T_g)T_g^4 - \alpha_g(T_w)T_w^4\right]$$

Eq. E.17

The $\alpha_g(T_w)$ is the total absorptance by the medium for radiation emitted from the black wall at temperature T_w. The $\varepsilon_g(T_g)$ is the total emittance by the medium at temperature T_g.

E.3 Some calculations

E.3.1 Total emissivity and absorptivity calculations

As it was presented in Table B.1, the combustion of natural gas in 10% excess air results 8.255 mol of N_2, 1.006 mol of CO_2, 1.978 mol of H_2O and 0.199 mol of O_2. These products are in the region of rectangular parallelepipeds with the cross section of 0.5m x 0.5m and with the length of 1.5m (experimental furnace size). We assumed that the products are uniformly mixed at a pressure of 1 atm. Only the polar gases take place in thermal radiation. The partial pressure of each constituent is equal to its mole fraction, thus: $p_{CO_2} = 0.088atm$ and $p_{H_2O} = 0.173atm$. The gas mean beam length for negligible self-absorption is $L_0 = 4V/A = 0.428m$. To include self absorption, according to Hottel et al. [87] and Eckert[88], a correction factor of 0.91 is applied to give $L = 0.386m$. Then $p_{CO_2}L = 0.0343atm \cdot m$, and $p_{H_2O}L = 0.0674atm \cdot m$. Using Figure E.1 and Figure E.2 for an average gas temperature of 1400°C, $(\varepsilon_0)_{CO_2} = 0.0525$ and $(\varepsilon_0)_{H_2O} = 0.0571$. Calculating the correction factors $\varepsilon/\varepsilon_0$ using Eq. E.11 and Table E.1, $(\varepsilon/\varepsilon_0)_{CO_2} = 1.001$ and $(\varepsilon/\varepsilon_0)_{H_2O} = 1.062$, thus, $\varepsilon_{CO_2} = 0.0525$ and $\varepsilon_{H_2O} = 0.061$. Calculating the correction on total emittance for overlap between the CO_2 and H_2O bands (Eq. E.13), one obtains $\Delta\varepsilon = 0.0096$. So the total emissivity using Eq. E.12 is $\varepsilon = 0.1035$.

Similarly to the gas emissivity, the total gas absorptivity can also be calculated. 900°C was chosen as a mean temperature of the furnace refractories. Thus, the total gas absorptivity is $\alpha = 0.2082$.

E.3.2 Total radiation exchange between entire medium volume and emitting boundary

The total radiation exchange is presented between the refractories and the gaseous medium. The radiative heat-flux is shown as a function of the refractory temperatures and of the flame temperature. In this case, methane is combusted in 10% excess air. The radiation exchange is calculated using Eq. E.17. The gas emissivity and absorptivity values, calculated in the previous section, were used.

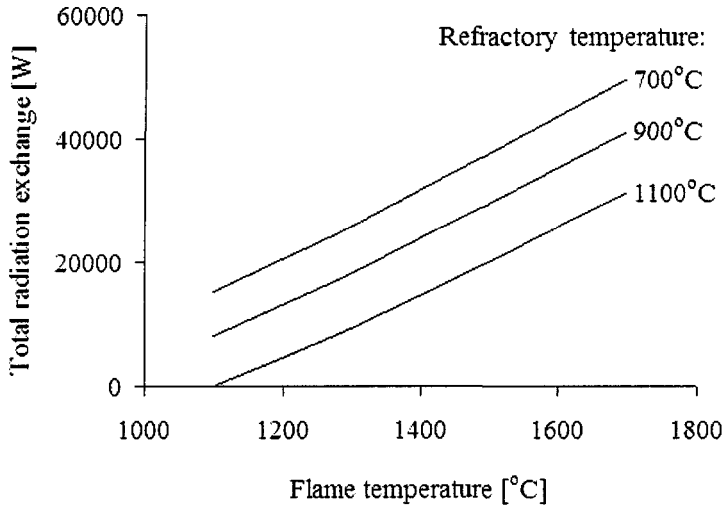

Figure E.3 Total radiation exchange between the refractories and the gaseous medium as a function of the flame temperature and of the refractory temperature – black refractories are assumed – total gas emissivities and absorptivities are calculated (natural gas combustion in 10% excess air)

E.3.3 Additional experiments to predict the proportion between direct and indirect radiation

In the present study, the incident radiative heat transfer toward the charge, which is represented by water-cooled calorimetric plates located at the bottom of the furnace, was continuously measured during the heat flux experiments. This total radiative heat flux consists of direct and indirect radiative parts. During the measurements, we were not able to suppress the indirect contribution namely the surface radiation in our experimental furnace.

For this reason, we tried to experimentally measure the proportion of the surface radiation by the help of an additional test. The method is relatively simple. When the refractories were adequately preheated (after about 12 hours of consecutive operation), the burner was stopped. The internal ventilation was kept at the lowest possible level. The incident radiative heat flux on the heat flux sensors was measured. In addition, the refractory temperature was also detected in multiple measurement points at different depth below the external refractory surface (see section 3.7.1). Thus, an empirical correlation was determined, which relates the refractory temperature to the incident radiation arriving from the refractory surface to the heat flux sensor at a given position.

APPENDIX F
FLAME VISUALIZATION

In a special series of tests, we visualized the structure and movement of all four flames. Using different metallic compounds, we dyed those high temperature regions of the flame where the self-illumination is weak without solid (soot) particles, Figure F.2 and Figure F.3.

We also introduced incandescent particles in order to show the streamlines in the combustion chamber. Using different exposure times even the magnitude of the velocities can be estimated (Figure F.1).

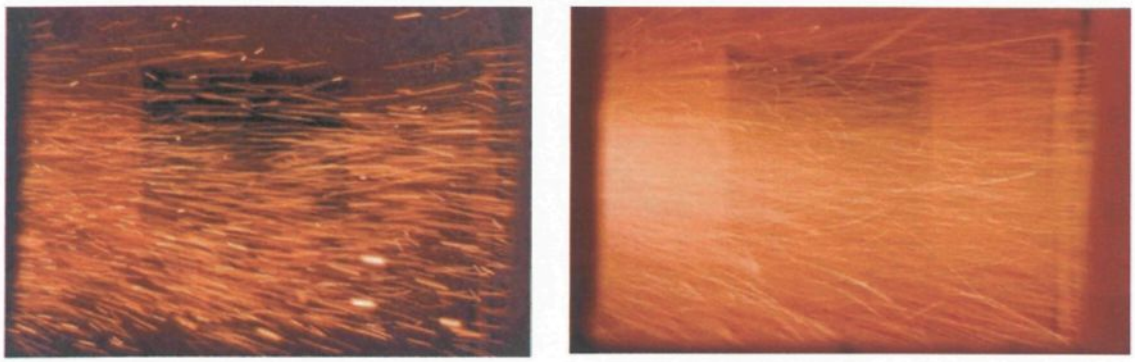

(a) (b)

Figure F.1 Visualization of the flow pattern by the injection of solid particles (long-flame)
(a) short exposure time, (b) long exposure time

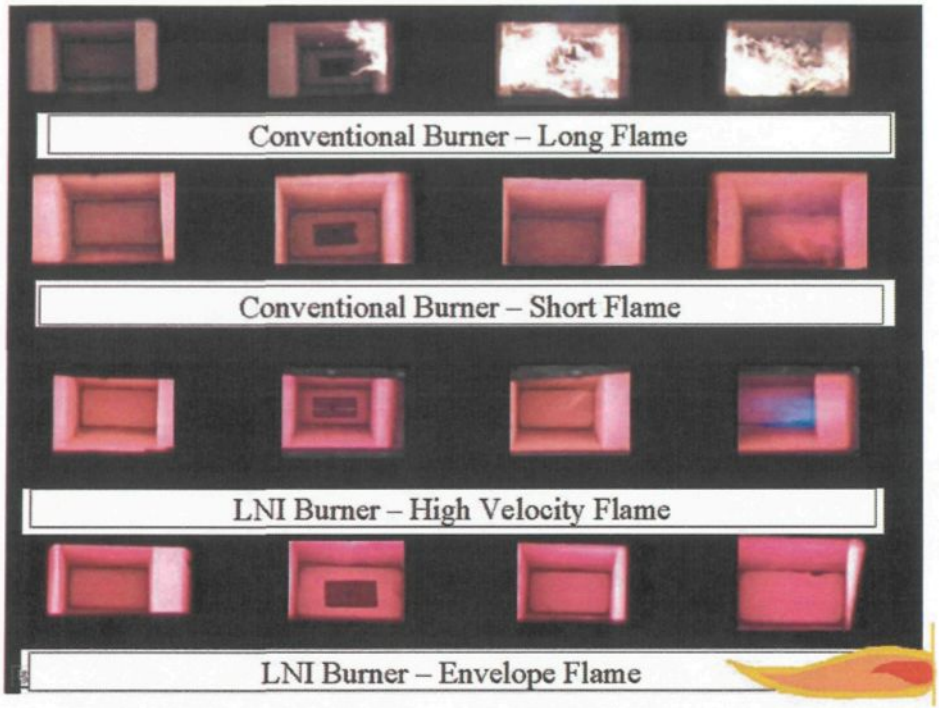

Figure F.2. Visualization of the four flame-types without colorization

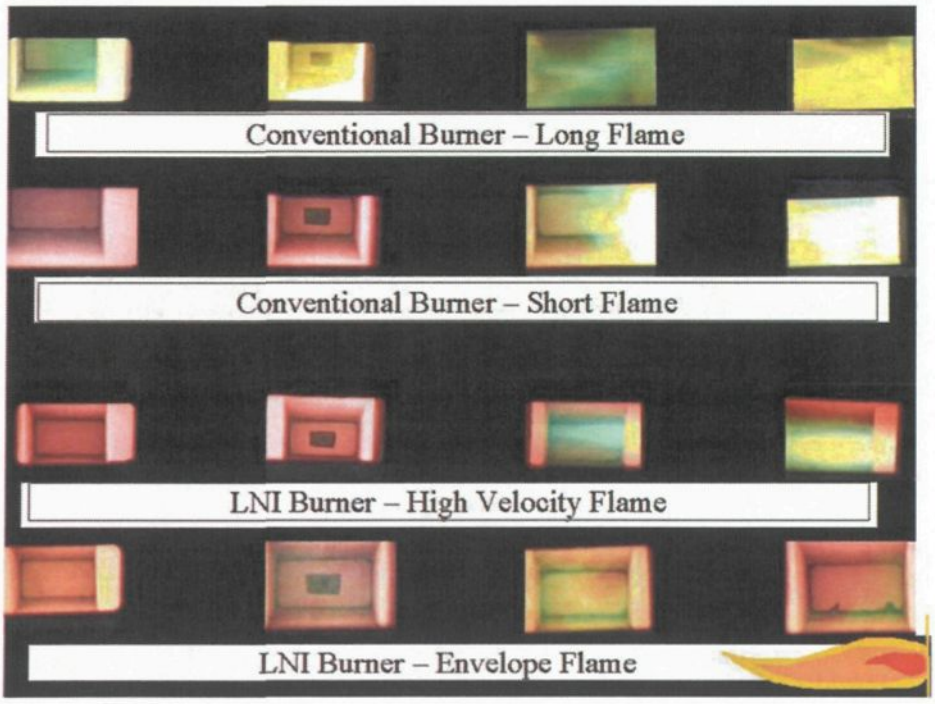

Figure F.3 Visualization of the four flame-types with the application of copper sulphate powder

APPENDIX G
TEMPERATURE MEASUREMENT IN GAS FLOW

G.1 Temperature Probes

The two types of probes most often used to measure gas temperature in flames are thermocouple probes and pneumatic probes. Within these two categories, there are a number of probe designs, each with its own special characteristics. The two most common configurations of thermocouple probes are:

- bare thermocouple, and
- aspirated thermocouple (suction pyrometer).

Bare thermocouples have been used extensively to measure gas temperatures in laboratory flames. Various thermocouple materials are suitable for making temperature measurements in flames, including platinum-rhodium and iridium-rhodium. The principal sources of error in using bare thermocouples to measure temperatures in laminar flames are heat losses due to radiation and conduction along the thermocouple leads and heat gains due to catalytic reactions occurring on the thermocouple surface. In high-velocity turbulent flames, additional errors can result from variations in recovery factor with local gas velocity and from the time-response of the thermocouple to turbulent fluctuations in

temperature. In particle-laden flows, further errors in gas temperature measurements can be introduced due to radiation from the particles and due to impacting of particles on thermocouple surfaces.

Radiation and conduction losses can be reduced by proper design of the thermocouple probe. One of the aspects is if the thermocouple leads are aligned with surfaces of nearly constant temperature in the flame, thereby reducing conduction losses. Radiation losses are reduced by using as small a thermocouple as possible for the temperature levels and aerodynamic loadings encountered. Even for very small thermocouples ($d < 0.05$ mm), radiation losses at elevated temperatures can be considerable, and some correction for these losses is required. Standard techniques for making heat loss corrections include comparison of thermocouple measurements with optical temperature measurements (e.g., line-reversal methods) and compensation for heat-loss by electrical heating. An alternative approach to reducing measurement errors caused by radiation heat transfer is installation of a shield assembly around the thermocouple bead. The increased size of shielded thermocouple probes can lead to increased errors due to probe disturbance, and, in general, these probes are utilized only in large-scale flames.

Errors in temperature measurements due to catalytic effects can be virtually eliminated by application of thin, impermeable coatings to the thermocouple surface. Coatings that have proved successful in this regard include silicon oxide and beryllium/yttrium oxides.

In general, use of uncooled thermocouples is restricted to flame temperatures below 2200K and to low aerodynamic loadings. The temperatures and velocities encountered in

many industrial flames preclude the use of uncooled thermocouple probes. In these flames, temperatures can be measured using a probe with a known heat loss.

Thermocouples measure the stagnation or total temperature of the gas in the vicinity of the thermocouple bead. In high velocity flows, the temperature of the surface of the thermocouple may differ from the true total temperature of the gas because of heat transfer in the boundary layer. There are published correlations relating the recovery factor of the thermocouple to its orientation in the flow and the flow velocity[97, 98]. The gas velocities encountered in most flames of practical interest are sufficiently low so that these losses are small and the thermocouple output will be a measure of the local static temperature.

In measuring temperature in turbulent flames, consideration must be given to the time response of the thermocouple probe. Fine-wire thermocouples tend to follow the turbulent temperature fluctuations. With proper compensation for phase-lag, these fine-wire thermocouples can be used to measure low-frequency ($f < 1$ kHz) temperature fluctuations in turbulent flames. Larger thermocouples cannot follow the temperature fluctuations and measure an average gas temperature that depends on time-response and on the average value of the heat-transfer coefficient for the thermocouple. Bilger[99] discusses the averaging properties of thermocouples used to measure temperature in turbulent flames.

The aspirated thermocouple or suction pyrometer is a refinement of the shielded thermocouple probe discussed earlier and is designed to reduce many of the measurement errors just outlined. A schematic diagram of a typical water-cooled aspirated thermocouple probe is shown in Figure G.1. The probe consists of a coated thermocouple located within a shield that isolates the thermocouple from radiation from the surroundings. Gas is aspirated

over the thermocouple at a controlled rate. Careful calibration of the probe is required, since measured temperatures depend on probe geometry and suction velocity[97]. Aspirated thermocouple probes find greatest application in measuring temperatures in highly luminous and/or particle-laden flames. Because of their relatively large size, these probes are best suited for measuring temperatures in large-scale flames.

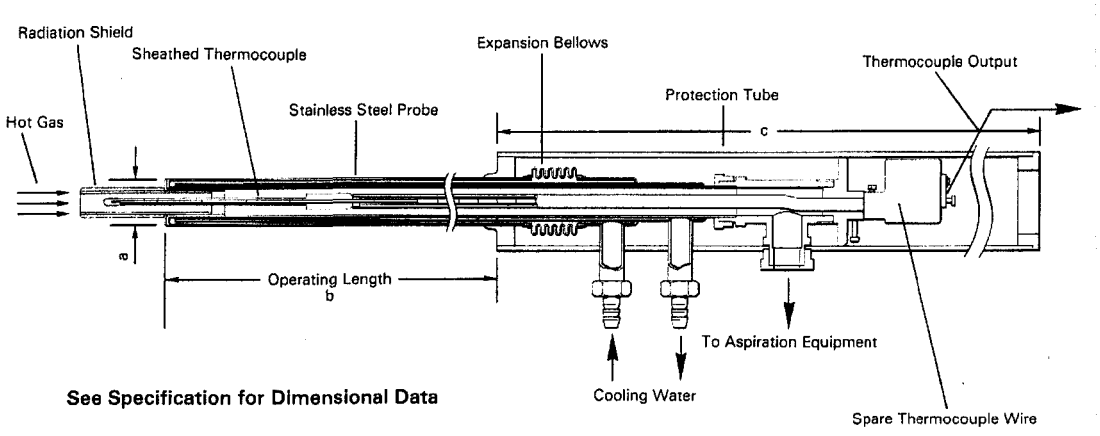

Figure G.1. Aspirated Thermocouple Probe (Land Combustion Ltd.)

Pneumatic temperature probes are based on the principle that the mass flow rate of a gas through an orifice of known area is a function of the total pressure and temperature of the gas and of the pressure drop across the orifice. The total temperature of the gas can be determined from a measurement of the other three parameters. Because these probes can be cooled, they find application in very high temperature flows. Since the measurement principle is based on aerodynamics, the measurements are not subject to errors resulting from radiation heat transfer. There are several significant sources of error in pneumatic probe measurements of flame temperatures. The major measurement error is introduced by deviation of measurement conditions (gas composition, temperature, Reynolds number)

from calibration conditions[97, 100, 101]. Changes in orifice area due either to thermal expansion or to erosion or plugging in particle-laden flows can introduce measurement errors. Utilization of pneumatic probes in flows containing particulates requires special precautions, including use of relatively large orifice diameters and frequent redetermination of orifice areas. The time-response of pneumatic probes to fluctuations in temperature generally is faster than aspirated thermocouple probes, but is considerably slower than fine-wire bare thermocouples. Hence, pneumatic probes measure some weighted average temperature. Bilger[99] discusses problems associated with using various types of pneumatic probes in turbulent flames. Temperature measurements made in hot combustion gases (1000-2400 K) using pneumatic probes have been compared with measurements using other types of temperature probes[101, 102]. These comparisons show that temperature data obtained from pneumatic probes have slightly greater scatter than that obtained using thermocouple probes.

Resistance thermometers have found limited application in measuring temperatures in combustion gases. The measurement technique is based on the change in resistance of sensing element with temperature. Resistance thermometers can be used to measure turbulent temperature fluctuations if a sufficiently small sensing element and a compensating circuit are employed. Resistance thermometers are subject to the same errors as bare-wire thermocouple probes and require individual calibration. At elevated temperature ($T > 1800$ K), resistance thermometers must be cooled[103, 104].

APPENDIX H
VELOCITY MEASUREMENTS

H.1 Laser Doppler Velocimetry

H.1.1 Fundamentals of the LDV technology

Laser Doppler Velocimetry (LDV) is an optical technique for measuring fluid velocities. For a given velocity direction, two laser beams must cross to create a small scattering volume. As a particle passes through that volume, a Doppler shift is produced (Figure H.1). This is detected by receiving optics. With proper processing, the velocity can be calculated from this signal.

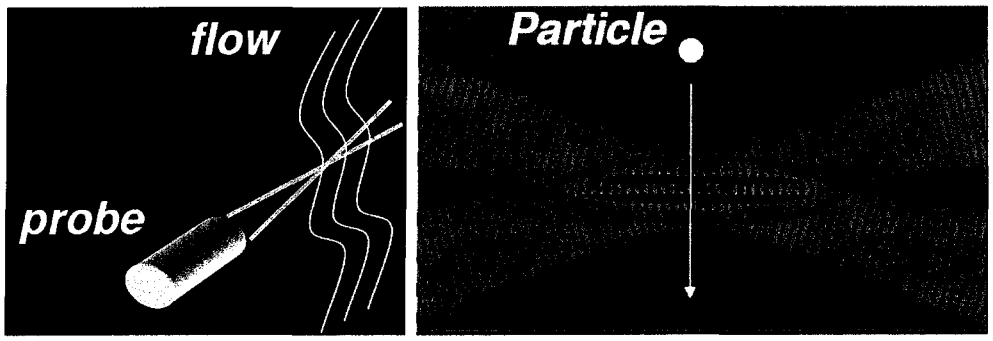

Figure H.1, Dual Beam LDV System

The LDV technology has the following general characteristics and advantages:

1.) Invented by Yeh and Cummins in 1964

2.) Able to sampling velocities in gas or liquid fluids

3.) Able to measure up to 3 components of velocity

4.) Non intrusive technology

5.) Absolute velocity sampling method (no calibration required)

6.) Measurement technology of high accuracy

Detailed description about LDV method is given for example in [105].

H.1.2 Principles of frequency shifting and measuring flow reversals

Frequency shifting is a very useful tool in Laser Velocimetry. Shifting one of the two beams can be thought of as causing a "moving fringe" system. In an LDV system, without frequency shifting, the fringes in the measurement volume are stationary. When frequency shifting is applied in a dual-beam LDV system, one laser beam is shifted in frequency while the other beam is not. This causes the optical fringes in the measurement volume to move in a direction from the shifted beam (at a higher frequency) to the unshifted beam (at a lower frequency) at a frequency equal to the shift (Figure H.2).

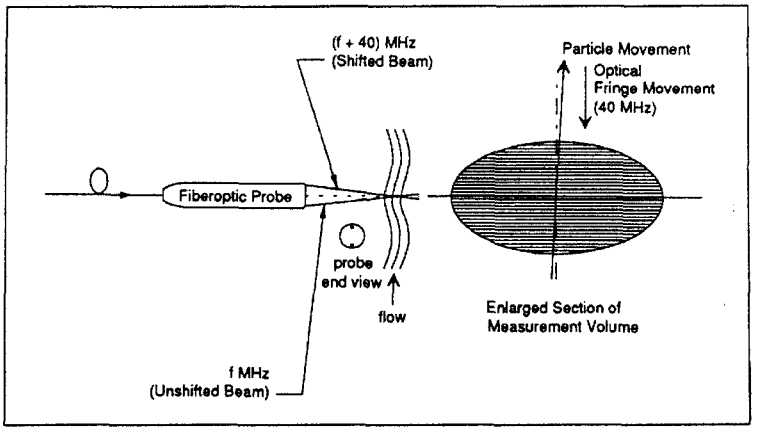

Figure H.2. Fringe Movement in a Frequency -Shifted System

A basic LDV system cannot distinguish between forward or reverse flow. This ambiguity can be eliminated by shifting (shown as a line with the label of "without frequency shifting" in Figure H.3) the velocity-frequency curve to yield a positive frequency at zero velocity.

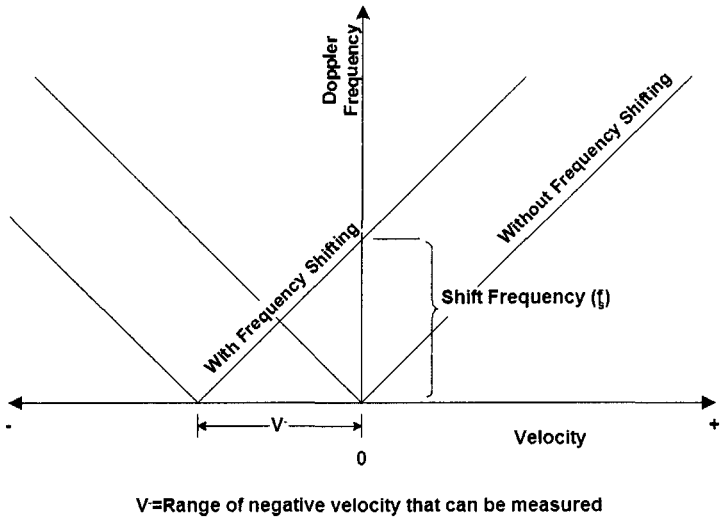

Figure H.3 Frequency Shifting - Graphical View of How Frequency Shifting Eliminates Directional Ambiguity

H.1.3 Main components of the LDV system used in our laboratory

The LDV system has the following main components (Figure H.4):

1.) The Coherent Innova 70 Series Ion Laser of the Coherent Inc.

2.) Model 9201 - ColorBurst Multicolor Beam Separator

3.) Model 9230 - ColorLink Multicolor Receiver System

4.) IFA 550 – Signal Processor

5.) FIND (Flow Information Display) Software

6.) Fiber Optic Probe

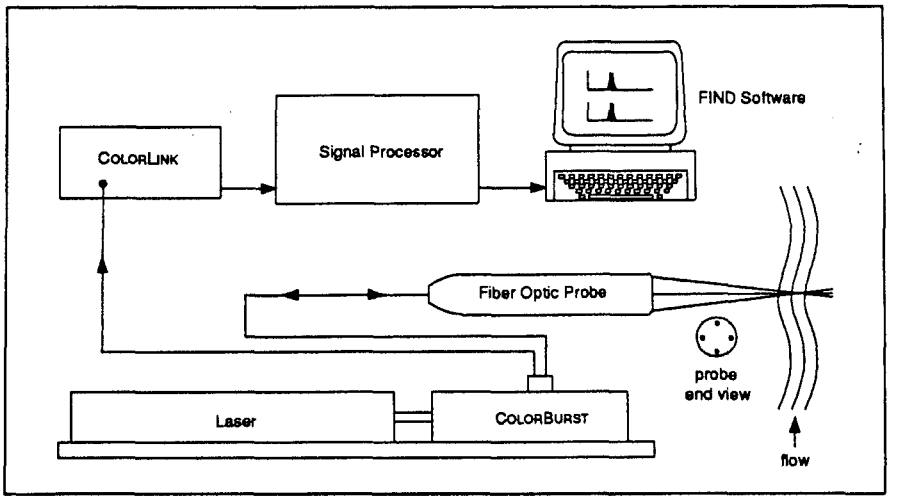

Figure H.4. LDV System Components of TSI

H.1.4 Characteristic of the components

The LDV system, applied in our experimental measurements, is fabricated in 1988 and released by TSI Incorporated. The Coherent Innova 70 Series Ion Laser is an argon-ion unit with reliable, continuous wave laser light in the visible spectrum.

COLORBURST Multicolor Beam Separator	
Specifications	
Colors separated	476.5 nm, 488 nm, 514.5 nm (violet, blue, green)
Efficiencies:	
COLORBURST	>85% for all beam colors
Color separation	100%
Acousto-optic driver frequency	40 MHz
User adjustements	Bragg angle, beam steering mirror
Input beam diameter (max)	1.6 mm
Laser capabilities	Ar-ion, He-Ne
Dimensions (LWH)	546 mm x 89 mm x 152 mm

Table H.1 Specifications LDV

The primary optical component in a TSI LDV system, the ColorBurst Multicolor Beam Separator provides beamsplitting, frequency shift and beam alignment for one- two- and three-component systems in a single, compact unit. The applied ColorBurst works with fiberoptic system, using argon-ion laser. Frequency shift is available in all channels. Detailed specifications are shown in Table H.1.

The measurement is made using backward-scatter. Seed particles of 0.4 [μm] alumina are introduced by a fluidized bed mixing system (Figure H.5) into the air flowing out an annulus. The fringe spacing (d_f) is 2.979 [μm], the wavelength of light λ=514.5 [nm] and the half angle κ=4.956°.

Figure H.5 Fluidized bed particles mixing system

At the basic adjustments, the velocity range is between 0 and 29.79 m/s, which correspond to the range of 0 to 10 MHz in frequencies. There are 10 low pass filters employed in this velocity range. If we are intended to make measurements in highest velocity ranges, we need to shift the frequencies with 10 or 20 MHz. With this operation

mode it is permitted to detect velocities in the upper ranges up to 119.16 m/s. The low pass filters and the "frequency-shift" ranges are presented in Figure H.6.

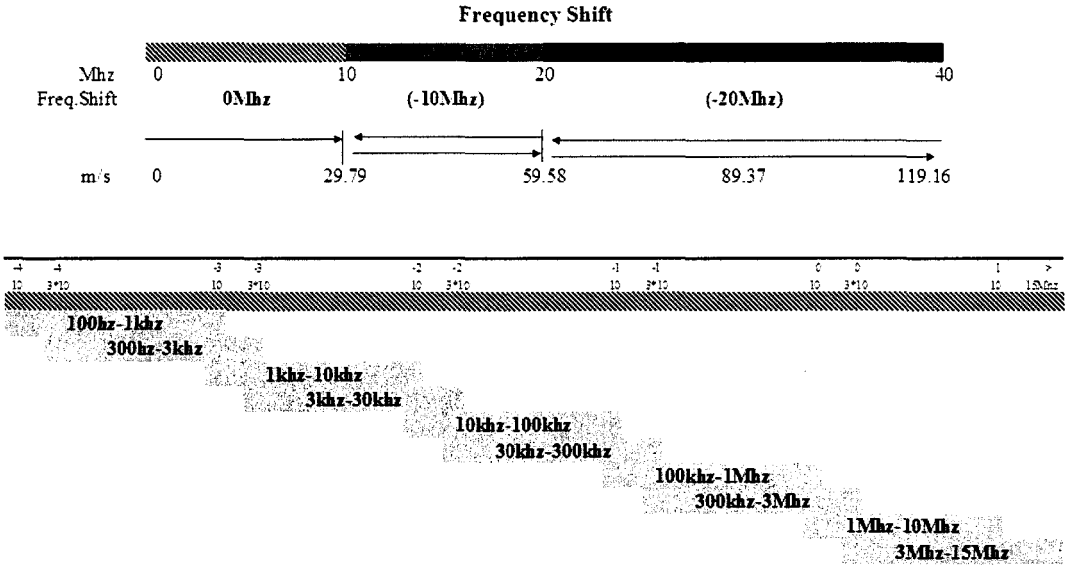

Figure H.6. Frequency shifting

H.2 Static pressure probes and Pitot probes

H.2.1 . Introduction

These probes are based upon the principle that a "pressure tap", typically a small hole in the surface of a solid object immersed in a stream, develops within it a pressure p_s that in some way represents the total molecular flux density incident across its mouth. This pressure is commonly expressed by the pitot formula

$$p_s = p + \frac{1}{2} C \rho u^2$$

Eq. H.1

where u and p are, for our purposes, the stream speed and static pressure in the undisturbed field at the nominal measurement point, i.e., at the position of the centre of the mouth of the pressure tap but with the probe absent. The pitot coefficient C is ideally zero for static pressure probes and unity for pitot probes. In the following text, only pitot probes are discussed

H.2.2 Pitot probes

Considerable information on pitot probes may be found in the classic book of Pankhurst and Holder[109] on wind tunnel techniques. Becker and Brown[107, 110], however, made the first comprehensive study of pitot response and developed and verified the theory of the effect of turbulence. The basic useful probe-head shapes, Figure H.7., may be described as square head, round head and ball-head. For all of these (Eq. H.1) can be expressed as

$$p_s = p + \frac{1}{2}\rho u^2\left(1 - K(\sin^2\Theta)^m\right)$$

$$p_s = p + \frac{1}{2}\rho u^2\left(1 - K\left(\frac{u_n^2}{u^2}\right)^m\right)$$

Eq. H.2

$\Theta < \Theta_m$, where K and m are functions of the head shape and of the ratio $\frac{D_i}{D_0}$ of the internal (pressure tap) and external diameters. The maximum yaw angle Θ_m can be as low as 36° but in most cases exceeds 45°. The probe Reynolds number $Re = \frac{uD_0}{\upsilon}$ is best kept above 1000 for round-head and ball-head probes but can be as low as 200 for square-head

probes of large $\frac{D_i}{D_0}$. Effects of compressibility are negligible at Mach numbers Ma<0.3 and never large at Ma<0.6. It is supposed in the following discussion that Re>1000 and Ma<0.3.

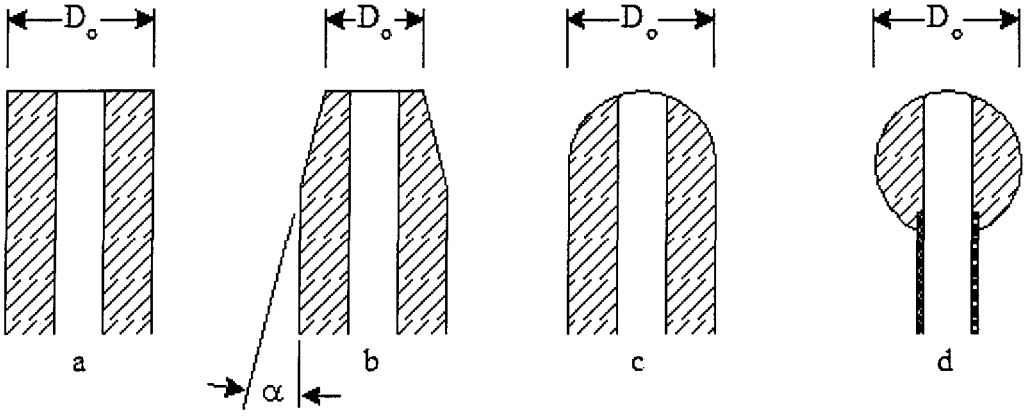

Figure H.7 Head shapes of pitot probes: (a) square head, (b) tapered head, (c) round head and (d) ball head. When $\alpha < 3^{\circ}$, the tapered probe behaves like a square- head probe of outside diameter D_o equal to the tip diameter, as shown.

H.2.3 Application of the one-hole Pitot probe in the furnace experiences

As it was discussed earlier, the LDV method were replaced by another technology to measure the velocity profiles. The theoretical background of the pitot probes has been presented briefly in the previous chapter. For more detailed description please refer to [106, 107, 108, 109, 110]. The application and the local parameters will be treated next.

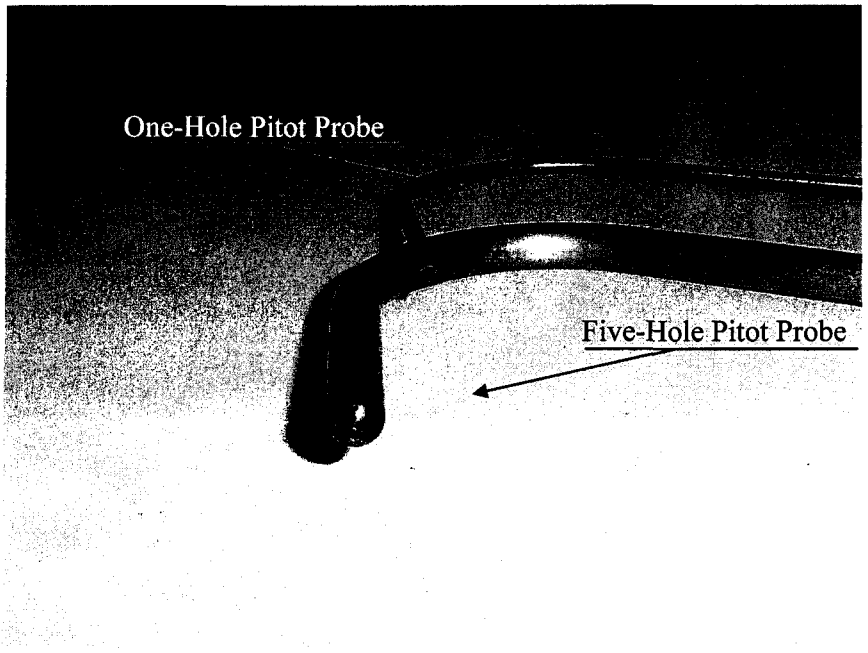

Figure H.8 The square head "one-hole Pitot probe" and the ball head "Five-Hole Pitot Probe"

The one-hole Pitot tube used in the experiences is shown in Figure H.8. The internal and external diameter ratio is $\frac{D_i}{D_o}$=0.62, which is slightly below of the recommendation ($\frac{D_i}{D_o}$>0.75). The exponent and the coefficient in law of response of the yawed pitot probe (m) and (K) are respectively:

$$m=1+0.225\cdot e^{\left(2.25\frac{D_i}{D_o}\right)}=1.908$$

$$K=\left(0.853+0.08\frac{D_i}{D_o}\right)m=1.722$$

The direction sensitivity of square head Pitot probes for different angles Θ between velocity vector u and the probe axis is presented in Figure H.9 and Figure H.10. The relevant equation is

$$p_s = p + \frac{1}{2}\rho u^2\left(1 - K(\sin^2\Theta)^m\right).$$

Here we can replace ρ with the state equation for ideal gases:

$$\rho = \frac{M_{mixture} \cdot p_{stat}}{\Re \cdot T_{corr}}$$

Eq. H.3

where $M_{mixture}$, p_{stat}, $\Re$ and T_{corr} are respectively the molar mass of the mixture in [kg/kmol], the atmospheric pressure in [Pa], the universal gas constant (8314,4 [J/kmol K]) and the temperature of the hot mixture in [K]. The mixture temperature is obtained with the suction pyrometer; the atmospheric pressure is the registered value of the actual weather conditions and the molar mass is calculated from the excess air ratio and the gas composition provided by the gas-company (Polygaz).

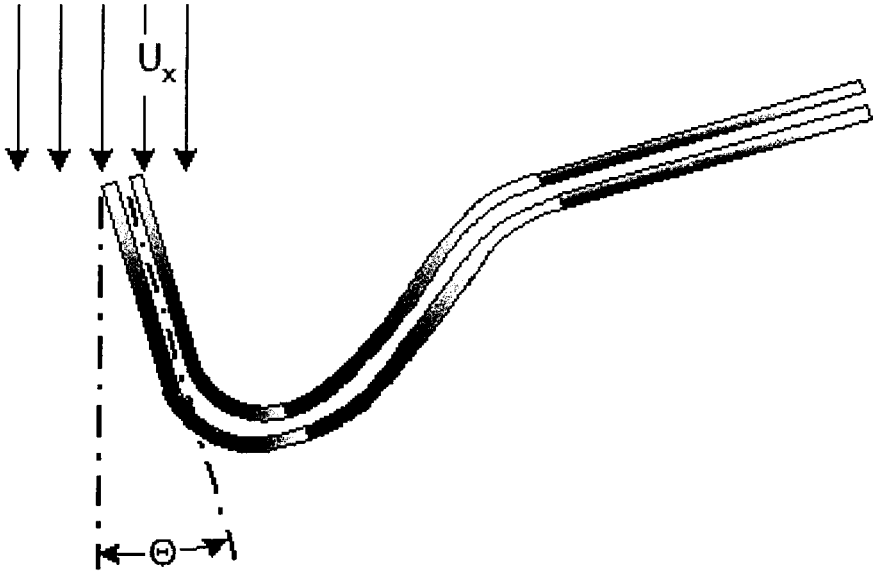

Figure H.9. Directional sensitivity of the Pitot probe

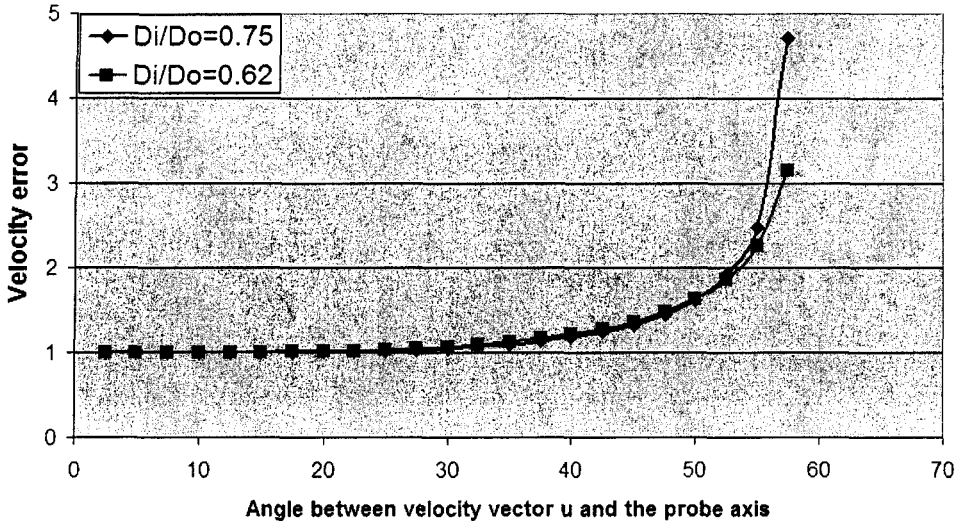

Figure H.10. Directional sensitivity calculation for the Pitot probe

APPENDIX I
ENTHALPY OF COMBUSTION AND FIRING RATES

I.1 The enthalpy of combustion of methane (LHV)

The stoichiometric combustion equation of methane (CH_4) becomes:

$$CH_4 + 2O_2 + 7.52N_2 \rightarrow CO_2 + 2H_2O + 7.52N_2$$

Eq. I.1

We must determine the values of $\overline{h}^o$ for each species in the reaction. These are as follows:

Species	M [kg/kmol]	$\overline{h}^o$ [kJ/kmol]	$\overline{h}^o$ [Btu/lbmol]
CH_4	16.042	-74894	-3.22E+04
O_2	32	0	0
N_2	28.016	0	0
CO_2	44.01	-393075	-1.69E+05
H_2O liquid	18.016	-286084	-1.23E+05
H_2O vapor	18.016	-241892	-1.04E+05

Table I.1 Enthalpy of species in the reaction

Assuming that the water is produced in the form of vapour, we can calculate the quantity $\overline{q}^o$ which is called the enthalpy of combustion or sometimes the heat of combustion.

$$\bar{q}^{o} = \frac{1}{n_{CH_4}}\left[\left(n\bar{h}^{o}\right)_{CO_2} + \left(n\bar{h}^{o}\right)_{H_2O} + \left(n\bar{h}^{o}\right)_{N_2} - \left(n\bar{h}^{o}\right)_{CH_4} - \left(n\bar{h}^{o}\right)_{O_2} - \left(n\bar{h}^{o}\right)_{N_2}\right] =$$

$$= \frac{1}{1}\left[(1)(-393075) + (2)(-241892) + 0 - (1)(-74894) - 0 - 0\right] = -801965\left[\frac{kJ}{kmol}\right]$$

Eq. I.2

Note that $\dot{n}/\dot{n}_f = n/n_f$ for a steady flow process. The enthalpy of combustion per mole of methane is thus $\bar{q}^{o}$ =-801965 [kJ/kmol] or q^{o} = - 801965 / 16.042 = - 49992 [kJ/kg].

The nitrogen in the air did not affect the result, so the enthalpy of combustion in the standard reference state is the same whether the methane is burned in stoichiometric air, pure oxygen, or excess air.

Note that if we had assumed that the water produced in the combustion reaction was in the form of liquid rather than vapour, then the calculated enthalpy of combustion would have been larger.

$$\bar{q}^{o}_{liquid} = \frac{1}{1}\left[(1)(-393075) + (2)(-286084) + 0 - (1)(-74894) - 0 - 0\right] = -890349\left[\frac{kJ}{kmol}\right]$$

or

$$q^{o}_{liquid} = - 890349 / 16.042 = - 55501 \text{ [kJ/kg]}$$

Eq. I.3

This occurs because more combustion energy (latent heat) is obtained from the reactor due to heat transfer when the vapour is condensed to water. The enthalpy of combustion when liquid water is produced is often called the higher heating value (HHV) of the fuel (usually the minus sign is dropped when this name is used). And the enthalpy of combustion is called the lower heating value (LHV) when water vapour is produced (again we drop the minus sign). In practical devices, the LHV is the only choice that we have,

APPENDIX J
CALIBRATION OF THE HEAT FLUX SENSORS

There are two different methods which we recurrently used to calibrate the plug-type and the plug-T-type heat flux sensors. These methods are the black body furnace and the thin-air-layer method. The calibration of the heat flux sensors is a long and labor consuming process. First the black ones are calibrated against a NIST traceable black-body radiator (Figure J.1) both for normal and hemispherical radiation[113]. The calibration for the normal radiation serves basically the verification purposes.

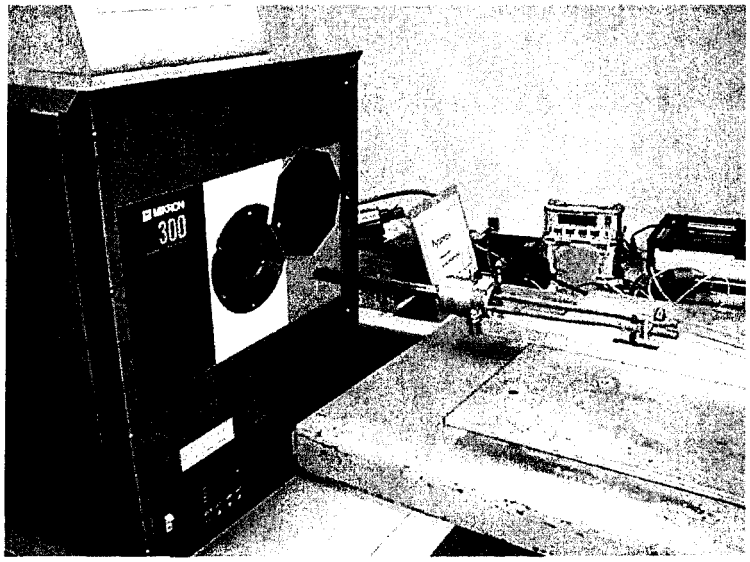

Figure J.1 NIST traceable black-body furnace

For the determination of the sensitivities of both sensors to radiation and convection, we developed a relatively simple method that is based on the heating of the sensors through a thin, horizontal, thermally stable air layer. By the way we can produce known radiative and convective (more precisely conductive through an air layer) heat flow. The method can be used even for the regular verification and recalibration of the built-in sensors inside the furnace (see Figure J.2).

The convective heat flow can be calculated as:

$$q_{conv} = \left[\frac{T_1 + T_2}{2} \cdot C_1 + C_2\right]\frac{A_2}{s}(T_1 - T_2)$$

Eq. J.1

where the first term on the right hand side in square brackets is the thermal conductivity of air (C_1 and C_2 are constants), and 's' is the air layer thickness.

$$q_{rad} = A_2\sigma\left[T_1^4 - T_2^4\right]\cdot\varepsilon_2$$

Eq. J.2

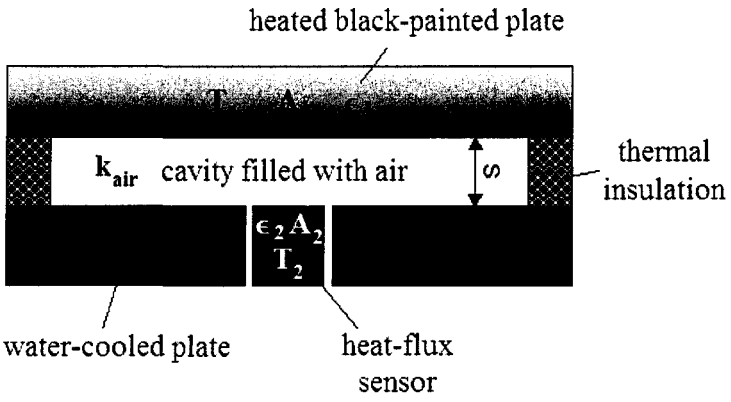

Figure J.2 Schematic view of the calibration unit basing on the thin-air-layer method

The measured voltage using the heat flux sensor with the bright (polished, gold) surface is the following:

$$U_{BR} = \left[q_{conv} + q_{rad} \cdot \varepsilon_{BR}\right] \cdot F_{c,BR}$$

Eq. J.3

where F_c is the conversion factor between voltage and heat flux and ε is the surface emissivity of the sensor. The measured voltage of the black-painted sensor is:

$$U_{BL} = \left[q_{conv} + q_{rad} \cdot \varepsilon_{BL}\right] \cdot F_{c,BL}$$

Eq. J.4

As it can be seen, we have two equations (Eq. J.3 and Eq. J.4) and four unknowns. Supposing that the conversion factors and the surface emissivities are constants, their values can be found by varying the incident heat fluxes. In the case of the incident heat fluxes, the only variable is the temperature. Keeping the temperature of the cold-side constant and varying the temperature of the heated black-painted plate, the incident heat flux on the sensor surface can be controlled.

APPENDIX K
PLUG-T-TYPE HEAT FLUX SENSORS

K.1 Numerical model for optimizing the sensor dimensions and materials

Due to the complex geometry of the plug-T-type heat flux sensor, numerical method was applied for optimizing the sensor geometry. Finite volume method was used for obtaining the temperature field. The numerical calculation was carried out for different sensor geometries and the best concept had been selected and fabricated.

The first step in the finite volume method is to divide the domain into discrete control volumes. We have placed a number of nodal points in the space between the two sides and between the top and the bottom of the domain. The boundaries (or faces) of control volumes are positioned mid-way between adjacent nodes. Thus each node is surrounded by a control volume or cell. It is a common practice to set up control volumes near the edge of the domain in such a way that the physical boundaries coincide with the control volume boundaries.

The steady state diffusion of a property ϕ in a three-dimensional cylindrical domain is governed by:

$$\frac{1}{r}\frac{\partial}{\partial r}\left(\Gamma r\frac{\partial \phi}{\partial r}\right)+\frac{1}{r^2}\frac{\partial}{\partial \varphi}\left(\Gamma\frac{\partial \phi}{\partial \varphi}\right)+\frac{\partial}{\partial z}\left(\Gamma\frac{\partial \phi}{\partial z}\right)+S=0$$

Eq. K.1

where Γ is the diffusion coefficient, ϕ is the dependent variable and S is the source term. Applying this governing equation to a three-dimensional steady state conductive heat transfer, it yields to:

$$\frac{1}{r}\frac{\partial}{\partial r}\left(kr\frac{\partial T}{\partial r}\right)+\frac{1}{r^2}\frac{\partial}{\partial \varphi}\left(k\frac{\partial T}{\partial \varphi}\right)+\frac{\partial}{\partial z}\left(k\frac{\partial T}{\partial z}\right)+S=0$$

Eq. K.2

where thermal conductivity k takes the place of Γ and the dependent variable is temperature T.

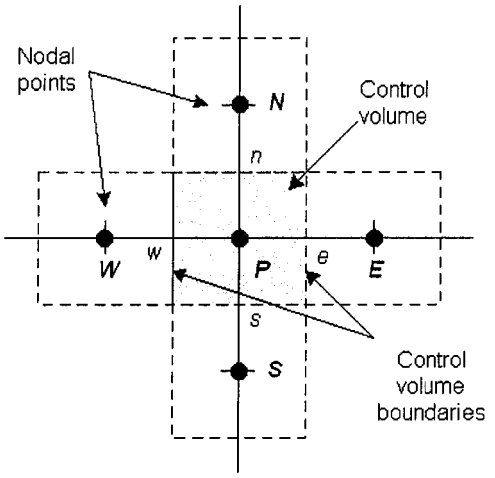

Figure K.1. General two dimensional domain in CFD

At this point it is appropriate to choose a system of notation that we will use in future developments. The usual convention of CFD methods is presented, for example, by Versteeg and Malalasekera[114]. For cylindrical coordinates, a two dimensional domain is

shown in Figure K.2, where the r-axis represents the radial direction while the z-axis is the axial direction.

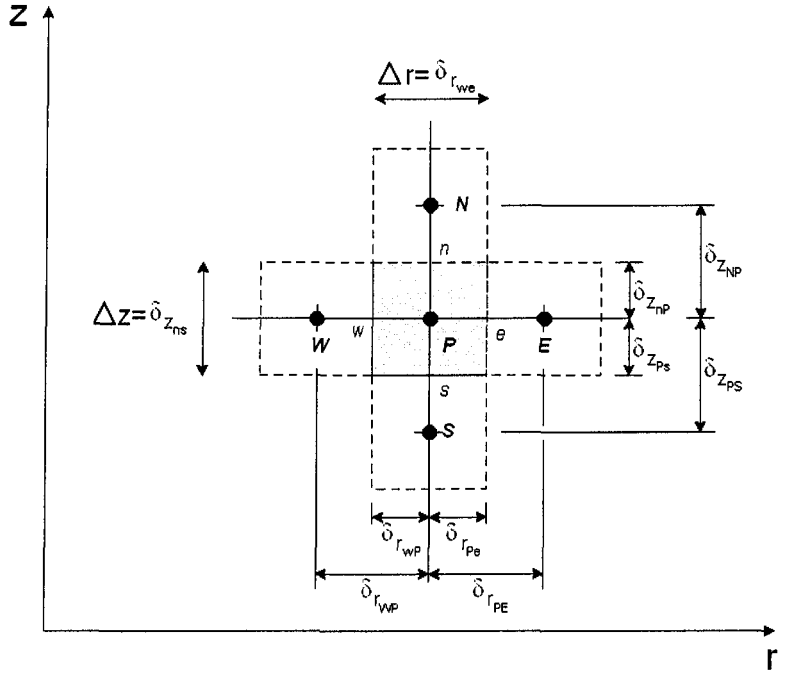

Figure K.2. Two dimensional domain using cylindrical coordinate system in CFD

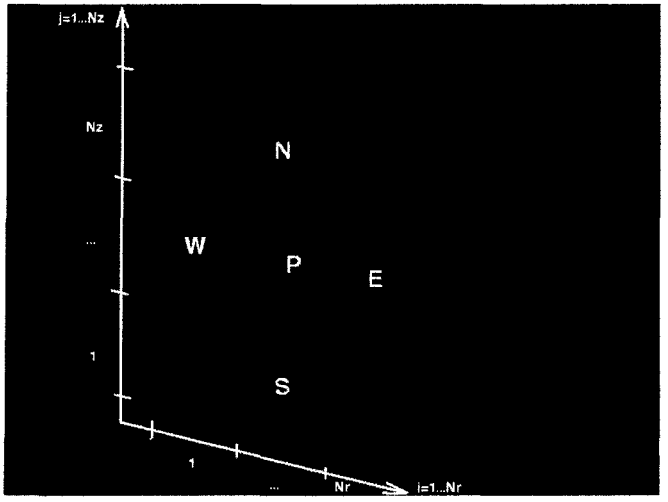

Figure K.3. Cylindrical coordinates in 3D

A general nodal point is identified by P and its neighbours in a two-dimensional geometry, the nodes to the west and east and the nodes to the north and south, are identified by W, E, N and S respectively. The side face of the control volume is referred to by appropriate minuscule that is meaning the west side control volume face by 'w', for example. Horizontally, the distances between the nodes W and P, and between the nodes P and E, are identified by $\delta_{r_{WP}}$ and $\delta_{r_{PE}}$ respectively. Vertically, the distances between the nodes N and P, as well as the nodes P and S are identified by $\delta_{z_{NP}}$ and $\delta_{z_{PS}}$ respectively. Similarly the distances between face 'w' and point 'P', between 'P' and face 'e', between face 'n' and 'P' and between point 'P' and face 's' are denoted by $\delta_{r_{wP}}$, $\delta_{r_{Pe}}$, $\delta_{z_{nP}}$ and $\delta_{z_{Ps}}$ respectively. Figure K.2 shows that the control volume width is $\Delta r = \delta_{r_{we}}$ horizontally and $\Delta z = \delta_{z_{ns}}$ vertically.

The key step of the finite volume method is the integration of the governing equation (or equations) over a control volume to yield a discretised equation at its nodal point 'P'. The integral form of the governing equation for the three-dimensional, cylindrical control volume is

$$\int_{\Delta V}\frac{1}{r}\frac{\partial}{\partial r}\left(\Gamma r\frac{\partial\phi}{\partial r}\right)dr\cdot rd\varphi\cdot dz+\int_{dV}\frac{1}{r^2}\frac{\partial}{\partial\varphi}\left(\Gamma\frac{\partial\phi}{\partial\varphi}\right)dr\cdot rd\varphi\cdot dz+$$
$$+\int_{\Delta V}\frac{\partial}{\partial z}\left(\Gamma\frac{\partial\phi}{\partial z}\right)dr\cdot rd\varphi\cdot dz+\int_{\Delta V}S_\phi dV=0 \qquad \text{Eq. K.3}$$

where ΔV is equal to $dr\cdot rd\varphi\cdot dz$ (see Figure K.4).

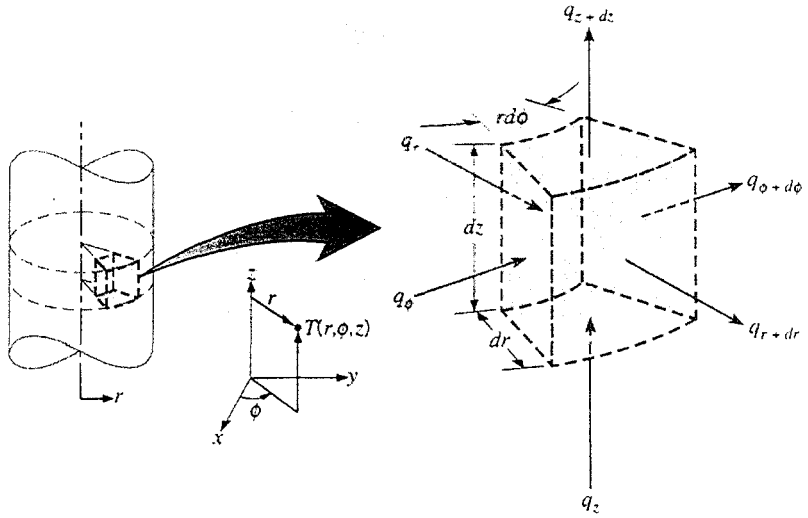

Figure K.4. Differential control volume, $dr \cdot rd\varphi \cdot dz$, for conduction analysis in cylindrical coordinates (r, φ, z)[29]

When the distribution of the dependent variable in the circumferential direction is taken to be uniform, the above equation can be simplified to two dimensions, so we obtain

$$\int_{\Delta V}\frac{1}{r}\frac{\partial}{\partial r}\left(\Gamma r\frac{\partial\phi}{\partial r}\right)dV+\int_{\Delta V}\frac{\partial}{\partial z}\left(\Gamma\frac{\partial\phi}{\partial z}\right)dV+\int_{\Delta V}SdV=0$$

Eq. K.4

so, noting that

$$A_e=r_e d\varphi\cdot dz;\quad A_w=r_w d\varphi\cdot dz;\quad A_n=A_s=\frac{r_e+r_w}{2}d\varphi\cdot dz=r_P\cdot d\varphi\cdot dz$$

Eq. K.5

we obtain:

$$\left[\frac{1}{r_e}\Gamma_e r_e A_e\left(\frac{\partial\phi}{\partial r}\right)_e-\frac{1}{r_w}\Gamma_w r_w A_w\left(\frac{\partial\phi}{\partial r}\right)_w\right]+$$
$$+\left[\Gamma_n A_n\left(\frac{\partial\phi}{\partial z}\right)_n-\Gamma_s A_s\left(\frac{\partial\phi}{\partial z}\right)_s\right]+\bar{S}dV=0$$

Eq. K.6

Here A_{index} is the cross-sectional area of the control volume face, ΔV is the volume and $\overline{S}$ is the average value of source 'S' over the control volume. It is a very attractive feature of the finite volume method that the discretised equation has a clear physical interpretation. Eq. K.6 states that the diffusive flux of ϕ leaving the east and north faces minus the diffusive flux of ϕ entering the west and south faces is equal to the generation of ϕ, i.e. it constitutes a balance equation for ϕ over the control volume.

In order to derive useful forms of the discretised equations, the interface diffusion coefficient Γ and the gradient $\frac{\partial \phi}{\partial r}$ at east 'e' and west 'w' as well as the gradient $\frac{\partial \phi}{\partial z}$ at north 'n' and south 's' are required. Following well-established practice, the values of the property ϕ and the diffusion coefficient are defined and evaluated at nodal points. To calculate gradients (and hence fluxes) at the control volume faces, an approximate distribution of properties between nodal points is used. Linear approximation seems to be the obvious and simplest way of calculating interface values and the gradients. This practice is called central differencing. In a uniform grid linearly interpolated values for Γ_e and Γ_w are given by

$$\Gamma_w = \frac{\Gamma_W + \Gamma_P}{2};\ \Gamma_e = \frac{\Gamma_P + \Gamma_E}{2};\ \Gamma_n = \frac{\Gamma_N + \Gamma_P}{2};\ \Gamma_s = \frac{\Gamma_P + \Gamma_S}{2}$$

Eq. K.7

For the diffusive flux terms through control volume faces, we can write the following expressions:

$$\text{Flux across the west face} = \Gamma_w A_w \left(\frac{\partial \phi}{\partial r}\right)_w = \Gamma_w A_w \frac{(\phi_P - \phi_W)}{\delta_{r_{WP}}}$$

$$\text{Flux across the east face} = \Gamma_e A_e \left(\frac{\partial \phi}{\partial r}\right)_e = \Gamma_e A_e \frac{(\phi_E - \phi_P)}{\delta_{r_{PE}}}$$

$$\text{Flux across the south face} = \Gamma_s A_s \left(\frac{\partial \phi}{\partial z}\right)_s = \Gamma_s A_s \frac{(\phi_P - \phi_S)}{\delta_{z_{SP}}}$$

$$\text{Flux across the north face} = \Gamma_n A_n \left(\frac{\partial \phi}{\partial z}\right)_n = \Gamma_n A_n \frac{(\phi_N - \phi_P)}{\delta_{z_{PN}}}$$

Eq. K.8

By substituting the above equation into Eq. K.6 we obtain

$$\Gamma_e A_e \frac{(\phi_E - \phi_P)}{\delta_{r_{PE}}} - \Gamma_w A_w \frac{(\phi_P - \phi_W)}{\delta_{r_{WP}}} + \Gamma_n A_n \frac{(\phi_N - \phi_P)}{\delta_{z_{PN}}} - \Gamma_s A_s \frac{(\phi_P - \phi_S)}{\delta_{x_{SP}}} + \bar{S}\Delta V = 0$$

Eq. K.9

When the source term is represented in linearised form $\bar{S}\Delta V = S_u + S_p \phi_p$, this equation can be rearranged as

$$\left(\frac{\Gamma_w A_w}{\delta_{r_{WP}}} + \frac{\Gamma_e A_e}{\delta_{r_{PE}}} + \frac{\Gamma_s A_s}{\delta_{z_{SP}}} + \frac{\Gamma_n A_n}{\delta_{z_{PN}}} - S_p\right)\phi_P =$$

$$= \left(\frac{\Gamma_w A_w}{\delta_{r_{WP}}}\right)\phi_W + \left(\frac{\Gamma_e A_e}{\delta_{r_{PE}}}\right)\phi_E + \left(\frac{\Gamma_s A_s}{\delta_{z_{SP}}}\right)\phi_S + \left(\frac{\Gamma_n A_n}{\delta_{z_{PN}}}\right)\phi_N + S_u$$

Eq. K.10

Identifying the coefficients of ϕ_W, ϕ_E, ϕ_S and ϕ_N in Eq. K.10 as a_W, a_E, a_S and a_N, and the coefficient of ϕ_P as a_P, the above equation can be written as

$$a_P \phi_P = a_W \phi_W + a_E \phi_E + a_S \phi_S + a_N \phi_N + S_u$$

Eq. K.11

where

$$a_W = \left(\frac{\Gamma_w A_w}{\delta_{r_{WP}}}\right);\quad a_E = \left(\frac{\Gamma_e A_e}{\delta_{r_{PE}}}\right);\quad a_S = \left(\frac{\Gamma_s A_s}{\delta_{z_{SP}}}\right);\quad a_N = \left(\frac{\Gamma_n A_n}{\delta_{z_{PN}}}\right);$$

$$a_P = a_W + a_E + a_S + a_N - S_p$$

Eq. K.12

The above discretised equations are basically the same as for a Cartesian coordinate system. For that very reason, the correct definition of face areas has crucial importance. In a two dimensional case, while the circumferential direction is taken to be uniform, the discretised face areas are:

$$A_e = r_e \cdot dz;\quad A_w = r_w \cdot dz;\quad A_n = A_s = \frac{r_e + r_w}{2} \cdot dz = r_P \cdot dz$$

Eq. K.13

Discretised equations of the form Eq. K.11 must be set up at each of the nodal points in order to solve a problem. For control volumes that are adjacent to the domain boundaries the general discretised Eq. K.11 is modified to incorporate boundary conditions. The resulting system of linear algebraic equations is then solved to obtain the distribution of the property ϕ at nodal points. Any suitable matrix solution technique may be enlisted for this task.

In the preceding section, the governing equation was presented and with appropriate technique this equation was discretised to attain linear algebraic equations. There are two families of solution techniques for linear algebraic equations: direct methods and indirect or iterative methods. The Thomas algorithm (developed by Thomas in 1949) or the tri-diagonal matrix algorithm (TDMA) is actually a direct method for one-dimensional

situations, but it can be applied iteratively in a line-by-line fashion, to solve multi-dimensional problems and is widely used in CFD programs. This method was also used in our FORTRAN program.

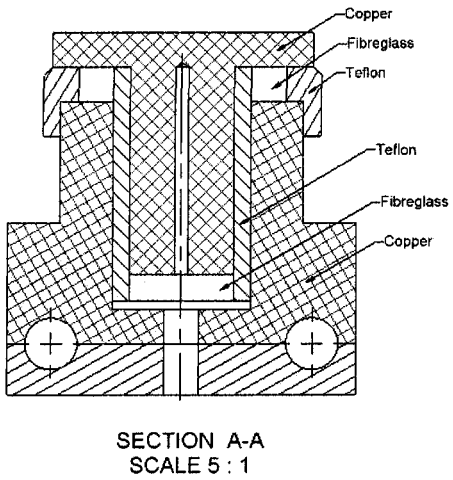

Figure K.5. The final conception of the new Heat-Flux Sensor - Broken view

In our heat-flux sensor (HFS) model, the source term in the internal nodes is always zero, since neither heat source nor heat sink are present there. (Let see the basic governing equation, Eq. K.2, or its integral, adapted form, Eq. K.4) The boundary conditions are first, second and third kinds. The third-kind boundary condition is non-linear. In the central axis, a symmetric plane is taken.

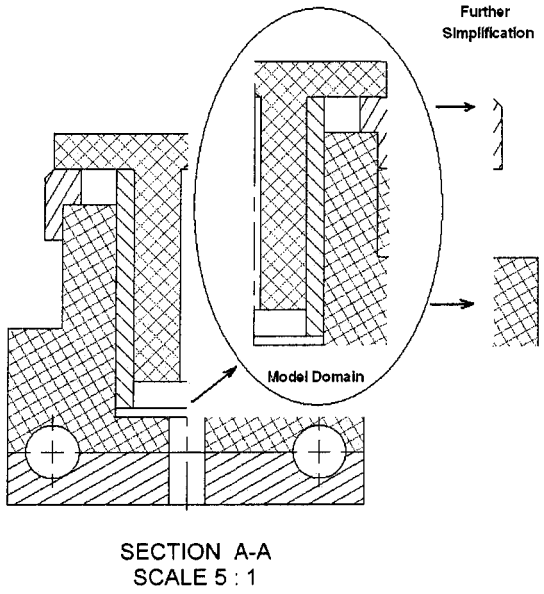

Figure K.6. Performed simplifications for the numerical modeling

The final conception of the new, plug-T-type heat flux sensor is presented in Figure K.5. Basically, the concept of this new HFS is similar to his ancestor. Considering its functionality, this sensor contains also three basic component. These are the T-shaped central cylindrical copper core, the isolating teflon ring, and the outer cylindrical cooling block. The other components, as the outer Teflon ring and the fibreglass packs are important for the heat-contact invariability as well as for the better positioning and gliding of the transducer in the guiding duct. The final conception of this plug-T-type heat-flux sensor is presented in Figure K.5.

In the mathematical model, we tried to simplify the geometry as far as possible. So, we applied a symmetric plane in the axis of revolution and some parts were simply neglected. Figure K.6 shows all the applied modifications.

The next step is to divide the domain into discrete control volumes. Obviously, by the division of the domain, there are a minimal number of cells needed in both directions which is depending on the geometry. Naturally, the accuracy of the calculation increases if the domain is divided into more cells.

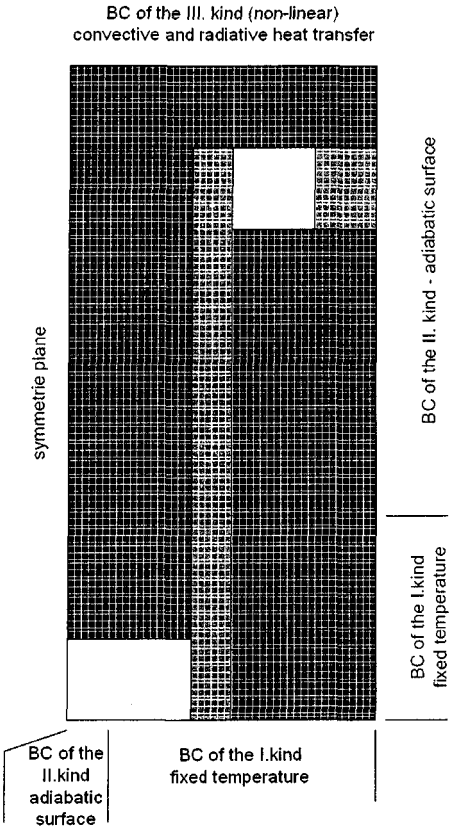

Figure K.7. Model geometry with the applied boundary conditions

Applying this numerical model, the optimal heat flux sensor parameters were found. As an example, a numerical result is shown in Figure K.8 from the preliminary period, when the optimal number of cells was searched. By other words, this is the required grid refining parameter.

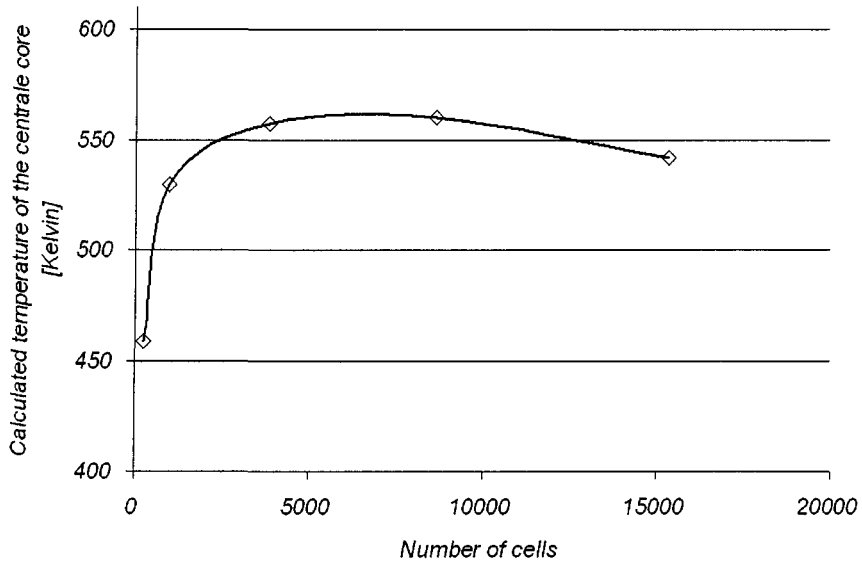

Figure K.8. Example of a typical numerical result – calculated central core temperature for a given incident heat flux as a function of the number of cells (grid refining parameter)

APPENDIX L

TRANSFORMATION OF THE FURNACE